The Development of a Novel *in vitro* Flow System to Evaluate Platelet Activation and Procoagulant Potential Induced by Bileaflet Mechanical Heart Valve Leakage Jets

A Thesis Presented to the Academic Faculty

By

Anna M. Fallon

In partial fulfillment of the requirements for the degree of
Doctor of Philosophy in Chemical and Biomolecular Engineering

Georgia Institute of Technology
May 2006

The Development of a Novel *in vitro* Flow System to Evaluate Platelet Activation and Procoagulant Potential Induced by Bileaflet Mechanical Heart Valve Leakage Jets

Approved by:

Dr. Ajit P. Yoganathan, Advisor
Wallace H. Coulter Department
of Biomedical Engineering
Georgia Institute of Technology

Dr. Stephen R. Hanson
Department of Biomedical
Engineering
Oregon Graduate Institute

Dr. Timothy M. Wick
Department of Biomedical
Engineering
University of Alabama, Birmingham

Peter J. Ludovice
School of Chemical and
Biomolecular Engineering
Georgia Institute of Technology

Dr. Dale E. Edmondson
Department of Biochemistry
EmoryUniversity

Approved: January 13, 2006

ACKNOWLEDGMENTS

The completion of my thesis research and writing has been an arduous task that would not have been possible without the help of many individuals. During my time at Georgia Tech, I have gotten married and had two wonderful children. For these blessings and for all his support, I must first give thanks to my husband, Tom. He has been both a comforter when I was discouraged and a motivator when I was not meeting my potential. For my happiness he has sacrificed and worked hard to support our family, and for this I give my eternal gratitude. I must also thank my children, Thomas and Alyssa, who give me joy and lift my spirits each time that I see them after a long day and our new child who will bring us even more joy in April, 2006. My children have been an unending source of optimism and happiness and help me to remember what is truly important in life.

I would also like to thank my family who believed in me and helped me in any way that they could. I am especially grateful to my father who always told me that I could accomplish anything. I hope that I can continue to meet his expectations as I continue towards my research goals.

For assisting in my professional development as a researcher, I thank my advisor Dr. Ajit Yoganathan. He accepted me as a graduate student despite the fact that I was four months pregnant and supported me both in my research and in caring for my children. I have learned a great deal from him about both performing meaningful research and managing time to complete the many tasks that are required of researchers to ensure

continuation of funding. The knowledge that I have accrued will serve me well as I continue in the academic field.

I would also like to thank Dr. Stephen Hanson and Ulla Marzec for their indispensable assistance in developing the blood experimental methodology. Their advice was instrumental in helping me to complete this research. The advice of my other thesis committee members, Dr. Tim Wick, Dr. Pete Ludovice, and Dr. Edmundson, has also been key in developing the specific aims and guiding me towards completing the goals of this research. For their advice and for the time that they spent at my thesis proposal and research updates as well as the time that they will spend reading this thesis, I thank them.

Thank you also to the cardiovascular fluid mechanics lab members who have helped me along the way. Many of them babysat for my children, and others helped me to learn the various techniques that I have used to complete my thesis research. I want to specifically thank Prasad and Leo for helping me with PIV and reading and commenting on my thesis. I also want to thank Hélène for helping me with Tecplot, and Yun and Suchitra for watching my children many times. Working in this lab has been an enriching experience, and I will cherish the friendships that I have made.

I must also give thanks to the two people who made working in this lab possible by their sweetness and organization. Chris Ruffin and, more recently, Michelle Mayberry both enabled me to work in this lab by helping me greatly with my administrative duties. Were it not for them, I would have never been reimbursed for anything, and lab life would not have gone as smoothly. Both of them have become friends who I will remember and cherish forever for their good natures and extreme patience.

Two other individuals who have made my research more meaningful are Tom and Shirley Gurley. I thank them for their kind donations to fund my research as well as there sincere interest in my research. It is very rewarding to know people like them. Their generosity and kind hearts remind me why I do my research.

Finally, I would like to thank Tracey Couse who assisted me greatly with my histology, and Jack Horner who coordinated efforts in the Georgia Tech clinic so that I could have blood drawn for my experiments. Without the two of them, my research would not have been possible.

TABLE OF CONTENTS

LIST OF TABLES

LIST OF FIGURES

LIST OF SYMBOLS AND ABBREVIATIONS

a	Jet decay constant (dimensionless)
D	Orifice diameter
f	Aperture number
g	Acceleration of gravity (m/s^2)
h	Height (m)
L	Length (m)
M_{cal}, N_{cal}	Grid size on CCD camera (pixels)
m	Total number of measurement locations studied (dimensionless)
N	Number of PIV image pairs
N_v	Array of totally independent vectors
N_{int}	Side of the interrogation area (pixels)
n	Number of measurements or normal vector (dimensionless)
ν	Kinematic viscosity (cSt, 1/1000,000 m^2/s)
p	Pressure (mm Hg)
ρ	Density (kg/m^3)
R_1 R_2	Correlation functions of CCD camera image pairs
T,t	Time (s)
U	Instantaneous axial velocity (m/s)
u_o,v_o	Average velocity (m/s)
u', v'	Fluctuating velocity (m/s)
u_i,v_i	Specific velocity measurement (m/s)

τ	Reynolds shear stress (dynes/cm^2, 10 × N/m^2)
V	Average centerline velocity at a point Y
V_c	Average centerline velocity at Y_o
X	Pixel coordinate on CCD camera (pixels)
Y	Pixel coordinate on CCD camera (pixels)
Y_o	Jet origin
CFD	Computational fluid dynamics
CM	CarboMedics
LDV	Laser Doppler velocimetry
MP	Medtronic Parallel
DPIV	Digital particle image velocimetry
PF4	Platelet factor 4
PReS	Principal Reynolds stress (dyn/cm^2)
PS	Phosphatidyl Serine
RBC	Red blood cell
SIPAct	Shear-induced platelet activation
SIPA	Shear-induced platelet aggregation
SJM	St. Jude Medical
TAT	Thrombin-Antithrombin III
vWF	von Willebrand Factor

SUMMARY

Thromboembolic events caused by implanted cardiovascular devices present serious challenges to surgeons and researchers alike. In particular bileaflet mechanical heart valves are prone to thrombus formation in the hinge region due to a combination of high shear stress and stagnation regions. Shear-induced platelet activation and aggregation is usually studied using viscometers, parallel plate flow, and other non-physiologic *in vitro* configurations. However, it is desirable to study this phenomenon in a more physiological environment.

The research presented in this thesis addresses the hypothesis that models that isolate and mimic bileaflet mechanical heart valve (BMHV) hinge geometries can be used to quantitatively characterize procoagulant potential using a novel *in vitro* blood flow system. Furthermore, these results can be correlated with digital particle image velocimetry measurements detailing flow fields for the same models. To test this hypothesis, sensitive markers of platelet activation and the presence of activated thrombin were used to quantitatively measure these endpoints in a novel *in vitro* flow system utilizing the recalcification of citrated blood to enable propagation of the coagulation cascade. Simple round and slit orifices were used to model the hinge region and B-datum line, respectively, of BMHVs. Channels that approximated the different geometries of various BMHV hinge designs were also developed and evaluated in this flow system. As a final test, BMHVs were also studied using these same techniques to assess the influence on hinge gap width and hinge geometry on platelet activation and procoagulant potential. Lastly, the jets originating from these orifices and channels were studied using digital

particle image velocimetry (DPIV), and the velocity data were analyzed to determine differences in these jets that may increase the propensity for coagulation as a result of flow through the different orifices and channels.

The significant findings were that: 1) recalcification of recirculating citrated blood markedly increases the magnitude of thrombus forming reactions and the sensitivity for their detection; 2) a shear-dependent threshold for thrombin generation and coagulation exists, suggesting that clotting in a BMHV is most likely due to leakage flow through the hinge area and not through the B-datum line; 3) platelet activation, and the presence of adequate platelet numbers, may be essential for the activation of coagulation under conditions of high shear; and 4) thrombin formation can be inhibited by blocking the platelet receptors that facilitate platelet aggregation.

The results from the DPIV studies give some insight into why the different channels resulted in varying propensities for coagulation as measured by TAT concentration. The channel geometries that induced significantly higher levels of TAT also formed jets that were subject to increased entrainment of the stagnant fluid in the chamber. This entrainment resulted in more rapid jet decay for the channel jets with more abrupt diameter changes relative to the channel jets with smoother transitions. Additionally, entrainment enables more mixing of the shear-activated platelets with the surrounding flow, which can propagate the coagulation cascade, thus increasing the chance for thrombus formation. The channel geometries that produced these jets that were more susceptible to entrainment had abrupt changes in diameter with 90 degree angles. Thus, these abrupt changes in diameter engender flow fields that are more favorable for propagation of the coagulation cascade.

The influence of abrupt changes in diameter was also evident in the human blood studies designed to investigate the effect of BMHV hinge geometry. The MP valve, which has a tortuous pathway through the hinge channel, induced significantly more TAT formation than the SJM Standard valve with a smoother hinge channel. This increased coagulation potential for the MP valve was not accompanied by an increase in platelet activation relative to the SJM Standard valve. Thus, although platelet activation was similar for both of the valves, procoagulant potential was not. This result shows that it is not necessarily platelet activation that is important in determining whether or not a valve will induce thrombosis *in vivo*. It is the subsequent flow fields after platelet activation has occurred that determine procoagulant potential. Nevertheless this study does show that MHV hinge geometry should be as smooth and free of diameter changes as possible to eliminate circulation and stagnation regions that enable activated platelets to congregate and propagate the coagulation cascade.

Leakage gap width also had a significant effect not only on procoagulant potential but also on platelet activation. Both the low and high leaker prototype valves had significantly higher levels of platelet activation compared to the SJM Standard valve, but only the low leaker valve demonstrated a higher propensity for coagulation. Since it is important to minimize both platelet activation and thromboemboli formation, an optimal gap width should be maintained for BMHVs that is similar to that of the SJM Standard valve to minimize both of these parameters.

CHAPTER 1

INTRODUCTION

Heart valve disease is a serious condition caused by congenital defects, rheumatic fever, calcification as a consequence of aging, myocardial infarction, and other cardiovascular disease. If the disease progression is serious enough, a bio-prosthetic or mechanical heart valve (MHV) must be implanted. Worldwide approximately 225,000 prosthetic heart valves are implanted each year, and about 50% of these are MHVs. MHVs are chosen for their durability, but they are prone to complications due to thromboembolic events, and recipients must undergo lifelong anticoagulant therapy.

Studies using laser doppler velocimetry (LDV) have implicated the hinge region of MHVs as the key region for thrombosis formation. In this region flow can stagnate, and if activated platelets and other thrombus components are not completely washed out, thombi can grow to obstruct leaflet movement or embolize, leading to a risk of strokes. The mechanism by which MHVs initiate thrombosis are unclear, but it is thought that platelets that travel through this high shear stress hinge region become activated by the shear and then aggregate in the subsequent low flow regions downstream of the hinge region.

Fluid dynamics methods such as laser Doppler velocimetry (LDV) or digital particle image velocimetry (DPIV) used to evaluate MHVs have indicated areas of bileaflet mechanical valves and times during the cardiac cycle that are vulnerable to thromboemboli formation caused by elevated shear stress. Studies on the St. Jude Medical (SJM), Carbomedics, and Medtronic Parallel valves utilizing LDV to investigate

the hinge area showed maximum Reynolds stress magnitudes of 7,200, 5510, and 8000 dynes/cm^2, respectively, during the leakage phase. Additionally, leakage flow studies on the Medtronic Parallel valve using markers for platelet activation and platelet damage showed that platelets were activated and damaged in a time dependent fashion with activation and damage increasing with time. Similar studies performed with SJM standard prototype valves with higher and lower leakage values than normal and found that there were differences in platelet activation, and that the high leaker valve had significantly more platelet activation than the standard valve.

These LDV measurements as well as the platelet activation studies imply that hinge geometry and leakage magnitude do have a significant effect on turbulent shear stresses and subsequent clot formation. However, there is difficulty in isolating the hinge region during blood studies because of the presence of the sewing ring, valve surface, and leakage through the periphery of the leaflets. In this study models were developed that isolate the hinge area so that hinge geometries can be directly compared without the complications introduced by the rest of the MHV. A novel *in vitro* flow loop that utilizes the recalcification of citrated blood to enable propagation of the coagulation cascade was also developed. This system allowed us to quantitatively assess procoagulant potential as a result of flow through these model geometries as well as through the bileaflet MHVs. In addition, this study correlated differences in the flow fields through these models measured using DPIV with propensity for coagulation as a result of flow through these different model geometries.

The results of these studies can be used to focus the efforts of bileaflet mechanical heart valve designers on the aspects of valve design that govern flow during the leakage

phase of the cardiac cycle. In addition, the novel *in vitro* flow system and recalcification strategy can be used in conjunction with the assays developed to investigate coagulation and platelet activation to assess these factors for other types of vascular devices that expose the blood to high or variable shear stresses.

CHAPTER 2

BACKGROUND AND LITERATURE REVIEW

2.1. Heart valves

The function of the heart is to pump blood throughout the body to transport oxygen and nutrients to all of the organs and tissues. The right side of the heart pumps blood through the lungs to be oxygenated, and the left side pumps the oxygenated blood through the body. Each side is divided into two chambers, an atrium and a ventricle, as shown in Figure 2.1.1.

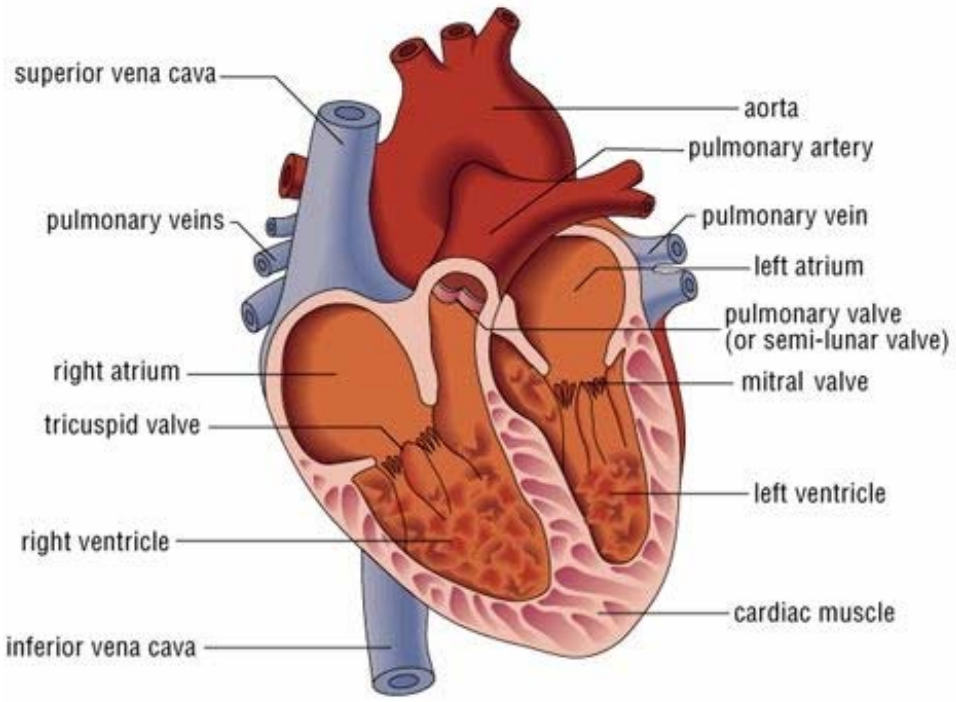

FIGURE 2.1.1 Diagram of the interior heart.

Valves separate these chambers from each other and from the exiting vessels to prevent backflow of the blood.

Blood flows from the vena cavae and the pulmonary vein into the right and left atria, respectively. Figure 2.1.2 shows typical pressure and flow waveforms for the aortic and mitral valves. Approximately 75% of this blood flows directly into the ventricles before atrial contraction, and the subsequent contraction expels the rest of the blood into the ventricles.

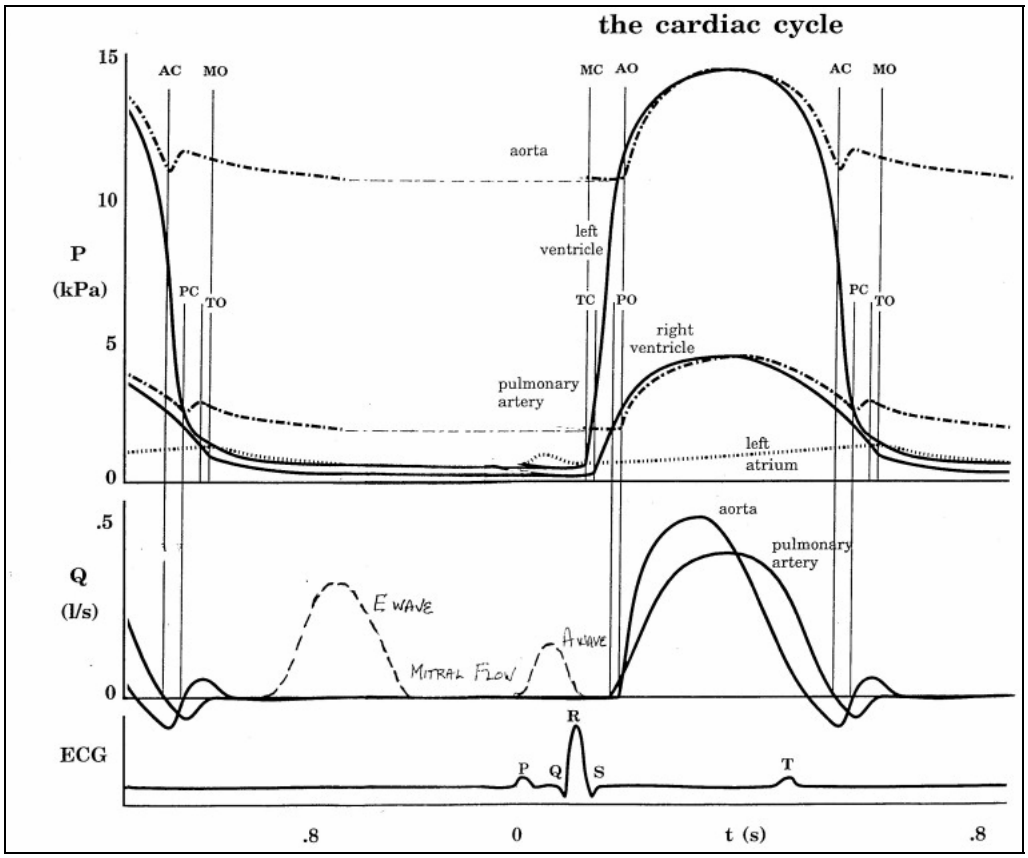

FIGURE 2.1.2 Typical pressure and flow waveforms and EKG during the cardiac cycle (Nichols and O'Rourke).

During ventricular systole the atrio-ventricular (A-V) valves are closed allowing blood to accumulate in the atria. When the ventricular pressure falls during diastole these valves open causing this accumulated blood to rush into the ventricles. This rapid filling stage lasts for the first third of diastole and is followed by a phase characterized by only a small amount of blood flow into the ventricles. During the last third of diastole, the atria

contract thus forcing the remaining 25% of the blood into the ventricles. Atrial contraction is followed by ventricular contraction. Immediately after the onset of ventricular contraction, the pressure in the ventricles increases causing the A-V valves to close. During this time all of the valves are closed so this is termed the isovolumic contraction period. About 0.02 to 0.03 seconds after these valves close, the pressure in the left and right ventricles rises to above 80 and 8 mmHg, respectively, and the aortic and pulmonary valves open expelling blood into the aorta and pulmonary arteries, respectively. About 70% of this ejection occurs during the first third of the period of ejection, or period of rapid ejection. The remaining 30% is expelled during the last two-thirds of ejection, or period of slow ejection. After systole the ventricles relax suddenly so that the intraventricular pressures decrease rapidly. The elevated pressure in the large arteries pushes blood backwards towards the ventricles resulting in immediate closure of the aortic and pulmonary valves. During this time all of the valves are closed so this is termed the isovolumic relaxation period. Ventricular relaxation continues for another 0.03 to 0.06 second, and during this time the intraventricular pressures decrease rapidly back to diastolic levels. The A-V valves then open to begin a new cardiac cycle [1].

Heart function is a delicate balance of contraction, relaxation, filling, and ejection with consequent pressure changes that control valve opening and valve closure to monitor blood flow. Thus, any malfunction in the muscular or valvular function of the heart can have serious implications in overall health. Under normal conditions all of these valves open and close passively in response to changes in pressure to prevent backflow of the blood from the ventricles to the atria during systole and from the aorta and pulmonary arteries into the ventricles during diastole. The A-V valves are connected to papillary

muscles located inside the ventricles by the chordae tendinae. These muscles contract when the ventricular walls contract to prevent the leaflets from bulging too far backward toward the atria during contraction. Chordae tendinae rupture or papillary muscle damage can result in valve leakage that can cause severe or even lethal cardiac incapacity. The aortic and pulmonary valves function differently with the main difference being the instant closure of these valves caused by the high arterial pressures compared to the softer closure of the A-V valves. Additionally, because of the smaller openings, the velocity of blood ejection through the aortic and pulmonary valves is much greater. The combination of the rapid closure and ejection subjects these valves to higher mechanical forces than those experienced by the A-V valves [1]. When closed the pulmonary and tricuspid valves must withstand a pressure of 30 mmHg [2]. However, the closed aortic valve must withstand a pressure of 100 mmHg, and the mitral valve closes against a pressure of up to 150 mmHg. Thus the left side of the heart is particularly predisposed to heart valve disease.

The aortic valve is composed of three semilunar leaflets contained within a connective tissue sleeve. The aortic sinus is located superior to the annulus ring and is comprised of three bulges at the root of the aorta that lead to either the left or right coronary arteries or to a blind, or empty, sinus. This valve varies in size and also translates along the axis of the aorta as the heart contracts and relaxes. The peak velocity of flow through the open aortic valve is approximately 1.35 m/s for adults and 1.5 m/s for children. The velocity profile at the orifice plane is almost flat with flow skewed slightly toward the septal wall [2]. During systole vortices develop in the sinuses behind the leaflets that help to close the valve quickly and efficiently [2]. At the end of systole there

is a small amount of reverse flow that can be measured with Doppler ultrasound. This closing volume has been estimated to be less than 5% of the forward flow.

2.2. Heart valve disease

Valvular heart disease is any dysfunction or abnormality of one or more of the heart's four valves. In the United States approximately 5 million people are diagnosed with heart valve disease each year. According to the American Heart Association's 2004 Heart and Stroke Statistical Update, valvular heart disease is responsible for nearly 20,000 deaths each year in the United States and is a contributing factor in about 42,000 deaths [3]. Aortic and Mitral valve dysfunction caused a majority of these deaths with 63% and 14.5% of the total, respectively. Aortic valve dysfunction usually results from valve stenosis in which the valve does not fully open, thus impeding blood flow into the aorta. Aortic valve stenosis occurs in approximately 5 out of every 10,000 people. The main causes of aortic valve stenosis are age-related calcification, rheumatic fever, endocarditis, and congenital heart valve problems. Mitral valve dysfunction can result from either valve stenosis or mitral regurgitation in which the valve does not close properly, thus allowing blood to leak back into the left atrium during ventricular systole.

In less severe cases of valve dysfunction, the valve can be repaired, but if the stenosis or regurgitation is severe enough the valve must be replaced. Every year surgeons perform over 250,000 heart valve operations worldwide. The choices for heart valve replacement include bioprosthetic valves made from porcine heart valves, bovine pericardial, or human cadaver tissue, mechanical heart valves, polymeric heart valves, and in the future tissue-engineered heart valves made from human-derived cells.

Mechanical heart valves are currently used in about 55% of all valve replacements with bioprosthetic valves making up the rest. Although mechanical heart valves (MHVs) have excellent durability, the flow characteristics of the valves subject the blood to high shear stresses that may damage blood elements or activate platelets leading to thromboembolic complications that can be fatal. Thus, MHV recipients must undergo lifelong anticoagulant therapy. Despite the risk of complications from MHVs, there is no doubt that their use has and still does improve the lives of many who face valvular disease.

2.3. Prosthetic heart valves

In October 1952 Dr. Charles Hufnagel implanted the first mechanical heart valve in humans to treat aortic valve insufficiency [4]. It was implanted in the descending aorta of patients. The design of the valve was a methacrylate ball contained in a methacrylate tube. During diastole the ball is passively positioned at the proximal end of tube effectively stopping blood regurgitation. In total over 200 patients received this prosthesis with no anticoagulant therapy. These valves were recovered up to 30 years after implantation with no obvious wear [4].

The advent of the heart-lung machine enabled surgeons to perform open-heart surgery, and in 1955 the first mechanical heart valve, a ball and cage design, was implanted in the aortic position in England by Judson Chesterman [5]. Unfortunately this patient survived only 14 hours, and long term survival was not achieved until 1961 when Charles Hufnagel implanted ball and cage valves into 8 patients and 6 survived [5]. Also during this time some work was being done to design fabric and fabric-coated valves and silicone rubber valves, but this work was ultimately unsuccessful [4]. The Harken ball

valve and the widely used Starr-Edwards ball valve (Figure 2.3.1a) were both introduced in 1960. Both valve designs incorporated a ball of silicone rubber held in place by a cage. The Harken valve initially had an additional cage to shield the valve from incursions into the aortic wall, but this was proved to be unnecessary and subsequently removed [4]. This type of valve functions on the principle that when downstream pressure increases, the ball is forced into the valve orifice thus stopping blood flow and preventing regurgitation. The cage holds the ball in place during forward flow when the upstream pressure is higher. Some innovations were introduced to improve the Starr-Edwards ball valve after 1960, but the valve has remained unchanged in the mitral position since 1965 and in the aortic position since 1968 [6].

Improvements to the ball and cage valve were attempted by changing the materials and altering the cage design; however, the next big innovation in valve design did not occur until the introduction of the tilting disc valve in 1963 by Lillehei, Cruz, and Kaster. Although this valve was unsuccessful in making it to the market due to an area of stasis between the open disc and the aortic wall it did mark an important turning point in valve design [4]. The ball and cage design had good characteristics as far as closing with little or no regurgitation, but the forward flow hemodynamics were not optimal. The ball was located along the center of the orifice jet during forward flow resulting in increased pressure drops and reduced flow efficiency. Also, the cage could become thromobosed and eventually occluded. Thus, the tilting disc valve was designed to provide a more central flow field and, consequently, better hemodynamics. The valve was designed with a disc held in place in a round orifice by struts that restrict its movement. During the forward flow phase the disc is tilted like a door so that it juts through the downtsream

side of the valve and two asymmetric orifices are created through which blood can flow. As the downstream pressure increases, the disc is tilted in the other direction until it is flush with the orifice thus stopping the flow.

Another major contribution to mechanical heart valve construction was provided by Jack Bokros in 1969 in the form of a new biologically compatible and highly durable material called pyrolite carbon. This coating revolutionized mechanical heart valves because it improved both their durability and their biocompatibility. Thus, two successful tilting disc valves, the Bjork-Shiley and Lillehei-Kaster valves, introduced in 1969 and 1970, respectively, were both constructed of this material [4]. The only tilting disc valve currently in use in the Medtronic-Hall valve (Figure 2.3.1b) introduced in 1977.

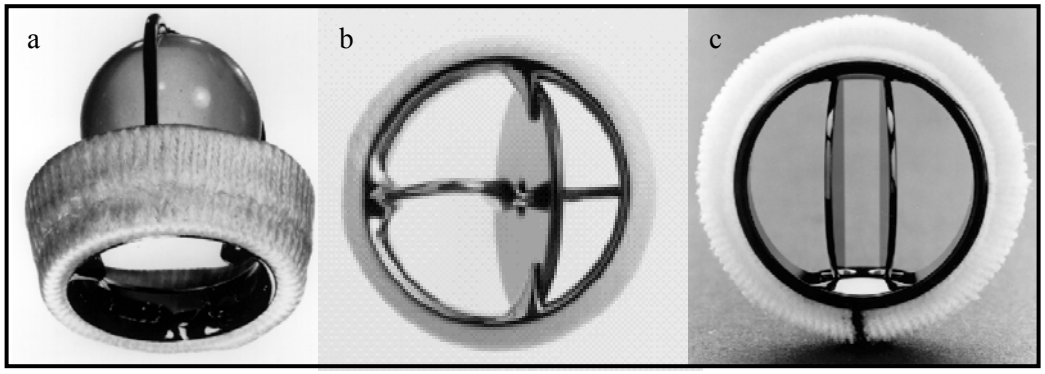

FIGURE 2.3.1. (a) The Starr-Edwards caged-ball valve, (b) Medtronic-Hall tilting disc valve, and (c) St. Jude Medical bileaflet valve

The bileaflet valve was introduced in 1978 with the St. Jude Medical (SJM) valve (Figure 2.3.1c) that is still in use today. This design consists of two semicircular, hinged occluders, or leaflets, that minimize flow disturbance in open position. The leaflets pivot within grooves in the valve orifice housing. The main differences between different bileaflet valves are in the valve opening angle and the hinge design. The SJM valve has an opening angle of 85° and the CarboMedics (CM) valve, which is also used

extensively, has an opening angle of 78°. Both of these valves have butterfly-shaped recesses machined into the housing into which the leaflets are inserted. The Medtronic Parallel (MP) valve, which was not successfully introduced into the market due to thrombosis in clinical trials, was designed with an opening angle of 90°. However, the hinge design resulted in flow fields that lead to thrombosis in these areas.

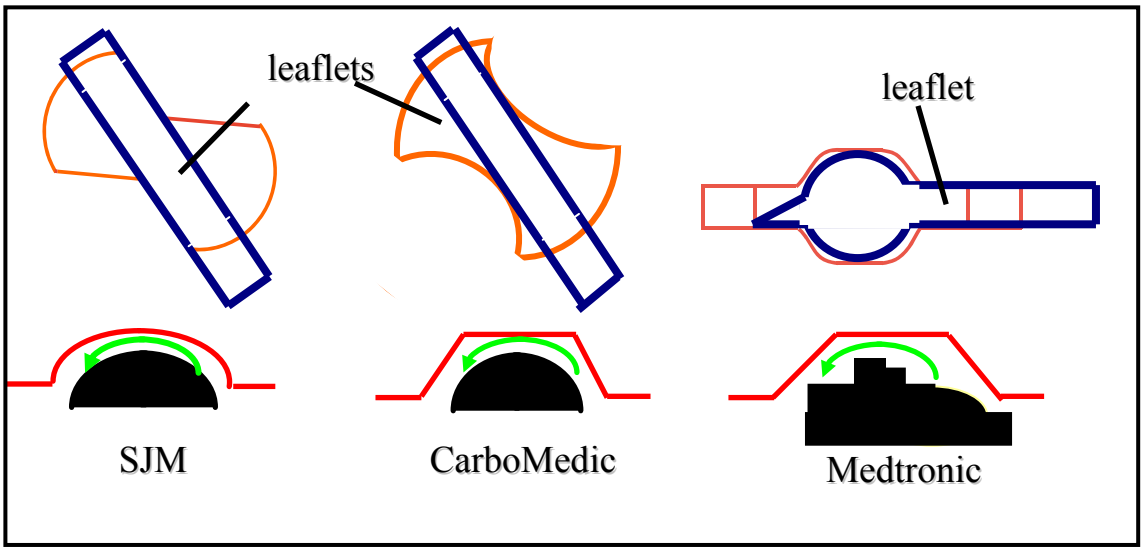

FIGURE 2.3.2. Hinge geometries and flow pathways for the SJM, CarboMedic, and Medtronic Parallel bileaflet MHVs.

During the leakage phase of the cardiac cycle, which occurs at the beginning of diastole for the aortic valve, some degree of leakage is built into the hinge region of bileaflet MHVs to wash out any entrapped blood elements. The geometry of this region has been shown to be very instrumental in the occurrence of thromboembolic complications. The hinge geometries for these three valves are shown in Figure 2.3.2 as well as the flow pathway through the hinge when the valve is closed. The SJM valve has a smooth hinge channel with minimal change in diameter while the Carbomedics valve has a somewhat more angular channel with a noticeable change in diameter. The MP valve, however, has

a very angular pathway with 90 degree steps leading to several changes in diameter and a larger internal diameter.

2.4. Valve-related complications

Recipients of MHVs are prone to complications including tissue overgrowth, thromboembolic complications, hemorrhaging, infection, paravalvular regurgitation, and hemolysis. After implantation, the body immediately begins to respond to the MHV. The exposure of blood to artificial surfaces initiates a series of events including protein adsorption, adhesion and activation of platelets and leukocytes, and the initiation of the coagulation cascade [7]. Initially, plasma proteins are adsorbed onto the valve surface and the sewing ring. These proteins are thought to mediate the blood interactions with the device. Platelets have been shown to attach to MHV's in studies with the Bjork-Shiley valve with the largest percentage on the sewing ring. Thrombus deposition on the sewing ring leads to the formation of either avascular fibrous tissue or granulation tissue accompanied by capillary growth to form vascular fibrous tissue [8]. Avascular tissue is most frequently seen covering the sewing ring while vascular tissue extends into the spaces in the sewing ring between the fibers. Eventually an uneven layer of endothelium covers parts of the tissue. If this tissue growth is completed satisfactorily a relatively non-thrombogenic surface is produced. However, in some cases a pathological overgrowth of this tissue, or pannus formation, occurs that can impair movement of the valve leaflets rendering it non-functional. The exact mechanism of this pathogenesis is uncertain, but it does appear to be related to low cardiac output leading to lower levels of shear stress. Other potential causes may be sporadic anticoagulant use leading to the buildup of layers

of thrombus deposition, overproduction of collagen, or excessive foreign body reaction to tissue adjacent to the sewing ring leading to the formation of successive layers of fibrous tissue [8].

Thrombosis caused by mechanical heart valves can also lead to the formation of emboli that detach from the valve or from a larger clot. These emboli can become lodged in smaller blood vessels, especially in the brain, causing occlusion of these vessels and subsequent strokes or other ischemic events. To prevent these complications implant patients undergo lifelong anti-coagulant therapy. However, along with the therapuetic benefits of anticoagulants come the risk of hemorrhage. Because anticoagulants affect people differently, their outcomes are difficult to predict. The same dosage can affect each person differently and the same person differently from day to day. Because of this difficulty in determining the optimal anticoagulant dosage, patients must be monitored closely to minimize the risk of hemorrhage.

2.5. Bileaflet MHV flow fields

Bileaflet MHVs tend to have better bulk flow hemodynamics than tilting disc or caged ball valves with lower transvalvular pressure drops. Flow profiles for various MHVs are shown in Figure 2.5.1. In bileaflet MHVs the leaflets divide the forward flow into 3 regions consisting of 2 lateral orifices and a central orifice. The primary differences between different bileaflet valve designs exist in the hinge design, opening angle and leaflet curvature. Hinge design variations control the opening angle, thus influencing local fluid mechanics, washout, and flow patterns in the hinge area. In general the three jets formed during forward flow by the lateral and central orifices have

similar peak velocities independent of valve design. There is more flow through the lateral orifices, and these jets are crescent-shaped in contrast to the planar shape of the central jet as seen from the side. The wakes from these jets persist several centimeters downstream, but the central jet is encompassed by the lateral jets 2-3 cm downstream.

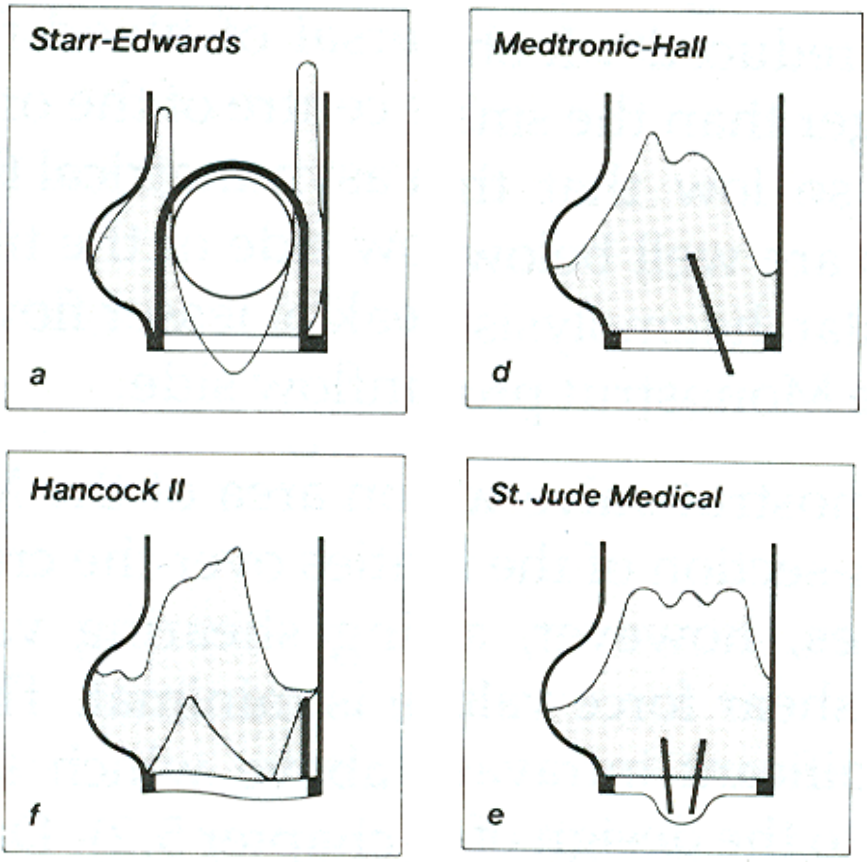

FIGURE 2.5.1. Flow profiles for various MHVs [9].

Velocity and turbulent shear stress (TSS) profiles for the SJM valve at peak systole are shown in Figure 2.5.2 to illustrate the features of these jets [10]. The flow is generally well-ordered during the early acceleration phase of the cardiac cycle, but becomes turbulent prior to peak systole. Separated regions with flow reversal are observed around the perimeter of the housing, and these regions of separation tend to be asymmetric with

larger spatial dimensions near the hinge than adjacent to the lateral jets. This asymmetry may lead to increased thrombogenicity in the hinge region since asymmetry usually leads to flow separation and consequent higher shear stresses. Bileaflet valves typically have lower turbulent shear stresses than tilting disc or caged ball valves during forward flow with peak aortic values from 1000-1500 dyn/cm^2.

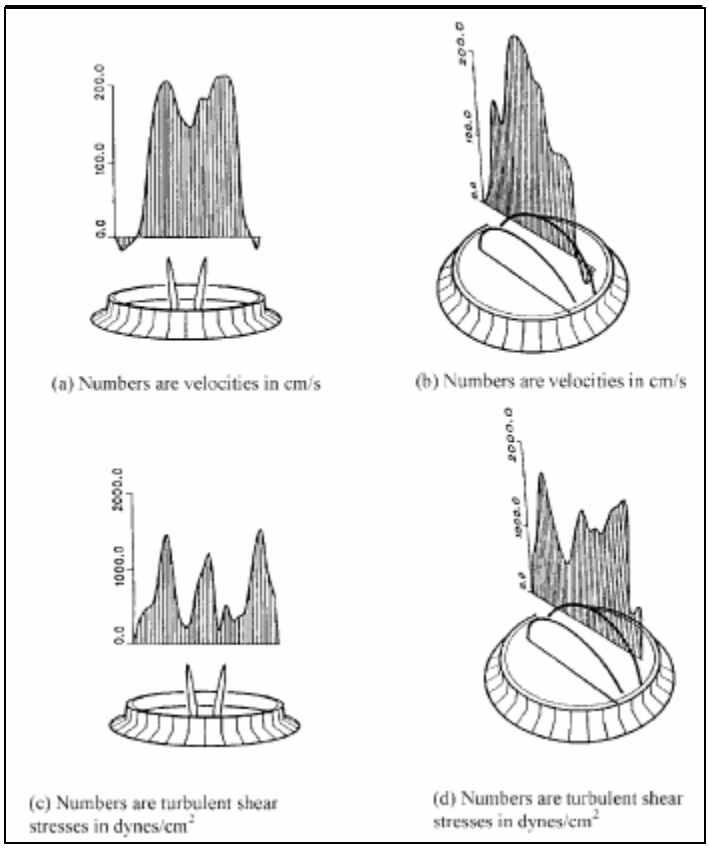

FIGURE 2.5.2. (a) Velocity profile on the centerline 13 mm downstream of the SJM valve at peak systole; (b) Velocity profile across the centerline 13 mm downstream of the SJM valve at peak systole; (c) TSS profile on the centerline 13 mm downstream of the SJM valve at peak systole; (d) TSS profile across the centerline 13 mm downstream of the SJM valve at peak systole [10].

However, regurgitant flow through bileaflet MHVs is generally higher than that of other valve types with leakage flow occurring mainly through the hinge pivots and around the periphery and gap between the leaflets. The major leakage jets have mean velocities of 2-

3 m/s with turbulent shear stresses (TSS) of over 3000 dyn/cm^2. These high TSSs coupled with stagnant flow can lead to thrombus formation since the shear stress may activate the platelets and the stagnant flow then affords the activated platelets sufficient residence time to interact with the necessary proteins to form clots [11]. Previous research utilizing LDV has further detailed the flow fields and turbulence characteristics of different bileaflet MHVs. Except where noted all studies described below are with the valve in the aortic position in physiologic pulsatile flow. Studies performed using a 27 mm SJM standard MHV with data collection at locations 8 and 13 mm downstream of the valve showed that peak velocities and TSS occurred during peak systole at 6.25 mm above centerline corresponding with the lateral jet. These values were 220 cm/s and 2000 dyn/cm^2, respectively. As expected high TSS occurred at locations of high velocity gradients and immediately distal to the leaflets. Regions of flow separation were observed around the jets adjacent to the flow channel wall resulting in flow separating from the orifice ring. This flow separation adjacent to the sewing ring could potentially lead to tissue overgrowth or thrombus formation, which has been reported in the literature. In addition, the region adjacent to the pivot region could also be vulnerable to thrombus formation due to high TSS and flow separation [12]. Studies by Ellis et. al. showed similar forward flow hemodynamics for the 17 mm SJM regent valve, which differs from the SJM standard in that it has 'thumbnail' regions downstream of the hinges that serve to expand the internal orifice. They characterized the central orifice as having a parabolic flow profile with the lateral jets having a more plug-like appearance. Because these measurements were made closer to the valve, facilitated by optically transparent leaflets, flow patterns influenced by the hinge region could be observed.

Interestingly, secondary flow patterns within the aortic sinus adjacent to the hinge region directed from the central orifice jet outward were downstream of and in the same radial-circumferential direction as flow in the thumbnail region. This behavior shows that even in forward flow the hinge region influences the near-field flow [13].

In a study comparing the downstream turbulence characteristics of the 25 mm SJM standard and CM MHVs, differences between the forward flow profiles and resulting Reynolds shear stresses were found. The flow profiles of the lateral jets in the SJM valve were parallel to the orifice jet at peak systole due the larger opening angle while the flow profile of the CM valve lateral jets were oriented toward the wall. The smaller opening angle of the CM valve resulted in a larger wake due to increased disturbance from the leaflets intruding upon the flow. There was also less recirculation flow at the lateral sides in the CM valve. Additionally, Reynolds normal stresses for the CM valve were larger in the central orifice at a maximum value of 1780 dyn/cm^2 compared to the largest Reynolds normal stress for the SJM valve in the lateral orifice of 1250 dyn/cm^2 [14]. The integral, Taylor, and Kolmogorov time and length scales corresponding to the largest, intermediate, and smallest eddies created by the flow were found to be similar for both valves with the smallest length scale between 20 and 70 μm. Based on these calculations, the smallest eddy at 20 μm would potentially damage and/or activate RBCs and platelets with diameters of 8 and 4 μm, respectively [14]. Studies focusing on the leakage jets that are produced when the valve is closed have shown that these jets can reach relatively high velocities and generate sufficient shear stresses to damage RBCs and platelets. Ellis et al showed that in the mitral position Reynolds stresses can reach levels as high as 3600 dyn/cm^2 in both the Medtronic Parallel and SJM

standard valves [13] [15]. Steegers et al analyzed the leakage jets of the SJM and CM valves immediately proximal to the hinge leakage gaps. They determined the velocities of the jets with LDV and pulsed Doppler ultrasound, and used this data combined with a mixing length model to estimate the Reynolds shear stresses in the jets. They found Reynolds stresses greater than 800 dyn/cm^2 [16]. Travis compared the blood damage potential of jets derived from forward and leakage flow based on the magnitudes of the Reynolds shear stresses and the exposure time of the blood. Theses studies with SJM standard, HP, and Regent MHVs indicated that in the aortic position forward flow creates higher Reynolds shear stresses and had longer exposure times than leakage flow. Exposure time to high Reynolds stresses incurred by the leakage jets reached a maximum of 3.7 ms with an average of 2 ms. Reynolds shear stresses in these jets ranged from 24 to 274 dyn/cm^2. However, during forward flow exposure time was as high as 8.9 ms in the 27 mm SJM standard valve with Reynolds shear stresses reaching 4400 dyn/cm^2. Kolmogorov scales for forward flow were between 20 and 96 μm and for leakage flow were between 36 and 73 μm [17]. Thus, these studies imply that forward flow is more damaging to blood elements than leakage flow for bileaflet MHVs in the aortic position.

Flow through mechanical heart valves has also been investigated using Doppler ultrasound both *in vitro* and *in vivo*. The most useful application for this technique is to assess regurgitation through both faulty native heart valves and MHVs *in vivo*. This technique utilizes the application of conservation of momentum principles in the turbulent regurgitant jet to centerline velocity measurements to quantitatively measure the regurgitant volume [18]. This method has been verified both *in vitro* [19] and *in vivo* in a canine model [20]. However, since the jets through bileaflet MHVs are more eccentric in

nature and can be very long compared to their width, this technique was modified to include these planar jets [21]. Furthermore, the time-varying nature of bileaflet MHV jets necessitated the extension of the calculation to total regurgitant volume by including a time velocity integral. This technique proved to have good accuracy with both steady and pulsatile flow through a bileaflet valve in the mitral position. More recently an *in vivo* ultrasound technique has developed using a pig model with a 29 mm SJM valve implanted in the mitral position [22]. This particular ultrasound transducer measured regurgitant velocities within 6 mm ^{2} interrogation areas. The obtained leakage patterns agreed well with previously reported *in vitro* experiments with LDV; however, the velocity magnitudes were somewhat higher. Tendencies for Doppler ultrasound to measure higher centerline velocities than those measured by LDV have been reported [10]. The turbulent shear stresses estimated in this study were over an order of magnitude less than those measured previously with LDV and appeared to be particularly dependent upon the analysis technique [22].

LDV has also been used to look into the hinge regions of valves to discern the differences in flow patterns imparted by different hinge geometries. Interest in the hinge area began after clinical trials with the Medtronic Parallel (MP) valve showed unacceptable numbers of explanted valves with thrombus deposition in the hinge region. These results were unexpected since the MP valve had performed well in forward flow hemodynamic studies. The MP valve also performed well in animal studies using sheep; however, the coagulation cascade in sheep differs significantly from that in humans. The hinge area of the MP valve differs from the SJM and CM valves in that the hinge mechanism consists of a projection from the leaflets that fits into an angular recess in the

valve housing instead of butterfly type recesses with less angular shapes. These differences are shown in Figure 2.5.3. In studies with an optically transparent model of a

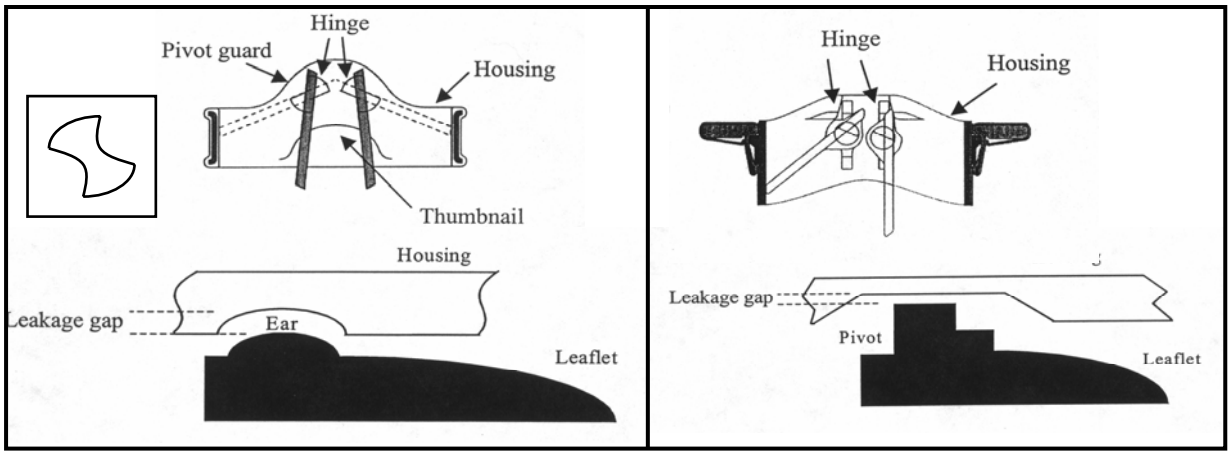

FIGURE 2.5.3. From left to right, hinge region of a SJM regent and MP MHV. Inset on left shows the different shape of the CM hinge recess.

clinical quality 27 mm MP valve, Ellis et. al. and Gross et. al. showed in both steady and pulsatile flow that the MP valve hinge geometry leads to flow within the hinge region that is generally unsteady with complex flow structures. The highest regurgitant jet velocity was observed at the inflow channel near the housing wall and was 2.5 m/s. High turbulent shear stresses were also seen at this region oscillating between 700 and 2900 dyn/cm^2. At this point of maximum TSS, the corresponding maximum turbulent normal stress was 17,000 dyn/cm^2 with a Kolmogorov length scale of 7.1 μm, which is on the order to damage and/or activate RBCs and platelets. The abrupt angular reduction in flow area in the inflow channel leads to vortical flow, and the abrupt enlargement prior to this reduction leads to low velocity reverse flow and consequent stagnation zones. Thus the high TSS can damage or activate platelets and/or RBCs, and the stasis region can entrap them [15] [23]. Additionally, the leaflet movement does not physically sweep the hinge region as it does in the SJM and CM designs.

A similar hinge study using a 23 mm SJM regent valve model with clear housing to expose the hinge region and delrin leaflets shows the differences between the flow fields of the MP valve and the SJM valves. A rotating structure is seen in the inflow hinge pocket during forward flow, but this rotating structure was abolished when the leakage jet traveled through the hinge during the leakage phase. In contrast to the MP valve the maximum leakage velocity was 1.5 m/s, and the maximum turbulent shear stress was 2600 dyn/cm^2. The highest velocities and TSS occurred in the region where the leaflet impacts the hinge walls during valve closure at which time a strong backflow jet is created. These results indicate that the leaflet action and subsequent jet formation does have a part in washing out the hinge area thereby eliminating stagnation zones [13]. Leo et al conducted hinge studies with a clear housing 23 mm CM valve showing that it also has a dynamic washout flow pattern that minimizes the formation of vortex structures and complex flows similar to the SJM valve. Additionally, the peak TSS and velocity values of 5640 dyn/cm^2 and 3.17 m/s for this valve also occurred the moment after valve closure. The more angular shape of the CM hinge recess does not allow the leaflets to completely sweep to the edge of the hinge geometry, thus regions of 'unmated' space are left at each corner during the fully open and fully closed positions. This more angular geometry may lead to higher leakage flow rates because of the unmated space as well as increased TSS due to greater flow disruption [24].

Differences in hinge flow fields due to variance in the size of the hinge leakage region were investigated using a 27 mm SJM standard valve with a clear housing and prototype low leaker and high leaker valves in the mitral position [25]. The diameters of the hinge channels for these valves was estimated by microCT to be 100 μm, 50 μm, and

200 μm for the Standard, low, and high leaker valves, respectively. The main differences in the flow fields were found during the leakage phase. The high leaker valve had the largest leakage jets corresponding with its higher leakage flow rate as well as an additional strong leakage jet at the lateral corner of the hinge.

Studies have also been performed to investigate differences in the hinge flow fields of the 23 mm SJM Standard and CM valves in the aortic and mitral position [26]. In general the peak forward flow velocities were higher in the aortic position for both valve designs, which is consistent with the difference in the cardiac flow rate at these positions. More dynamic flow was noticed under aortic conditions with a strong forward flow jet developing in the outflow pocket and a swirling structure in the inflow pocket inside the hinge recess. Higher peak RSS were also recorded in the aortic position than in the mitral position for both valves.

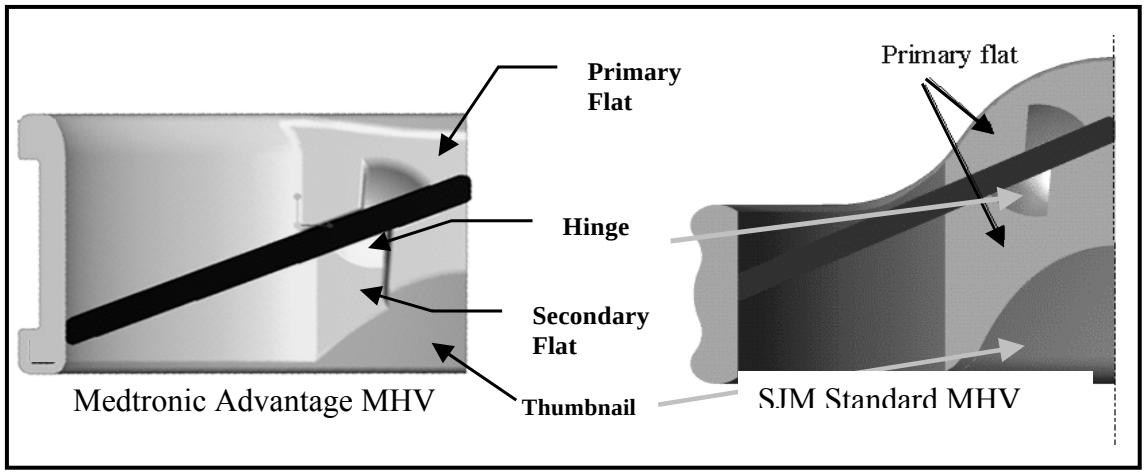

FIGURE 2.5.4. Diagram showing the differences between the Medtronic Advantage and SJM hinges [27].

Saxena et al [27] took hinge measurements of the Medtronic Advantage bileaflet MHV prior to clinical trials comparing its hinge flow dynamics to those of the SJM standard bileaflet MHV. The Medtronic Advantage valve design is very similar to that of

the SJM standard with a recessed butterfly hinge design, a thumbnail region downstream of the hinge, and a cylindrical housing that allows the leaflets to seat entirely within the housing during valve closure. The main difference is that the Advantage valve has a secondary flat area downstream of the hinge region that is intended to decrease the resistance that flow encounters as it enters and exits the hinge area by channeling the flow through the hinge recess (Figure 2.5.4). Measurements were taken in the mitral position using LDV with valve models manufactured with clear, clinical-quality housings that exposed the flow in the hinge area. The measurement levels taken for each valve were the same to allow for direct hydrodynamic comparisons. The results of this study indicated that the hinge flow was similar for both valves with regard to velocity and turbulence measurements. The velocities were somewhat higher in the SJM valve, but these differences were not significant. Additionally, the forward flow through the Advantage hinge when the valve was open was more dynamic in nature, but it is not known what kind of effect, if any, this more dynamic flow will have on washout patterns *in vivo* [27].

Computational fluid dynamics (CFD) is also being used increasingly to investigate flow through MHVs, and can be particularly useful in the future for assessing changes in flow fields induced by changes in MHV design. After the abrupt removal of the Medtronic Parallel (MP) valve from clinical trials, CFD was performed on the hinge area of this valve. This study found areas of stagnation within the hinge region that compared well to LDV studies on this valve [28] [23]. CFD studies were also performed to look at flow through the hinge region of a bileaflet MHV with a protruded hinge and another with a recessed hinge similar to the SJM valve under steady, forward flow with

the leaflets fixed in the open position [29]. Wang et al found that although low velocity vortices developed downstream of the protruded hinge, overall the hinge area appeared to be well washed. Vortices were also found in the recessed hinge design escpecially at higher Reynolds numbers. In general flow structures in the resessed hinge were dominated by reverse flow whereas flow through the protruded hinge was mainly forward flow with some reverse flow behind the stopper [29].

Digital particle image velocimetry (DPIV) has also been used to study the hemodynamics of MHVs, although to a lesser extent. Historically, PIV has not been thought to have sufficient resolution to capture in detail the dynamic flow fields associated with MHVs; however, advances in DPIV technology are bridging this gap. Additionally, DPIV can be a good companion to LDV since it enables researchers to have more qualitative views of flow fields. Kini et. al. used a combination of LDV and DPIV to characterize the flow fields of a 27 mm Bjork-Shiley monostrut valve during the closure and leakage phases of the cardiac cycle [30]. They showed that DPIV is better for visual displays of data while LDV is still inherently better for acute point measurements of velocity. Another study using an optically clear model of a 25 mm standard SJM MHV obtained instantaneous velocity fields at the fully open, closing, fully closed, and opening phases of the cardiac cycle in pulsatile flow. In addition to obtaining velocity vectors, they were also able to see the valve leaflets in the images and their opening and closing behavior while also showing flow fields within the lumen of the valve. The flow structures visualized in this study did not differ from what has been elucidated using LDV, but it does show the feasibility of using DPIV to obtain detailed mapping of MHV flow fields in pulsatile flow [31].

The characterization of flow fields through MHVs enables researchers to better understand the mechanisms behind the thromboembolic complications that plague MHV recipients. The RSS levels measured in all MHVs is well above that necessary to activate platelets, but all MHVs do not have the same thromboemobolic complication rates. Thus, more than jet velocity and subsequent RSS levels must dictate the formation of thrombus. The natural accompaniment to these conditions is stagnation regions that form and enable activated platelets to aggregate and to recruit more platelets and other blood elements into the clot. Therefore, thrombus formation is a combination of shear stress activation of platelets followed by regions flow separation and stagnation.

2.6. Coagulation cascade

Clot initiation caused by the presence of MHVs can occur via three basic pathways: phospholipid and/or tissue factor exposure to blood during cell damage caused by excessive shear stress; platelet activation caused by exposure to excessive shear stress; and contact activation by foreign materials. Clotting occurs in three steps: initiation, amplification, and propagation. In the tissue factor pathway, a cell or cells are ruptured during the initiation phase to expose tissue factor (TF) to the blood. Factor (f) VII in the plasma binds to TF, thus activating it to fVIIa. As shown in Figure 2.6.1, this complex activates fX and fIX, and fXa can activate fV. On the cell surface fXa can bind with fVa, which activates prothrombin to produce small amounts of thrombin, which can activate platelets, fVIII, and fXI during amplification. During amplification, platelets adhere to the damaged tissue and are activated. The thrombin generated earlier enhances platelet adhesion, thus fully activating platelets and also activating fV, fVIII and fXI. During the

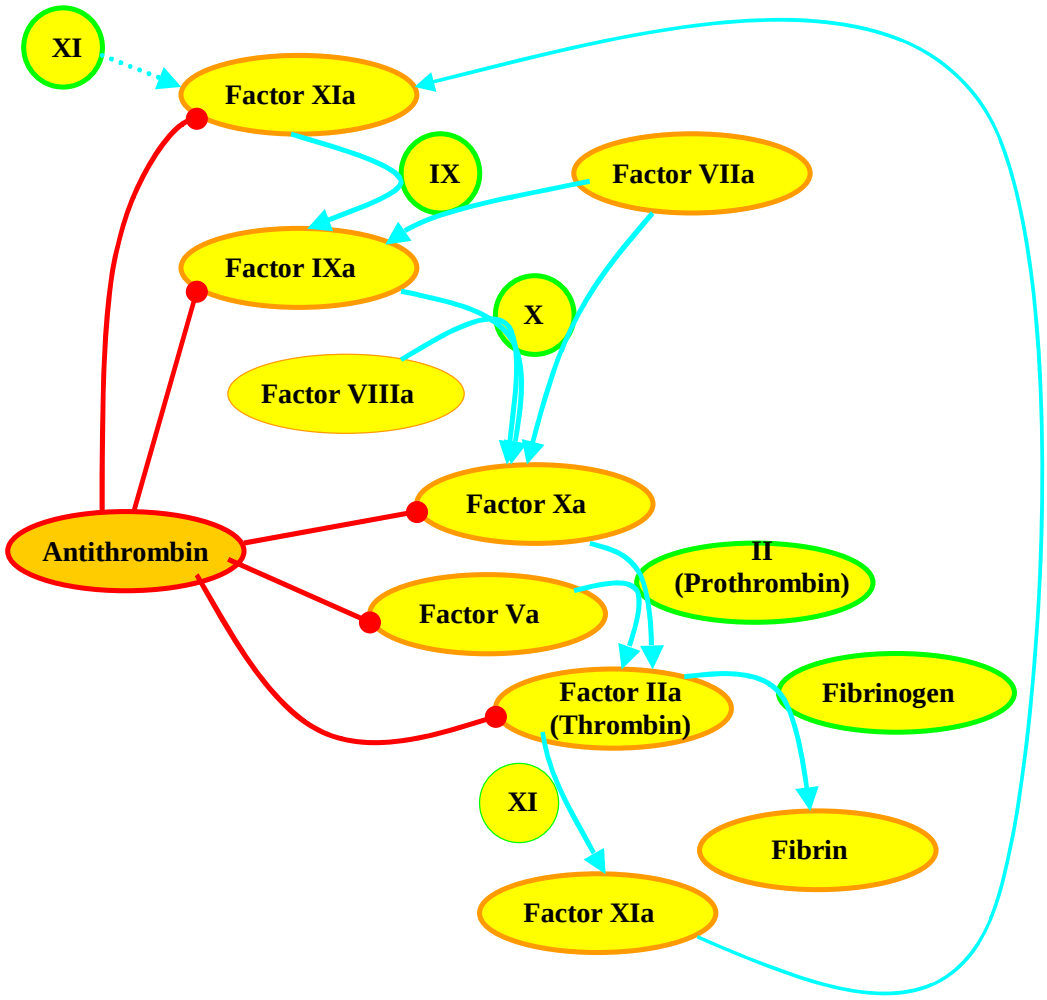

FIGURE 2.6.1. Simplified diagram of haemostasis.

propagation phase large-scale thrombin generation takes place leading to the formation of fibrin, which enmeshes the platelets and stabilizes the clot [32].

Contact activated clotting (Figure 2.6.2) is initiated by the binding of fXII to a negatively charged surface, thus forming fXIIa. The proteins prekallikrein (PK), fXI, and high molecular weight kininogen (HK) are then activated by fXIIa, and PK and fXIa bind to the foreign surface through HK. On the surface fXIIa cleaves PK to kallikrein and fXI to fXIa, and kallikrein generates additional fXIIa. Kallikrein also hydrolyzes HK into its activated forms and releases bradykinin. Thus, HKa-PK and HKa-fXI complexes are

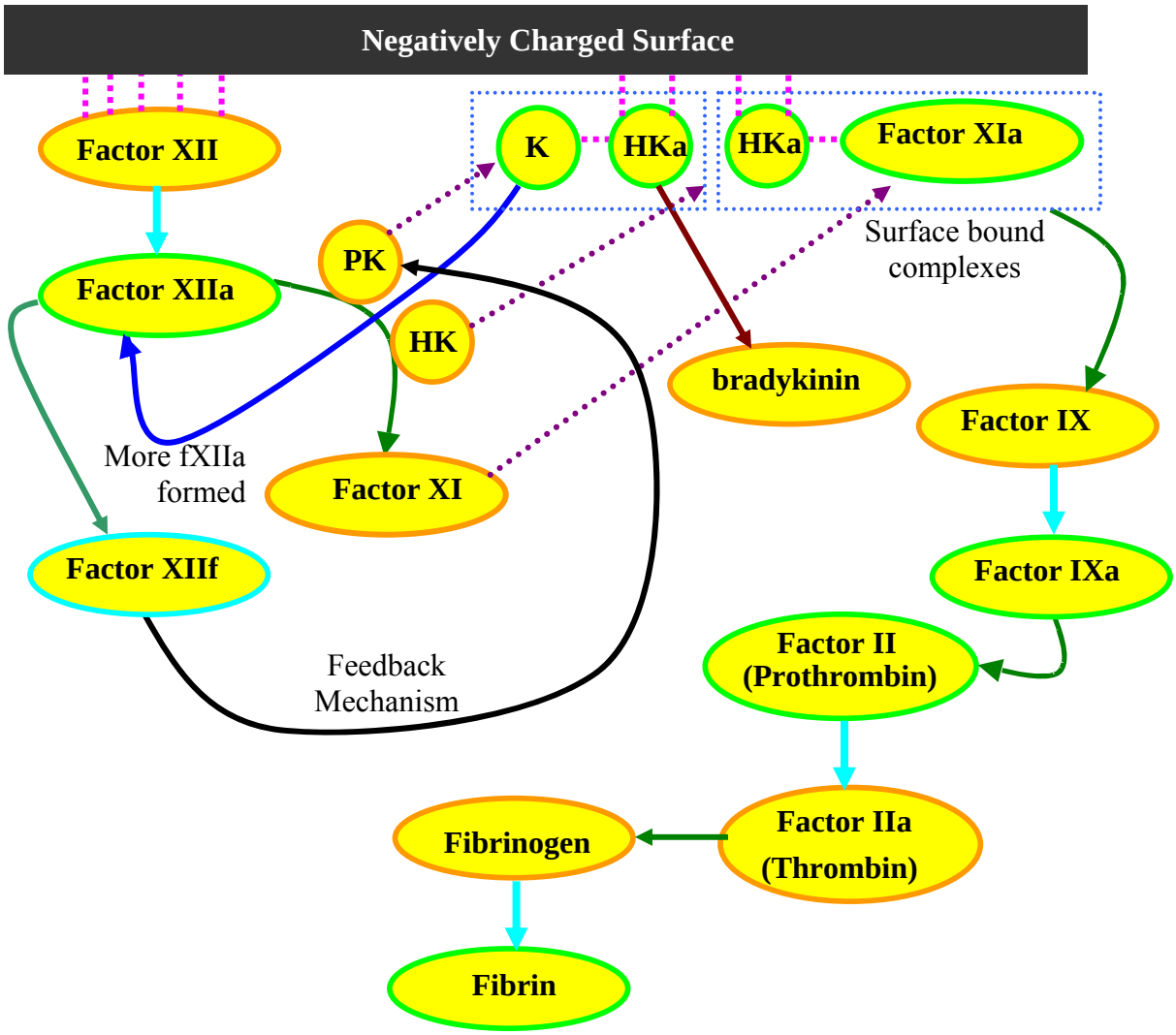

FIGURE 2.6.2. Simplified diagram of contact-activated coagulation.

formed on the surface near to fXIIa. During amplification fXIIa acts on these complexes to form surface bound Hka-kallikrein and Hka-fXIa complexes. The Hka-fXIa complex activates fIX to fIXa, which acts in a cascade to form thrombin, and thrombin activates platelets. Kallikrein is released to activate more fXIIa and convert existing fXIIa to fXIIf, which is still activated, but is no longer bound to the surface so that it can activate more PK. In addition, fibrinogen is adsorbed to the material surface. A buildup of a layer of

proteins on the material helps mediate platelet adhesion and subsequent tissue growth [33].

Shear stress can lead to thromboemboli formation by inducing blood cell damage thus exposing tissue factor to the plasma and/or by activating the platelets directly. The shear stress magnitudes shown to cause damage to both red blood cells (RBCs) and platelets have been quantified. RBCs are vulnerable to lethal damage at shear stresses of 1500 to 4000 dynes/cm^2 and by as little as 10 to 100 dynes/cm^2 in the presence of foreign surfaces. Sublethal damage occurs at 500 dynes/cm^2 [11]. Shear stress initiated coagulation begins with the activation of the platelets by mechanical forces. Studies using cone and plate viscometers have shown that platelet activation can occur at shear stresses as low as 60 to 80 dynes/cm^2. Platelets have been shown to undergo damage after exposure to 100 to 500 dynes/cm^2 [11]. Platelet damage is also dependent upon the duration of the shear stress; however, platelet damage increases linearly with time during exposure to a constant shear stress implying that shear induced platelet damage is cumulative [11]. Shear-induced platelet activation has been studied in viscometers and is also a function of magnitude and duration [11]. At 150 dynes/cm^2 platelet aggregates are formed after 300 seconds. At 600 dynes/cm^2 aggregates form after 30 seconds, and at 6500 dynes/cm^2 in less than 5 milliseconds. These studies also show that as the magnitude increases, formed aggregates tend not to separate when the force is discontinued [11]. This behavior points to a different mechanism for platelet activation at higher levels of shear stress.

Although the exact mechanism of activation and initiation of the coagulation cascade by shear stress is not known, studies have shown that in the presence of purified

vWF multimers platelets exposed to fluid shear stresses of 90 and 120 dynes/cm^2 have an increase in intracellular calcium (Ca^{2+}) and aggregation [34]. Since the chelation of the extracellular Ca $^{2+}$ abolished this response, the intracellular increase is due to a transmembrane influx of extracellular Ca^{2+}. Additionally, inhibition of the GPIb platelet receptor completely abolished these responses while inhibition of the GPIIb/IIIa platelet receptor only partially inhibited these responses [34]. Thus, vWF binding to GPIb is essential for shear stress-induced increase in platelet Ca^{2+} and aggregation, and vWF binding to GPIIb/IIIa potentiates platelet responses, but is not essential. This influx of Ca^{2+} activates the platelet, and leads to the amplification phase during which GPIIb-IIIa interacts with adhesive proteins to mediate platelet-platelet interaction and subsequent aggregation. GPIIb-IIIa usually binds to fibrinogen, but under high-shear conditions it binds to vWF to mediate platelet aggregation [35]. Thus, this pathway may not be dependent upon fibrinogen since vWF both activates the platelets as well as supports platelet cohesion. However the GPIIb/IIIa receptor on activated platelets can bind with at least four different ligands (fibrinogen, vWF, fibronectin, and vitronectin) and only immobilized fibrinogen when not activated. However, the GPIb receptor can bind with immobilized vWF in the absence of shear stress and only soluble vWF in the presence of shear stress. Based on this knowledge, it is apparent that these two platelet receptors represent different pathways of platelet activation and aggregation under shear stress conditions [35]. The mechanism by which the vWF binding function of GPIb is activated has been shown to be via a dissociation of this receptor from the membrance skeleton caused by actin filament rearrangement [36]. This mechanism supports previous studies pointing to shear stress as a mechanical initator for binding to this receptor. Furthermore,

Shankaran et al [37] have shown that platelet activation by shear stress occurs via a two-step process in which fluid shear and vWF are required for the first step when vWF-GPIb binding occurs, and subsequent platelet activation requires fluid forces but not vWF. Thus, vWF-GPIb binding is separable from platelet mechanotransduction. Although the exact target of the fluid forces is still unknown, they may be applied to the vWF-GPIb complex. This is supported by a study showing that although platelets interact with vWF over a range of shear stresses, interacting cells only exhibit calcium fluxes at the higher shear stresses [38].

There is also evidence that vWF and fibrin have a cooperative effect on platelet adhesion and aggregation under high shear conditions. These studies indicate that resting platelets under flow conditions at high shear stresses adhere to immobilized vWF via the GPIb platelet receptor and are consequently slowed down and activated. This activation turns on the GPIIb/IIIa receptor an allows it to bind to vWF since this adhesive reaction appears to take longer than the reaction between vWF and GPIb. This step is necessary for thrombus formation since the vWF-GPIb interaction is characterized by a fast dissociation rate and reversible bonds, and the vWF-GPIIb/IIIa interaction is irreversible. After immobilization by the vWF-GPIIb/IIIa interaction, fibrinogen binding to the GPIIb/IIIa receptor may function to recruit more platelets and to stabilize the clot [39] [40] [41] [42]. Thus, the vWF-GPIb interaction is crucial to initiating platelet arrest and activation, but the vWF-GPIIb/IIIa interaction is necessary for permanent thrombus formation and increasing the size of the clot. In addition to simple development of the clot by fibrinogen binding to GPIIb/IIIa, fibrinogen may also gradually replace the vWF that initially constructed the thrombi under high flow conditions [43].

A role for RBCs in platelet aggregation has also been explored because of the relatively large size of RBCs and their consequent role in transport of coagulative factors. In *vitro* RBCs are concentrated in the center of the blood stream thus colliding with platelets and pushing them to the periphery of the blood stream near the vessel walls where shear rate and shear stress are highest. In studies with a cone and plate viscometer, platelets in the presence of RBCs exhibited a hematocrit-dependent increase in both adhesion and aggregation with an increase in hematocrit from 0 to 30%. Test with active and inactive RBCs showed that this effect is mediated partly by chemical effects of RBCs and partly by physical effects of RBCs, with physical effects being more important in adhesion and chemical effects being more important in aggregation [44]. These results show the importance of the presence of RBCs in *in vitro* studies designed to explore shear-induced thrombosis.

Detailing the kinetics of thrombus formation is critical in determining whether or not a thrombus will form under various flow conditions, especially in regions of high velocity such as MHV leakage jets. Studies done using a 10-micron filter to retain platelet aggregates while applying a predetermined pressure leading to elevated shear stress have shown that activation and aggregation can occur with 8 milliseconds [45]. Thus, activated platelets, if brought together could aggregate in a very short time period. Another study investigating the cytosolic calcium flux that occurs with platelet activation and subsequent thrombus formation found that interactions between a resting and a preformed thrombi containing activated platelet undergoing sustained calcium flux oscillations must occur within a temporal window of less than 0.6 seconds in order for the signal to be propagated [46]. This activation was dependent upon the platelets coming into contact

when the activated cell was expressing its peak calcium flux. Therefore, calcium flux propogation appears to be dependent upon timely and intimate platelet interactions between activated and resting platelets.

In a model of a stenosis with a subsequent enlargement, radiolabeled platelets were used to determine the locations of highest adhered platelet density at different physiological flow rates [47]. In this model the stenosis generates a region of high shear stress in which platelets are activated, and the enlargement induces flow separation and consequent recirculation regions [47]. As expected, this study showed that net platelet density was elevated in areas of flow recirculation and reattachment. Furthermore, the extent of the platelet density correlated with the length of the recirculation region. Thus, under the effect of shear stress alone, emboli are most likely to develop in recirculation areas, and they may or may not attach in areas of stagnant flow to become thrombi. In the immediate vicinity of MHVs in the aortic and mitral positions, similar recirculation regions are observed. These regions of recirculation allow platelets to aggregate with the primary adhesion occurring downstream. Under the influence of tissue overgrowth or an exposed sewing ring, platelets may also attach at these locations due to contact activation or shear stress activation and subsequent adhesion.

2.7. Blood flow studies

Many studies have been done to better elucidate the shear stress-activated thrombosis pathway and relate it to physiologic stress levels and flow patterns seen in flow through stenoses and MHVs. In vitro blood studies with both porcine and human blood have correlated blood damage with both forward and leakage flow through MHVs. In a study

with porcine blood using a Bjork Shiley monostrut disc valve, hemolysis was shown to increase with time during both forward and leakage flow for the mitral and aortic positions. Furthermore, in comparisons of hemolysis between the aortic and mitral position, the mitral position was shown to be more damaging than the aortic valve during forward flow while the aortic position was more damaging during leakage flow [48]. Cavitation was also studied, and it was found that its contribution increases depending upon the duration of the cavitation, and that if the duration was long enough it became the dominant hemolysis mechanism. The hemolysis contributions during forward and leakage flow were about the same, but considering that leakage flow only affects 2-5% of the total blood volume, this contribution is significant [48]. Leakage flow studies on the Medtronic Parallel valve and SJM standard, high leaker and low leaker prototype valves using markers for platelet activation and blood element damage in human blood, showed that platelets were activated and damaged in a time dependent fashion with activation and damage increasing with time. Additionally, the high leaker prototype valve showed more platelet activation and blood damage than the SJM standard valve [49]. This result shows the effect of leakage magnitude on blood damage and platelet activation. Although a larger leakage area results in lower shear stresses during the leakage phase, a higher leakage volume through the valve exposes more of the blood to high shear stresses encountered during leakage flow. Thus, an optimal leakage area exists that minimizes blood damage.

Flow-induced platelet activation for two Bjork-Shiley monoleaflet MHVs was investigated using a modified prothrombinase method with washed platelets [50]. In this assay the amount of acetylated thrombin generated correlates with the activation state of

the platelet sample. This study found that in a physiologic flow loop powered by a pulsatile pump, platelet activation was dependent upon the restriction of the valve with the free valve resulting in no significant platelet activation and the severely restricted valve resulting in significantly platelet activation.

Clinical studies have found high incidences of circulating platelet/leukocyte aggregates in patients with MHVs, which may be an indication of platelet activation [51]. However, no correlations were found between valve type or implant location. Platelet dysfunction has also been detected in patients with heart valve replacement [52]. This dysfunction was not isolated to a particular position of valve type and was manifested by impaired function in a high shear environment. This dysfunction may be related to repeated activation by the MHV and subsequent increased susceptibility to damage by normal flow through the body. This damage may render a great number of the platelets refractory to further shear stress activation. Thus, after the initial risk of thromboembolic complications perhaps this platelet dysfunction compounds the risk of hemorrhage imposed by anticoagulant therapy.

Studies focusing on the fluid mechanics properties of the SJM bileaflet valve, and the CarboMedics bileaflet valve have correlated areas of high shear stress, stagnation, and flow separation to thrombus formation [10]. Bileaflet valves are also vulnerable to high turbulent shear stresses during both forward and leakage flows They also exhibit asymmetric separated regions with flow reversal around the perimeter of the housing with larger spatial dimensions near the hinges adjacent to the lateral jets as well as high regurgitant flow volumes that lead to high shear stresses [10]. Coupled with adjacent stagnant flow, these high shear stresses could lead to thrombus formation in the hinge

area. The Medtronic Parallel valve demonstrated such thrombus formation in clinical trials. It passed all pre-clinical trials including animal blood studies with sheep in forward flow; however, once implanted in clinical trials, many patients experienced thromboembolic complications, and valve explants showed thrombus deposition in inflow region of the hinge area [10]. The St. Jude and CarboMedics bileaflet valves have also demonstrated thrombus formation in the hinge area [53] [8].

CHAPTER 3

CLINICAL SIGNIFICANCE

Presently, vascular prostheses undergo rigorous testing before they can be placed in clinical trials. These *in vitro* tests include fluid dynamics studies to gain insight into whether or not a device will damage blood cells or activate platelets to initiate thromboemboli formation as well as tests with bovine blood to investigate hemolysis. After these *in vitro* tests have been completed satisfactorily, the device is then implanted into an animal model, such as an ovine model, to assess propensity for thromboembolic complications in this setting. After these tests are passed, the device can then be placed in clinical trials. However, this system is imperfect. The animal models available for use in these studies do not have the same biochemistry as humans with respect to haemostasis and thrombosis. Thus, these models cannot predict thromboembolic complications in all cases. Indeed, the Medtronic Parallel valve was one such case in which it passed all the preliminary tests, but failed in clinical trials. To minimize such events, it is desirable to develop an *in vitro* flow system that can test for procoagulant potential of devices without such dire consequences. Such was the aim of this research using bileaflet mechanical heart valves as a test case.

In addition to illuminating the importance of the hinge geometry and gap width on platelet activation and propensity for coagulation, this study also describes a system that can be used to investigate these parameters for other vascular devices that expose the blood to high or varying shear stresses. This methodology has the sensitivity to detect changes in both platelet activation and procoagulant potential based on changes in the

hinge geometry. It also has a small volume requiring only relatively small amounts of human blood that can be drawn from one donor. Thus, this study provides a simple yet powerful methodology to investigate various vascular devices for both platelet activation and thromboembolic potential.

CHAPTER 4

HYPOTHESIS AND SPECIFIC AIMS

Heart valve disease is a life-threatening condition that can be caused by rheumatic fever, ischemic heart disease, infection, connective tissue disorders, trauma, malignant carcinoma, and congenital defects. Patients with severe heart valve disease in which repair is not an option must undergo heart valve replacement or face a reduced quality of life and ultimately death. Because of their significantly better durability than the other prosthetic choices, mechanical heart valves (MHVs) are most often used to replace native valves. Unfortunately, the design of bileaflet MHVs, particularly the hinge area, produces flow fields that may impart damage upon blood elements. This damage can activate platelets leading to initiation of the coagulation cascade and subsequent thromboembolic events. Thus, lifelong anticoagulant therapy is necessary to reduce the risk of thrombosis. However, even with anticoagulant therapy many patients still have thromboembolic complications leading to emboli formation, which may cause strokes or valve thrombosis that impairs valve function. Since the advent of MHVs in 1952, researchers have been making improvements to MHVs to reduce the adverse hemodynamic effects of valves that cause damage to blood elements or activate platelets. An important part of this improvement is the understanding of the hemodynamic effects produced by different valve designs, and how the consequent flow fields affect thromboemboli formation.

Shear stress can lead to thromboemboli formation *in vitro* by inducing blood cell damage thus exposing Tissue Factor (TF) to the plasma and/or by activating the platelets directly via von Willebrand Factor (vWF) and thrombin. The shear stress magnitudes

shown to cause damage to both red blood cells (RBCs) and platelets *in vitro* have been quantified using both flow and viscometer studies. RBCs are vulnerable to lethal damage at shear stresses as low as 1500 to 4000 dyne/cm^2 and by as little as 10 to 100 dyne/cm^2 in the presence of foreign surfaces. Sublethal damage occurs at 500 dyn/cm^2 [11]. Platelets have been shown to undergo damage after exposure to between 100 and 500 dyne/cm^2. Platelet damage is also dependent upon the duration of the shear stress such that platelet damage increases linearly with time during exposure to a constant shear stress implying that shear induced platelet damage is cumulative. This cumulative damage is especially relevant in recirculating systems. Shear-induced platelet activation has been studied in viscometers and is also a function of magnitude and duration. At 150 dyne/cm^2, platelet aggregates are formed after 300 seconds. At 600 dyne/cm^2, aggregates form after 30 seconds, and at 6500 dyne/cm^2, they form after less than 5 milliseconds. These studies also show that as the magnitude increases, formed aggregates tend not to separate when the force is discontinued [11].

Experimental fluid mechanics techniques such as laser Doppler velocimetry (LDV) or digital particle image velocimetry (DPIV) can be used to measure velocities in areas of MHVs and at times during the cardiac-cycle that are characterized by elevated shear stresses that exceed the levels capable of inducing thromboemboli formation. LDV studies performed on the St. Jude Medical (SJM), Carbomedics, and Medtronic Parallel valves in the vicinity of the hinge area [15] [23] [24] showed maximum Reynolds stress magnitudes of 7200, 5510, and 8000 dyne/cm^2, respectively, during the leakage phase. Additionally, leakage flow studies on the Medtronic Parallel valve using markers for platelet activation and damage [49] showed that platelets were activated and damaged in

a time dependent fashion with activation and damage increasing with time. Similar studies performed with prototype valves with hinge leakage values that were higher (230 μm) and lower (80 μm) than the normal tolerances for the SJM standard valve (100 μm) found that there were differences in platelet activation, and the high leaker valve had significantly more platelet activation than the standard valve. These LDV measurements as well as the platelet activation studies imply that hinge geometry and leakage magnitude do have a significant effect on shear stresses and subsequent thrombus formation. However, there is difficulty in isolating the hinge region during blood studies because of the confounding presence of the sewing ring, valve surface, and leakage around the periphery of the leaflets.

The objective of this study is to design a system to assess quantitatively platelet activation and thrombosis in models that approximate different mechanical heart valve hinge geometries as well as flow through the valves themselves. Models are developed that isolate the hinge area so that geometries can be directly compared without the complications introduced by the rest of the MHV such as the sewing ring and b-datum line. In addition, the fluid shear stresses through these model geometries are calculated and measured using DPIV to correlate platelet activation and thrombosis with wall-shear stress and Reynolds stress.

Hypothesis: **Thrombus formation in models that isolate and mimic mechanical heart valve hinge geometries can be characterized quantitatively using a novel *in vitro* blood flow system, and these results can be correlated with digital particle image velocimetry measurements detailing flow fields for the same models. This hypothesis will be addressed by investigating the following specific aims:**

SPECIFIC AIM 1: *Develop a system in which thrombi can be initiated at locations that are vulnerable to thrombus formation.* A steady flow system is developed in which thrombogenic areas are minimized so that thrombosis formation is contained within the area of interest. Anticoagulant and a reversing agent are balanced so that the coagulation cascade can be initiated without inducing gross thrombosis in the entire loop. The anticoagulated blood is returned to as normal a state as possible by continuously infusing the reversing agent so that the coagulation cascade can proceed in response to activating factors such as shear stress.

SPECIFIC AIM 2: *Develop orifice models that validate this shear-mediated steady flow system and models that mimic MHV hinge geometries to characterize quantitatively coagulation and platelet activation induced by these geometries.* To accomplish this specific aim, simple orifice models as well as more complicated hinge channel models are placed in the steady flow loop to test the correlation between thrombus formation and shear stress levels. Human blood experiments are used to assess platelet activation and thrombus formation, and wall shear stress calculations and DPIV Reynolds stress and

shear stress measurements are correlated with quantitative biological endpoints for the different models that indicate platelet activation, thrombus formation, and hemolysis.

SPECIFIC AIM 3: *To show a difference in coagulation and platelet activation for different valve designs of the same size.* To accomplish this specific aim, 27 mm SJM standard, and 27 mm Medtronic Parallel (MP) bileaflet valves are placed in a steady flow loop in the leakage position. The hinge designs of these valves are different with the SJM valve having a more curved design versus the more angular designs of the MP and CM valves. Human blood experiments are used to assess quantitatively platelet activation and thrombus formation for each of these valves.

SPECIFIC AIM 4: *To show a difference in coagulation and platelet activation for valves with the same design and size, but with different leakage magnitudes.* To accomplish this specific aim, 27 mm SJM standard, high leaker, and low leaker valves are used in a steady flow loop in the leakage position. The high leaker and low leaker valves are specifically designed to have higher (200 μm) and lower (50 μm) leakage, respectively, than the standard valve (100 μm) during the leakage phase of the cardiac cycle. Human blood experiments are used to assess quantitatively platelet activation and thrombus formation for each of these valves.

SPECIFIC AIM 5: *To correlate digital particle image velocimetry (DPIV) flow field data with procoagulant potential for the orifices and channels.* To accomplish this specific aim, the orifices and channels developed in Specific Aim 2 were placed in the

steady flow loop with a blood analog solution consisting of water, glycerine, and sodium iodide to match both the kinematic viscosity of blood and the refractive index of the orifice chamber. DPIV was then used to characterize the flow field through the orifices and channels. The acquired velocity vectors were used to calculate shear stress, Reynolds stress, and vorticity for these different jets. These data were analyzed to illuminate important differences in the jet flow fields that influenced the procoagulant potential of these jets.

CHAPTER 5

EXPERIMENTAL DESIGN

The methods section is divided into two sections: the blood experimental design and the digital particle image velocimetry (DPIV) experimental design. Each section will detail the rationale and methods for the development of these experiments as well as the general protocols. Detailed protocols for the blood are in Appendix A.

5.1. Blood experimental design

The experimental design for the blood experiments is a culmination of bench tests and preliminary experiments that were performed to determine the proper protocols and assays to quantitatively assess platelet activation and procoagulant potential of different MHVs, orifices and channels. This section will detail these preliminary experiments and the detailed protocols that were subsequently developed.

5.1.1. System development and validation

For the development of a reversible anticoagulant system, bench tests were first performed to determine the best reversible anticoagulant to use as well as the optimal ratio of anticoagulant to reversing agent to enable thrombus formation without causing gross thrombosis of the entire flow loop. The two anticoagulants tested for their feasibility in these studies were heparin (Elkins-Sinn, Inc., Cherry Hill, NJ) and sodium citrate (Sigma, St. Louis, MO) with their respective reversing agents, protamine (CP Pharmaceuticals, UK) and Ca^{2+} found in calcium chloride (Sigma, St. Louis, MO). Bench

tests with sodium citrate and calcium chloride were performed by measuring whole blood clotting times with different concentrations of calcium chloride. In these experiments blood was drawn into a 3.2% citrate solution in a blood:citrate volume ratio of 9:1, and the fluid mixture was placed into glass test tubes with various amounts of 100 mM calcium chloride The tubes were sealed and placed in a rocker to continuously invert the tubes. The glass in the test tubes acted as the agonist to initiate the coagulation cascade. The time at which a thrombus formed was recorded as the whole blood clotting time. The optimal citrate:Ca^{2+} ratio was defined at the time just before the clotting time decreased to the minimum clotting time. Figure 5.1.1.1 shows that the clotting time decreased quickly from infinity to 200 seconds at a molar citrate:calcium ratio of approximately 6.5 and then remained constant before rising again. Thus, an initial ratio of 7 was used for the steady flow blood experiments that will be discussed in a later section.

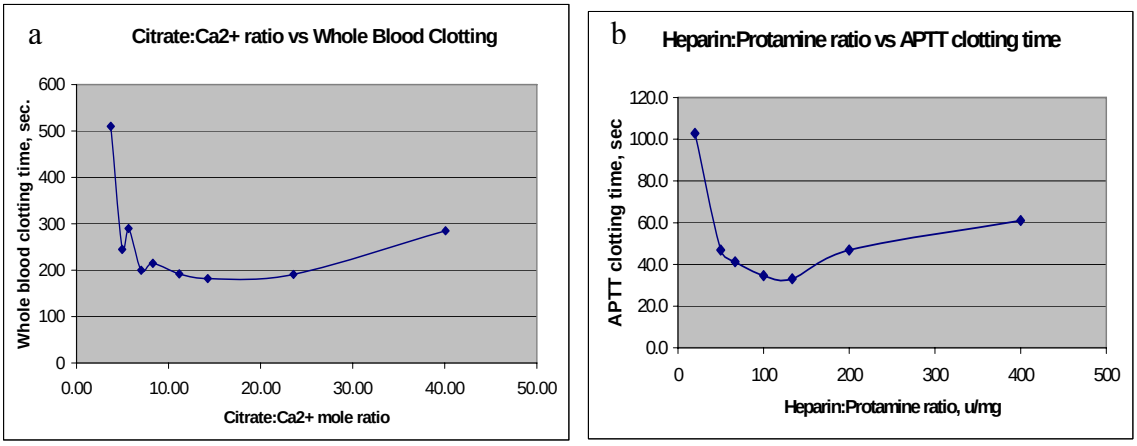

FIGURE 5.1.1.1 Plots of bench tests done with (a) citrate/Ca^{2+} and (b) heparin/protamine.

For bench tests with heparine and protamine, the activated partial thromboplastin time (APTT) was used to measure the clotting time. The APTT test could not be used for the citrate/calcium bench tests because it utilizes the addition of calcium as an agonist.

The APTT was determined for whole blood by adding 100 μl of 20 mM calcium chloride to 200 μl of platelet poor plasma obtained from blood heparinized with one unit of heparin per ml of blood and then measuring the length of time before the blood clotted using a fibrometer. By adding different amounts of protamine to the heparinized blood, the optimal ratio of heparin to protamine was determined. The results of these bench tests are shown in Figure 5.1.1.1. From these bench tests it was determined that the heparin/protamine system was too sensitive to be used for these experiments. The addition of just a small amount of protamine resulted in APTTs of 30 seconds, which is too low and would probably result in a grossly thrombosed flow loop. Thus, this system would be too difficult to regulate. Additionally, heparin and protamine are known to interact with blood components in many different ways whereas the sole anticoagulant mechanism of citrate is to reversibly chelate the extracellular calcium. Thus, the simplicity of the citrate/calcium system also makes it a more attractive option.

5.1.2. Steady flow loop development

After determining that the citrate/Ca^{2+} system could be used and beginning with a final molar citrate:Ca^{2+} ratio of 7, the system was tested in a steady flow loop in which a thrombogenic surface, a 6.35 mm OD glass tube, was inserted. This flow loop consisted of 6.35 mm ID silicone tubing (VWR, Bridgeport, NJ) connected to a bypass pump and the glass tube by forcing the tubing over the entrances to the pump head and the glass tube. The glass tube was designed to fit snugly into the silicone tubing without leaking, and the tubing also fit snugly around the entrance and exit of the pump head without leaking. The loop was filled with anticoagulated human blood, and the blood was pushed

through the loop using a Model 540E Bioconsole Medtronic centrifugal pump (Biomedicus, Eden Prairie, MN). The reversing agent was continuously infused into the flow loop with a syringe pump (Harvard Apparatus, Holliston, MA) for 30 minutes until the predetermined citrate:Ca^{2+} ratio was reached. At this time the glass tube was isolated from the rest of the loop, removed, rinsed with saline, and then inspected for thrombus formation. Two flow rates were used in these experiments, 1 l/min and 2 l/min, with slightly different results at each of the flow rates. At 1 l/min thrombi were found in each case at both the inflow and outflow sides of the glass tube where the silicone tubing meets the glass tube, but at 2 l/min thrombi were only found at the inflow edge of the glass tube. Thrombi were not found in any other part of the flow loop. Two-dimensional computational fluid dynamics (CFD) simulations of the flow fields induced by the inflow and outflow regions of the glass tube at these flow rates showed that the vortices formed at the outflow region were much larger at 2 l/min than at 1 l/min. Thus, these larger vortices may have dislodged the thrombi formed at 2 l/min, which explains why thrombi were not found at this flow rate.

Once reproducible thrombus formation was demonstrated using a glass tube as the agonist, a 17 mm SJM Regent MHV was inserted in place of the glass tube, and inspected in the same way for thrombi. As shown in Figure 5.1.2.1, this steady flow loop was also connected with 6.35 mm ID silicone tubing, and the valve was placed in an acrylic valve chamber designed to approximate the geometry of the aortic sinus. The valve was placed in the leakage position so that it was closed at all times while flow went through it, and the upstream pressure was set at 120 mmHg to approximate the upstream pressure during leakage flow across the aortic valve. The experiments with the 17 mm MHV served

mainly to aid in refinement of the citrate:Ca^{2+} ratio for a shear-mediated system. The resulting value found to enable reproducible thrombus formation without gross thrombosis of the entire flow loop was a citrate:Ca^{2+} ratio of 5.8:1. Quantitative assays were not performed so these results were only qualitative.

FIGURE 5.1.2.1 Picture of the steady flow loop setup for a MHV.

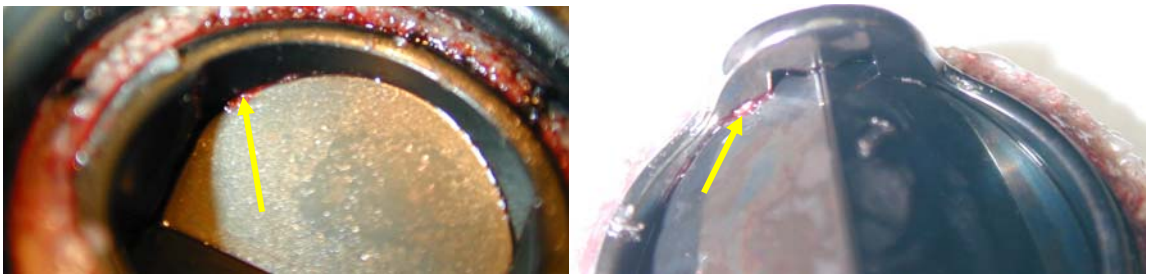

FIGURE 5.1.2.2 Pictures of clots on the inflow and outflow sides of a 17 mm SJM MHV set in the leakage position.

Pictures were taken of the thrombi while they were on the valve (Figure 5.1.2.2), then these thrombi were removed from the valve, fixed in formalin, and stained with a standard Hematoxylin and Eosin (H & E) stain for cell nuclei and membranes or with a

Carstairs stain specific for fibrin, platelets, and RBCs. These results are shown in Figures 5.1.2.3a and 5.1.2.3b. These histology results showed that the thrombi produced had normal morphology with RBCs and platelets enmeshed in fibrin strands. The presence of fibrin showed that the coagulation cascade was initiated, and that the thrombi formed were not merely aggregates of cells.

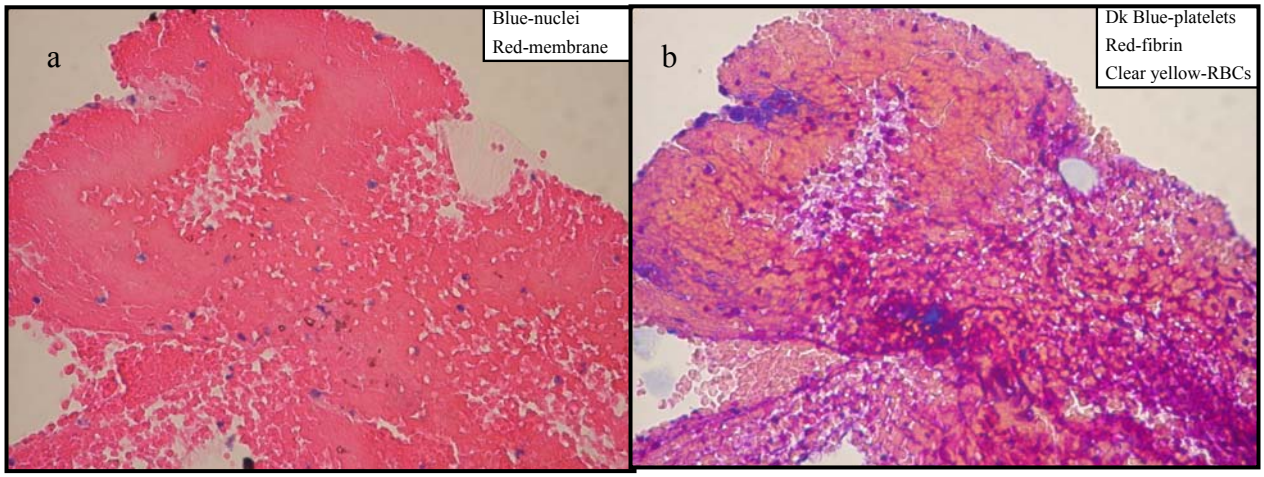

FIGURE 5.1.2.3. (a) Microscopy pictures of clots stained with a hemotoxylin and eosin stain. viewed under 40X . (b) Microscopy pictures of clots stained with a Carstairs stains. viewed under 40X

5.1.3. Orifice/Channel experiments

For the final experiments the orifice plates and channels were placed in the chamber as shown in Figure 5.1.3.1 and connected to a Biomedicus centrifugal bypass pump using 6.35 mm ID silicone tubing as shown in Figure 5.1.3.2. The total volume of the loop was approximately 77 ml. The flow loop was rinsed with saline and then filled with human blood drawn into 3.2% sodium citrate at a 10:1 blood to citrate ratio. Air was purged from the system, and the bypass pump was operated at 2000 RPM.

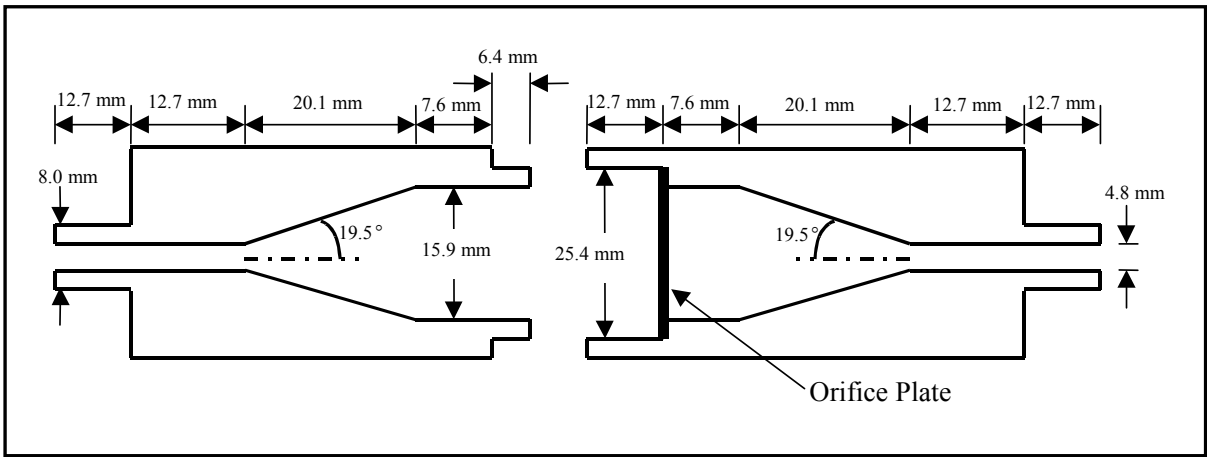

FIGURE 5.1.3.1. Diagram of the orifice/channel chamber used for this study.

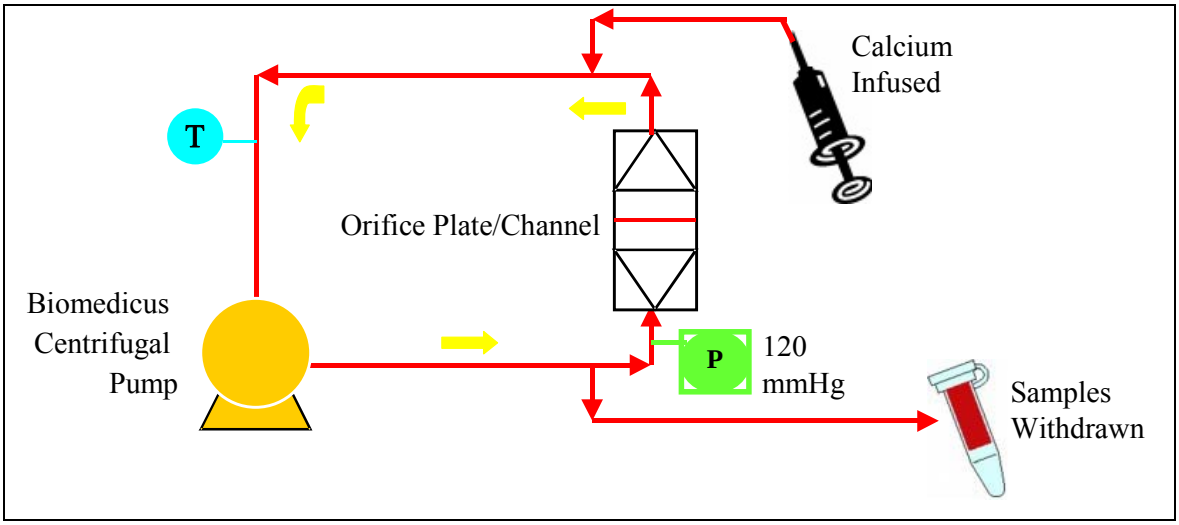

FIGURE 5.1.3.2. Diagram of the steady flow loop used for this study.

Simultaneously, to partially reverse the citrate anticoagulation, 100 mM calcium chloride was infused into the loop with a steady flow syringe pump at a rate of 17.3 μL/min. Calcium chloride was injected just prior to the pump head since experiments with dye injection showed complete mixing of substances injected at this point by the centrifugal action of the pump head. This infusion rate resulted in an end calcium chloride volume in the flow loop of 1.04 ml. The dilution effect from this addition was accounted for in the calculations of TAT, PF4, and plasma hemoglobin concentrations.

The calcium infusion rate was chosen based on initial bench tests in which the whole blood clotting times in response to glass-mediated clotting were measured using different ratios of sodium citrate to calcium chloride. In response to calcium chloride addition, the whole blood clotting times were decreased from infinity to approximately 200 seconds. Based on these results an initial molar citrate to Ca^{2+} ratio was chosen at 6:1 for contact-activated thrombosis which was adjusted to meet the current shear stress-mediated clotting conditions. The citrate:Ca^{2+} ratio for these studies was fixed at an end molar ratio of 8.3:1 at 60 minutes after initial experiments with the 400 μm round orifice at the predetermined ratio resulted in gross thrombosis of the entire flow loop. Apparently, initiation of the coagulation cascade by contact activation with glass required more Ca^{2+} than initiation by shear stress. Based on direct interactions of this added Ca^{2+} with $citrate^{+}$, this end molar ratio was not sufficient for the Ca^{2+} to bind with all of the $citrate^{+}$. In fact, by the end of the experiment, the added Ca^{2+} would only remove 24% of the $citrate^{+}$ by direct binding.

To further test whether or not TAT formation, or thrombus formation, was due to contact activation instead of shear stress, samples were removed at the end of the experiments to test the whole blood clotting times in response to contact with glass. Since the clotting times were infinite, it was concluded that the TAT formation was due to shear stress and not contact activation.

During the experiment the pressure upstream of the orifices was monitored using the pressure transducer on the pump and maintained at 120 mmHg (+/- 5 mmHg) resulting in flow rates of 0.01, 0.045, 0.19, and 0.32 l/min for the 200, 400, 800, and 1200 μm orifices, respectively. These flow rates were measured using a blood analog fluid at a

pump speed of 2000 RPM and upstream pressure of 120 mmHg. The flow rate was also monitored during the experiment with an inline flow meter and flow transducer supplied with the Biomedicus centrifugal pump (Biomedicus TX50, Minneapolis, MN). Two 0.5 ml samples were withdrawn at 0, 15, 30, and 45 minutes and also at the end of the 60-minute experiment and placed in 3 ml EDTA Vacutainer tubes (Becton Dickinson, Franklin Lakes, NJ) for the TAT and hemolysis assays and in a mixture of aspirin (Sigma, St. Louis, MO), acid citrate dextrose (ACD) (Sigma, St. Louis, MO), and Prostaglandin E_1 (EMD Biosciences, San Diego, CA) for the PF4 assay (Detailed mixture recipe in Appendix A). This volume was replaced with 1 ml of saline after each sample was withdrawn. These samples were centrifuged at 14,000 RPM for 15 minutes at room temperature to obtain platelet poor plasma. The plasma was frozen at 4 °C until it was assayed for TAT, PF4, and hemoglobin concentrations. At the end of each experiment, the chamber was isolated from the rest of the loop and rinsed with saline. After disassembly the orifice plate was removed and visually inspected for gross clotting. Any thrombi were carefully removed and placed in 10% neutrally buffered formalin (VWR) for later histological observation.

5.1.4. Blood collection

These studies were approved by the Institutional Review Board for human subject research at the Georgia Institute of Technology. Blood was collected by venipuncture using a 19-gauge needle into 60 ml syringes filled with 3.2% sodium citrate to prevent clotting. Volunteers were randomly selected from a population of healthy individuals

both male and female who had not taken aspirin for at least two weeks. Ages ranged from 20 to 50 years old with an average age of 24. Blood was used within 3 hours of drawing.

5.1.5. Orifice plate construction

The orifice plates were constructed from 25.4 mm diameter, 400 μm thick acrylic plates with central round orifices or rectangular slits. The fabrication was done by a machinist using precision drill bits (McMaster Carr, Atlanta, GA) for the round orifices and thin saw blades (McMaster Carr, Atlanta, GA) for the rectangular slits. All entrances and exits to the orifices and slits were 90-degree solid edges that were polished to minimize burrs. The geometries used for this study were 200 μm, 400 μm, 800 μm, and 1200 μm round orifices, and slits, which were 200 μm, 400 μm and 800 μm wide by 12.7 mm long. The round orifices were designed to simulate the hinge area of the bileaflet MHV and the slits to simulate the b-datum line of the MHV during valve closure. The average diameter of the hinge region through which blood flows is approximately 100 to 200 μm, and the width of the b-datum line is approximately 200 μm. Thus, the orifice and slit sizes were chosen to characterize the upper and lower limits for these leakage regions. The 1200 μm round orifice served as a control to demonstrate that thrombin-antithrombin III (TAT) concentration was not increased by the flow loop. The measured flow rates, cross-sectional areas, estimated bulk velocities, Reynolds numbers, and calculated wall shear stresses are listed in Table 5.1.5.1. The wall shear stress for the round orifices was calculated as the dynamic viscosity, ν, times the magnitude of the partial derivative with respect to the radial direction, *r*, of the laminar pipe entrance velocity profile [54] in Equation 5.1.5.1:

$$\frac{u}{U} = 2\left(1 - \frac{r^2}{a^2}\right) + \sum_{i=1}^{\infty} \frac{4}{\alpha_i^2} e^{-\frac{\alpha_i^2 x}{\mathrm{Re}\, a}} \left[\frac{J_o\left(\alpha_i \frac{r}{a}\right)}{J_o(\alpha_i)} - 1 \right] \qquad \text{Equation 5.1.5.1}$$

where u is the instantaneous velocity, U is the bulk velocity through the orifice, a is the radius, x is the axial distance from the inlet, J_o is the zeroth order Bessel function, and α_i is the i^{th} root of the second order Bessel function, J_2. The Reynolds number was based on U and a. The resulting wall shear stress equation is:

$$\tau_s = \mu \frac{\partial(u)}{\partial r}\Big|_{r=a} = \mu U \left(-\frac{4}{a} + \sum_{i=1}^{\infty} \frac{4}{a \alpha_i J_o(\alpha_i)} \left(J_o{}'(\alpha_i) \right) e^{-\frac{\alpha_i^2 x}{\mathrm{Re}\, a}} \right) \qquad \text{Equation 5.1.5.2}$$

For the slit orifices, the wall shear stress was calculated as the dynamic viscosity, ν, times the magnitude of the partial derivative with respect to the transverse direction, y, of the laminar parallel plate channel velocity profile [54] in Equation 5.1.5.3:

$$\frac{u}{U} = 1.5\left(1 - \frac{y^2}{h^2}\right) + \sum_{i=1}^{\infty} \frac{2}{\alpha_i^2} e^{-\frac{\alpha_i^2 x}{\mathrm{Re}\, h}} \left[\frac{\cos\left(\alpha_i \frac{y}{h}\right)}{\cos(\alpha_i)} - 1 \right] \qquad \text{Equation 5.1.5.3}$$

where h is the channel halfwidth and α_i is the i^{th} root of the equation $\tan \alpha_i = \alpha_i$. The Reynolds number was based on U and h. The resulting wall shear stress equation is:

$$\tau_s = \mu \frac{\partial(u)}{\partial y}\Big|_{y=h} = \mu U \left(-\frac{3}{h} - \sum_{i=1}^{\infty} \frac{2\tan(\alpha_i)}{h \alpha_i} e^{-\frac{\alpha_i^2 x}{\mathrm{Re}\, h}} \right) \qquad \text{Equation 5.1.5.4}$$

For all of the wall shear stress calculations, the derivative was calculated 50 μm downstream of the orifice inlet at x=50 μm.

TABLE 5.1.5.1. Flow rate, Cross-sectional area, bulk velocity, Reynolds number (Re=aU/ν for the round orifices, Re= hU/ν for the slit orifices), and estimated wall shear stress for the orifices used in this study. Bulk velocity was calculated based on the cross-sectional area and measured flow rate, and wall shear stress was estimated using a laminar pipe entrance flow profile for the round orifices and a parallel plate channel entrance flow profile for the slit orifices 50 μm downstream of the inlet.

	Flow rate (L/min)	**Cross-sectional Area (mm^2)**	**Bulk Velocity (U) through orifice (m/s)**	**Reynolds number**	**Estimated Wall Shear Stress Magnitude ($dynes/cm^2$)**
200 μm round orifice	0.01	0.0314	5.31	150	21,700
400 μm round orifice	0.045	0.126	5.97	340	19,100
800 μm round orifice	0.15	0.503	5.0	570	9,200
1200 μm round orifice	0.32	1.13	4.72	810	6,000
200 μm slit orifice	0.90	2.54	5.91	170	24,200
400 μm slit orifice	1.7	5.08	5.58	320	21,100
800 μm slit orifice	3.06	10.16	5.02	570	15,800

5.1.6. Channel construction

The channels were constructed from 25.4 mm diameter, 1.5 mm thick acrylic plates. Four different geometries were studied with small (400 μm) and large (800μm) diameters as shown in Figure 5.1.6.1. The channels were designed to represent different nuances that could be present in hinge geometries to test the efficacy of the system at detecting these differences in geometry. Channels 1 and 2 were constructed using 400, 800, and 1200 μm precision drill bits. The smaller inner orifices were drilled straight through while the angled inlet portion was constructed by inserting a 130° micro drill bit into the orifice only until the main portion of the bit touched the outside of the plate. Thus, an angled opening with a 130° opening was created. The inner orifices of Channels 3 and 4 were also drilled through in the same way as those of Channels 1 and 2.

However, the entrance and exit to these channels were constructed using 800 and 1200 μm end mills (McMaster Carr, Atlanta, GA) that created 90° angles to the plate.

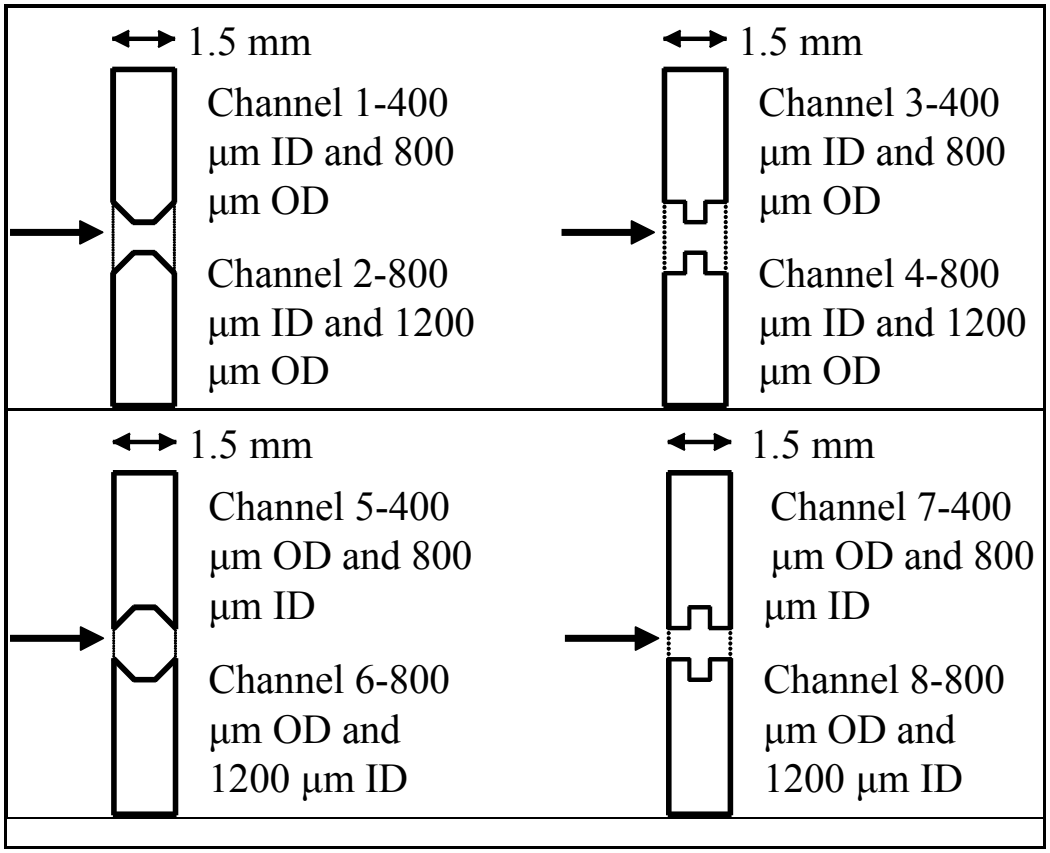

FIGURE 5.1.6.1. Channel diagrams.

Channels 5 and 6 were constructed from two pieces that were made the same way as Channels 1 and 2. These pieces were then glued together with acrylic glue. Similarly, Channels 7 and 8 were constructed from two pieces that were made in the same manner as Channels 3 and 4 that were then glued together with acrylic glue.

5.1.7. Valve experiments

For the final experiments the valves in Table 5.1.7.1 were placed in the chamber shown in Figure 5.1.7.1 and connected to a centrifugal bypass pump (Biomedicus Bioconsole Pump, Minneapolis, MN) using 6.35 mm ID silicone tubing as shown in Figure 5.1.7.2.

TABLE 5.1.7.1. Valves used in this study with measured flow rates and approximate hinge geometries and minimum diameters. Diameters for the SJM standard and low and high leaker prototype valves are estimated from CT scans of similar valves scaled by the respective leakage flows for the valves used in this study.

Valve type	**Leakage flow rate, l/min**	**Hinge geometry**	**Approximate min. hinge diameter, μm**
27mm SJM Standard	0.37 +/- 0.06	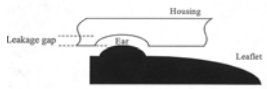	100
27mm low leaker prototype	0.13 +/- 0.05		80
27mm high leaker prototype	0.69 +/- 0.1		240
27mm Medtronic Parallel	0.41 +/- 0.07		127 (Ellis, 1996)

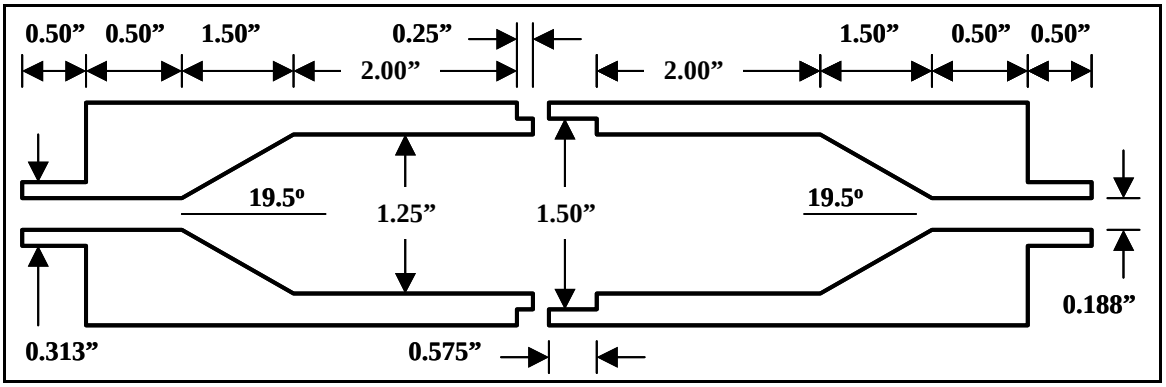

FIGURE 5.1.7.1. Diagram of the orifice/channel chamber used for this study.

The total volume of the flow loop was approximately 160 ml. The flow loop was rinsed with saline and then filled with human blood drawn into 3.2% sodium citrate at a 10:1 blood to citrate ratio. Air was purged from the system, and the bypass pump was operated at 2000 RPM. Simultaneously, to partially reverse the citrate anticoagulation, 100 mM

calcium chloride was infused into the loop with a syringe pump at a rate of 38.6 µL/min. This infusion rate resulted in an end calcium chloride volume in the flow loop of 2.3 ml. The dilution effect from this addition was accounted for in the calculations of TAT, PF4, and plasma hemoglobin concentrations. Calcium chloride was injected just prior to the pump head since experiments with dye injection showed complete mixing of substances injected at this point by the centrifugal action of the pump head. The citrate:Ca^{2+} ratio for these studies was fixed at an end ratio of 8.3:1 at 60 minutes.

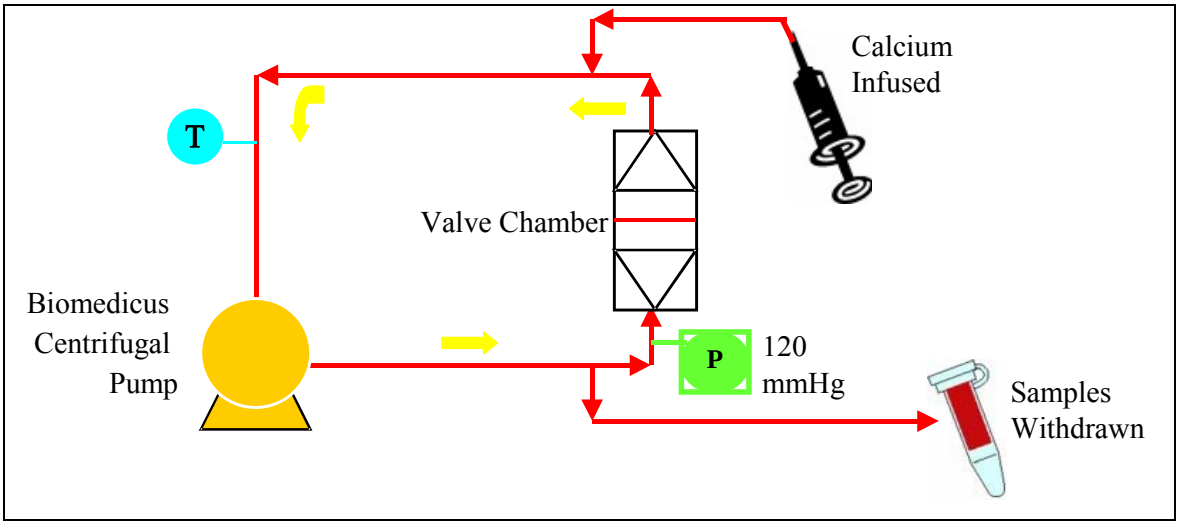

FIGURE 5.1.7.2. Diagram of the steady flow loop used for this study.

During the experiment the pressure upstream of the orifices was monitored using the pressure transducer on the pump and maintained at 120 mmHg (+/- 5 mmHg). Flow was also monitored during the experiment. Two 0.5 ml samples were withdrawn at 0, 15, 30, and 45 minutes and also at the end of the 60-minute experiment and placed in 3 ml EDTA vacutainer tubes for the TAT and hemolysis assays and in a mixture (detailed protocol in Appendix A) of aspirin, acid citrate dextrose (ACD), and Prostaglandin E_1 for

the PF4 assay. This sample volume was replaced by 1 ml saline at each sample time. These samples were centrifuged at 14,000 RPM for 15 minutes to obtain platelet poor plasma, which was subsequently assayed for TAT, PF4, and hemoglobin concentrations. At the end of each experiment, the chamber was isolated from the rest of the loop and rinsed with saline. After disassembly the orifice plate was removed and inspected for gross clotting.

5.1.8. Biological assays

Once the recalcification system was set up, the next step was to develop reproducible assays to quantitatively assess thrombus formation. Different methods were investigated to measure this endpoint. RBC quantification and the d-dimer ELISA assay are two of these preliminary assays discussed briefly here. The final assays, Thrombin-Antithrombin III (TAT) and platelet factor 4 (PF4) ELISAs and plasma hemoglobin, used for quantitative analyses in these studies will then be discussed in detail.

5.1.8.1. Preliminary assays

For the RBC quantification assay, gross thrombosis and loose blood was removed and then the valve was soaked in Drabkin's reagent (Ricca Chemical Company, Arlington, TX) to lyse the RBCs to release the hemoglobin. The absorbance of the resulting solution was measured with a spectrophotometer (SpectraMax Plus 384, Molecular Devices, Sunnyvale, CA) and correlated with the amount of RBCs on the valve. The problem with this method of quantification was that RBCs became attached to the sewing ring, despite coating the fabric with silicone to reduce this likelihood. Because these cells contributed

to the final number, the sensitivity of this method was dependent upon very few or no RBCs attaching to the sewing ring. Due to this lack of sensitivity and the high standard deviations, this method was not the best for determining thrombus size.

The d-dimer ELISA (American Diagnostica, Stamford, CT) assay is routinely used for diagnosis of venous thromboemobolism, pulmonary embolism or other conditions that result in clot lysis *in vivo* [55]. These assays are commercially available and measure reliably the amount of D-dimer present in a patient's plasma. D-dimer is one of the degradation products of cross-linked fibrin that is only present in clots. Soluble fibrin found in the bloodstream does not form d-dimers. Thus, d-dimer is only a measure of clot lysis, not of soluble fibrin. For the purposes of this study, the amount of D-dimer found on the valve or orifice/hinge model after each run was measured using the ELISA test. First the orifice plates were removed at the end of the experiment, rinsed, and then incubated with tissue plasminogen activator (TPA, Biosciences, Inc., La Jolla, CA). The TPA activates the plasminogen in the sample to plasmin, which degrades the fibrin into its base monomers. In this assay d-dimer was attached to a monoclonal antibody fixed to wells in the test plate by adding the mixture to the plate, incubating for a period then rinsing off any unbound proteins. A dye conjugated with a secondary antibody was then added to the wells to bind to the primary antibody for d-dimer. In this way the d-dimer was labeled with a colored substance that could be detected and quantified with a spectrophotometer. The excess dye was rinsed from the plate, and the color magnitude was quantified. A calibration curve was then used to determine the sample concentrations. Assuming that the mixture obtained from the dissolution and degradation of the sample was well mixed, this number was converted from a concentration to an

actual quantity of fibrin in the entire clot. However, because of the unpredictability of thrombus formation and embolization in these studies, the d-dimer assay proved to have poor reproducibility and was thus not suitable for quantitative assessment of thrombus formation for these studies.

5.1.8.2. Final assays

Thrombin is an essential agonist for the formation of thrombi containing both platelets and fibrin. Accordingly, to assess the thrombus forming potential of MHV geometries, the present study focused on the generation of thrombin as measured by the TAT assay. The TAT complex is formed when the inhibitory molecule, Antithrombin III (ATIII), binds to active thrombin, consequently preventing it from propagating the coagulation cascade. Thus, TAT formation is a positive indication of cumulative thrombin generation. This assay is limited, however, because all thrombin and antithrombin present may not be bound in a TAT complex. The presence of TAT in the samples was measured using an Enzygnost TAT micro assay (Dade Behring, Deerfield, IL). In this assay (detailed protocol in Appendix A), a primary antibody for thrombin was affixed to the bottom of each well of a 96 well plate. Duplicates of each sample were inserted into these wells and incubated. Unbound proteins were then rinsed, and a peroxidase-conjugated ATIII antibody was added to bind with the unbound ATIII constituent of the complex. The unbound ATIII antibodies were then rinsed, and chromogen was added to initiate a reaction with hydrogen peroxide. This reaction was stopped by the addition of sulfuric acid. For this chromogenic assay, color intensity was measured with a microtiter absorbance plate reader (SpectraMax Plus 384, Molecular

Devices, Sunnyvale, CA) at a wavelength of 492 nm. The intensity was proportional to concentration based on a standard curve in the range from 2 to 60 μg/L. Samples with higher concentrations were diluted with plasma prior to the start of the assay.

PF4 was measured using a Zymutest PF4 (Hyphen Biomed, Neuville sur Oise, France) micro assay (detailed protocol in Appendix A). Once again the antibody specific for human PF4 was affixed to the bottom of each well in a 96 well plate. The samples were inserted into the wells and incubated. Unbound proteins were then rinsed, and the secondary antibody, an immunoconjugate to the unbound PF4 epitope coupled to horseradish peroxidase, was added, and the mixture was incubated. The unbound secondary antibody was then rinsed off, and a peroxidase substrate, Tetramethylbenzidine (TMB), was added, which in the presence of hydrogen peroxide developed a blue color. Upon termination of the reaction by the addition of sulfuric acid the color became yellow. Absorbance was determined using a SpectraMax Plus 384, (Molecular Devices, Sunnyvale, CA) at a wavelength of 450 nm. Concentration of the samples was determined using a standard curve ranging from 0.5 to 10 μg/l. Samples with higher concentrations were diluted with sample diluent prior to the start of the assay.

Hemolysis in the samples was determined using a microplate assay (detailed protocol in Appendix A). The plasma samples were mixed with Drabkins reagent (Ricca Chemical Co., Arlington, TX) in a 1:3 ratio of plasma to Drabkins, and 100 μL of the mixture was added to each of the wells. The resulting color intensities of the samples were measured with a microtiter absorbance plate reader (SpectraMax Plus 384, Molecular Devices, Sunnyvale, CA) at a wavelength of 540 nm. A standard curve was constructed with known amounts of whole blood and Drabkins reagent, and from the

standard curve the concentration of hemoglobin in each of the samples was determined. The standards were prepared by measuring the RBC count and hemoglobin concentration of the whole blood using a cell counter (CoulterMAX). This whole blood was then mixed with different amount of Drabkins reagent to obtain a range of hemoglobin concentrations from 0 to 0.55 mg/ml.

5.1.9. Experimental variations

5.1.9.1. 400 μm round orifice

Variations of the normal experiments were performed with the 400 μm round orifice as a positive control to assess important variables in TAT generation and platelet activation. These experiments were performed only with the 400 μm round orifice since the normal blood experiments with this orifice showed reproducible and significant increases in TAT at all sample times. The role of platelets was assessed by removing platelets from the blood prior to the experiments, and experiments were performed without calcium chloride addition to assess the effect of this variable. The role of the GpIIb/IIIa platelet receptor in the aggregation of activated platelets was assessed by blocking this receptor using Aggrastat (Merck & Co., Inc. East Point, PA), a drug that binds to this platelet receptor thus rendering it inactive. The role of vWF binding to the platelet GpIb receptor was assessed by blocking the CD42 region of vWF using the commerically available AN51 antibody (Dako, Carpinteria, CA).

To assess the role of platelets in thrombin generation and thrombosis in the model, platelets were removed from blood by first centrifuging 33 ml aliquots of blood in 60 ml Taylor tubes at 4000 RPM to prepare platelet poor plasma (PPP), a buffy layer, and

RBCs. The PPP was largely removed and set aside. The remaining PPP, the buffy layer, and about 2.5 ml of the RBCs were removed and discarded. The PPP was then centrifuged for 5 minutes at 4000 RPM and added back to the remaining RBCs. Blood cell counts were taken before and after centrifugation to determine the efficiency of platelet removal and to ensure that the blood counts were still in the range of normal blood (Coulter Multisizer III, Beckman Coulter, Fullerton, CA). In normal blood, platelet counts averaged 170,000 +/-65,000 cells per μl, while in platelet-depleted blood the counts averaged 20,000 +/- 6,000 cells per μl. The hematocrit was modified by this protocol from 41 +/- 14 to 32 +/- 5, which was still in the acceptable range.

Runs without calcium chloride addition were performed as a control. These runs were identical to previous runs except that no calcium chloride was infused.

Aggrastat (Merck & Co., Inc. East Point, PA) was used to block the platelet GPIIb/IIIa receptor binding to fibrin. The amount of Aggrastat necessary was determined to be 2.17 μg/ml in preliminary steady flow tests with the 400 μm round orifice. This amount is tenfold the concentration used clinically to block 90% of ADP aggregation. Aggrastat was added to the blood prior to filling the loop to ensure that it was well mixed.

AN51 (Dako, Carpinteria, CA) was selected to block the platelet GPIb receptor binding of vWF thereby preventing platelet aggregation via this pathway. The amount of AN51 necessary was initially estimated from the literature [56] and confirmed in preliminary steady flow tests with the 400 μm round orifice to be 0.25 μg/ml. AN51 was added to the blood prior to filling the loop to ensure that it was well mixed.

5.1.9.2. 800 μm round orifice

Variations of the normal experiments with the 800 μm round orifice with different flow rates were performed to investigate the effect of shear stress and flow rate on platelet activation and thrombus formation. Table 5.1.9.2.1 shows these different conditions along with the estimated wall shear stress and Reynolds numbers for the variations. For these experimental variations with the 800 μm round orifice, the flow rate was varied to change the shear stress. The volume and run time were also varied to maintain the same number of passes for the low, normal, and high flow experiments. The passes were calculated as the number of times a single volume would pass through the orifice during the experiment assuming a homogeneous distribution. The total number of passes was approximately 100, and samples were withdrawn at times corresponding to 0, 25, 50, 75, and 100 passes.

Table 5.1.9.2.1. Flow rate, bulk velocity, Reynolds number (Re=aU/ν), and estimated wall shear stress for the variations on the 800 μm round orifice experiments. Bulk velocity was calculated based on the cross-sectional area and measured flow rate, and wall shear stress was estimated using a laminar pipe entrance flow profile for the round orifices 50 μm downstream of the inlet.

	Flow rate (L/min)	**Bulk Velocity (U) through orifice (m/s)**	**Reynolds number**	**Estimated Wall Shear Stress Magnitude (dynes/cm^2)**
800 μm round orifice-low flow	0.09	3.0	340	5,300
800 μm round orifice-normal	0.15	5.0	570	9,200
800 μm round orifice-high flow	0.19	6.6	750	12,400

5.1.10. General histology

Two basic stains were used to better elucidate the morphology of the thrombi. A Hematoxylin and Eosin (H & E) stain was used to show the cell membranes and nuclei of

the cells. A Carstairs stain was used to positively identify the platelets and fibrin in the thrombus. A perfused rat heart section was used a positive control for the Carstairs stain to show the presence of fibrin, platelets, and RBCs in an artificially induced thrombus in the rat heart.

5.1.10.1. Tissue preparation

For all of the stains the tissue was fixed in 10% neutrally buffered formaldehyde (VWR, 3323-1) overnight then transferred to 70% alcohol and stored at 4°C before tissure processing. The fixed tissue was then placed into plastic cassettes and placed in a tissue processor (Shandon Pathcentre Tissue Processor, Shandon, Pittsburgh, PA) for routine overnight tissue processing. There are three steps in tissue processing: 1. Tissue is dehydrated by successive incubation in graded alcohol from low to high concentrations; 2. The tissue is cleared of alcohol using xylene; 3. The tissue was infiltrated with liquid paraffin. The block of paraffin with the tissue embedded in it is then sliced using a microtome (Rotary microtome HM 355S, Microm International GmbH) into 5 μm thick sections. The tissue was then affixed to positively charged glass slides and placed in a drying oven at 37°C overnight. Prior to staining the slides were deparaffinized in a Leica Autostainer (Leica, #74710254). Removal of the paraffin is necessary so that the stains can penetrate the tissues.

5.1.10.2. Basic staining

Hematoxylin and Eosin (H and E) staining is a common staining method for tissue structure visualization. Hematoxylin is a basic dye that stains acid structures, such

as chromatin in the cell nuclei, purple or blue. Eosin is an acidic dye that stains basic structures, such as RBCs, red. The H and E stain (detailed protocol in Appendix A) was performed automatically by the autostainer up to the point at which the slides were ready to be coverslipped.

The Carstairs stain is a three color stain used specifically to look for platelets, RBCs, fibrin, and collagen. This stain allowed us to see the thrombus morphology more clearly and to disinguish the different components. For this stain (detailed protocol in Appendix A) the slides were first incubated with 5% ferric alum then stained in order with hematoxylin, picric acid-orange G solution, ponceau fuchsin, and aniline blue solution. Differentiation with 0.25% acid alcohol and 1% phosphotungstic acid was performed to ensure the proper uptake of the stain in the different tissues. The timing of these different steps and incubation periods was optimized to achieve the colors that best matched the scheme outlined in the initial protocol.

5.1.11. Immunohistochemistry

Immunohistochemistry (IHC) is the localization of proteins in tissue sections with labelled antibodies as specific reagents through antigen-antibody interactions. Protein localization can be visualized uisng fluorescent dyes, enzymes, radioactive elements, colloidal gold, or colorimetric dyes. The Avidin-Biotin-Complex (ABC) method was used for this particular IHC, and both fluorescent and colorimentric dyes were used. Avidin is a large glycoprotein that can be labelled with enzymes or fluorophores and has a high affinity for Biotin. Biotin can be conjugated to a variety of antibodies. Thus the ABC IHC technique involves three layer placed on the tissue section. The first layer is an

unlabeled primary antibody, the vWF antibody in this case. The second layer is a biotinylated secondary antibody that will bind to the primary antibody, and the third layer is a complex of avidin-biotin conjugated peroxidase. The peroxidase is then developed by diaminobenzidine (DAB) or other substrate to produce different colored end products. Briefly, the steps for the IHC (detailed protocol in Appendix A) were to first block the endogenous peroxidase using 3% H_20_2, followed by blocking of nonspecific binding using a 1% gelatin/PBS mixture. The primary vWF antibody was then added to the slides and incubated. A biotinylated secondary antibody was then added to the slides and incubated. Finally, the slides were incubated with diaminobenzidine (DAB) to bring out the color, and then counterstained with hematoxylin to show the nuclei. All incubation steps were carried out in a humid chamber to prevent drying of the slides.

5.1.12. Scanning electron microscopy

Scanning electron microscopy (SEM) provides high resolution imaging of surface morphology and was used in this study to evaluate thrombus morphology. SEM produces a highly magnified image by using electrons instead of light to form an image. The sample is placed in a vacuum chamber and is then bombarded with a beam of electrons that is focused on the area on interest by a series of electromagnetic fields and lenses. Once the beam hits the sample surface, electrons and X-rays are ejected from the sample, and an image is obtained using these secondary electrons. The orientation of the sample surface influences the number of electrons that reach the seconday electron detector, thus creating variation in image contrast that represents the surface topography of the sample.

Since the SEM is performed in a vacuum, all water must be removed from the sample to prevent the water from vaporizing under the vacuum conditions. The sample surface must also be made conductive by coating it with a thin layer of conductive material. The orifice plates were fixed in 10% neutral buffered formalin overnight then placed in 70% ethanol. For SEM preparation (detailed protocol in Appendix A) [20] the samples were placed in 2.5% glutaraldehyde (Electron Microscopy Science: 16019) in cacodylate buffer (pH 7.2, Electron Microscopy Science: 11652) for 1-2 hours. The samples were then rinsed in 0.2M cacodylate buffer and dehydrated in increasing concentrations of alcohol. In place of critical point drying, the sample was dried with hexamethyldisilazane (HMDS, Electron Microscopy Science: 16700) using the following protocol: 100% ethanol, 2:1 ethanol:HMDS, 1:1 ethanol:HMDS, 1:2 ethanol:HMDS, and 100% HMDS. The samples were then rinsed three times in HMDS and then left overnight in the fume hood in the last wash to allow the HMDS to evaporate. After overnight drying the samples were adhered to an aluminum stub (SPI: 01506-BA) using conductive, double sided carbon tape (SPI: 05081-AB) and then sputter coated with gold to a thickness of about 100 Angstroms. After sputter coating, the samples were kept desiccated until ready until ready to be observed using a Hitachi S-800 scanning electron microscope.

5.1.13. Statistics

Because the data for the biological endpoints was not normally distributed and the samples sizes (as low as 6) were small, non-parametric tests were used to determine the statistically significance of the data. These non-parametric tests place no restriction on

the distribution of sample size. Instead of specific parameters of a population, the non-parametric tests compare the relative locations of the probability distributions of the sampled populations. Many of these tests use the relative ranks of the sample observations rather than their actual numerical values.

The Kruskal Wallace test was used to initially determine the influential variables that affected the end quantitative measures. Statistical significance between the samples was determined using the Mann-Whitney test with a sample size of 6 for all experiments. Comparisons were made to the 400 and 1200 μm round orifices as positive and negative controls, respectively. The Kruskal-Wallis test is a nonparametric method of testing the hypothesis that several populations have the same continuous distribution versus the alternative that measurements tend to be higher in one or more of the populations. To apply the test, we obtain independent random samples of sizes n_1, n_2, . . , n_m from m populations. Assume that there are N observations in all. We rank all N observations and let R_i be the sum of the ranks of the n_i observations in the i^{th} sample. The Kruskal-Wallace statistic is:

$$H = \left[\frac{12}{(N(N+1))}\right] * \sum_{i}^{m} \frac{R_i^{\,2}}{n_i} - 3(N+1) \qquad \text{Equation 5.1.13.1}$$

When the sample sizes are large and all m populations have the same continuous distribution, then H has an approximate chi-square distribution with (m – 1) degrees of freedom. When H is large, creating a small right-tail probability (p-value), then we reject the null hypothesis that all populations have the same distribution.

The Mann-Whitney test compares medians rather than means. In the two-tailed case, the null and alternative hypotheses for the t-test and Mann-Whitney test are:

	Independent Samples t-Test	**Mann-Whitney test**
H_0	$\mu_1 = \mu_2$	$\eta_1 = \eta_2$
H_A	$\mu_1 \neq \mu_2$	$\eta_1 \neq \eta_2$

where η stands for the median and μ stands for the mean. For either case, you reject the null-hypothesis if the p-value is below a specified level (perhaps .01, .025, or .05 depending on the situation). Specifically, in the Mann-Whitney test the observations from both samples are listed together in increasing order and each observation is given a rank showing its position in this combined listing (1 for the lowest and n_1+n_2 for the highest). An adjustment has to be made if there are ties. One of the groups is chosen and its "rank-sum" is computed. If there is no difference between the populations the groups are sampled from, then each group should have about the same "rank-sum" proportional to its sample size. If there is a difference between the population medians, then one sample will have a lower-than-expected rank-sum (because disproportionately many of the lower observations are in that sample) and the other will have a higher-than-expected rank-sum (because disproportionately many of the higher observations are in that sample). There is also a confidence interval associated with the Mann-Whitney test, as there is for the t-test, which includes likely values for differences between population medians.

5.1.14. Ex vivo experiments

The *ex vivo* experiments were performed using an arterio-venous shunt from the femoral artery to the femoral vein of a baboon. The animals for these experiments were chosen to have similar platelet counts (400+/-17.2 million/ml) that were above 375 million/ml since this was determined to be an important factor in thrombus formation on the orifice plate. For the platelet radiolabeling (detailed protocol in Appendix A), blood was initially removed from the baboon and the platelets were isolated and labeled with ^{111}Indium. The blood was then mixed with the plasma and RBCs that had been removed, and re-injected into the animal. After allowing the labeled platelets to circulate at least overnight, the *ex vivo* experiments were performed.

Prior to beginning the experiments, Heparin was first administered as a bolus in 60 IU/kg quantities until the APTT time was between 75 and 100 seconds. Heparin was then administered during the experiment at a rate of 50 IU/kg/hr. This heparinized blood traveled from the arterial side of this shunt through the 800 μm slit orifices in the orifice plate chamber (Figure 5.1.14.1) then back to the venous side of this shunt for a duration

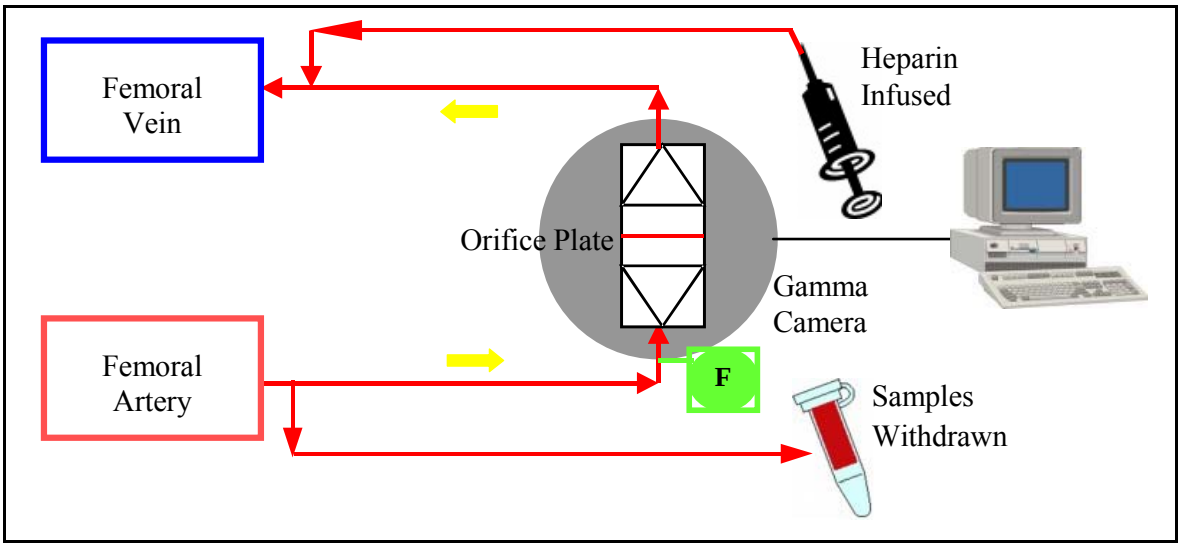

Figure 5.1.14.1 Diagram of ex vivo shunt flow loop with orifice chamber.

of 60 minutes. During the experiment the buildup of radiolabeled platelets on the orifice plate was measured at either 3 or 5 minute time intervals using a gamma camera. Flow and APTT times were also measured at 0, 15, 30 and 60 minutes. After the experiment the chamber was isolated from the *ex vivo* shunt and rinsed with saline. An image of the rinsed chamber was then acquired to quantify the platelets that were bound to the chamber and the orifice. Subtraction of the measured radioactivity from the rinsed chamber from that in the last image acquired prior to isolating the chamber yields the background radioactivity emitted from the flowing platelets. This background radioactivity is subtracted from all of the images to calculate the net platelet deposition on the plate and chamber during the experiments. After rinsing with saline, the orifice was removed and placed on the gamma camera to allow better visualization and quantification of the areas in which platelets are present. An image of the entire orifice was first acquired. Then the proximal side of the orifice was scraped, and second image was acquired. In this way the thrombus formation could be quantified on each side of the plate. During data processing the previously determined relationship between radiation and platelet count was used to calculate platelet count at each time step.

5.2. Digital Particle Image Velocimetry (DPIV)

Planar DPIV is a non-invasive velocity measurement technique that can be used to measure the in-plane velocity field component in a planar region of interest. The instantaneous fluid velocity field is determined by estimating the displacements of neutrally buoyant particles that are seeded in the flow. A double pulsed laser combined

with optics produces two pulses of uniform laser light that illuminates the particle-laden flow in the region of interest. Paired images corresponding to the respective laser pulses are captured using a digital camera and stored on a computer in real time. The image data is subsequently analyzed to obtain particle velocities by estimating the particle displacement over the known time interval between laser pulses using a cross correlation scheme applied over small interrogation regions between the image pair. The output from this analysis is the in-plane vector field measurement corresponding to the velocity in the axial direction, u, and the velocity in the transverse direction, v.

5.2.1. Materials

The working fluid used for the DPIV experiments was a solution of saturated sodium iodide, glycerin, and deionized water in a volumetric ratio of 79/20/1. The kinematic viscosity of this solution was measured with a viscometer to be 3.5 cSt, and the refractive index was measured with a refractometer to be 1.49. Although the density of this blood analog solution (1.62 g/cm^3) differs from that of blood (1.05 g/cm^3), its kinematic viscosity (3.5 cSt) matches that of blood under normal physiological conditions. Based on this similarity of kinematic viscosity between blood and the blood analog under Newtonian conditions, dynamic similarity was assumed between the fluid flow through the orifices and channels in the DPIV setup and the blood flow through them in the *in vitro* flow loop. The refractive index of the blood analog (1.49) was mixed to match that of the acrylic orifice plate/channel mounting chambers so as to minimize optical distortion in these studies.

A typical batch of NaI saturated solution has a life span of approximately 6-8 months depending on the frequency of usage because of the oxidation of the NaI constituent of the blood analog, which turns dark brown after contact with the atmosphere, thereby interfering with the accuracy of the velocity measurement. To prolong the life of the solution, it was periodically filtered with a 5μm carbon impregnated filter cartridge (US Filter, Plymouth Products, MD) to deoxidize the solution and also to remove any contaminants. Additionally, the viscosity and refractive index of the solution had to be corrected occasionally by incrementally adding components of the solution to account for the evaporation of the water in the solution.

Fluorescent polymer particles (FPP-RhB-10, Dantec Dynamics, Denmark) based on melamine resin were used in all of the PIV experiments to seed the flow. The introduction of these fluorescent particles was to reduce the unwanted laser glare reflected from the surface of the chamber or orifice plate/channel surface and to improve the signal to noise characteristics of the raw images. The fluorescent particles, which had a diameter range of 1 – 20 μm, were delivered in suspension with water. The particles absorb the laser light at a wavelength of 532 nm and emit light at above 560 nm. An orange cutoff filter (Edmund Optics) mounted on the chamber permitted only light with wavelengths in the range of 560 – 600 nm to pass through it for detection by the camera. This filter ensured that only the fluorescent particles, which emitted light in response to excitation by the laser sheet at a wavelength of 560 nm, would be detected by the camera.

5.2.2. Experimental setup

For the DPIV experiments the orifice plates and channels were placed in the chamber as shown in Figure 5.2.2.1 and connected to a Biomedicus centrifugal bypass pump using 6.35 mm ID silicone tubing as shown in Figure 5.2.2.2. The total volume of the loop was approximately 77 ml. The flow loop was filled with the blood analog fluid seeded with the fluorescent particles. Air was purged from the system, and the bypass pump was operated at 2000 RPM. During the experiment the pressure upstream of the orifices/channels was monitored using the pressure transducer on the pump and maintained at 120 mmHg (+/- 5 mmHg) resulting in flow rates of 0.01, 0.045, 0.15, and 0.32 l/min for the 200, 400, 800, and 1200 μm orifices, respectively. These flow rates were measured using a blood analog fluid at a pump speed of 2000 RPM and upstream pressure of 120 mmHg. The flow rate was also monitored during the experiment with an inline flow meter and flow transducer supplied with the Biomedicus centrifugal pump.

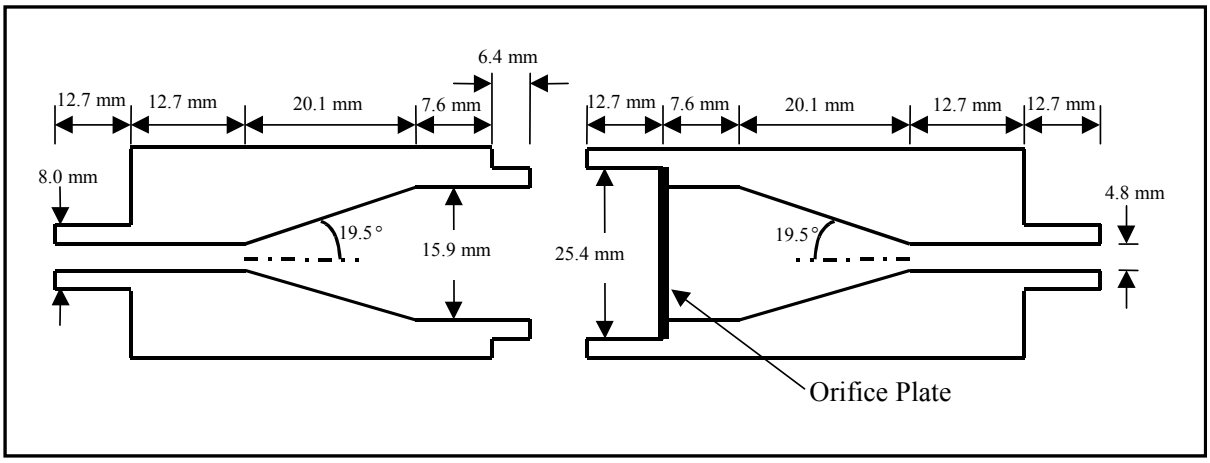

FIGURE 5.2.2.1. Diagram of the orifice/channel chamber used for this study.

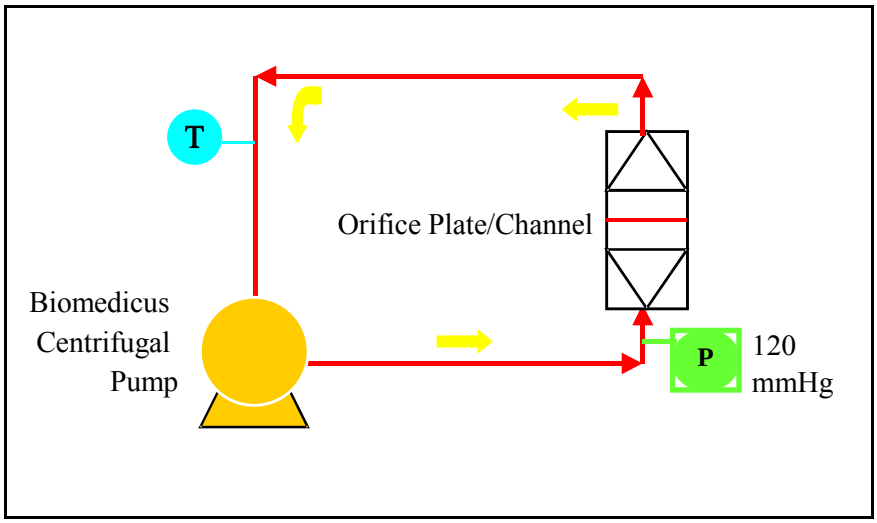

FIGURE 5.2.2.2. Diagram of the steady flow loop used for this study.

5.2.3. DPIV system

The DPIV system (Figure 5.2.3.1) consists of two Nd:YAG lasers (Model MiniLaser-I, New Wave Research, CA) that have an energy of 17 mJ per pulse and a maximum repetition rate of 15 Hz, and a light arm (Model 610015, TSI, MN) to transfer the laser beam to the area of investigation. A 12-bit 1600X1200 grey scale CCD camera (Model 1101MPRO, LaVision, Germany) equipped with a 1-5X fixed focal length zoom lens (Edmund Optics) was used for image acquisition. A programmable timing unit (Model 1108013, LaVision, Germany) was used to synchronize image capture with the laser pulse illumination of the particles, and an A/D converter (Model 1108033, LaVision, Germany) to integrate sampling control and data logging of the images. All of these components were connected to a host computer, which controlled the measurement and post-processing using image capture and analysis software (Davis 7.0, LaVision, Germany).

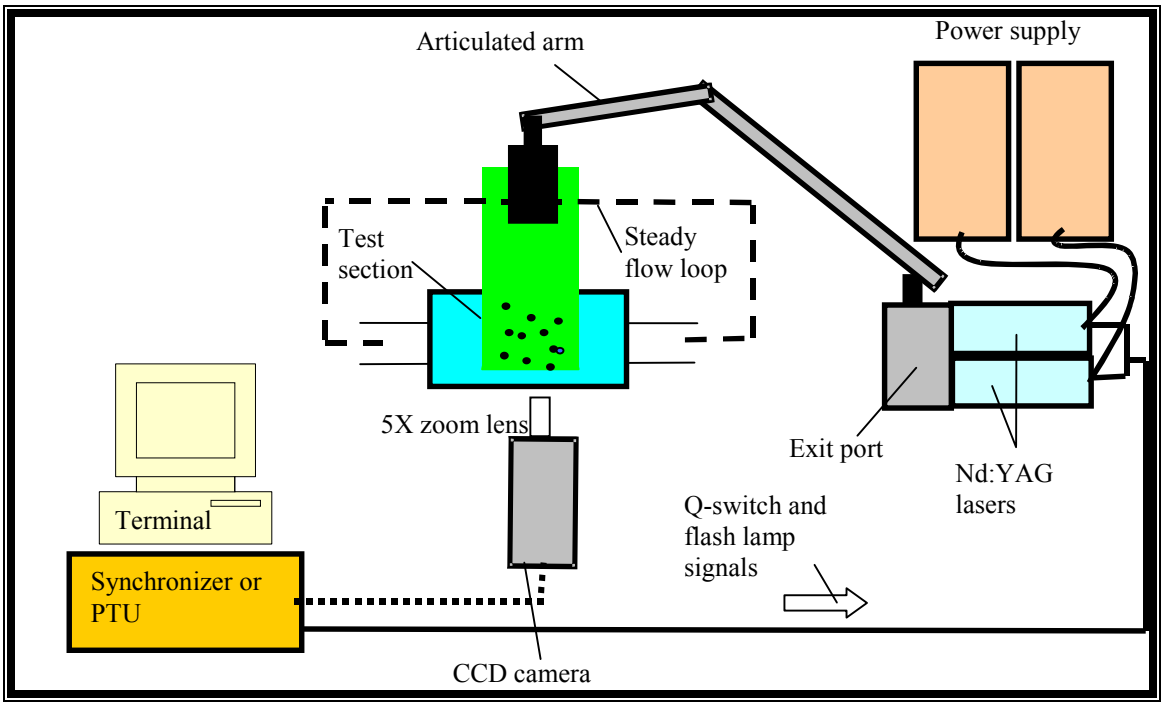

FIGURE 5.2.3.1 Diagram of DPIV system.

The basis of velocity measurement using DPIV is the simple tracking of particle displacement using paired images taken over a fixed time interval. The particles in the flow are illuminated for about 50 ns by a pulsed laser light sheet of approximately 1 mm in width. The width of this laser sheet was produced by diffracting the laser beam with a cylindrical lens combined with a spherical lens mounted at the end of the articulated light arm. At the instant of illumination by the first laser sheet, the CCD camera, which is placed orthogonal to the light sheet, captures an image. After a set time interval, termed the pulse separation, the second laser pulse illuminates the particles, and a second image is acquired. The pulse separation is prescribed based on the expected particle velocity, seeding density, and interrogation region size. As a rule a particle should be displaced by no more than ¼th the size of the interrogation region during the pulse separation. Preliminary analysis, however, determines the optimal pulse separation. These paired

images are stored in the RAM of the host computer and quickly transferred to the hard drive, and the procedure is repeated. The velocities in the field of investigation was subsequently calculated from the acquired paired images and the known pulse separation using a correlation algorithm, The final DPIV results are planar velocity fields, which describe the flow fields in the area of interest. With the known velocity field, it is possible to calculate quantities such as the total kinetic energy, the vorticity, and the viscous dissipation. The following section will describe in detail the components of the PIV system, which can be separated into several subsystems:

1) Solid state YAG laser
2) Laser transmitting articulated arm
3) Receiving camera
4) Velocity calculation software

5.2.3.1. Solid state YAG lasers

The two solid state Nd:YAG or Neodimium Doped Yttrium Aluminum Garnet (LaserPulse Mini YAG 12) lasers are mounted on a Breadboard (SA series, Newport, CA). Each laser consists of a flash lamp and a YAG crystal placed inside a mirrored elliptical cavity to maximize the energy transfer from the flash lamp to the crystal. The flash lamp in the laser has an excitation duration of approximately 250 μs, and a repetition frequency of 15 Hz. Each YAG laser is equipped with a Q-switch, which acts as a shutter to quickly open and close the laser cavity. The Q-switch is used to control the duration of the laser emission from the cavity so that the cavity is closed for the majority of the time and is only allowed to open for a brief period. The Q-switch mechanism allows the YAG rod to build up the lasing energy so that a high-energy pulse can be released. The laser also contains a harmonic generator device to divide the wavelength of

the emitted YAG laser light in half to 532 nm to improve the efficiency of the cameras, which are more sensitive to the blue-green spectrum. An additional advantage of having a visible light beam is to facilitate the alignment of the beam path. The double-pulsed laser beams pass through an exit port unit, which consists of a series of mirrors used to align the two beams to ensure that they overlap.

5.2.3.2. Laser transmitting articulated arm

The articulated arm assembly was coupled to the exit port of the YAG lasers. The assembly consists of a series of mirrors and joints connected by hollow tubes to direct the laser beams from one mirror to the next irrespective of the orientation of the joint. At the end of the arm assembly is an output ring, which enables the coupling of various optical configurations. In these experiments, a cylindrical lens (f = –25.4 mm) and a spherical lens (f = 500 mm) were mounted in series to the arm assembly to produce a laser sheet with a thickness of approximately 1 mm. The output end of the arm was mounted on a traversing mechanism to enable movement of the laser sheet.

5.2.3.3. Receiving camera

The term CCD stands for charge-coupled device. A CCD camera is comprised of receiving chip consisting of an array of CCD detectors called pixels. Each pixel is a Metal Oxide Silicone (MOS) capacitor that is charged by converting incident photons of light into electrons, as in a photodiode. The charge falling on the individual pixels is transformed to a voltage during read-out of the CCD chip, and the value of the voltage is seen as a gray scale distribution on the PIV image map. Ideally, particles in the image

should have a high charge (i.e. appear white), and the background noise should have a low charge (i.e. appear dark).

5.2.3.4. Velocity calculation software

The cross correlation of the digital image pairs to calculate the velocity fields was performed using commercially available PIV software (DaVis 7.0, LaVision, Germany). In the cross correlation program, each of the camera images are divided into rectangular regions called interrogation areas, and for each of these interrogation areas the particle images captured during the first and second pulse of the light-sheet are correlated to produce an average particle displacement vector (Figure 5.2.3.4.1). The cross correlation function statistically measures the degree of match between the two samples. The highest value in the correlation plane can then be used as a direct estimate of the particle image displacement. During cross correlation it is assumed that all particles within one interrogation region move homogeneously between two laser pulses.

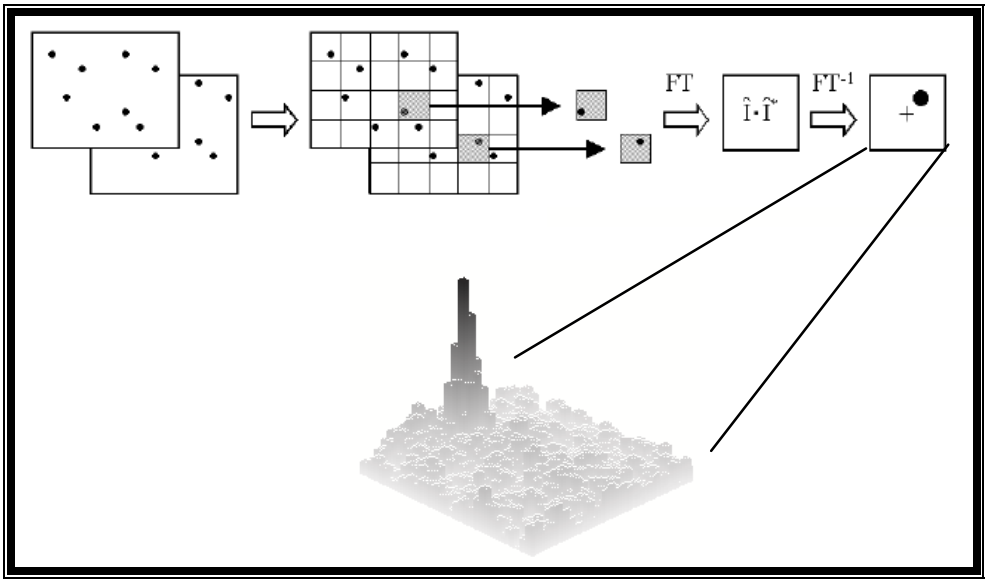

FIGURE 5.2.3.4.1 Diagram of DPIV image processing steps.

This calculation is performed for all interrogation regions to produce a vector map of average particle displacements. The displacement vectors are divided by the known pulse separation time and thus converted into a map of raw velocity vectors. Fast Fourier Transform (FFT) processing is used to increase the speed of the cross correlation. It is important to note that with FFT processing there will always be an outcome whether the input is meaningful or not. Since PIV is an instantaneous measurement technique, all spatial information is sampled at the same time. Consequently, there is a finite statistical probability that there will be some regions where the input is not meaningful. Therefore, it is necessary to validate the PIV vector map. The validation algorithms in DaVis can be applied to the raw vector maps so that outliers can be detected and removed. To remove these outliers the vector files obtained from the cross correlation were filtered to remove vectors that were more than five standard deviations from the local mean velocity at each measurement location.

5.2.4. Data Analysis

The filtered vectors are then used to calculate the axial and transverse turbulence intensities, u_{rms} and v_{rms}, the Reynolds shear stress, τ_{xy}, the Reynolds normal axial stress, τ_{xx}, and the Reynolds normal transverse stress, τ_{yy}, using the following equations:

$$u_{rms} = \sqrt{\frac{\sum_{i=1}^{n}\left[u-\bar{u}\right]^2}{n}} \qquad \text{Equation 5.2.4.1}$$

$$v_{rms} = \sqrt{\frac{\sum_{i=1}^{n}\left[v-\bar{v}\right]^2}{n}} \qquad \text{Equation 5.2.4.2}$$

where $\bar{u}$ and $\bar{v}$ are the mean of the local velocity vector in the axial and transverse direction, respectively, and n is the number of velocity vectors.

$$\tau_{xy} = \rho\overline{u'v'} \qquad \text{Equation 5.2.4.3}$$

where u' and v' are the instantaneous velocity fluctuations acting in the x (axial) and y (transverse) directions.

$$\tau_{xx} = \rho\overline{u'u'} = \rho u_{rms}^2 \qquad \text{Equation 5.2.4.4}$$

$$\tau_{yy} = \rho\overline{v'v'} = \rho v_{rms}^2 \qquad \text{Equation 5.2.4.5}$$

Once these quantities are calculated they are plotted on either contour or vector maps in which the contour colors correspond to the magnitudes of the values and the vector lengths and directions correspond to magnitude and net direction, respectively.

5.2.5. DPIV experimental considerations

Illumination of the particles is a critical aspect of the PIV setup. The laser sheet must be bright enough to illuminate the seed particles in the flow so that sufficient scattered light reaches the CCD camera. Ideally, the width of the light sheet should be as thin as possible to reduce the effect of out-of-plane particles. Thus, the test section should

be located where the light sheet is the thinnest; for these experiments, this region is approximately 500 mm from the lens. Another way to maximize the laser power is through the Q-switch control, which enables the opening and closing of the shutter to the laser cavity. The optimal firing time for maximum laser power is 186 μs, which corresponds to the time at the peak of the laser power (Figure 5.2.5.1). There is a trade-off between allowing the energy to build up by the action of the flash lamp and the natural dissipation rate of the cavity so the Q-switch is normally fired 150-200 μs after the start of the flash lamp. The advantage of the Q-switch is that all of the energy is released in a high-energy pulse, and since the duration of the laser beam is short, the seeding particles move very little during illumination. Another consideration for the lasers is to be sure that both lasers have the same brightness, or that the paired images have the same brightness. If one of the images is considerably brighter than the other, particles that are illuminated in this image may not be shown in the dimmer image. Consequently, these images will not be correlated by the correlation software and could result in erroneous vectors or noise. Thus, to equalize the brightness in the images, it may be necessary to reduce the brightness of one of the lasers by adjusting the firing time of the Q-switch to a time past the optimal firing time of 186 μm.

Particle size and seeding density is also a crucial consideration for accurate DPIV measurements. Larger particles have better light scattering properties; however smaller particles follow the flow more faithfully. In general particles used to represent the flow of a fluid continuum should be: (1) able to follow the flow faithfully; (2) scatter light well; (3) cheap and conveniently generated; and (4) chemically inactive and clean. Typical particle size ranges between 1- 100 μm, and these are considered sufficient for most PIV

applications. Fluorescent polymer particles with a mean diameter between 1 – 20 μm were used for these studies. Particles with less variation in the mean diameter are considerably more expensive. For the experiments with the 400 μm round orifice, the larger particles (>5μm) had a tendency to occlude the orifice within 30 minutes of beginning the experiment. Consequently, these particles were filtered with a 5 μm filter to yield 1-5 μm particles.

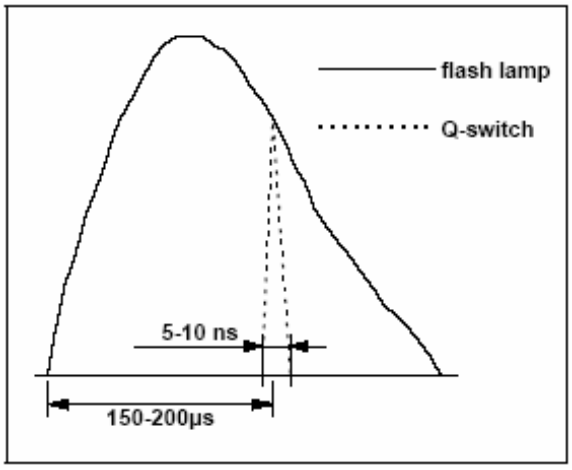

FIGURE 5.2.5.1 Q-switch Control of the lasing cavity.

The pulse separation between laser pulses is dependent upon the velocity of the flow and the particle density. It must be sufficiently long to enable determination of the particle displacement between image pairs with adequate resolution as well as short enough to prevent particles with an out-of-plane velocity component from leaving the light sheet between pulses. The complex flows encountered in the orifice/channel experiments complicated the pulse separation setting. For each image pair, there were both very high and low velocity flows. Thus, a choice had to be made as to what important structures were to be captured. For the jet, a pulse separation of 10-15 μs was

used, and to capture the stagnant and circulation regions beside the jet, a pulse separation of 50-100 μs was used.

Besides the particle density and size and the camera resolution, the size of the interrogation area also affects the spatial resolution of the vector maps. In fluid flow experiments, 32 x 32 pixels is a typical interrogation window size. Studies have shown that, given a window side length of N, a maximum particle displacement of N/4 is recommended to ensure a reasonable signal-to-noise ratio. The recommended minimum number of particles within each interrogation area is about 7 particles/interrogation area to ensure a good signal-to-noise ratio for cross correlation calculations.

The number of images can also affect the accuracy of the calculated velocity components. Even though an increased number of image pairs can invariably lead to improved signal-to-noise ratio and a lower percentage of error in the measured values, there must be a balance between the greater time and expense spent on data acquisition, processing, and storage space and measurement accuracy. Typical allowable percentage error in the measured velocity components is 5 to 6 percent in fluid flow experiments. Using the following relation:

$$\text{percent error in } R = \frac{\delta R}{\overline{R}} \times 100 = \frac{R'}{\overline{R}\sqrt{N}} \times 100 \qquad \text{Equation 5.2.5.1}$$

where R is the principal Reynolds shear stress, an estimated number of images required to meet the error requirement can be calculated. The percentage error for the Reynolds shear stress obtained at a point with maximum turbulence intensity is showed in Figure 5.2.5.2. From this figure a percentage error of less than 6 percent in R can be achieved at

approximately 1000 image pairs. The number of image pairs acquired in these experiments was 1000 or 1500, resulting less than 6 or 3 percent error, respectively.

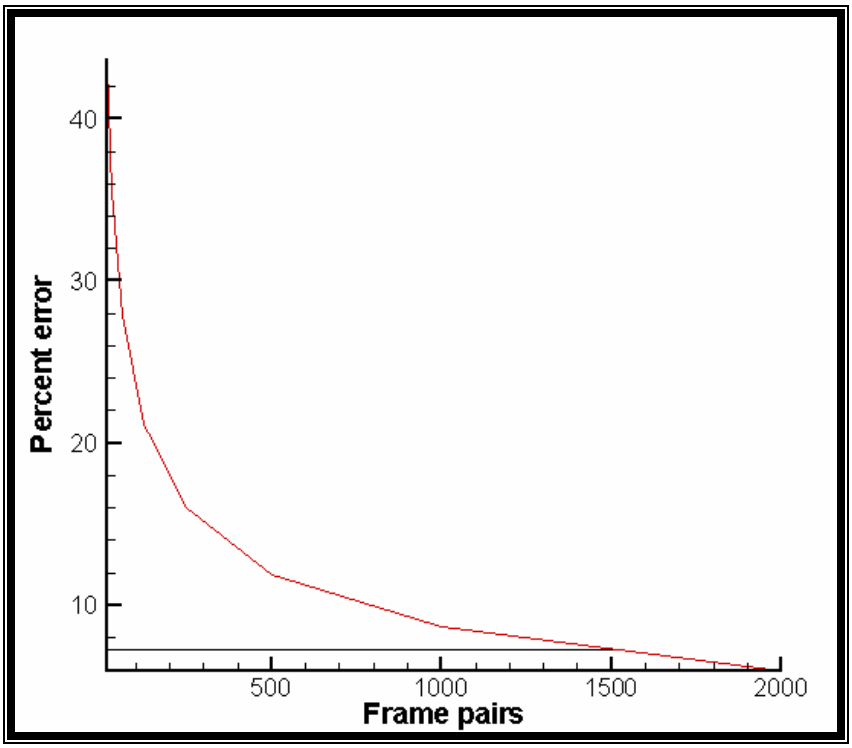

Figure 5.2.5.2 Percentage error in principle Reynolds stress at a point with maximum turbulence intensity.

In these studies, a 1600X1200 12-bit CCD camera (Model 1101MPRO, LaVision, Germany) was used with a frame rate of 30 frames/sec and a CCD size of 7.4 x 7.4 mm. The number of vectors in the vector map is dependent upon the number of pixels in the CCD camera and the size of the interrogation area. The array of totally independent vectors, N_v is determined by the following equation:

$$N_v = \frac{\text{no. of pixels in CCD row}}{N_{\text{int}}} \times \frac{\text{no. of pixels in CCD column}}{N_{\text{int}}} \qquad \text{Equation 5.2.5.2}$$

where N_{int} is the side of the interrogation area in pixels.

In practice the number of independent vectors is greater than this because successive interrogation areas were overlapped to optimize the use of the information in the image map. Overlapping the interrogation regions by 50 percent of the side length is recommended. If a particle is near the outer edge of an interrogation area it may be displaced into the neighboring interrogation area so these particles would not contribute to the calculation of a velocity vector if there were no overlap. Therefore, overlapping interrogation areas can help maximize the use of the available information. With 50 percent overlapping of the interrogation areas the number of vectors obtained is:

$$N_v = \frac{\text{no. of pixels in CCD row}}{(1-0.5)N_{int}} \times \frac{\text{no. of pixels in CCD column}}{(1-0.5)N_{int}} \qquad \text{Equation 5.2.5.3}$$

The choice of N_{int} is constrained by both the velocity dynamic range and spatial resolution considerations. A smaller value provides better resolution, but also increases the risk of not capturing the higher velocity particles. Thus, the interrogation window size is a compromise between these two constraints. For these experiments an interrogation window size of 16 pixels was used for all of the data processing.

CHAPTER 6

RESULTS

The results section is divided into two sections: the human blood study results, the digital particle image velocimetry (DPIV) study results, and the *ex vivo* baboon study results. Each section will present the results of these experiments. Detailed tabulations of the raw experimental data are in Appendix B for the blood study and Appendix C for the DPIV study.

6.1. Human blood experimental results

The human blood study results are separated into sections for the round and slit orifices, the channels, and the mechanical valves as well as the experimental variations using the 400 μm round (non-calcium infused, platelet-reduced, and Aggrastat and AN51 addition) and 800 μm round (lower and higher than normal flow rates) orifices. In each section there is initially a plot to show all of the experimental results over time, and then the results that are statistically different from one another are broken down and discussed in detail to better elucidate the findings in these studies. The negative control for these experiments was the empty chamber without an orifice, channel, or valve inserted into it. Thus, blood flowed unimpeded through the chamber with little change in the shear stress and little or no stagnation or recirculation.

6.1.1. Round orifices

The endpoints for the round orifices were plasma TAT and plasma hemoglobin concentrations. The clinical baseline values for TAT and plasma hemoglobin are 7 ng/ml and 2 mg/ml, respectively.

6.1.1.1. TAT results

The TAT results for all the round orifices over time are shown in Figure 6.1.1.1.1. This plot shows that there is a transition between the 400 μm and the 800 μm size at which TAT formation becomes significant.

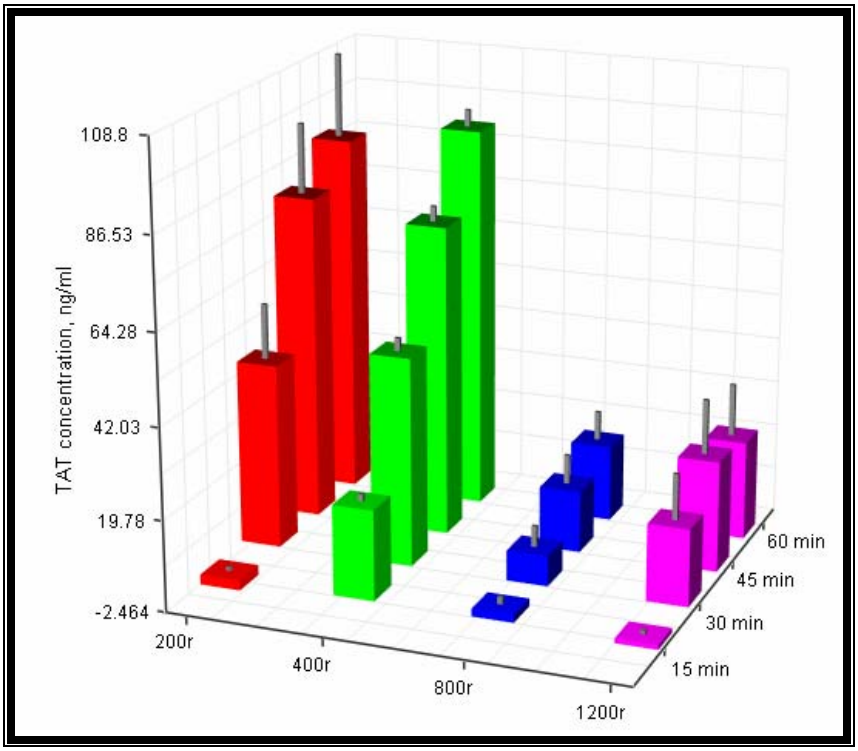

FIGURE 6.1.1.1.1. TAT concentration over time for all the round orifices. The 200 and 400 μm round orifices show a significant increase in TAT formation over time whereas the 800 and 1200 μm round orifices show only a moderate increase in TAT formation.

As shown in Figures 6.1.1.1.2 and 6.1.1.1.3, at 45 and 60 minutes, respectively, TAT formation for the 800 µm and the 1200 µm round orifice was not significantly more than the baseline level (N=6, p>0.05).

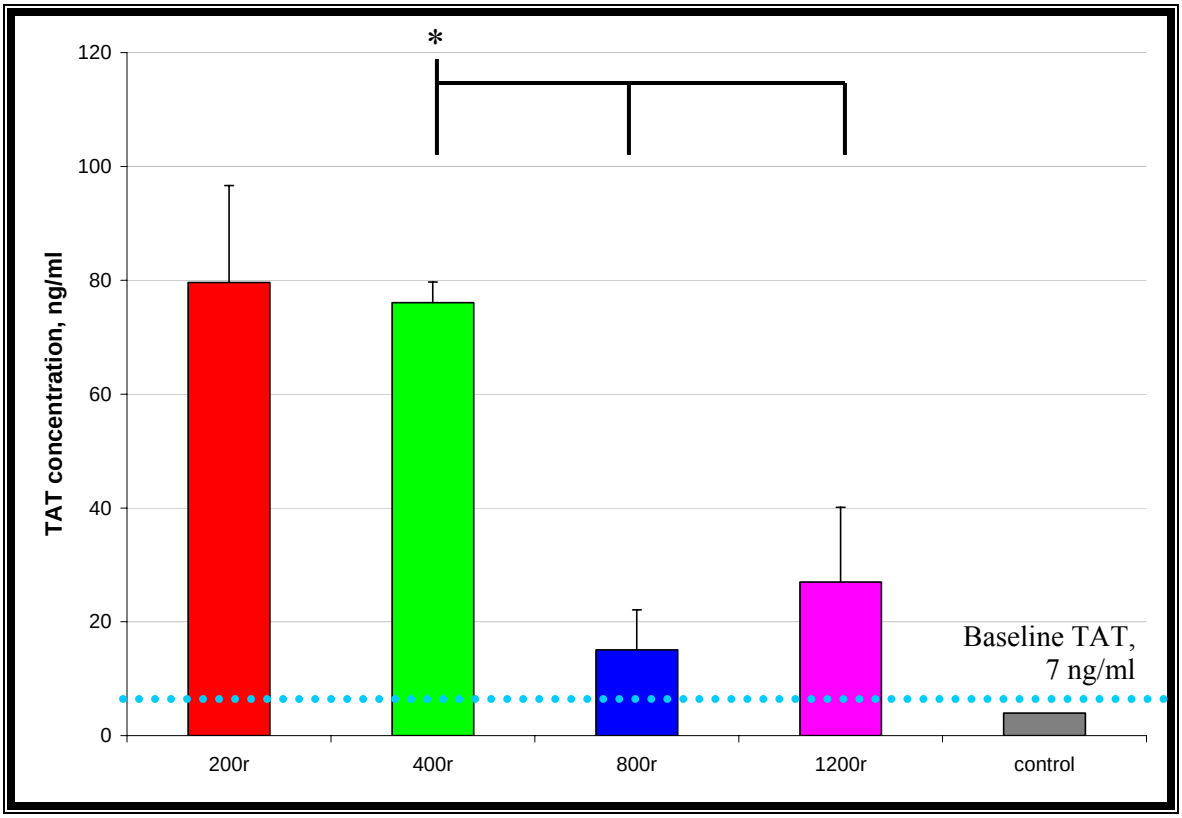

FIGURE 6.1.1.1.2. TAT concentration for the round orifices at 45 minutes (N=6, *p<0.05). The 200 and 400 µm round orifices have significantly higher TAT concentrations than both the 800 and 1200 µm round orifices at 45 minutes.

However, TAT formation for the 200 µm and the 400 µm round orifices was significantly above the baseline level (N=6, p<0.05) as well as significantly more than that for the 800 µm and 1200 µm round orifices (N=6, p<0.05). Also, in Figure 6.1.1.1.4, it is interesting to note that at 15 minutes the TAT concentration for the 200 µm round orifice is significantly less than that for the 400 µm round orifice (N=6, p<0.05), despite the fact that they are nearly equal at all other sample times. This behavior implicates a dependence of TAT formation in this system on the number of times that a blood volume

passes through the orifice. At 15 minutes the estimated number of times that a blood volume passes through the 200 µm round orifice is 2, and the number of 'passes' through the 400 µm round orifice at 15 minutes is 10. Thus, cumulative blood damage may not be sufficient to initiate the coagulation cascade for the 200 µm round orifice until after the 15 minute sample time.

Observations after each experiment showed that the 200 µm round orifice was occluded at 60 minutes in every instance as shown in Figure 6.1.1.1.5. The 400 µm round orifice was occluded approximately 20% of the time, and the 800 µm and 1200 µm round orifices were never occluded.

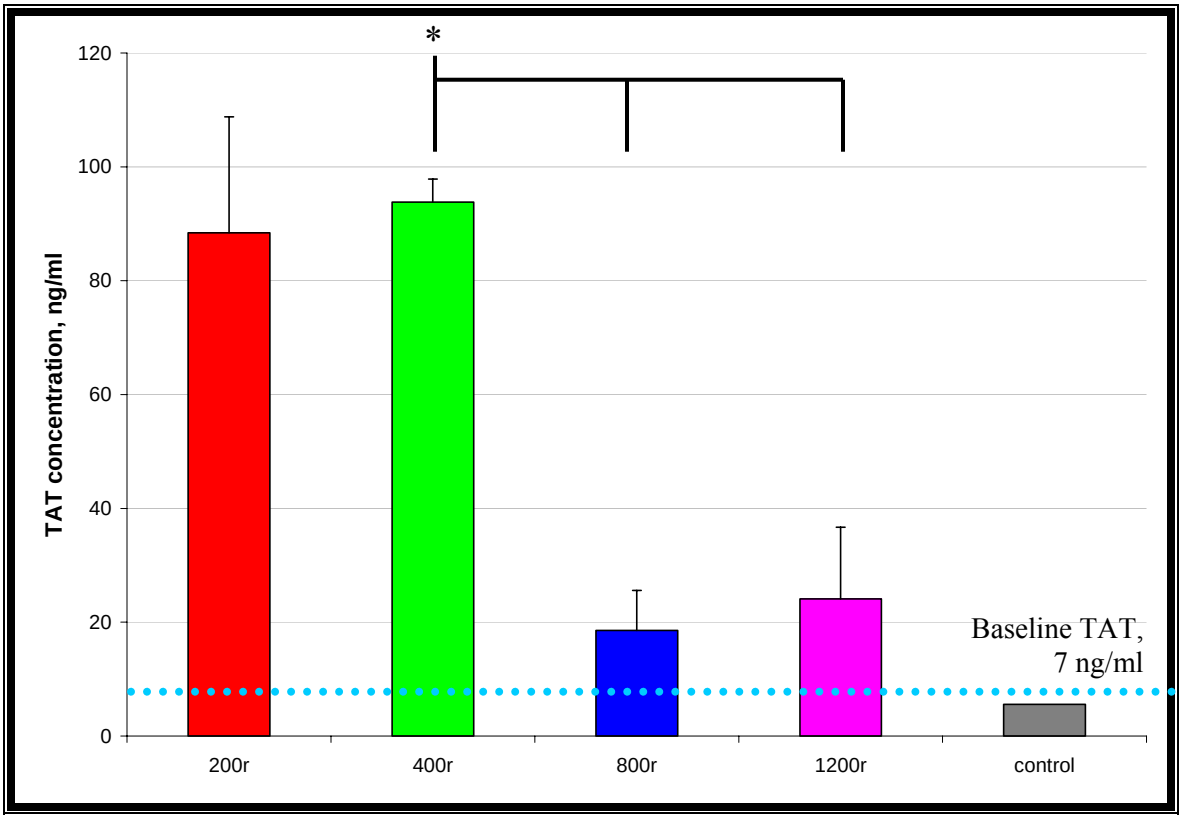

FIGURE 6.1.1.1.3. TAT concentration for the round orifices at 60 minutes (N=6, *p<0.05). The 200 and 400 µm round orifices have significantly higher TAT concentrations than both the 800 and 1200 µm round orifices at 60 minutes.

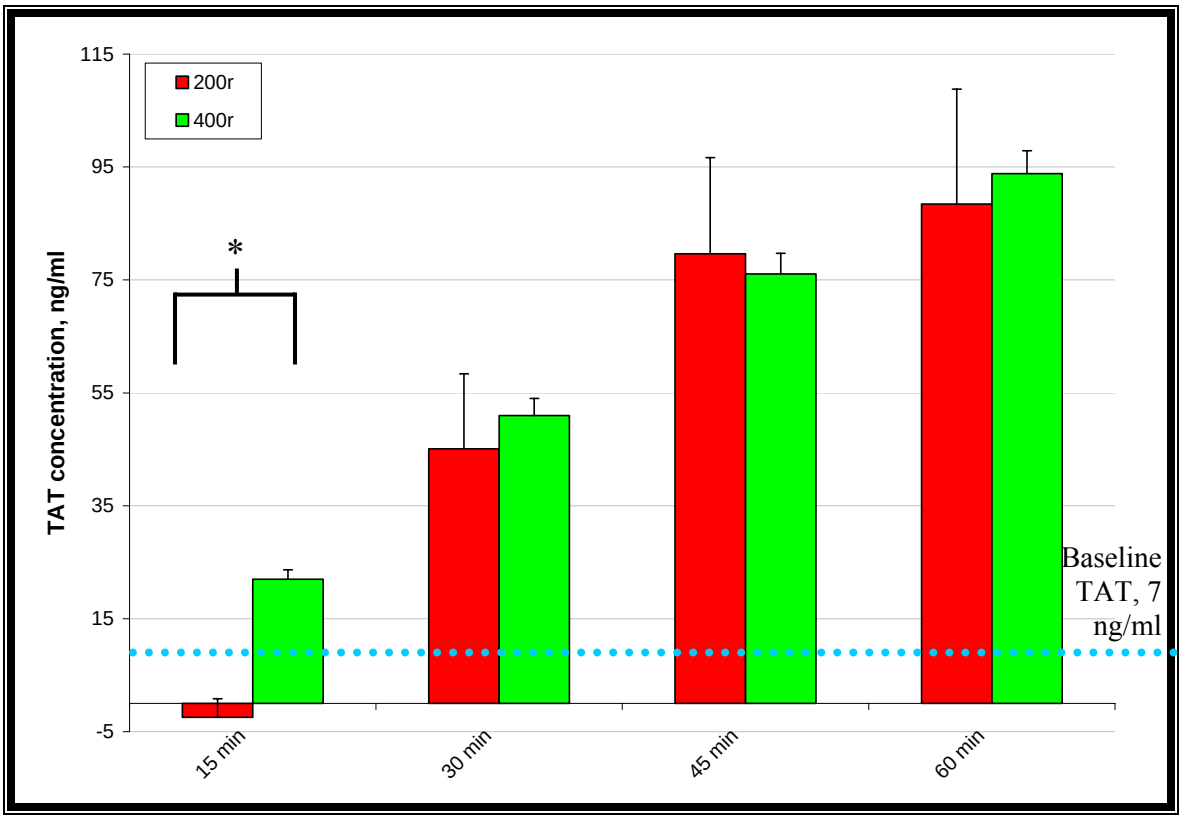

FIGURE 6.1.1.1.4. TAT concentration for the 200 and 400 µm round orifices over time (N=6, *p<0.05). The 400 µm round orifice has a significantly higher TAT concentration than the 200 µm round orifice at 15 minutes, but the TAT concentrations are approximately equal at all other time points.

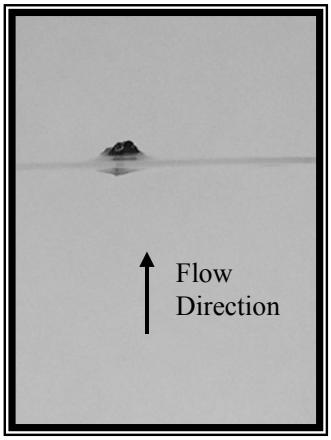

FIGURE 6.1.1.1.5. Picture of an occluded 200 µm round orifice. This orifice was removed at the end of the experiment.

Further investigation into the 400 µm round orifice results shows that there is a linear relationship between time and the increase in TAT concentration. As shown in Figure 6.1.1.1.6, a linear equation can be obtained that describes the increase over time.

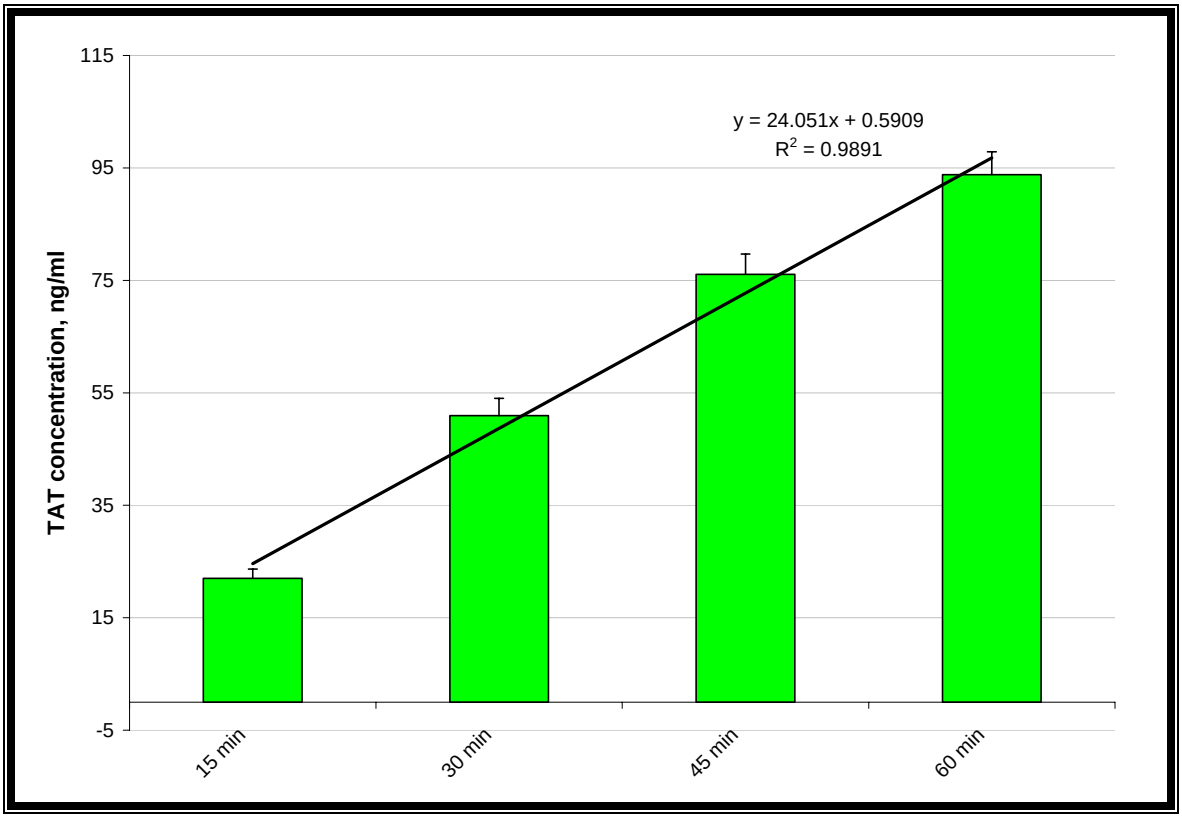

FIGURE 6.1.1.1.6. TAT concentration over time for the 400 µm round orifice. Trendline shows the linear increase in TAT during the experiment with a TAT production rate of 24 ng/ml*min.

6.1.1.2. Hemolysis results

The results for the plasma hemoglobin concentration, which is an indication of hemolysis, are shown in Figure 6.1.1.2.1. From these results it is evident that only the 200 µm round orifice exhibits significantly more hemolysis than the other round orifices at all time points ($N=6$, $p<0.05$). Furthermore, the 200 µm round orifice is the only one that induced hemolysis at levels significantly above the clinical baseline level of 2 mg/ml by the end of the experiment ($N=6$, $p<0.05$). Thus, this system did not damage the red

blood cells appreciably in the experiments with the 400 µm, 800 µm, or 1200 µm round orifices.

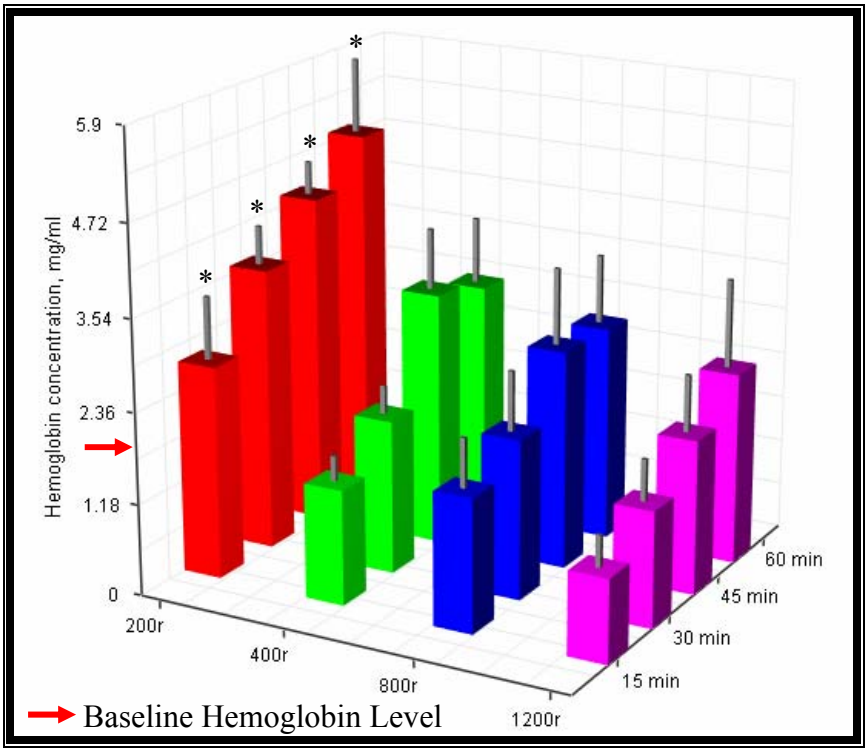

FIGURE 6.1.1.2.1. Plasma hemoglobin concentration over time for all the round orifices (N=6, *p<0.05). Hemolysis was significantly more for the 200 µm round orifice than for all of the other round orifices.

6.1.2. Slit orifices

The endpoints for the round orifices were plasma TAT and plasma hemoglobin concentrations. The clinical baseline values for TAT and plasma hemoglobin are 7 ng/ml and 2 mg/ml, respectively.

6.1.2.1. TAT Results

As shown in Figure 6.1.2.1.1, the experiments with the slit orifices did not produce significant amounts of TAT over time. Thus, even though the wall shear stress, which was previously calculated to be 24,200 dyn/cm^2, 21,100 dyn/cm^2, and 15,800

dyn/cm^2, for the 200 μm, 400 μm, and 800 μm slits, respectively, is sufficient to activate the platelets, the stagnation regions may not afford the activated platelets sufficient time to propagate the coagulation cascade.

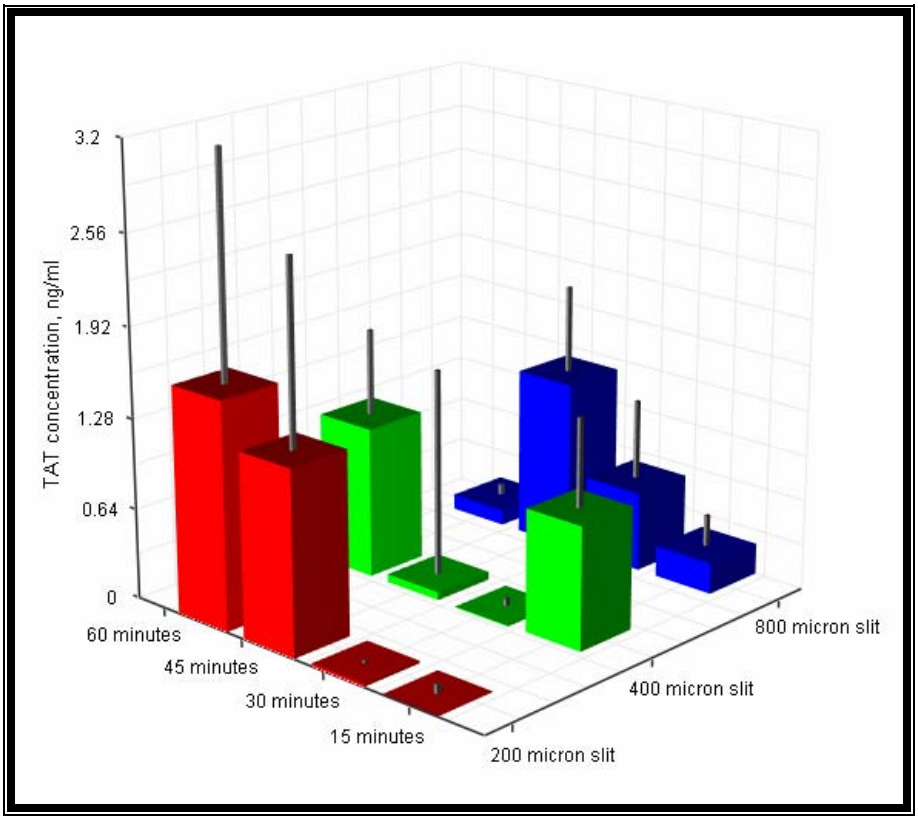

FIGURE 6.1.2.1.1. TAT concentration over time for all the slit orifices. TAT concentrations were below the clinical baseline level for all the slit orifices at all sample times.

6.1.2.2. Hemolysis results

The plasma hemoglobin results for the slit orifices are shown in Figure 6.1.2.2.1. Similar to the larger round orifices, the hemolysis for the slit orifices was not significant compared to the clinical baseline level ($p>0.05$). Thus, even with the higher flow rates, which result in an increased number of 'passes' through the orifice for each blood volume, the red blood cells did not experience significant damage.

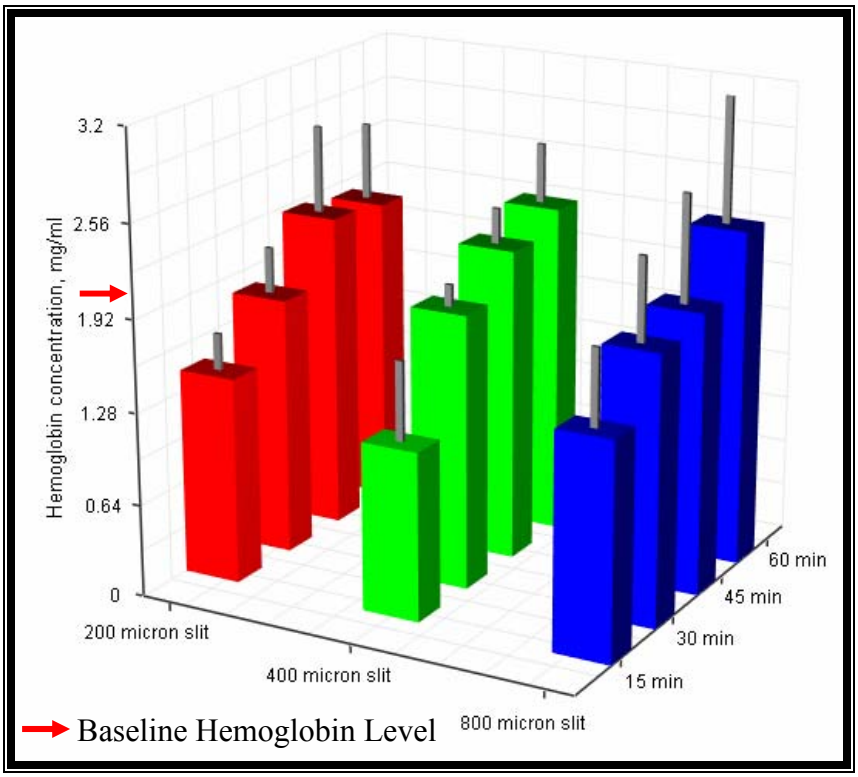

FIGURE 6.1.2.2.1. Plasma hemoglobin concentration over time for all the round orifices. None of the slit orifices induced hemolysis that was significantly more than the clinical baseline level.

6.1.3. 800 µm round orifice low and high flow rate experiments

Experiments with the 800 µm round orifice were performed at different flow rates to assess the importance of shear stress in this system without a corresponding change in orifice size. Unfortunately, because of limitations imposed by the pump, these experiments were not successful at demonstrating the importance of high shear. At higher RPMs, the pump head became too hot, thus warming the blood to above physiological levels (up to 104 °F) consequently inducing unacceptable levels of hemolysis. Nevertheless, these results are presented below. To eliminate the variation in 'passes' for these experiments, the blood volume was varied, and the time was lengthened for the low shear experiments. The total number of passes for each experiment was 100. The sample

times were chosen to represent the approximate number of 'passes' for each blood volume for standardization between the experiments. These sample times, which were measured in minutes during the experiments, equated to 0, 25, 50, and 100 passes. The biological endpoints studied for these experiments were TAT and plasma hemoglobin. The clinical baseline values for TAT and plasma hemoglobin are 7 ng/ml and 2 mg/ml, respectively.

6.1.3.1. TAT results

The TAT results for the varying shear experiments with the 800 µm round orifice are shown in Figure 6.1.3.1.1.

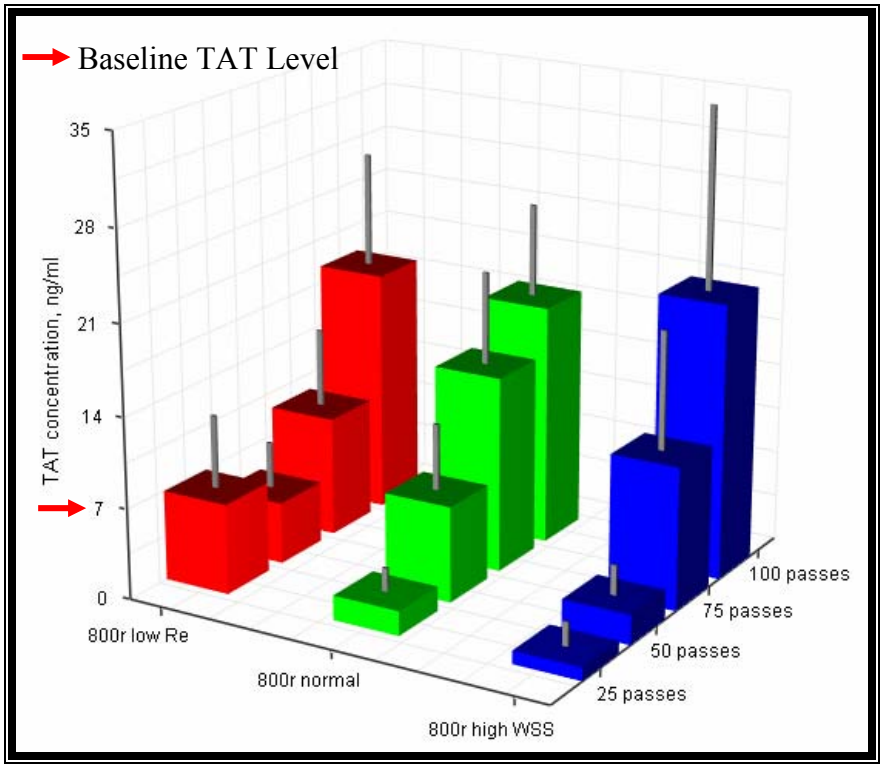

FIGURE 6.1.3.1.1. TAT concentration over time for the varying shear experiments with the 800 µm round orifice. TAT concentrations for the 800 µm high and low flow rate experiments did not differ significantly from those for the 800 µm normal flow rate experiments (N=6, $p>0.05$).

There was no significant difference between any of the experimental variations, and the cumulative TAT formed was not significantly above the clinical baseline level (N=6, $p>0.05$).

6.1.3.2. Hemolysis results

The plasma hemoglobin results are shown in Figure 6.1.3.2.1. From this plot it is evident that the high shear experiments resulted in significantly more hemolysis than the low shear or normal 800 µm round orifice experiments (N=6, $p<0.05$). Furthermore, the cumulative plasma hemoglobin concentration is significantly above the clinical

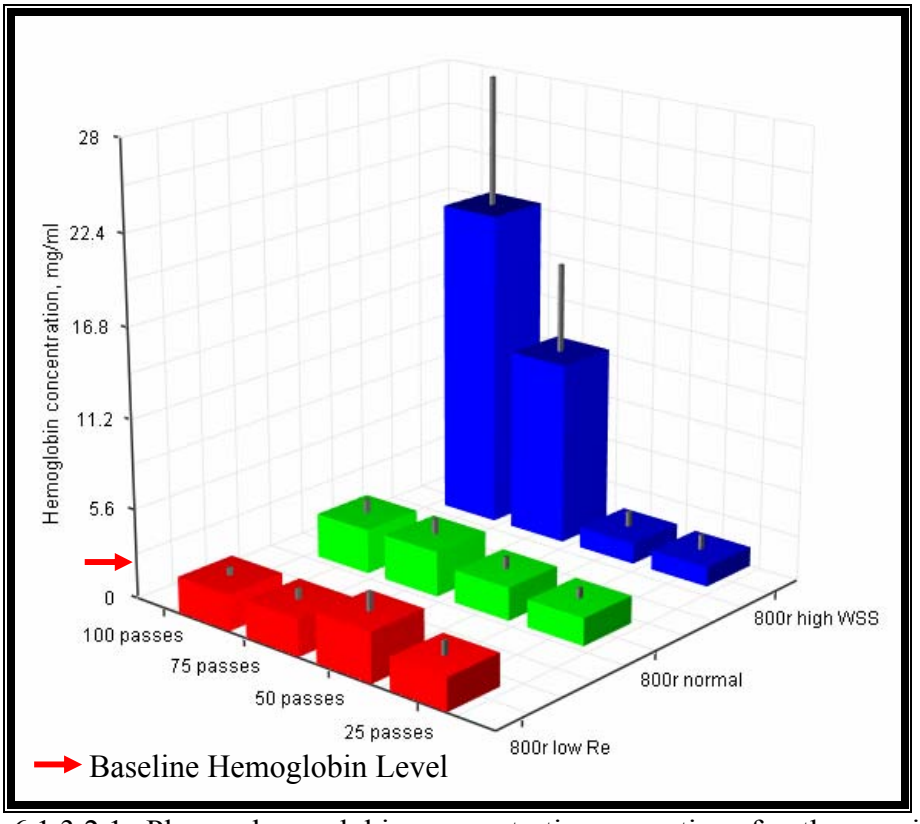

FIGURE 6.1.3.2.1. Plasma hemoglobin concentration over time for the varying shear experiments with the 800 µm round orifice. Only the high WSS, or high flow rate, experiments induced a significant amount of hemolysis, most likely due to increases in temperature above 104 °F.

baseline level (N=6, $p<0.05$). The error bars for the high shear experimental results also indicate that there is a large variation in the hemolysis levels between the experiments. This variation may be due to the increase in temperature (up to 104° F) that resulted from heat transfer from the pump head at the higher RPMs for the high shear experiments. This excessive increase in temperature and the concomitant hemolysis invalidate the high shear experiments.

6.1.4. Experimental variations with the 400 μm round orifice

In the initial experiments the 400 μm round orifice demonstrated reproducible TAT formation at levels significantly above the clinical baseline level. Furthermore, this orifice did not occlude in all cases, and when a thrombus did cause occlusion, the occurrence was usually after 45 minutes. Thus, this orifice was used to look at different variables to assess their importance in this system. In particular, the importance of calcium chloride (Ca^{2+}) addition, platelets, the GPIIa/IIIb platelet receptor, and the GPIb platelet receptor were investigated. The flow rate, experimental duration, sample times, upstream pressure, sodium citrate concentration in the blood, and blood volume in the steady flow loop were maintained the same for all of the experiments with the 400 μm round orifice. To assess the importance of Ca^{2+} addition, experiments were performed without the continuous infusion of Ca^{2+}. To investigate the importance of platelets in the system, platelets were removed from the blood (approximately 80% removal efficiency) prior to placing the blood in the flow loop. To assess the importance of the GPIIb/IIIa and GPIb platelet receptors, Aggrastat and AN51, respectively, were added to the blood prior to placing the blood in the flow loop. For the non-calcium infused and reduced platelet

experiments, TAT concentration was the only endpoint investigated. For the Aggrastat and AN51 experiments, TAT and PF4 concentrations were the assayed endpoints. The clinical baseline values for TAT and PF4 are 7 ng/ml and 20 ng/ml, respectively.

6.1.4.1. TAT results

The TAT results for all of the experimental variations with the 400 µm round orifice are shown in Figure 6.1.4.1.1. These results show that TAT formation for the normal 400 µm round orifice experiments was significantly greater than that for all of the experimental variations (N=6, $p<0.05$). Furthermore, the experimental variations did not exhibit TAT concentrations significantly above the clinical baseline level at any of the

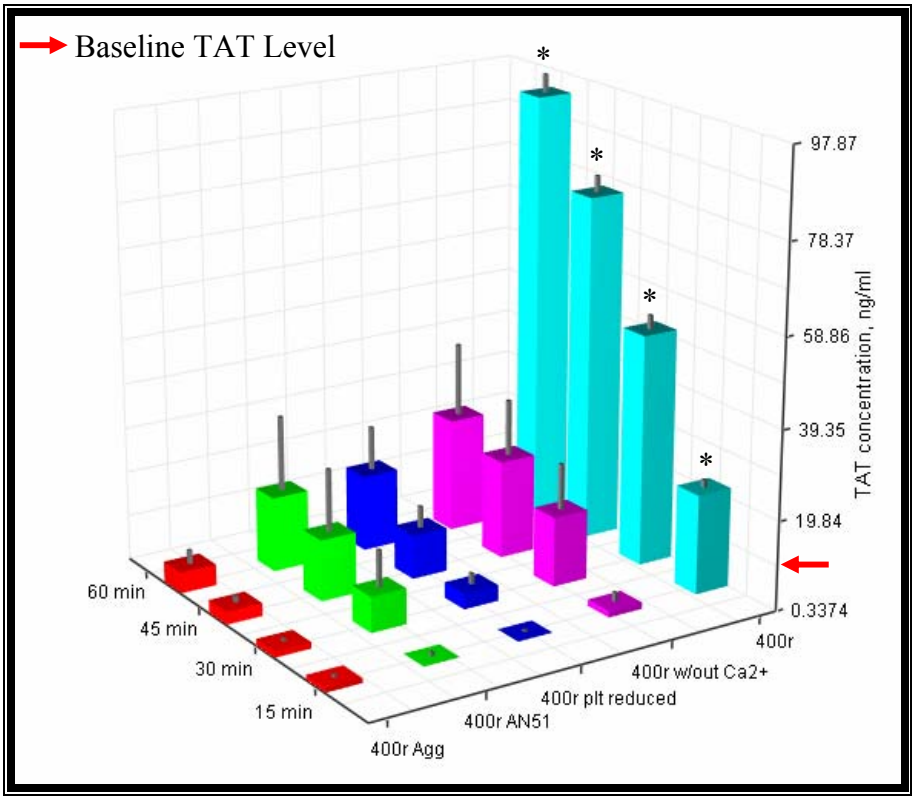

FIGURE 6.1.4.1.1. TAT concentration over time for the various experiments with the 400 µm round orifice (N=6, *$p<0.05$). At all sample times, the normal 400 µm round orifice experiments resulted in significantly higher TAT concentrations than the variations (non-Ca^{2+} infused, platelet-reduced, and Aggrastat and AN51 addition).

sample times. These results indicate that all of these variables are necessary for TAT formation and thus the propagation of the coagulation cascade in this system.

To further investigate the importance of these variables in relation to one another, trendlines were used to determine the rate of increase in the TAT concentration over time. Figure 6.1.4.1.2 shows these trendlines, and they are summarized again in Table 6.1.4.1.1.

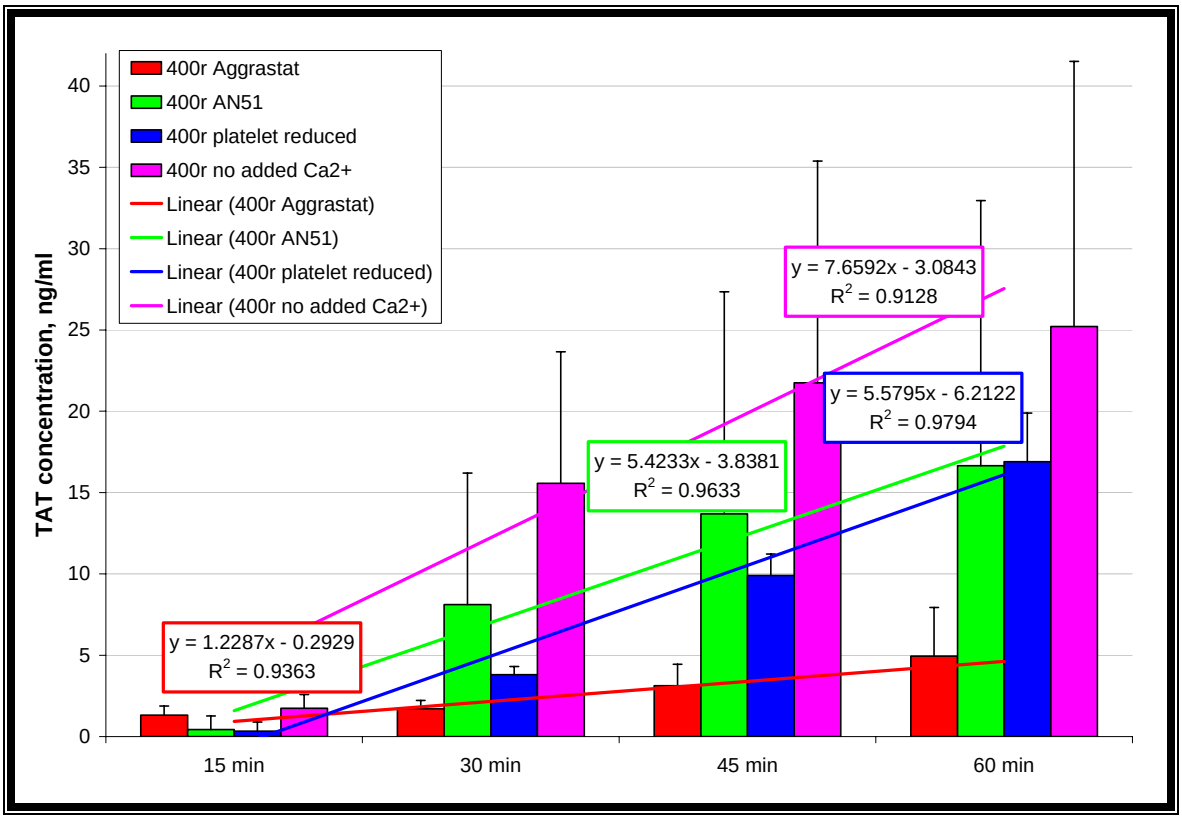

FIGURE 6.1.4.1.2. TAT concentration for the 400 µm round orifice experiments with Aggrastat, AN51, reduced platelet count, and no added Ca^{2+}. Trendlines have been added to show the varying effectiveness of these experimental variations in suppressing TAT formation over time.

Based on the results in Table 6.1.4.1.1 and Figure 6.1.4.1.2, the most important variable appears to be the GPIIb/IIIa receptor. Blocking this receptor with Aggrastat resulted in the lowest cumulative TAT concentration as well as the lowest rate of TAT increase.

Reducing the platelet count seems to have a similar result to blocking GPIb with the AN51 antibody, since these two have similar cumulative TAT concentration and rates of TAT increase. The suspension of Ca^{2+} addition appears to be the least important of these factors, with the highest cumulative TAT concentration and rate of TAT increase.

TABLE 6.1.4.1.1. Cumulative TAT increase and rate of TAT increase for the experimental variations with the 400 μm round orifice.

	Cumulative TAT increase, ng/ml	Rate of TAT increase, (ng/ml)/min
400r normal	93.8	24.1
400r w/out Ca^{2+} addition	25.2	7.7
400r platelet reduced	16.9	5.6
400r w/AN51 addition	16.6	5.4
400r w/Aggrastat addition	4.9	1.2

6.1.4.2. PF4 results

The PF4 results for the Aggrastat and AN51 experiments shown in Figure 6.1.4.2.1 indicate that blocking the GPIIb/IIIa and GPIb platelet receptors is not effective in suppressing platelet activation since the PF4 levels for the Aggrastat and AN51 experiments is not significantly less than that for the normal 400 μm round orifice experiments ($N=5$, $p>0.05$).

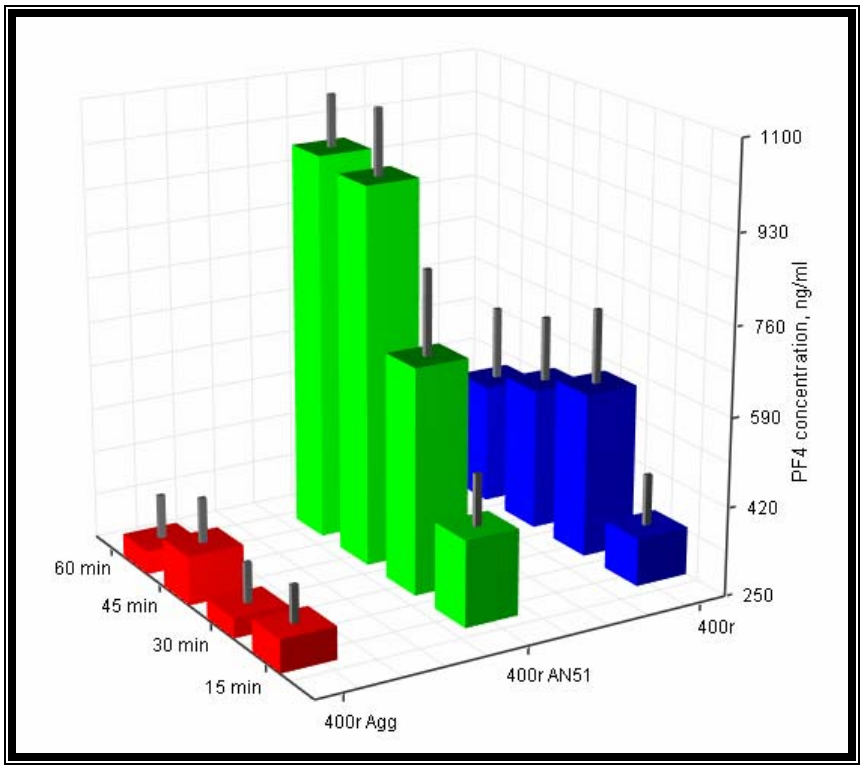

FIGURE 6.1.4.2.1. PF4 concentration over time for the Aggrastat and AN51 experiments with the 400 μm round orifice. The AN51 experiments demonstrated significantly more PF4 release than either the normal or Aggrastat experiments with the 400 μm round orifice experiments (N=6, $p<0.05$). There was no significant difference in PF4 release between the Aggrastat and normal 400 μm round orifice experiments.

Although the PF4 concentration is moderately less for the Aggrastat experiments than for the normal experiments, it is significantly more at 45 and 60 minutes for the AN51 experiments than for both the normal and Aggrastat experiments as shown in Figure 6.1.4.2.2. This moderate decrease in platelet activation for the Aggrastat experiments implies that although blocking the GPIIb/IIIa receptor does not inhibit initial platelet activation, it may suppress further feedback activation. The increase in platelet activation for the AN51 experiments may represent an artefactual release of PF4 that occurs when the AN51 antibody binds to the GPIb receptor. This release would be in addition to any PF4 release that occurs due to shear, which explains the elevation above the normal 400 μm round orifice experiments.

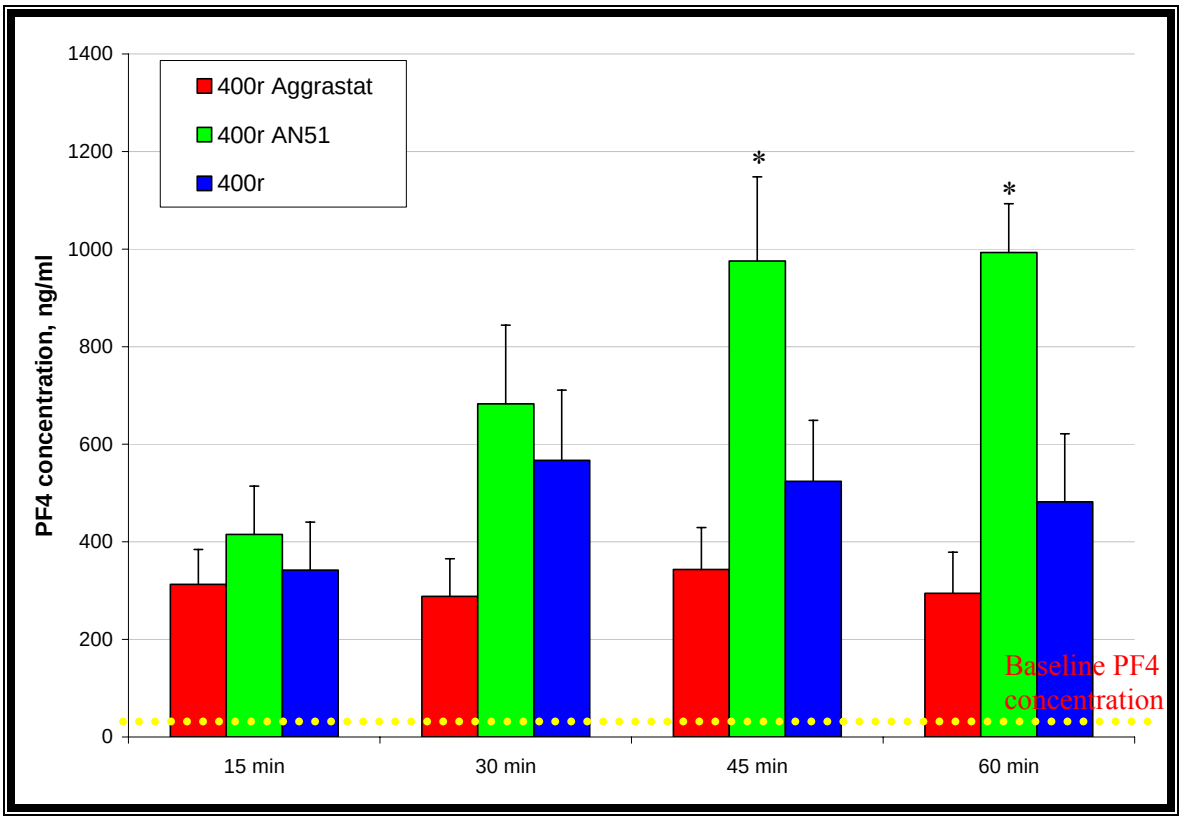

FIGURE 6.1.4.2.2. PF4 concentration for the 400 round orifice Aggrastat and AN51 experiments over time (N=6, *=p<0.05). The AN51 experiments demonstrated significantly more PF4 release than either the normal or Aggrastat experiments with the 400 µm round orifice experiments. There was no significant difference in PF4 release between the Aggrastat and normal 400 µm round orifice experiments.

6.1.5. Channels

The channel geometries used in these experiments were described in detail in Section 5.1.6. As shown in Figure 6.1.5.1, the channel geometries were chosen to mimic the different geometrical features of various MHV hinge pathways. The endpoints for these experiments were TAT, PF4, and plasma hemoglobin concentrations. The clinical baseline values for TAT, PF4, and plasma hemoglobin are 7 ng/ml, 20 ng/ml, and 2 mg/ml, respectively.

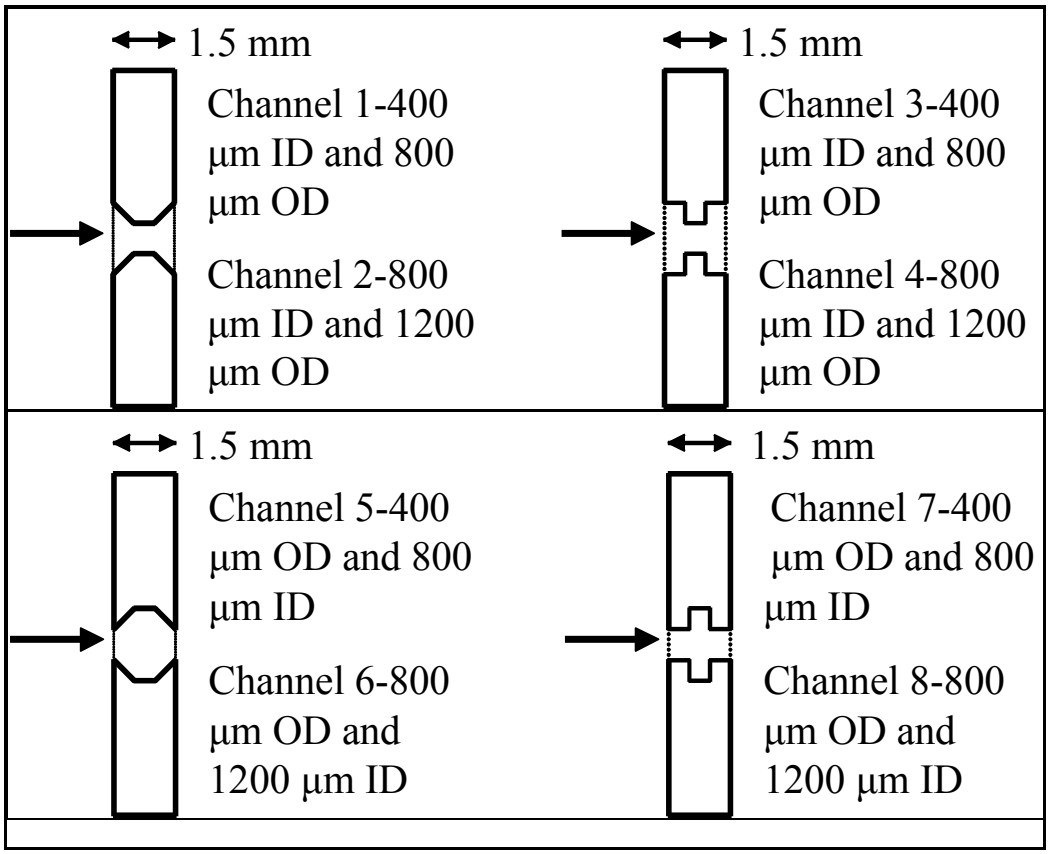

FIGURE 6.1.5.1. Channel diagrams.

6.1.5.1. TAT results

The TAT results for all of the channels are shown in Figure 6.1.5.1.1. This plot shows that all of the channels with a minimum diameter of 400 μm, or small channels (odd-numbered), have approximately the same TAT concentration at each sample time. However, the channels with a minimum diameter of 800 μm, or large channels (even-numbered), do differ from one another. Figure 6.1.5.1.2 shows these differences more clearly at 60 minutes. This plot shows that Channel 4 has a significantly higher TAT concentration at 60 minutes than Channel 4 ($N=6$, $p<0.05$). These channels have similar geometries except that Channel 2 has a smoother transition to the smaller internal diameter, and Channel 4 has a 90 degree angle leading into the smaller internal diameter.

Similarly, Channel 8 has a significantly higher TAT concentration at 60 minutes than Channel 6 (N=6, $p<0.05$). Both of these channels have a larger internal diameter, but Channel 6 has a smoother transition than Channel 8, which has a 90 degree angle. Additionally, Channel 4 has significantly higher TAT than Channel 6, and Channel 8 has significantly higher TAT than Channel 2 at 60 minutes (N=6, $p<0.05$).

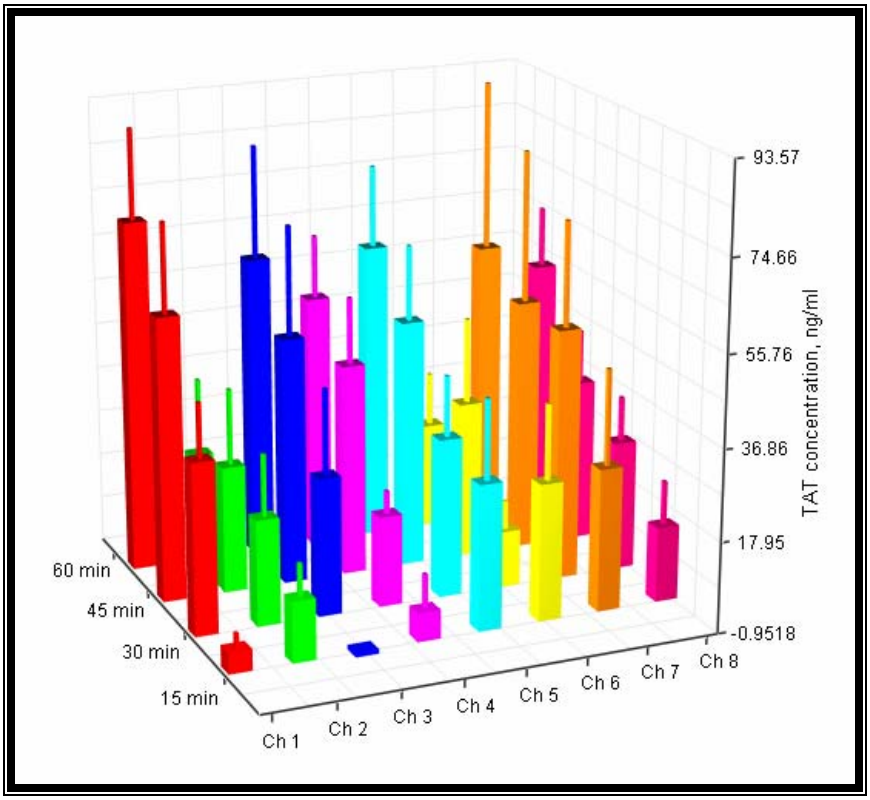

FIGURE 6.1.5.1.1. TAT concentration over time for the channel experiments. TAT concentration appears to be lower for Channels 2 and 6 than for all of the other channels.

Figure 6.1.5.1.3 shows a comparison between all of the channels and the 400 µm round orifice at 60 minutes. The significance of this plot is that it shows that despite the fact that Channels 4 and 8 have a minimum diameter of 800 µm, they still produce approximately the same amount of TAT as the 400 µm round orifice. This is direct contrast to the results for Channels 2 and 6, which produce significantly less TAT than the 400 µm round orifice at 60 minutes (N=6, $p<0.05$). This result also differs from the

results with the 800 µm round orifice, which produced significantly less TAT than the 400 µm round orifice at 60 minutes. Based on these results, it is evident that for the small channels, size is more important to TAT formation than the geometry, but for the larger channels, the geometry does play an important role.

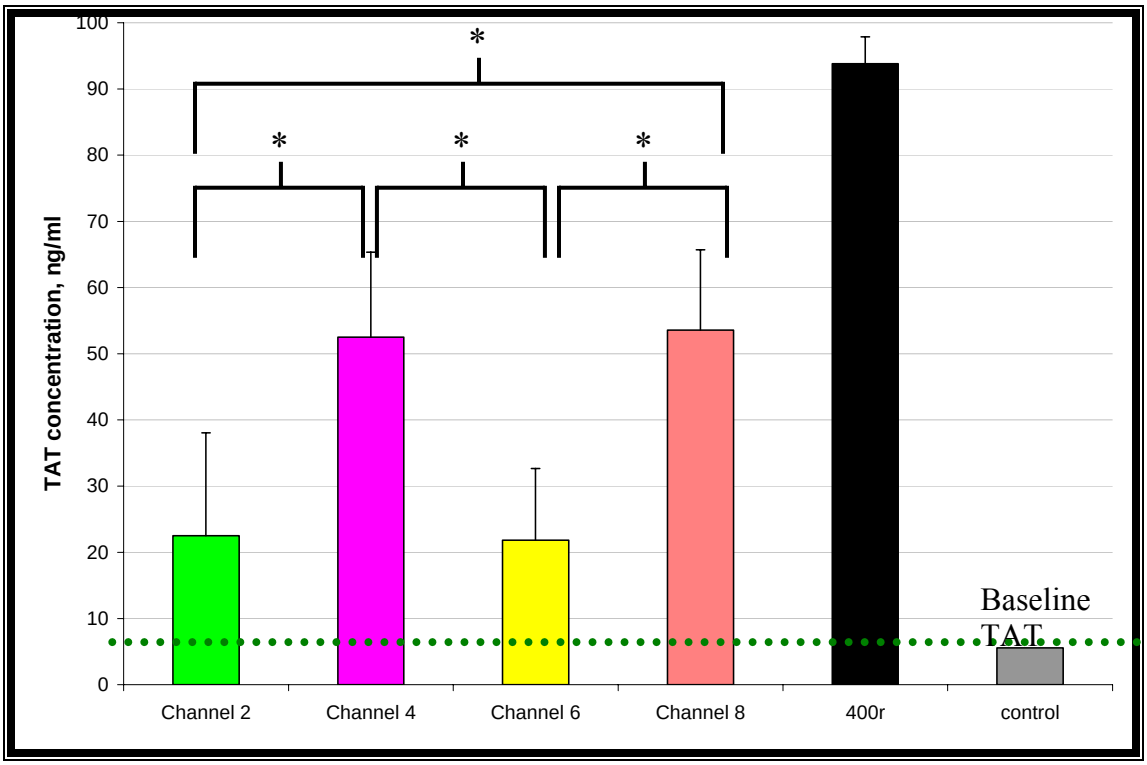

FIGURE 6.1.5.1.2. TAT concentration for the large (800 µm) channels at 60 minutes (N=6, *=p<0.05). Experiments with Channel 4 produced significantly more TAT than those with Channels 2 and 6. Experiments with Channel 8 also produced significantly more TAT than those with Channels 2 and 6.

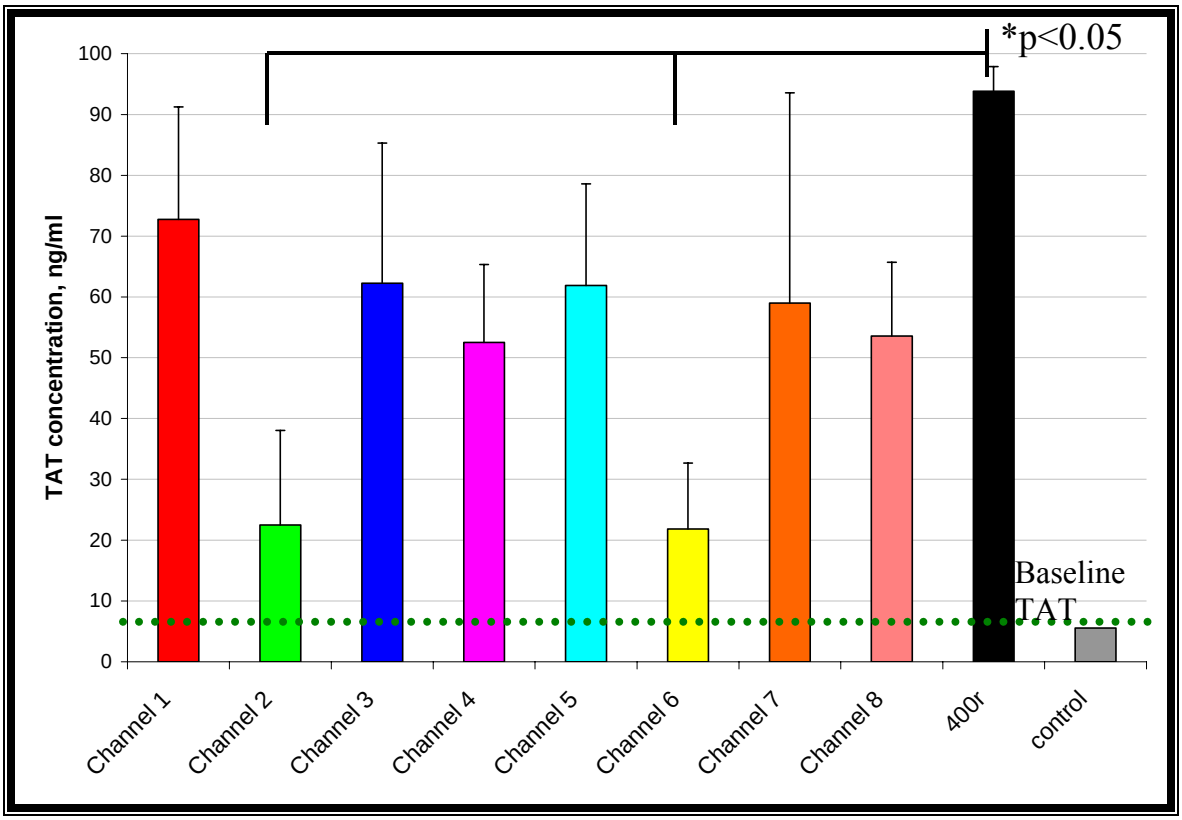

FIGURE 6.1.5.1.3. TAT concentration for the channels at 60 minutes compared with the 400 μm round orifice (N=6, *=p<0.05). Experiments with channels 2 and 6 produced significantly less TAT than those with the 400 μm round orifice. However, TAT concentrations at 60 minutes for experiments with all of the other channels did not differ significantly from that for the 400 μm round orifice.

6.1.5.2. PF4 results

The PF4 results for all of the channels are shown in Figure 6.1.5.2.1. These results show that there is not a significant difference in PF4 concentration for the channels at any of the sample times. Furthermore, the cumulative PF4 concentration is well above the baseline level. Thus, all of the channels activate the platelets at about the same level with PF4 concentrations that are at least an order of magnitude higher than the baseline level (20 ng/ml).

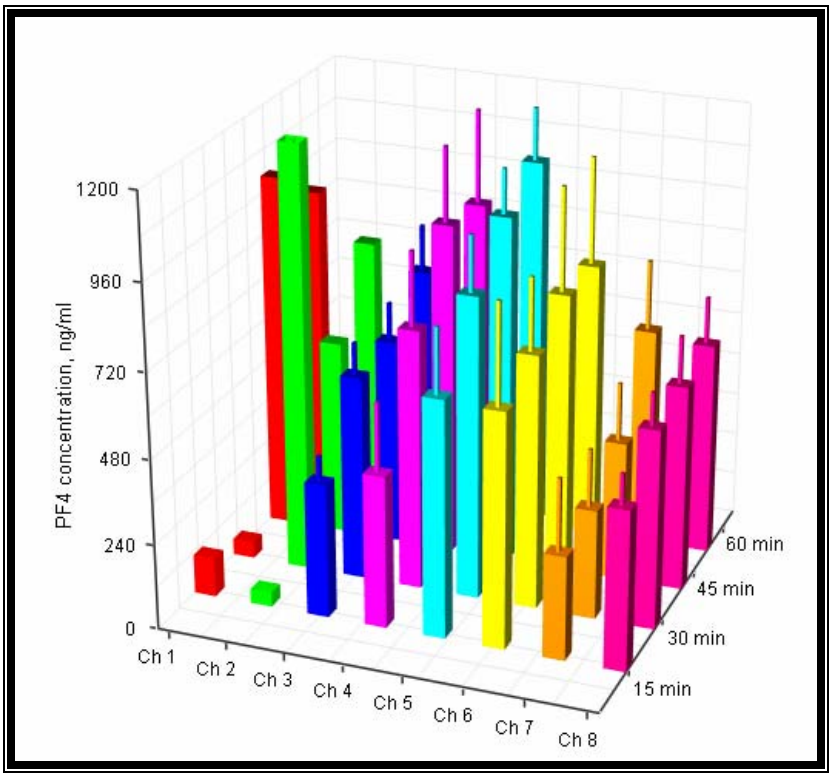

FIGURE 6.1.5.2.1. PF4 concentration over time for the channel experiments. There was no significant difference in PF4 release between any of the channels (N=6, $p>0.05$). PF4 release was at least an order of magnitude higher than the baseline level (20 ng/ml).

6.1.5.3. Hemolysis results

The hemolysis results for the channel experiments are shown in Figure 6.1.5.3.1. There was no significant difference in plasma hemoglobin concentration for the channels nor was the hemolysis significantly higher than the clinical baseline level for any of the channels.

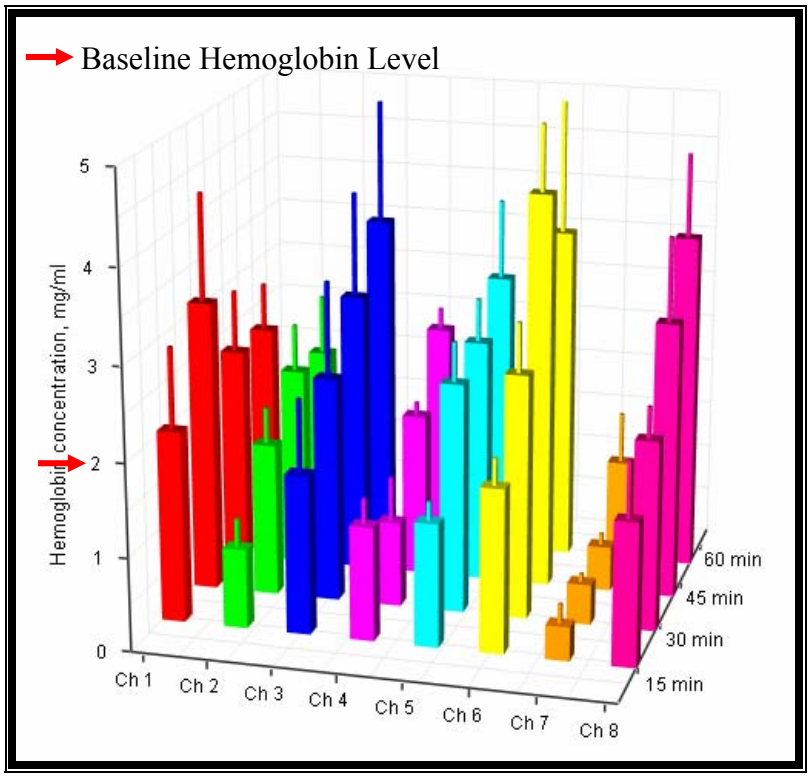

FIGURE 6.1.5.3.1. Plasma hemoglobin concentration over time for the channel experiments. There was no significant difference in PF4 release between any of the channels (N=6, p>0.05). Hemolysis was not significantly above the baseline level.

6.1.6. Mechanical heart valves

The valves used in these experiments were described in detail in Section 5.1.7. These valves are the SJM Standard valve, a low leaker prototype valve, a high leaker prototype valve, and the MP valve. The endpoints for these experiments were TAT, PF4, and plasma hemoglobin concentrations. The clinical baseline values for TAT, PF4, and plasma hemoglobin are 7 ng/ml, 20 ng/ml, and 2 mg/ml, respectively.

6.1.6.1. TAT results

The TAT results for all of the valves are shown in Figure 6.1.6.1.1. This plot indicates that the SJM Standard valve produces a negligible amount of TAT. However, the high leaker, low leaker and MP valves do show an increase in TAT concentration.

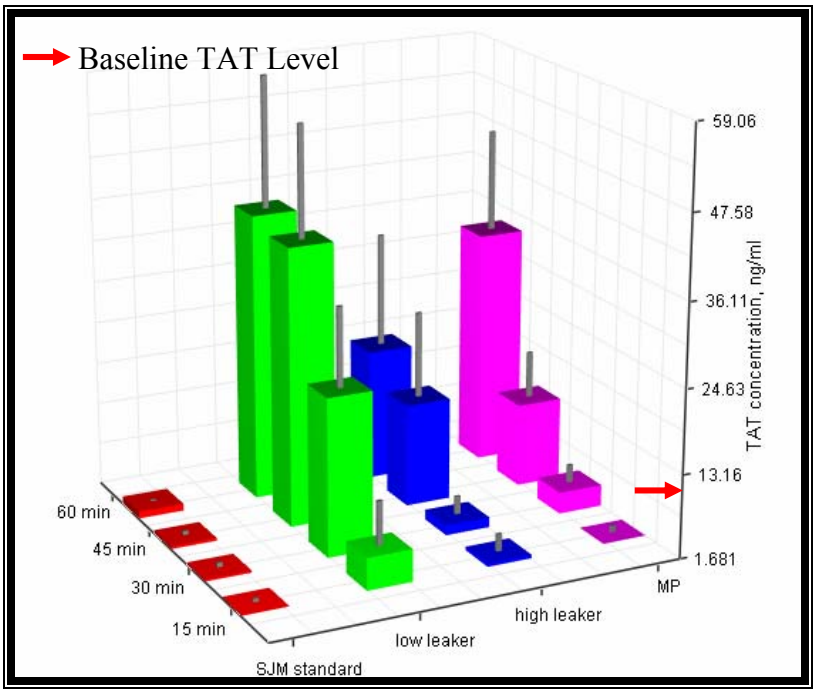

FIGURE 6.1.6.1.1. TAT concentration over time for the MHV experiments. TAT concentration was significantly higher for the low leaker prototype valve and the MP valve compared to the SJM Standard MHV (N=6, $p<0.05$).

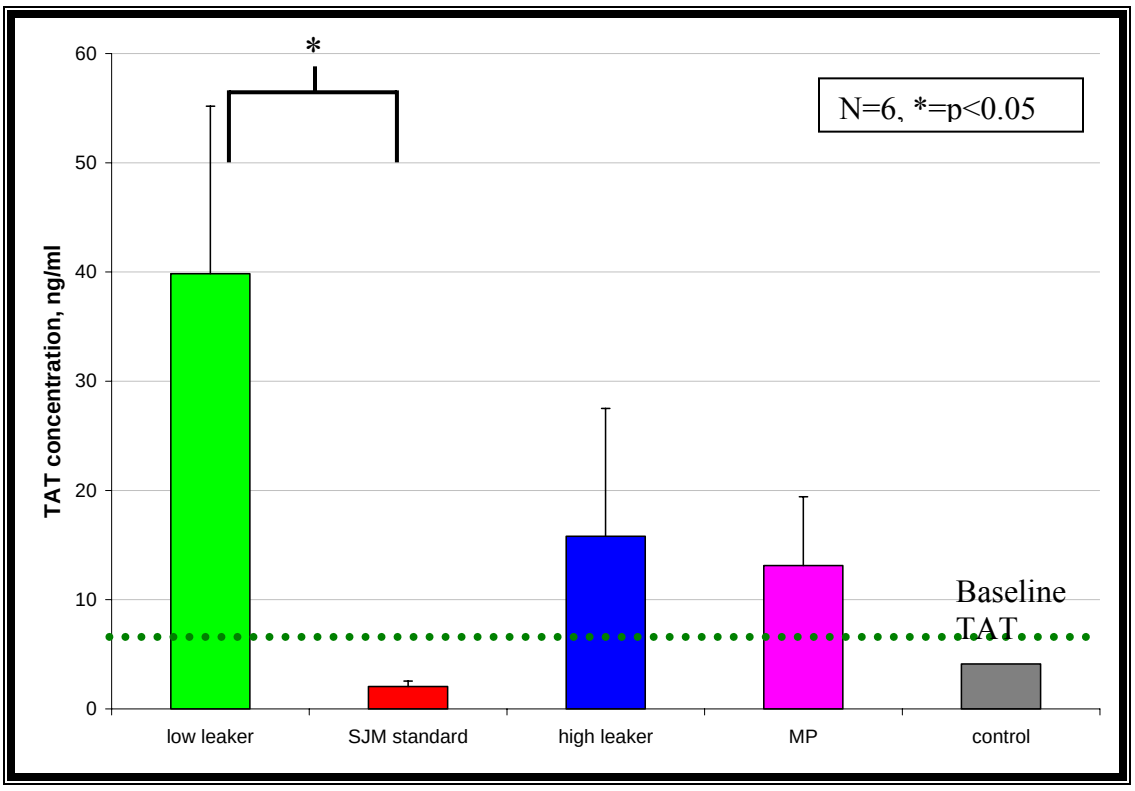

FIGURE 6.1.6.1.2. TAT concentration for the different valves at 45 minutes (N=6, *=$p<0.05$). TAT concentration was significantly higher for the low leaker prototype valve than the SJM Standard MHV at 45 minutes.

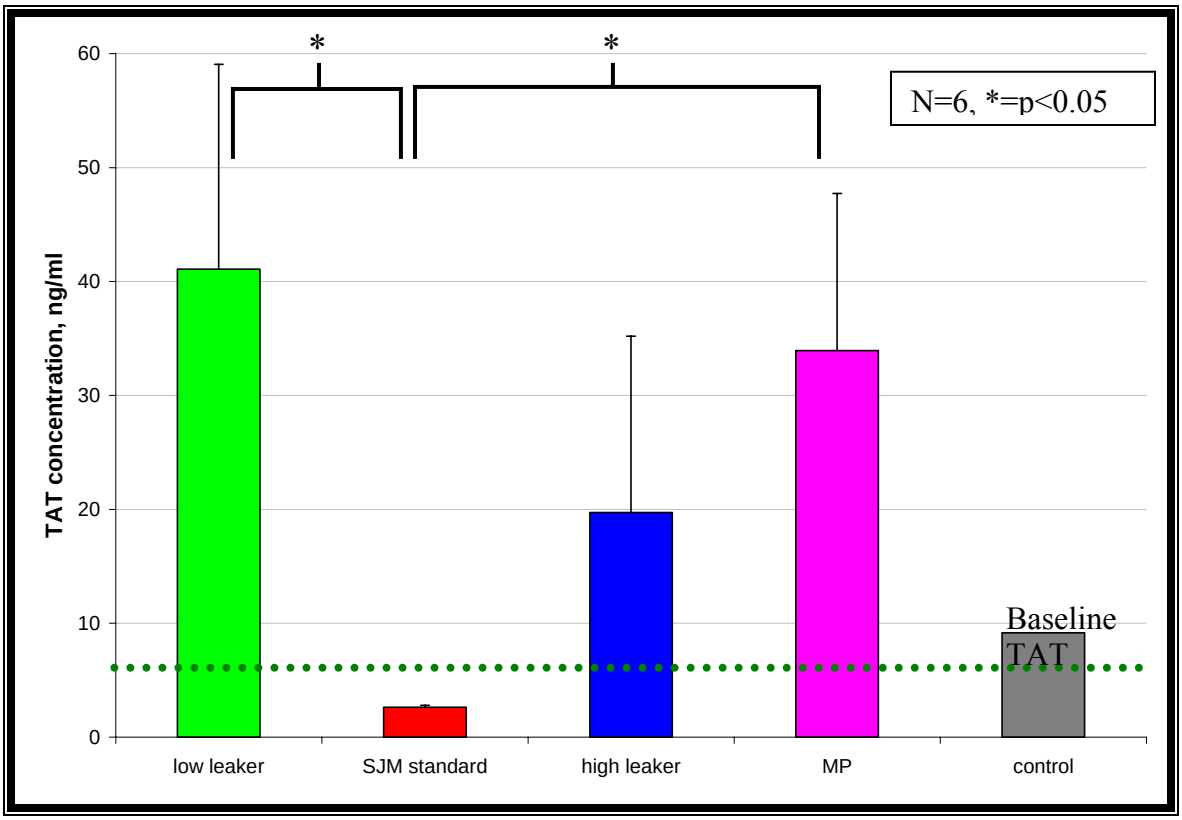

FIGURE 6.1.6.1.3. TAT concentration for the different valves at 60 minutes (N=6, *=p<0.05). TAT concentration was significantly higher for the low leaker prototype valve and the MP valve compared to the SJM Standard MHV at 60 minutes.

Figures 6.1.6.1.2 and 6.1.6.1.3 show the differences in TAT production between these valves more clearly at 45 and 60 minutes, respectively. At 45 minutes there is significantly more TAT produced in the experiments with the low leaker valve than with the SJM Standard valve, and at 60 minutes experiments with both the low leaker and MP valves resulted in significantly more TAT production than the SJM standard valve (N=6, $p<0.05$). These results indicate that the low leaker and MP valves have a higher thromboembolic potential than the SJM Standard valve, which is used clinically with low thromboembolic complication rates (less than 5%).

6.1.6.2. PF4 results

The PF4 results for all of the valves are shown in Figure 6.1.6.2.1. This plot shows that all of the valves induced platelet activation at levels above baseline levels. However, the experiments with the SJM Standard valve did not result in an increase in PF4 concentration over time. The experiments with the MP valve resulted in a moderate increase, whereas the experiments with the low and high leaker prototype valves resulted in a significant increase over time (N=6, $p<0.05$).

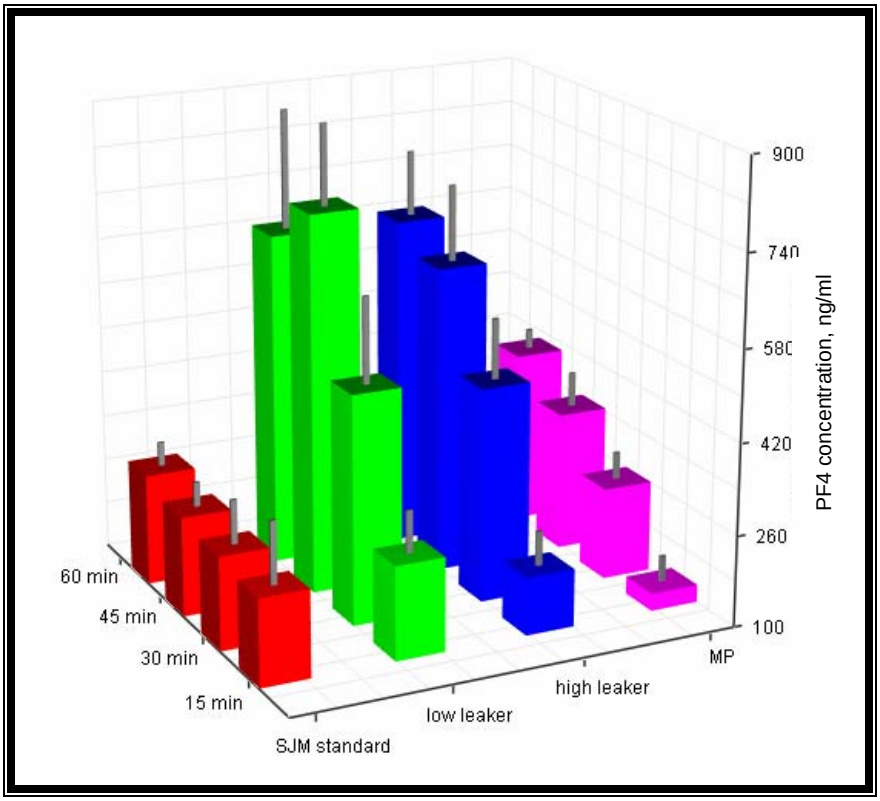

FIGURE 6.1.6.2.1. PF4 concentration over time for the MHV experiments. PF4 concentration was significantly higher for the low and high leaker prototype valves compared to the SJM Standard MHV (N=6, $p<0.05$).

Figures 6.1.6.2.2 and 6.1.6.2.3 show these differences in PF4 concentration between the different valves more clearly at 45 and 60 minutes, respectively. At 45 minutes, the low leaker prototype valve had significantly higher PF4 release than both the SJM Standard

and the MP valves (N=6, $p<0.05$). However, at 60 minutes only the high leaker valve produced significantly more PF4 than only the SJM Standard valve because of the high standard deviations for the low leaker valve (N=6, $p<0.05$). These high standard deviations are due to the variability in different donor blood as well as to experimental variability associated with the PF4 assay. Additionally, the low leaker valve was more prone to thrombus formation, which led to valve occlusion in some of the experiments. This occlusion reduced the amount of platelet activation since the platelets were no longer flowing through the hinge region, but instead remained stagnant in the flow loop. This effect was more prominent at 60 minutes since the occlusion did not occur until after the 45 minute sample time in most cases.

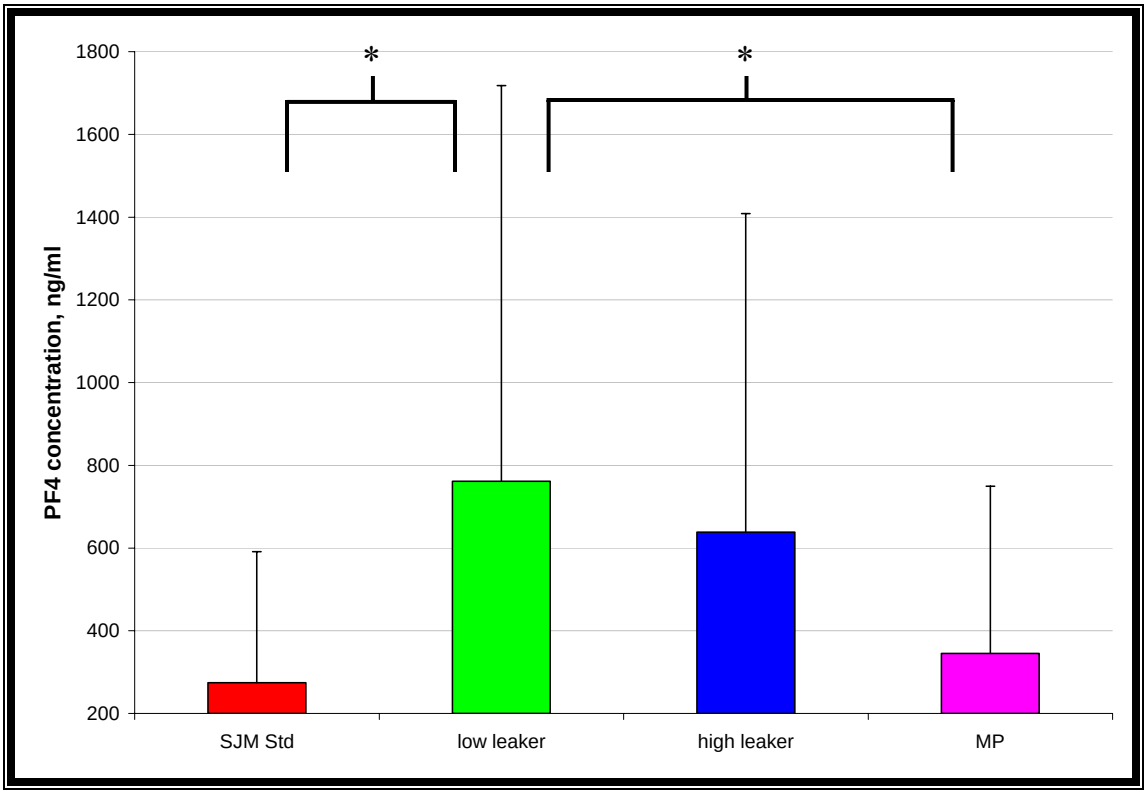

FIGURE 6.1.6.2.2. PF4 concentration for the different valves at 45 minutes (N=6, *=$p<0.05$). PF4 concentration was significantly higher for the low leaker prototype valve than for the SJM Standard and MP MHVs.

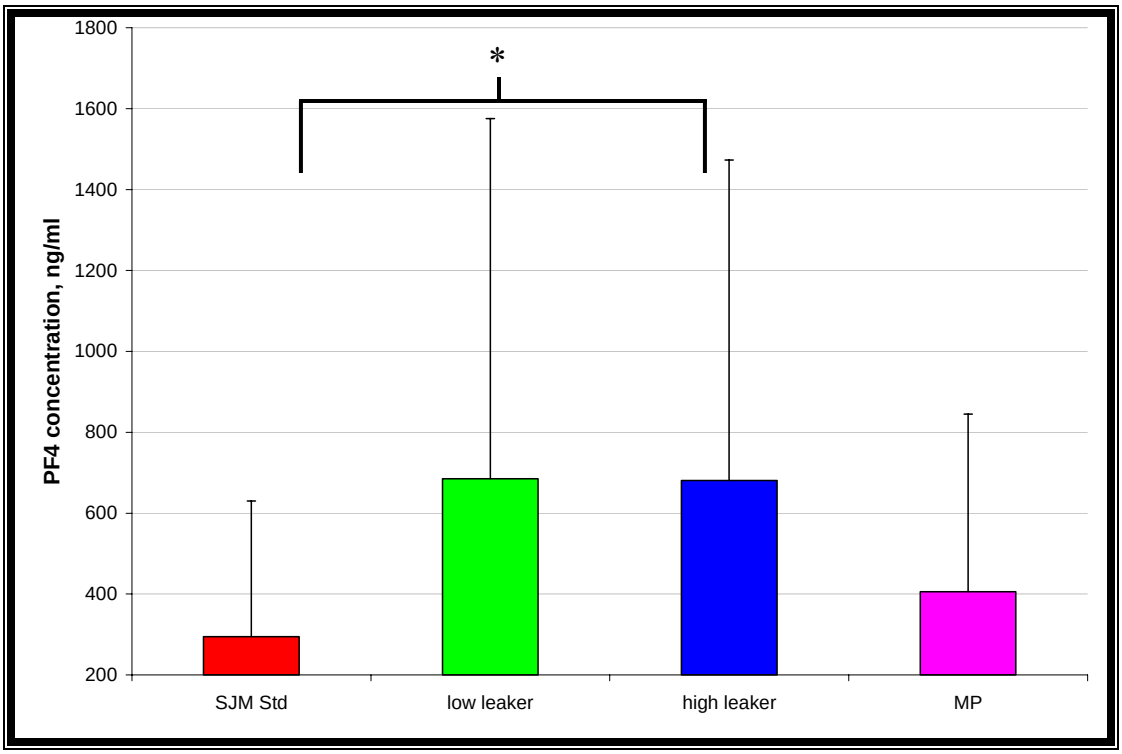

FIGURE 6.1.6.2.3. PF4 concentration for the different valves at 60 minutes (N=6, *=p<0.05). PF4 concentration was significantly higher for the high leaker prototype valve compared to the SJM Standard MHV.

6.1.6.3. Hemolysis results

The plasma hemoglobin results for all of the valves shown in Figure 6.1.6.3.1 indicate that hemolysis was not significant for the valve experiments. None of the valves exhibited plasma hemoglobin levels significantly above the baseline clinical levels (N=6, P>0.05)

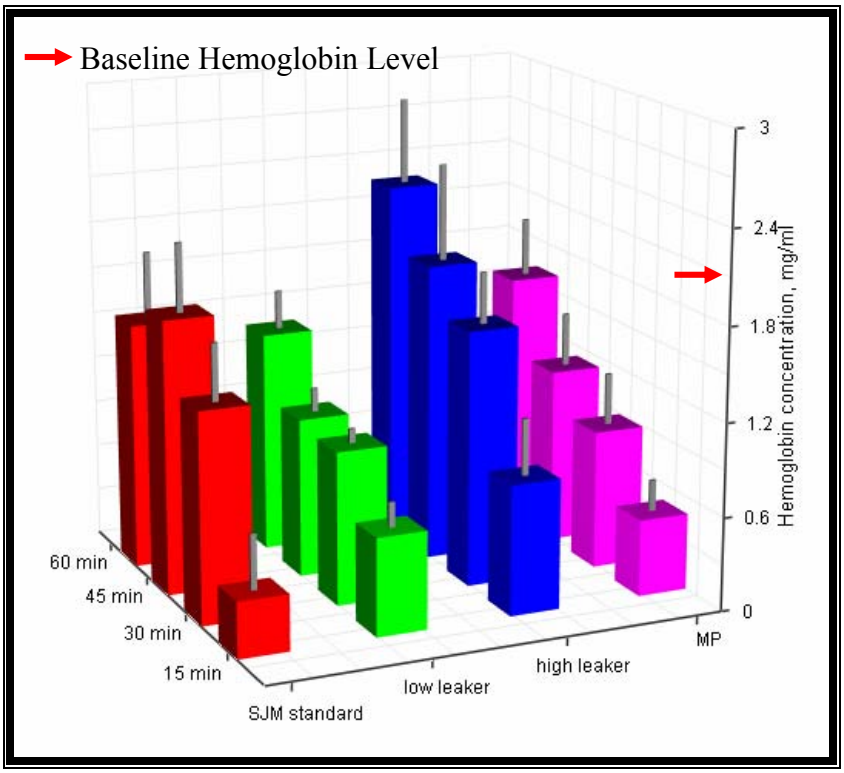

FIGURE 6.1.6.3.1. Plasma hemoglobin concentration over time for the valve experiments. Hemolysis was not significantly above the baseline level for any of the valves (N=6, $p>0.05$).

6.1.7. Scanning electron microscopy

Scanning electron microscopy (SEM) was performed to closely investigate the morphology of the thrombus as well as the surrounding area of the orifice plate. Figures 6.1.7.1a and 6.1.7.1b show the SEM results for an upstream and downstream thrombus. The pictures of the thrombi indicate that they have a normal clot morphology with RBCs and platelets enmeshed in a fibrous network. The fibers in the two thrombi appear to have different structure such that the fibers in the inlet thrombus are thicker and the fibers in the outlet thrombus are thinner and wispier. The histology in the next section will illuminate these types of fibers more clearly.

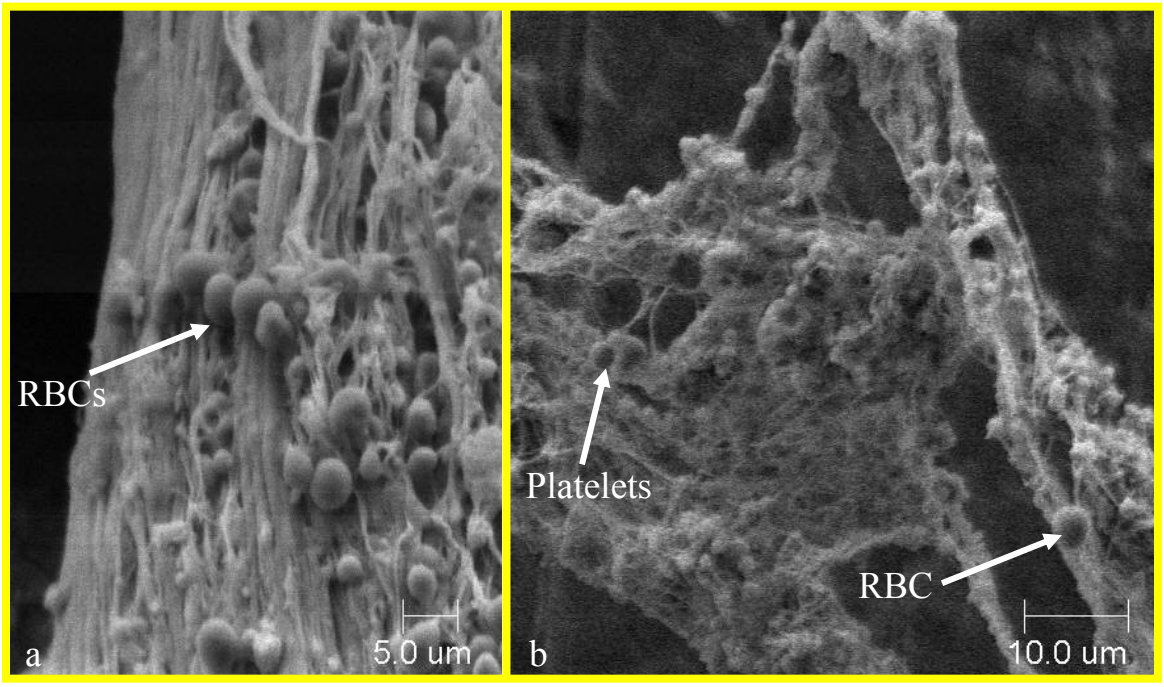

FIGURE 6.1.7.1(a) SEM Pictures of the inlet thrombus under 1300X magnification and (b) the outlet thrombus under 1200X magnification. The SEM images show a normal thrombus morphology with platelets and RBCs enmeshed in fibers that are presumably either fibrin or vWF.

Figure 6.1.7.2 shows a region of the orifice plate away from the outlet thrombus. It is evident from this figure that a small amount of RBCs and platelets do adhere to the orifice plate along with some fibrous strands, but there does not appear to be any thrombus formation. Thus, the orifice plate material does not induce platelet attachment and aggregation.

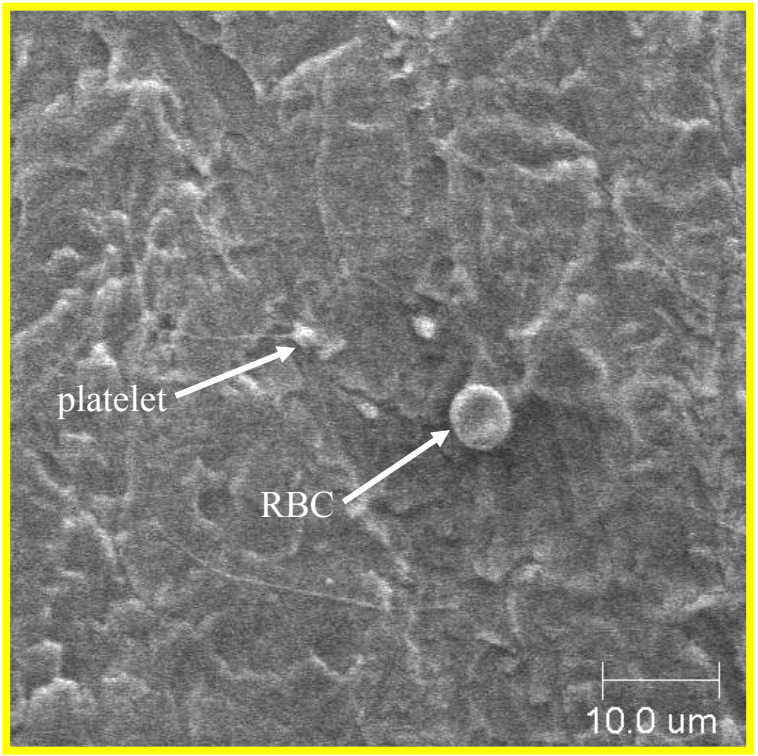

FIGURE 6.1.7.2. SEM picture of the orifice plate region away from the downstream thrombus under 1200X magnification. This SEM image shows that platelets and RBCs attach only sparsely to the orifice plate.

6.1.8. Histology results

Three different staining methodologies were used to investigate the morphology of the thrombi formed in this system. The Hematoxylin and Eosin (H&E) staining was used to see the cell membranes and nuclei, the Carstairs stain was used to identify the platelets, fibrin, and RBCs, and immunostaining with an antibody to vWF was used to identify vWF in the thrombi. Representative images are presented in the following sections, and the rest of the images are in Appendix B.

6.1.8.1. H&E staining results

Figure 6.1.8.1.1 shows a representative H&E stained slice from an experiment with Channel 1 in which a thrombus was formed. The red stain denotes cell membranes,

and the blue shows cell nuclei. The deep red bodies are RBCs and the pink are platelets. The blue nuclei most likely belong to leukocytes since RBCs and platelets do not have nuclei. Although the proportion of RBCs to platelets varied somewhat between samples H&E staining was not used to detect these differences. Thus, this representative image shows the general thrombus morphology for all of the samples.

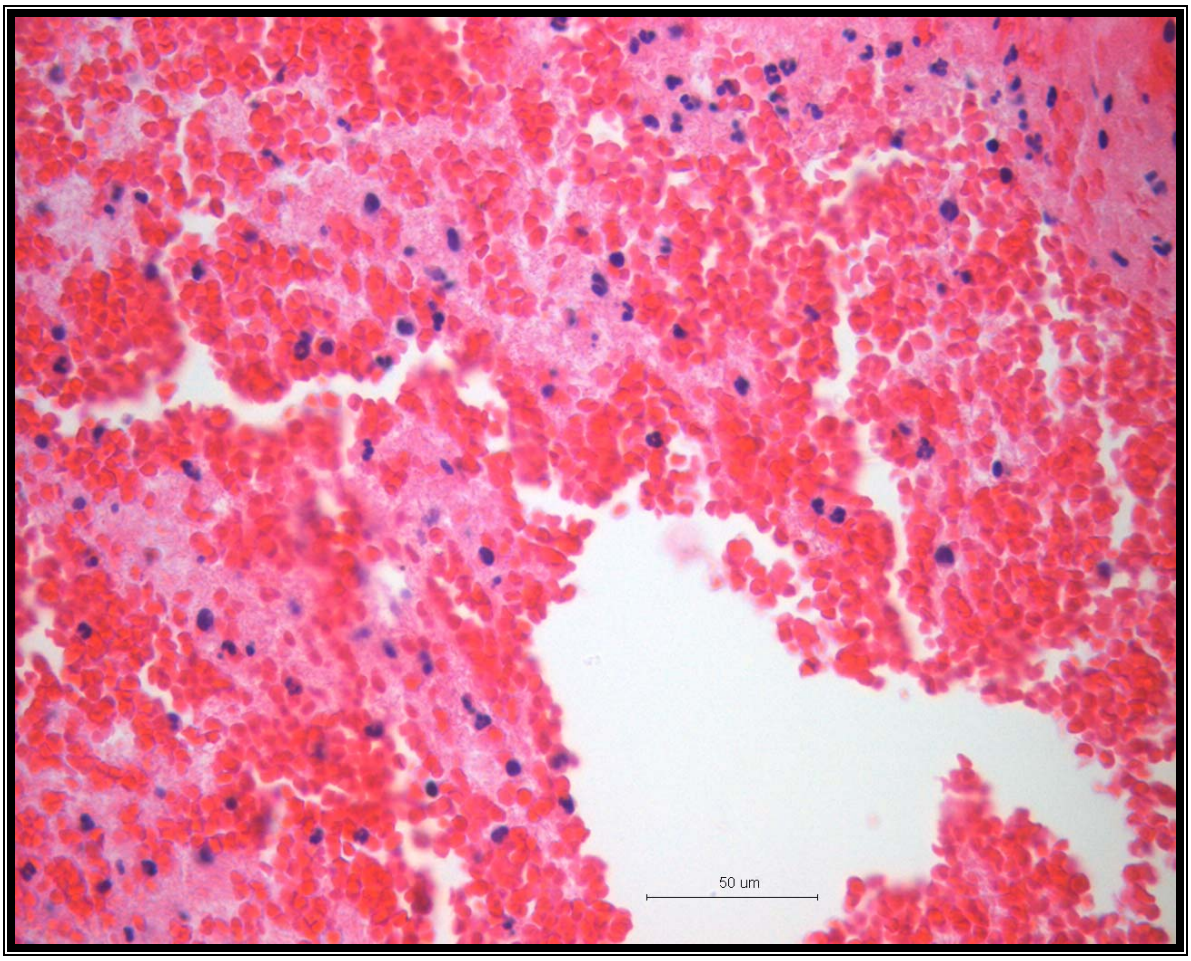

FIGURE 6.1.8.1.1. H&E stain of a thrombus formed in an experiment with Channel 1. Red denotes cell membrane, and blue denotes cell nuclei. Magnification is 40X.

6.1.8.2. Carstairs staining results

The result of the Carstairs stain for the 200 μm round orifice is shown in Figure 6.1.8.2.1. Red-orange denotes RBCs, navy blue denotes platelets, and red strands denote fibrin. In areas where platelets and fibrin are present the color is purple. As was the case

for the H&E stain for the Channel 1 thrombus, RBCs are abundant. Platelets are present in clusters, and fibrin can be seen co-localized with the platelets.

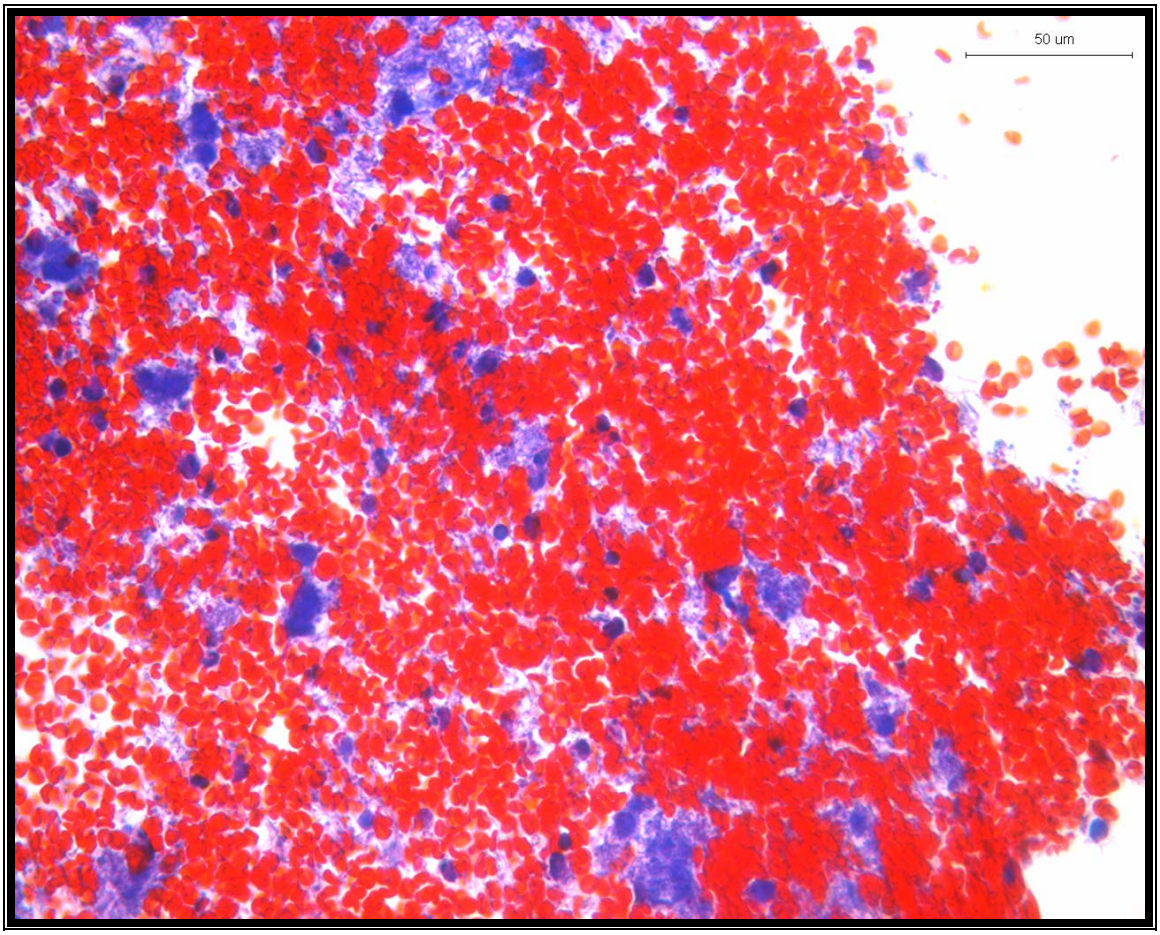

FIGURE 6.1.8.2.1. Carstairs stain of a thrombus formed in an experiment with a 200 μm round orifice. Red-orange denotes RBCs, navy blue denotes platelets, and red strands denote fibrin. In areas where fibrin and platelets overlap, the strands appear purple. This image shows a homogeneous mixture of RBCs and platelets with some fibrin interspersed. Magnification is 40X.

The Carstairs stain results for a Channel 1 thrombus are shown in Figure 6.1.8.2.2. This image looks similar to that for the 200 μm round orifice thrombus. However, the thrombus is less compact in the lower left, and there is a region in the lower right that is almost exclusively fibrin and platelets. Thus, instead of being a homogeneous mixture

like the thrombus collected from the 200 μm round orifice experiments, the Channel 1 thrombus has areas that appear to be in different stages of development.

Figure 6.1.8.2.3 shows the Carstairs stain results for different regions from an elongated thrombus formed in the hinge of the low leaker prototype valve. These thrombi were extracted, as shown in Figure 6.1.8.2.4, beginning at the inlet (1) to the hinge region extending into the hinge recess (4). Thus, the last thrombus collected should represent the most mature thrombus. The first, second, and third thrombus regions are similar to one another in morphology. These regions all have RBCs enmeshed by fibrin with small,

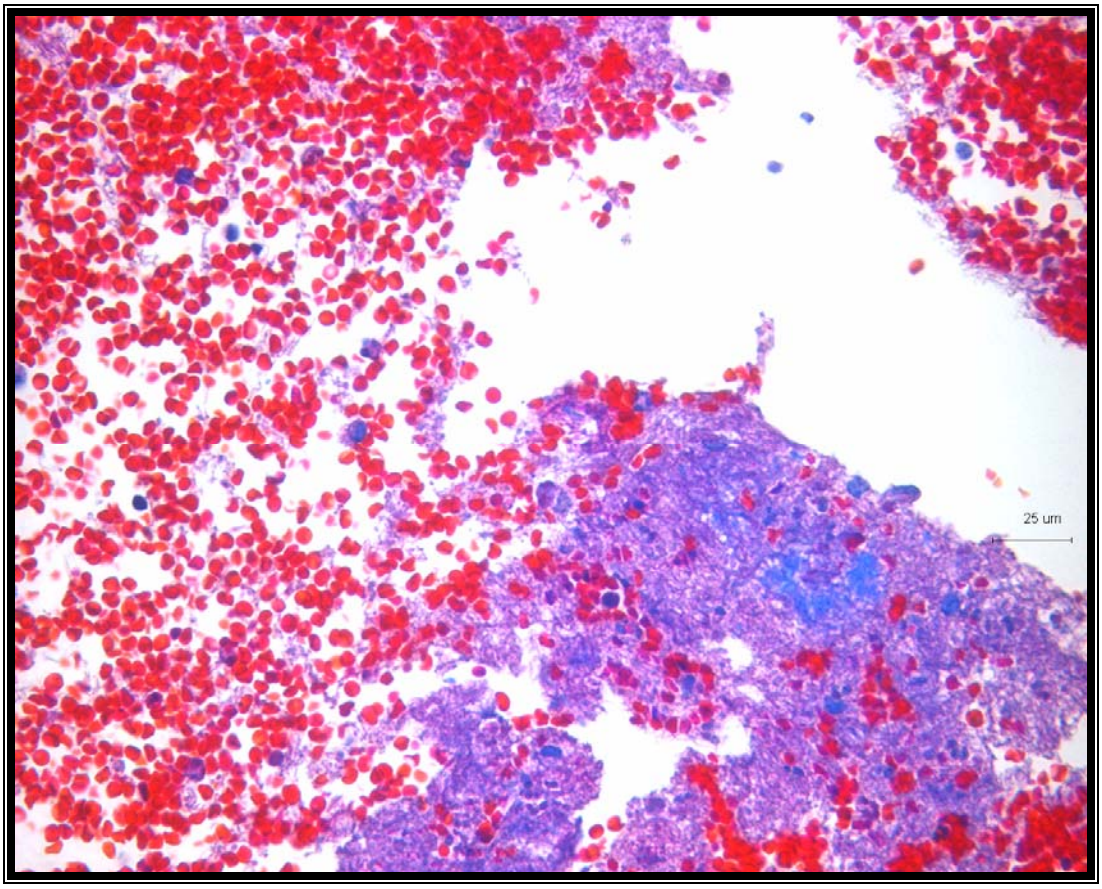

FIGURE 6.1.8.2.2. Carstairs stain of a thrombus formed in an experiment with Channel 1. Red-orange denotes RBCs, navy blue denotes platelets, and red strands denote fibrin. In areas where fibrin and platelets overlap, the strands appear purple. This image shows a concentration of platelets enmeshed in fibrin with very few RBCs included. Magnification is 40X.

platelet-rich regions. However, the last image (4) is almost completely platelets with some fibrin and a few RBCs. During the thrombus extraction, this thrombus appeared to be all white whereas the other thrombi had some red color. Thus, if this does represent the most mature thrombus, it shows that the thrombus was indeed initiated by an accumulation of platelets with very few RBCs.

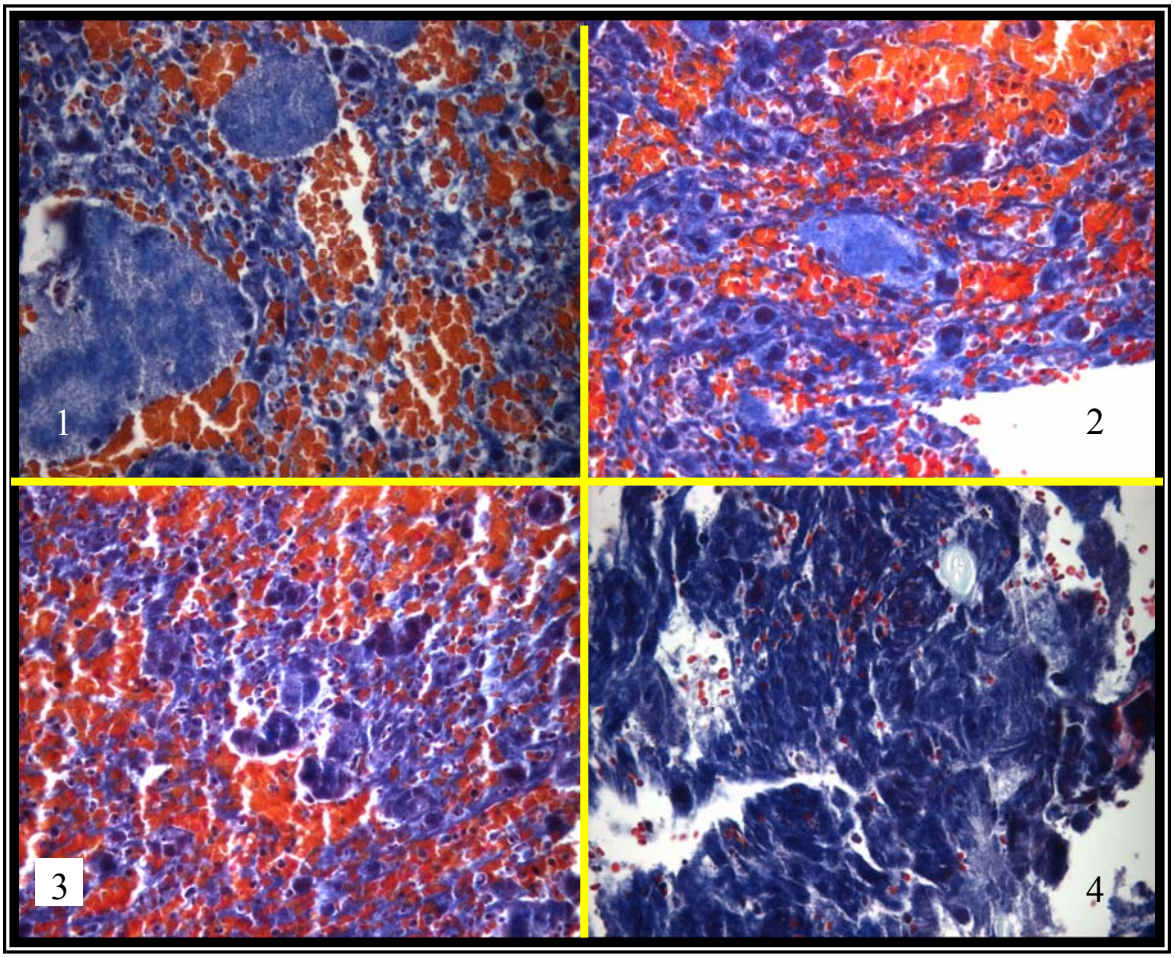

FIGURE 6.1.8.2.3. Carstairs stain of a thrombus formed in an experiment with the low leaker prototype valve. The numbering refers to where in the hinge the thrombus was found: (1) The first thrombus region at the inflow area of the hinge and (4) Embedded inside the hinge recess. Red-orange denotes RBCs, navy blue denotes platelets, and red strands denote fibrin. In areas where fibrin and platelets overlap, the strands appear purple. The outermost thrombi appear to be a mixture of platelets, RBCs, and fibrin whereas the thrombus farthest inside the hinge is mostly platelets and fibrin. Magnification is 40X.

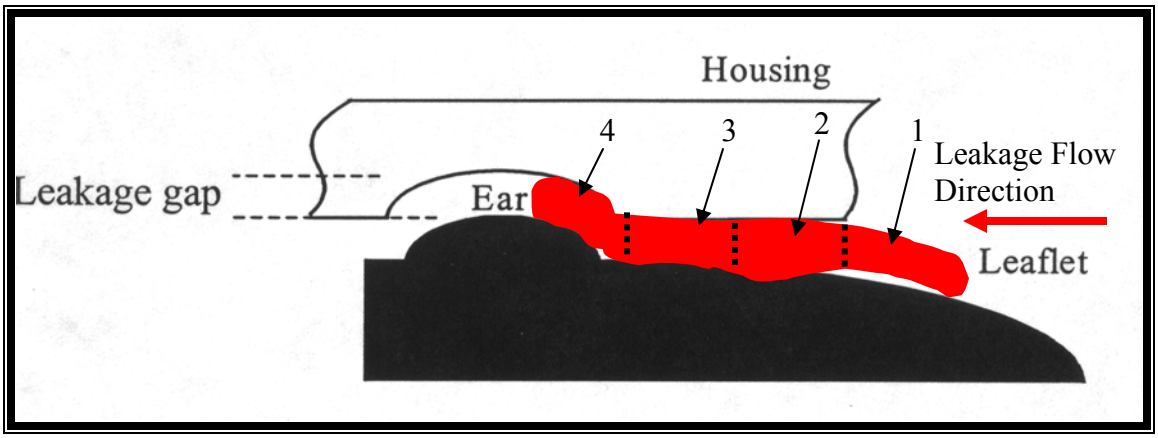

FIGURE 6.1.8.2.4. Diagram of the thrombus shown in Figure 7.8.1.2.3. Arrows denote regions of the thrombus as described in Figure 7.8.1.2.3 with region (1) at the inlet to the hinge, and region (4) inside the hinge recess. Arrow shows the leakage flow direction.

Figure 6.1.8.2.5 shows two thrombi formed upstream and downstream of Channel 3. The upstream thrombus is a homogeneous mixture of RBCs, platelets, and fibrin. However, the downstream thrombus is predominantly platelets and fibrin. Thus, based on the morphology of these thrombi, the downstream thrombus appears to be the more mature thrombus.

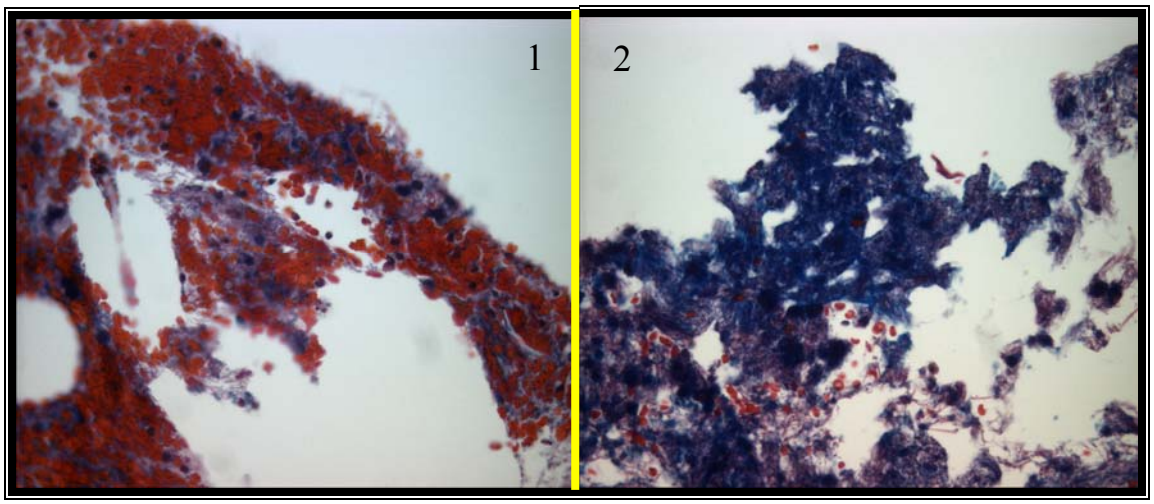

FIGURE 6.1.8.2.5. Carstairs stain of a thrombus formed upstream (1) and downstream (2) of Channel 3. Red-orange denotes RBCs, navy blue denotes platelets, and red strands denote fibrin. In areas where fibrin and platelets overlap, the strands appear purple. The upstream thrombus appears to be a mixture of platelets, RBCs, and fibrin whereas the downstream thrombus is mostly platelets and fibrin. Magnification is 40X.

6.1.8.3. vWF immunostaining results

A representative image of a colorimetric anti-vWF stain for a 200 μm round orifice thrombus is shown in Figure 6.1.8.3.1. The dark pink indicates the presence of vWF, and blue denotes cell nuclei.

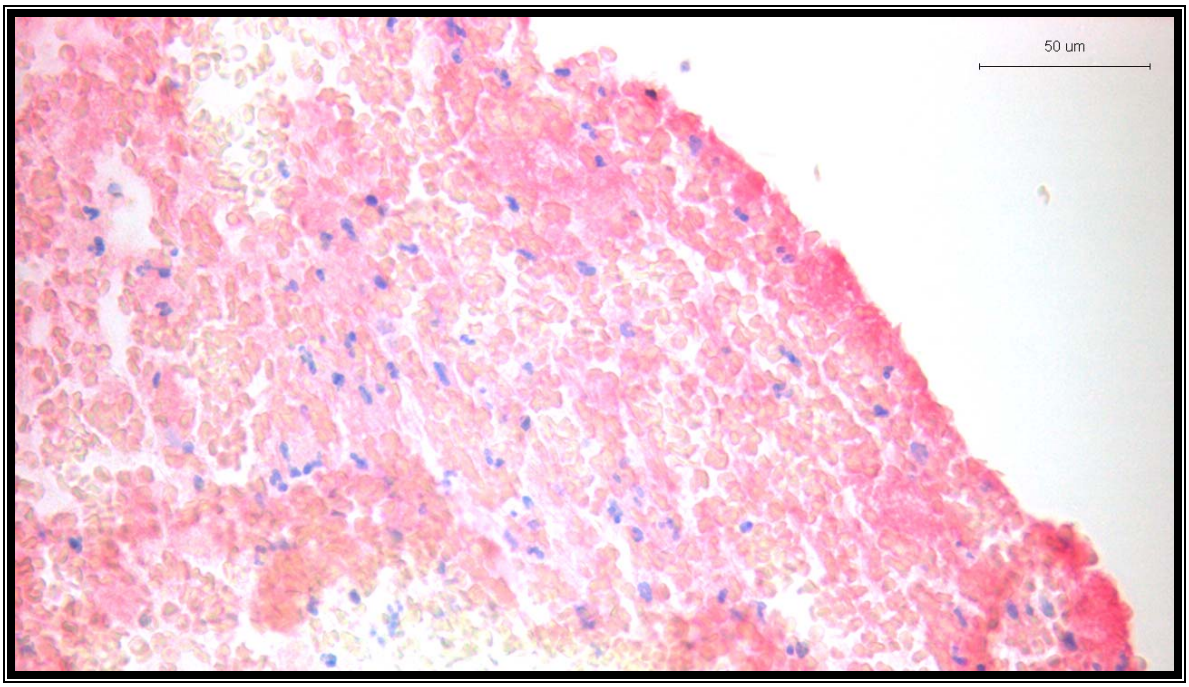

FIGURE 6.1.8.3.1. Colorimetric anti-vWF stain of a thrombus formed in an experiment with the 200 μm round orifice. Red denotes vWF and blue denotes cell nuceli. This figure shows that the vWF is interspersed throughout the thrombus with slightly higher concentrations at the edges where the thrombus may have been growing Magnification is 40X.

This figure shows that the vWF is interspersed throughout the thrombus with slightly higher concentrations at the edges where the thrombus may have been growing. Figure 6.1.8.3.2 shows the fluorescent anti-vWF images for regions (1) and (4) of the low leaker prototype valve thrombus that was also stained with the Carstairs stain (Figure 6.1.8.2.3).

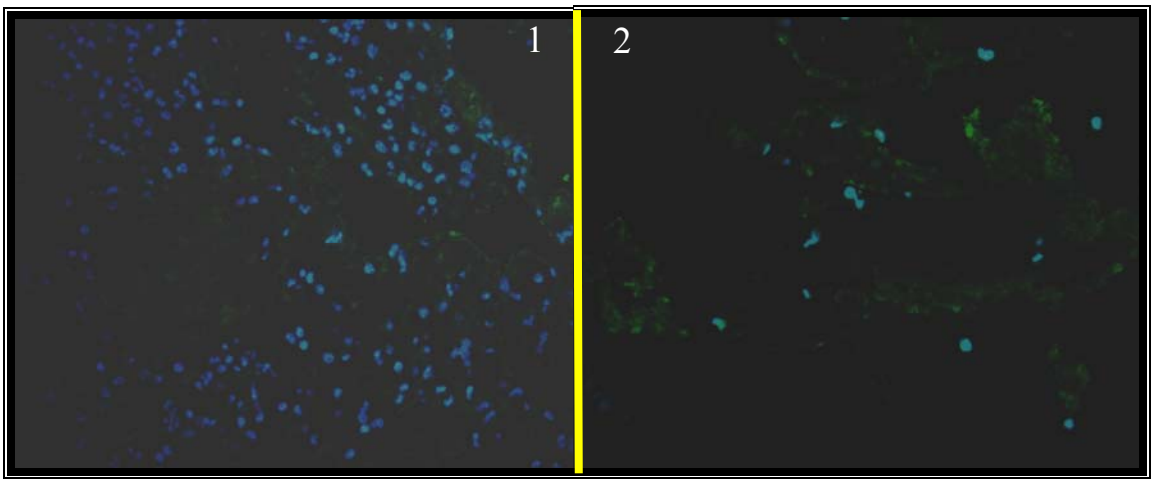

FIGURE 6.1.8.3.2. Fluorescent anti-vWF stain of a thrombus formed in an experiment with the low leaker prototype valve. The numbering refers to where in the hinge the thrombus was found: (1) The first thrombus region (Region 1) at the inflow area of the hinge and (2) Embedded inside the hinge recess (Region 4). The first thrombus appears to contain more cell nuclei than the embedded thrombus, which appears to contain more vWF. Green denotes the presence of vWF, and blue is cell nuclei. Magnification is 40X.

As in Figure 6.1.8.3.1 with the colorimetric anti-vWF stain, the vWF is interspersed throughout the thrombi. Additionally, the edges appear to have a higher concentration of vWF. Region 4 shown in panel 2 of Figure 6.1.8.3.2 appears to have a greater concentration of vWF than region 1, which is shown in panel 1 of Figure 6.1.8.3.2. This correlates well with the higher concentration of platelets seen in the Carstairs stain for region 4, which is shown in panel 4 of Figure 6.1.8.2.3, compared to that in region 1 shown in Figure 6.1.8.2.3. Since platelet aggregation can occur under high shear conditions via linkage with vWF this part of the thrombus found in the hinge recess of the low leaker valve may be held together via vWF binding.

Figure 6.1.8.3.3 shows the upstream and downstream thrombi formed in an experiment with Channel 3. These sections are from the same region of the thrombus as those shown in Figure 6.1.8.2.4 with the Carstairs stain. The upstream thrombus is composed of more vWF than the downstream thrombus, which has only patches of vWF.

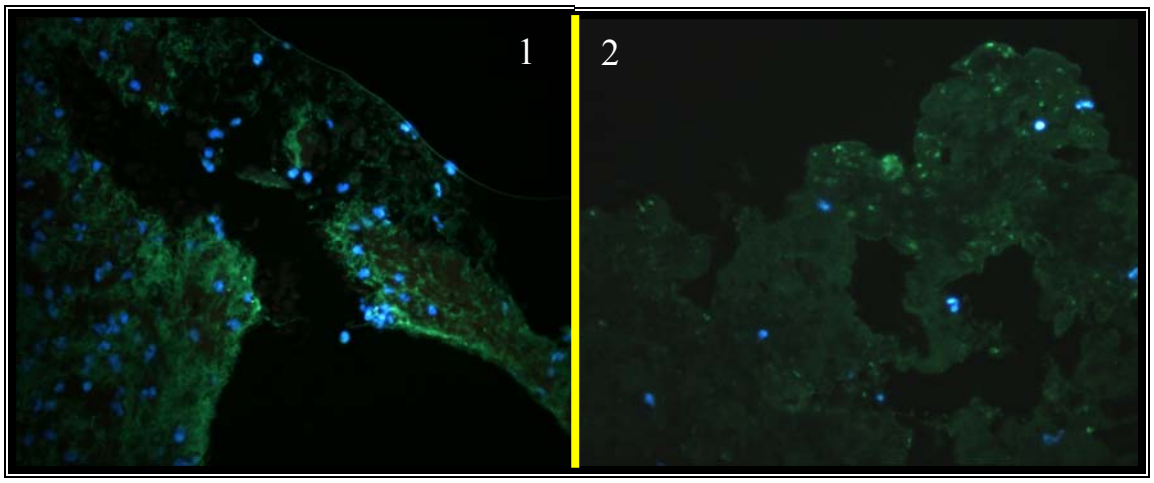

FIGURE 6.1.8.3.3. Fluorescent anti-vWF stain of a thrombus formed upstream (1) and downstream (2) of Channel 3. Green denotes the presence of vWF, and blue is cell nuclei. The upstream thrombus appears to contain more cell nuclei and vWF than the downstream thrombus. Magnification is 40X.

This result correlates well with the Carstairs stain result in Figure 6.1.8.2.4, which shows that the downstream thrombus contained more fibrin than the upstream thrombus. Thus, in the downstream thrombus fibrin may enable platelet aggregation and thrombus formation, and in the upstream thrombus this may be mediated by vWF linkage.

6.2. Particle image velocimetry results

The digital particle image velocimetry (DPIV) results are separated into sections for the different orifices and channels. Additional results are presented in Appendix C. PIV was not performed with the 200 μm round orifice because the seed particles aggregated and occluded the orifice before images could be acquired. In each section, figures are shown for the centerplane average velocity, the square of the root mean of the axial velocity (V_{RMS}), principle Reynolds stress (PReS), and shear stress fields. V_{RMS} is a measure of the velocity fluctuations in the flow field. Similarly, PReS is a standard measure of fluctuations in velocity that also incorporates the viscosity and density of the

fluid in its calculation. These velocity fluctuations can be damaging to blood elements if the length scale of the fluctuations is small enough to affect these cells. Generally, the length scale must be on the order of the diameter of the blood element. Thus, for PReS values that are on this length scale and above a given threshold indicate that these velocity fluctuations are sufficient to damage blood cells or activate platelets. However, because most blood damage and platelet activation studies are performed under laminar flow conditions, this exact threshold is not known. Also, determining the length scale of the PReS is theoretical and these estimations may not be valid for the transitional and low Reynolds number turbulence studied here. For this reason, the shear stress (SS) data is also presented. This value is a measure of the velocity gradient with respect to the transverse direction of the flow. SS magnitudes of 80 dyn/cm^2 have been implicated in platelet damage and activation leading to platelet aggregation.

6.2.1. Round orifice results

6.2.1.1. Average velocity fields

The average velocity field for the 400 μm round orifice with a laser pulse separation time of 5 μs is shown in Figure 6.2.1.1.1. This pulse separation allows for the measurement of the highest velocity particles that are passively advected in the orifice jet. There were problems with occlusion of the 400 μm round orifice, but an adequate number of images could be taken for this orifice before the flow rate decreased significantly. The figure shows the measured jet downstream of the orifice plate along the centerplane through the orifice. The peak centerline velocity for the 400 μm round orifice is much lower than expected from the measured flow rate, of 0.05 L/min. Since the laser sheet

width was approximately 1 mm, and the orifice is only 400 µm in diameter, particles outside the center plane, moving much slower than the jet, were included in the raw PIV images. These slower moving particles could have resulted in a decrease in the measured velocity. Also, the particle density for the 400 µm round orifice experiments had to be lower to prevent almost instant occlusion at the higher particle densities used for the larger orifices. Figure 6.2.1.1.1 also shows that the jet is dissipated very quickly most likely because of the entrainment of the large volume of slower moving reverse flow. This reverse flow is evident in Figure 6.2.1.1.2, which was acquired with a pulse separation time of 50 µs. This pulse separation allows for the capture of the lower velocity particles while eliminating the higher velocity particles from the vector field.

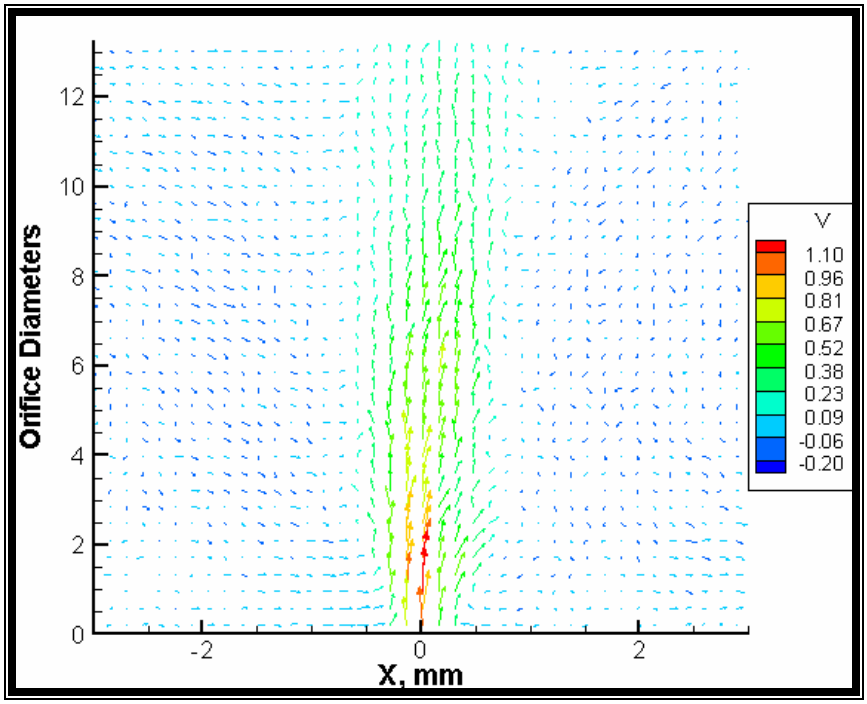

FIGURE 6.2.1.1.1. Average velocity vector field downstream of the 400 µm round orifice. The pulse separation was 5 µs, and the vector plot is an average of 1000 image pairs. Velocity in m/s is color coded according to the legend.

Thus, in this image the recirculation zones on either side of the jet are apparent. It is clear from Figure 6.2.1.1.2 that the fluid that impinges on the chamber wall at the throat of the

chamber is directed back to the orifice jet resulting in mixing of this low flow fluid with the jet. This mixing could also contribute to the rapid dissipation of the jet.

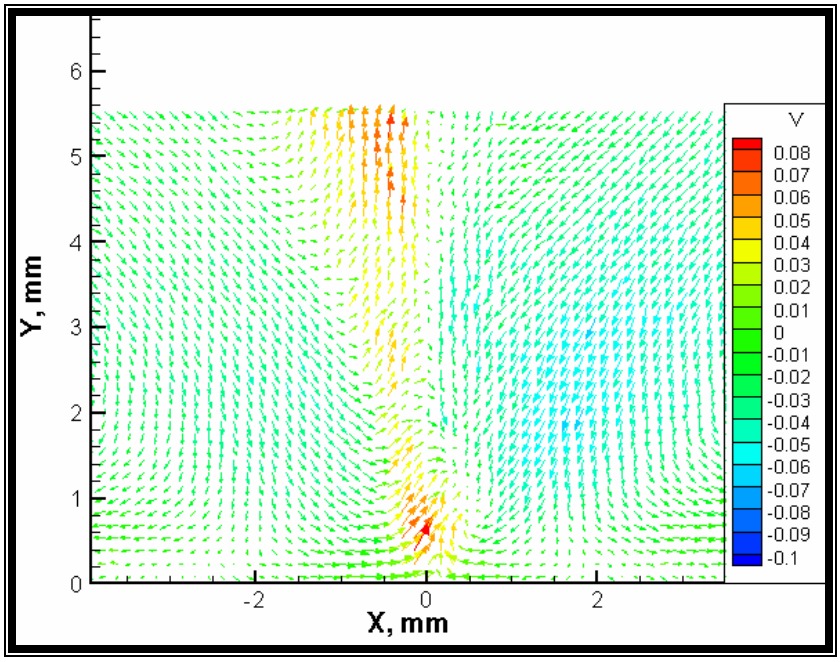

FIGURE 6.2.1.1.2. Average velocity vector field downstream of the 400 µm round orifice. The pulse separation was 50 µs, the vector plot is an average of 1000 image pairs. Velocity in m/s is color coded according to the legend.

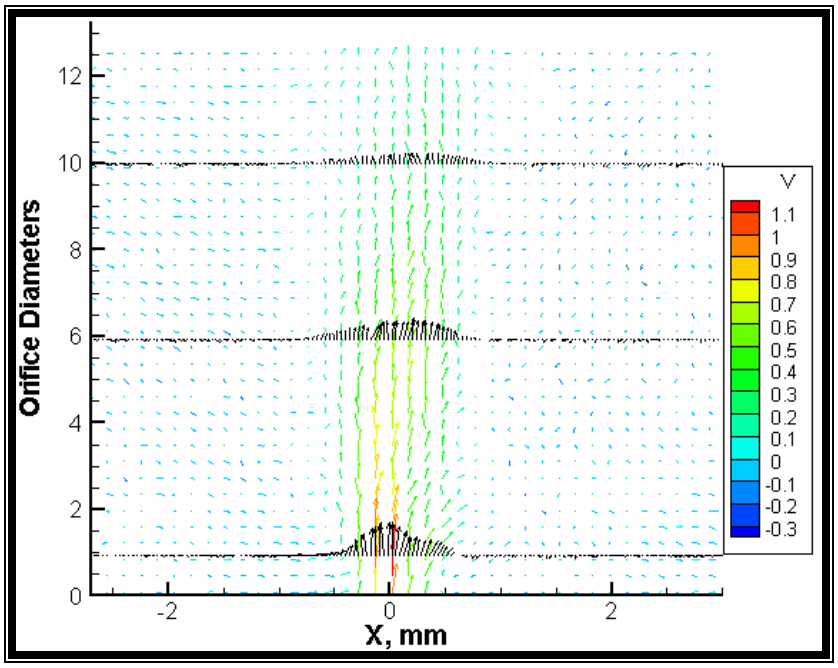

FIGURE 6.2.1.1.3. Flow profiles at 1, 3, and 5 diameters downstream of the 400 µm round orifice. The pulse separation was 5 µs, the vector plot is an average of 1000 image pairs. Velocity in m/s is color coded according to the legend.

Figure 6.2.1.1.3 shows the velocity profiles at 1, 6, and 10 diameters downstream of the 400 μm round orifice. These flow profiles show the decay of the jet as the flow moves downstream of the orifice. It is evident from this plot that the profile flattens out very quickly indicating that the jet momentum diffuses very rapidly. Additionally, the profile is skewed, which shows the asymmetry of the jet. This asymmetry may be a result of seed particle accumulation at the orifice, which altered the shape of the orifice.

The average velocity fields for the 800 μm round orifice with a pulse separation time of 10 μs is shown in Figure 6.2.1.1.4. This pulse separation allows for the tracking of the highest velocity particles that are entrapped in the orifice jet. The peak centerline velocity for the 800 μm round orifice of approximately 6 m/s corresponds with the measured flow rate of 0.15 l/min. The measurements for this orifice were more accurate compared to those for the 400 μm round orifice due to the higher particle density, larger

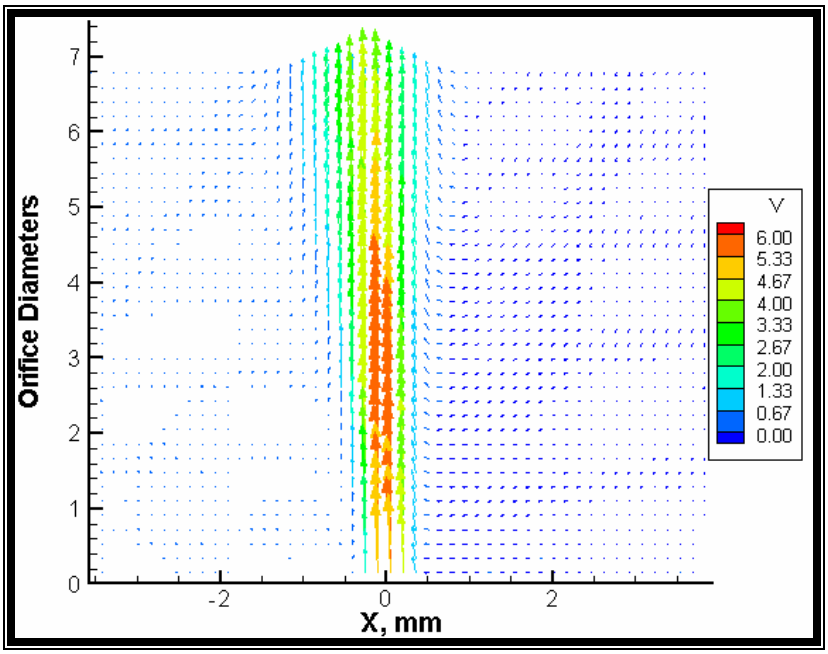

FIGURE 6.2.1.1.4. Average velocity vector field downstream of the 800 μm round orifice. The pulse separation was 10 μs, the vector plot is an average of 1000 image pairs. Velocity in m/s is color coded according to the legend.

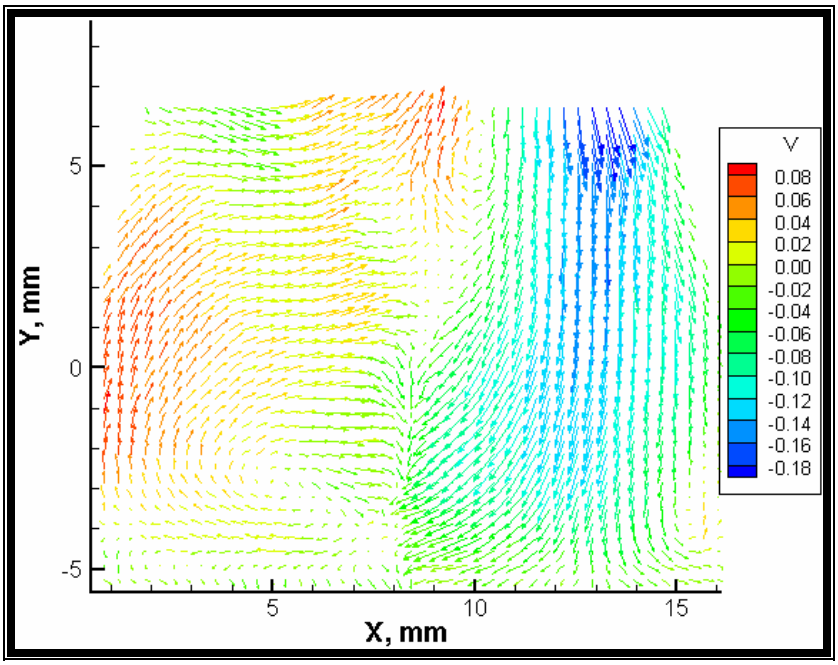

FIGURE 6.2.1.1.5. Average velocity vector field downstream of the 800 µm round orifice. The pulse separation was 200 µs, the vector plot is an average of 1000 image pairs. Velocity in m/s is color coded according to the legend.

orifice diameter, and higher flow rate, which reduced the amount of out of plane particles captured in the images as well as the tendency for particles to build up on the orifice.

Figure 6.2.1.1.5 shows the average velocity field measured with a pulse separation of 200 µs. As was the case for the 400 µm round orifice, large recirculation regions are evident on both sides of the jet. However, for this larger diameter jet the reverse velocities are about twice those for the 400 µm round orifice jet. Figure 6.2.1.1.6 shows the centerplane jet velocity profiles at locations 1, 3 and 6 diameters downstream of the 800 µm round orifice. Unlike the 400 µm round orifice jet, this jet maintains a Gaussian jet-like profile indicating that it is able to persist for a longer distance downstream of the orifice due to the larger jet diameter and higher flow rate.

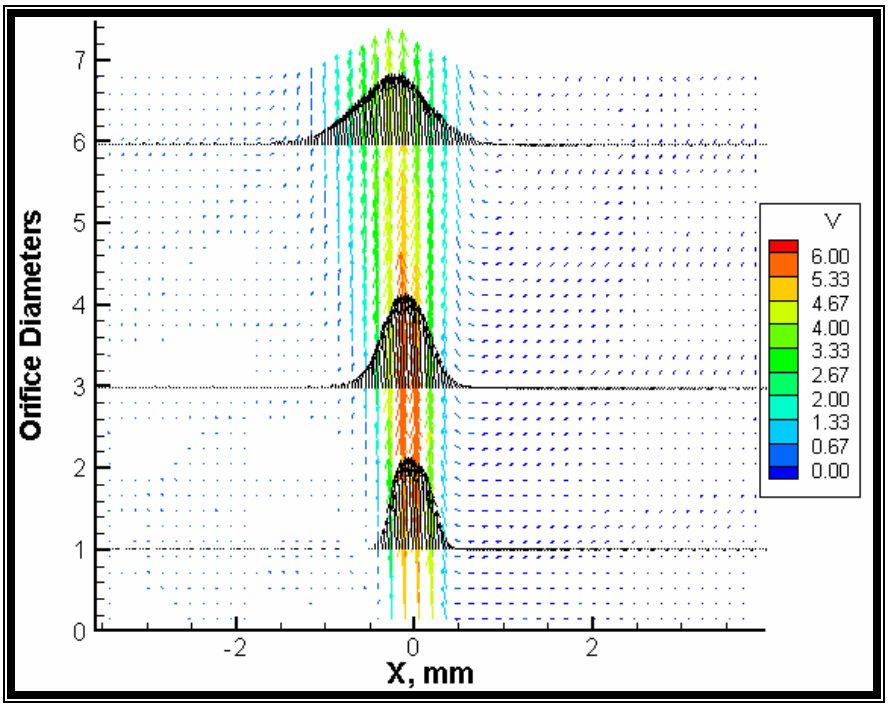

FIGURE 6.2.1.1.6. Flow profiles at 1, 3, and 6 diameters downstream of the 800 μm round orifice. The pulse separation was 10 μs, and the vector plot is an average of 1000 image pairs. Velocity in m/s is color coded according to the legend.

PIV measurements were also performed at a lower flow rate for the 800 μm round orifice corresponding to the low flow rate blood experiments. The flow rate for the low shear stress experiments was chosen to have the same Reynolds number as the 400 μm round orifice experiments. These results are shown in Figure 6.2.1.1.7 along with the results for the normal shear experiments. These images show that, as expected, the peak velocities for the low shear experiments are approximately 70% of the values for the normal shear experiments, which corresponds to the different bulk flow rates of 0.09 and 0.15 l/min for the low and normal shear experiments, respectively. The low shear jet also appears to dissipate more rapidly.

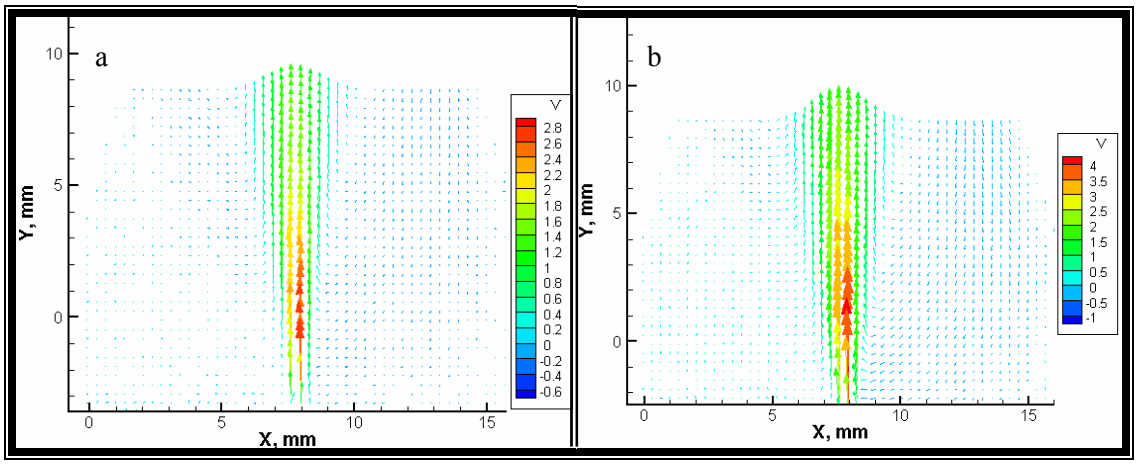

FIGURE 6.2.1.1.7. Average velocity vector field downstream of the (a) low shear and (b) normal shear 800 µm round orifice experiments. The pulse separation was 10 and 8 µs, respectively, and the vector plots are an average of 1000 image pairs for both acquisitions. Velocity in m/s is color coded according to the legend.

The average orifice centerplane velocity fields for the 1200 µm round orifice with a pulse separation time of 10 µs is shown in Figure 6.2.1.1.8. This pulse separation allows for the tracking of the highest velocity particles that are entrapped in the orifice jet. The peak velocity for the 1200 µm round orifice of approximately 6 m/s corresponds with the measured flow rate.

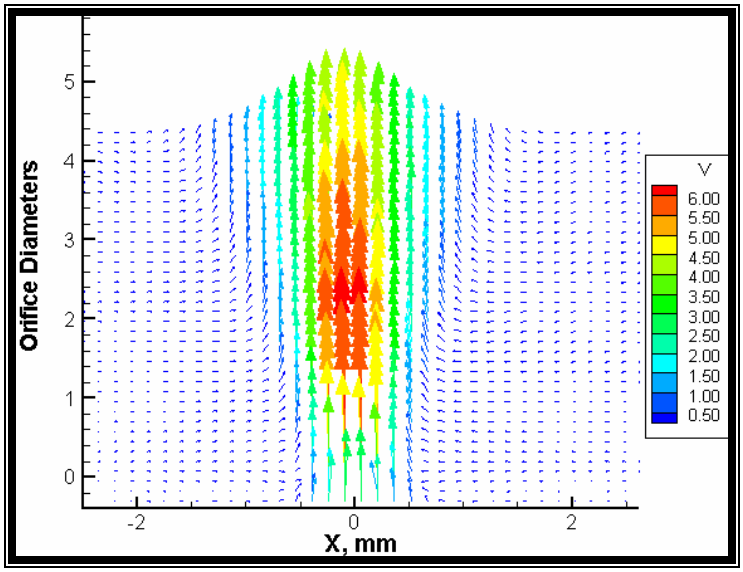

FIGURE 6.2.1.1.8. Average velocity vector field downstream of the 1200 µm round orifice. The pulse separation was 10 µs, and the vector plot is an average of 1000 image pairs. Velocity in m/s is color coded according to the legend.

Figure 6.2.1.1.9 shows the average velocity field measured with a pulse separation of 75 μs upstream and downstream of the orifice plate. As was the case for the 400 and 800 μm round orifices, large recirculation regions are evident on both sides of the jet. However, for this larger diameter jet the reverse velocities are about 30% higher those for the 800 μm round orifice jet. Figure 6.2.1.1.10 shows the average velocity field upstream of the orifice plate measured with a pulse separation of 100 μs. This plot shows the flow field narrowing towards the orifice with an increase in velocity as it approaches the orifice.

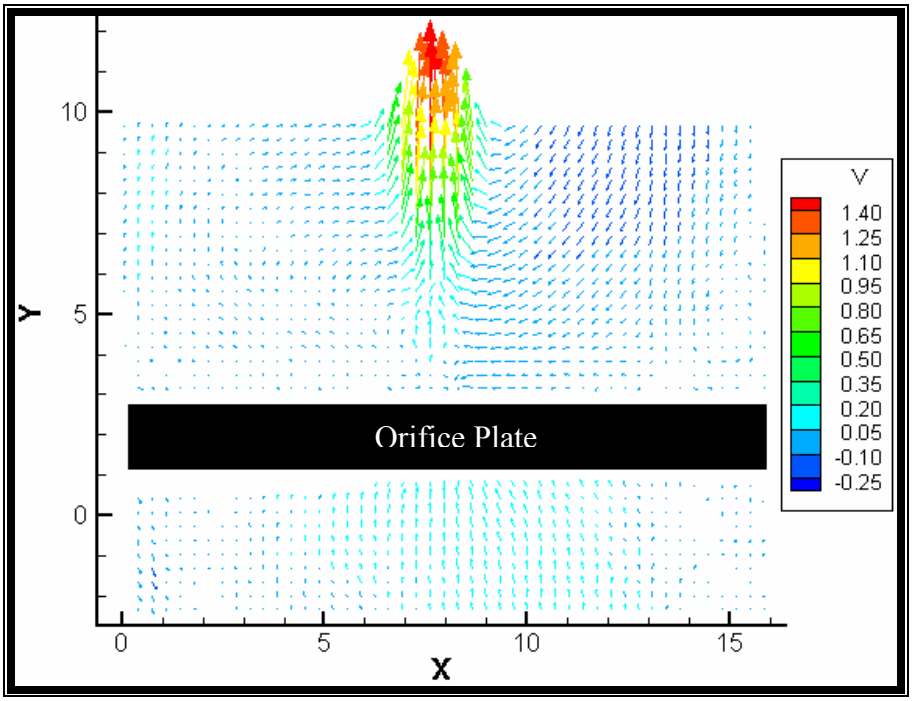

FIGURE 6.2.1.1.9. Average velocity vector field for the 1200 μm round orifice on both sides of the orifice. The pulse separation was 75 μs, and the vector plot is an average of 500 image pairs. Velocity in m/s is color coded according to the legend.

The general flow pattern is in the forward direction towards the orifice with very little reverse flow. The upstream flow profiles for the 1200 μm round orifice shown in Figure 6.2.1.1.11 further illuminate this upstream flow field. These profiles clearly show the narrowing of the flow towards the orifice opening. They also show some skewing of the

flow, which is a result of the inlet flow that is not fully developed. However, this skewing is not reflected in the downstream jet as evidenced by the symmetric downstream flow profiles at 1, 2.5, and 4 diameters downstream of the orifice shown in Figure 6.2.1.1.12. These flow profiles indicate that the jet persists to this point with Gaussian flow profiles similar to those seen for the 800 μm round orifice jet.

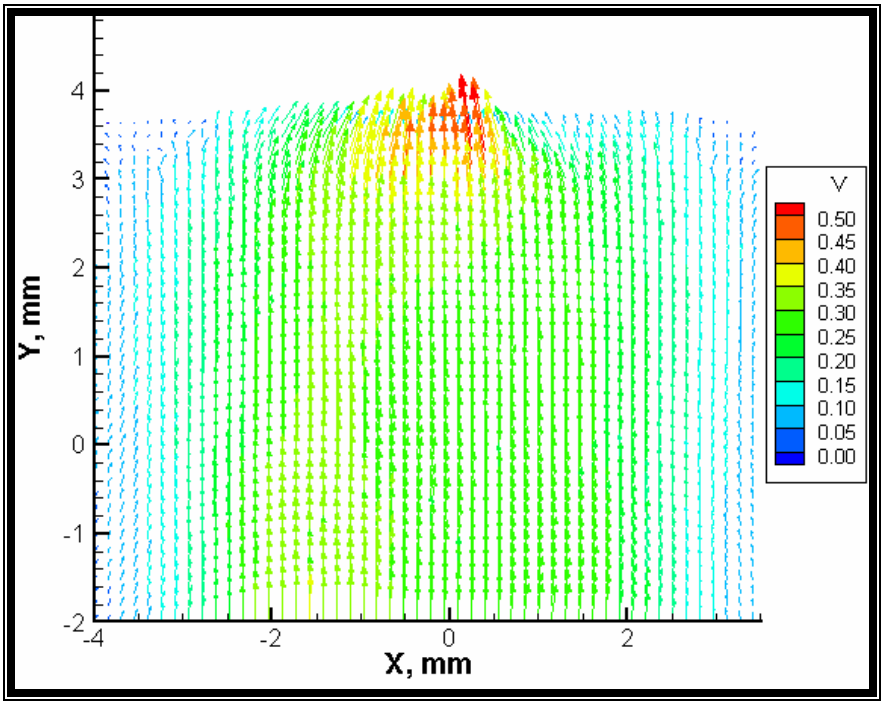

FIGURE 6.2.1.1.10. Average velocity vector field for the 1200 μm round orifice. The pulse separation used was 10 μs, and the vector plot is an average of 1000 image pairs. Velocity in m/s is color coded according to the legend.

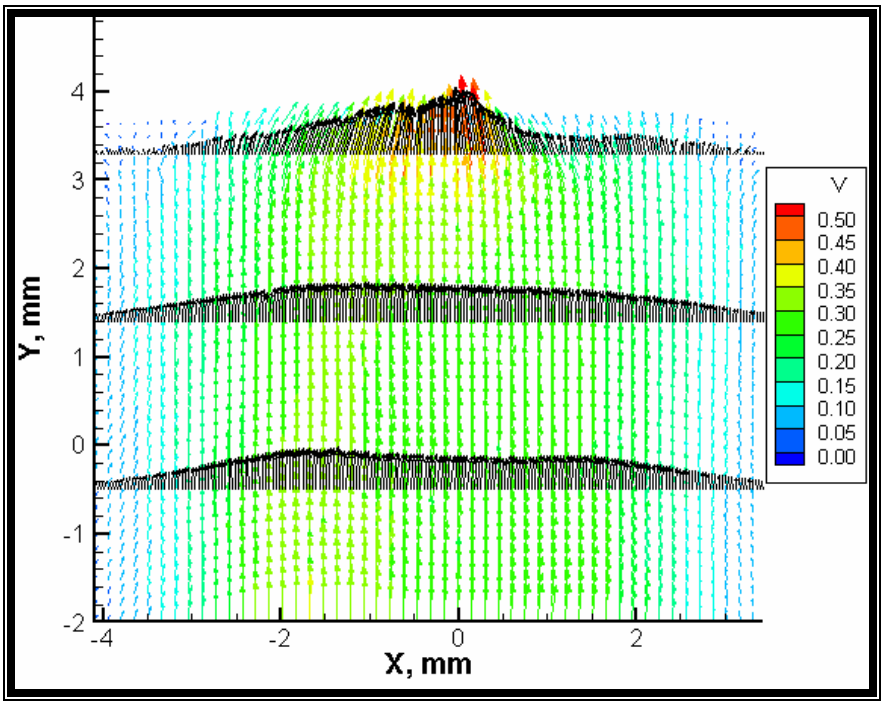

FIGURE 6.2.1.1.11. Flow profiles upstream of the 1200 µm round orifice. The pulse separation was 100 µs, and the vector plot is an average of 1000 image pairs. Velocity in m/s is color coded according to the legend.

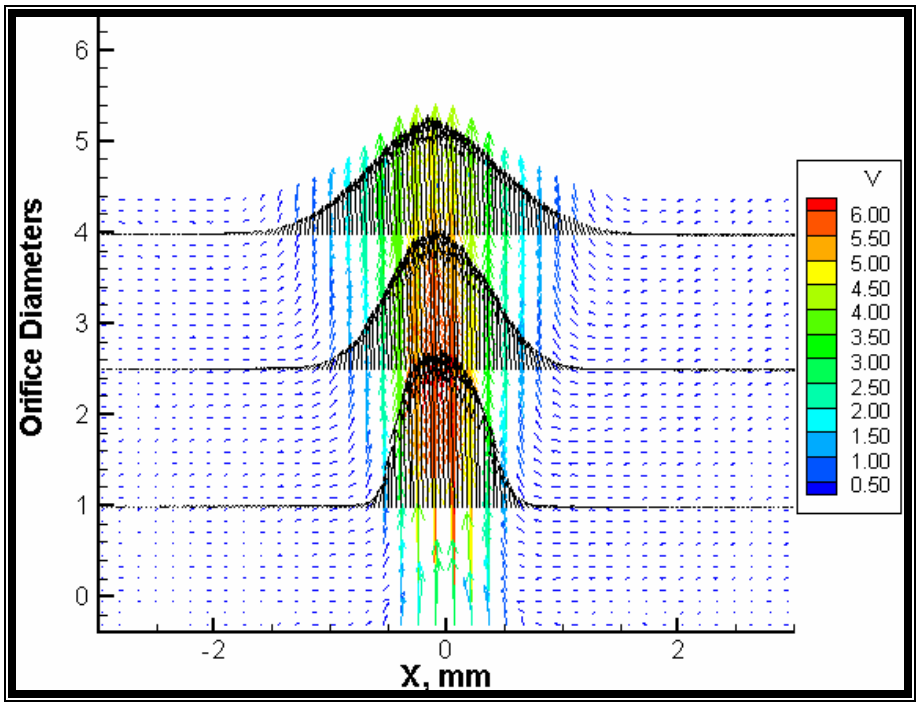

FIGURE 6.2.1.1.12. Flow profiles at 1, 2.5, and 4 diameters downstream of the 1200 µm round orifice. The pulse separation was 10 µs, and the vector plot is an average of 1000 image pairs. Velocity in m/s is color coded according to the legend.

6.2.1.2. V_{RMS} fields

The V_{RMS} fields corresponding to the jet average velocity fields presented in the previous section will be shown in this section. These plots show the magnitude of the velocity fluctuations present in the jets. The V_{RMS} fields for the 400, 800, and 1200 µm round orifice jets are shown in Figures 6.2.1.2.1, 6.2.1.2.2, and 6.2.1.2.3, respectively. The rough contours and high apparent V_{RMS} (between 0.6 and 1.4 m/s) in the low flow region in Figure 6.2.1.2.1 indicate the preponderance of velocity fluctuations present in the 400 µm round orifice jet flow field, even where the fluid should be relatively stagnant. This plot shows that the highest V_{RMS} is found in the core of the jet and has a peak value of approximately 2 m/s.

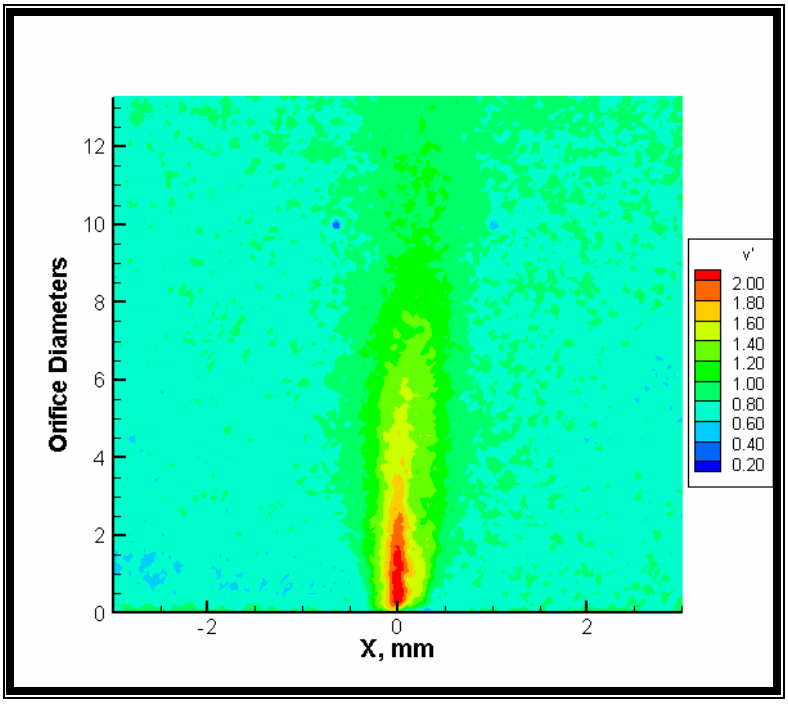

FIGURE 6.2.1.2.1. V_{RMS} field for the 400 µm round orifice jet. V_{RMS} units are m/s. V_{RMS} magnitudes are color coded according to the legend.

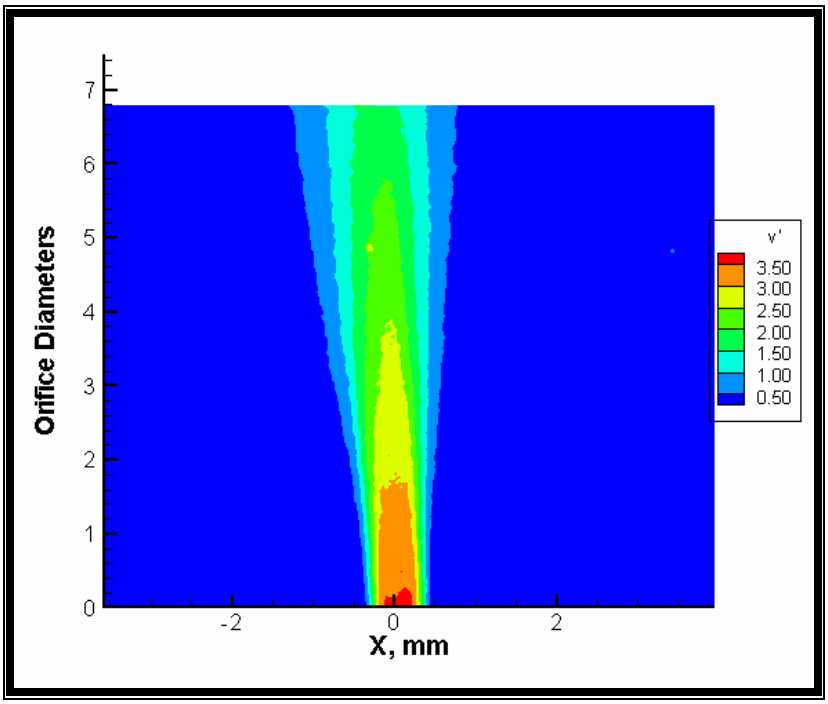

FIGURE 6.2.1.2.2. V_{RMS} field for the 800 µm round orifice jet. V_{RMS} units are m/s. V_{RMS} magnitudes are color coded according to the legend.

The V_{RMS} field for the 800 µm round orifice jet in Figure 6.2.1.2.2 is more homogenous with smoother contours. The highest V_{RMS} is still found in the core of the jet, but the peak value is roughly 1.75 times that for the 400 µm round orifice jet at 3.5 m/s. The V_{RMS} field for the 1200 µm round orifice jet in Figure 6.2.1.2.3 is slightly different from those for the smaller round jets. Instead of the peak V_{RMS} being concentrated in the jet core, they are on either side of the core near the orifice. In addition, the peak values are lower than they are for the 800 µm round orifice jet at 2.8 m/s.

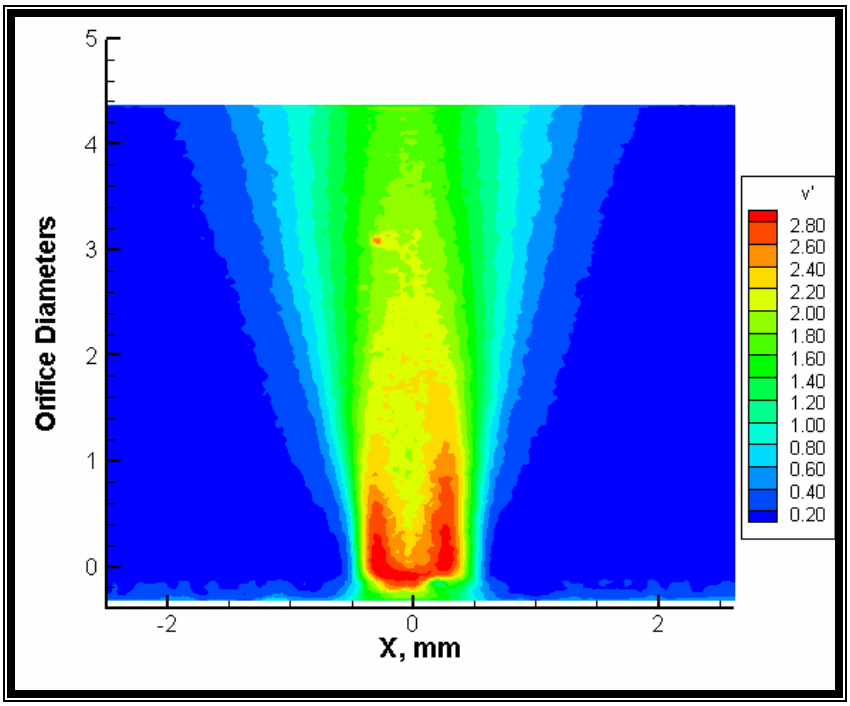

FIGURE 6.2.1.2.3. V_{RMS} field for the 1200 μm round orifice jet. V_{RMS} units are m/s. V_{RMS} magnitudes are color coded according to the legend.

6.2.1.3. Reynolds stress fields

The principal Reynold stress (PReS) fields corresponding to the jet average velocity fields presented in the previous section will be shown in this section. These plots give an indication of the velocity fluctuations that can cause blood element damage and/or platelet activation. The Reynolds stress fields for the 400, 800, and 1200 μm round orifice jets are shown in Figures 6.2.1.3.1, 6.2.1.3.2, and 6.2.1.3.3, respectively.

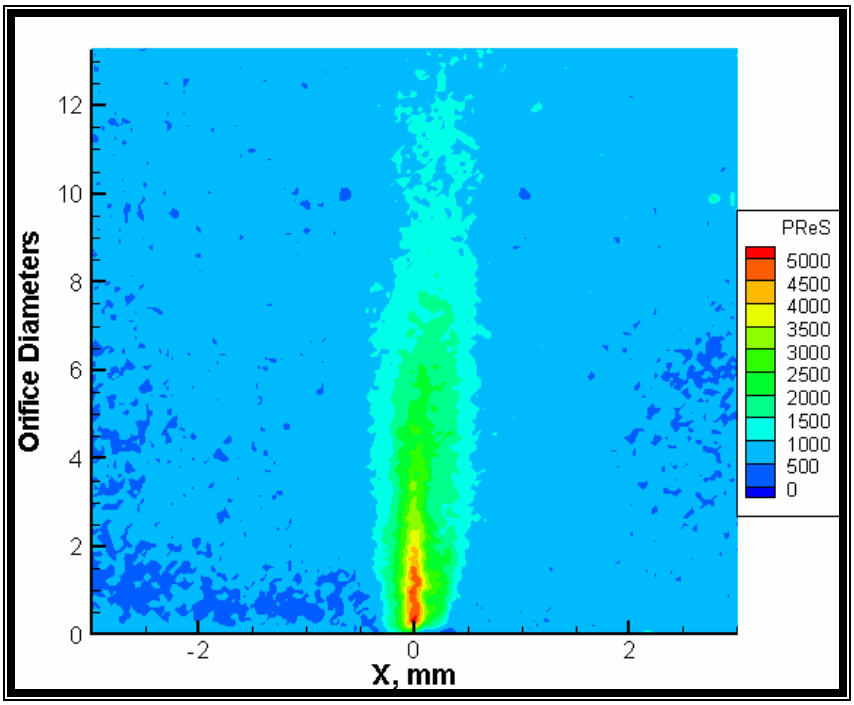

FIGURE 6.2.1.3.1. Principal Reynolds stress (PReS) field for the 400 µm round orifice jet. PReS units are dyn/cm^2. PRes magnitudes are color coded according to the legend.

The rough contours and high apparent PReS (approximately 1000 dyn/cm^2) in the low flow region in Figure 6.2.1.2.1 indicate the preponderance of velocity fluctuations present in the 400 µm round orifice jet flow field, even where the fluid should be relatively stagnant. This plot shows that the highest PReS is found in the core of the jet and has a peak value of approximately 5,000 dyn/cm^2. The PReS field for the 800 µm round orifice jet in Figure 6.2.1.2.2 is more homogenous with smoother contours. The highest PReS is still found in the core of the jet, but the peak value is roughly 3 times that for the 400 µm round orifice jet at 15,000 dyn/cm^2.

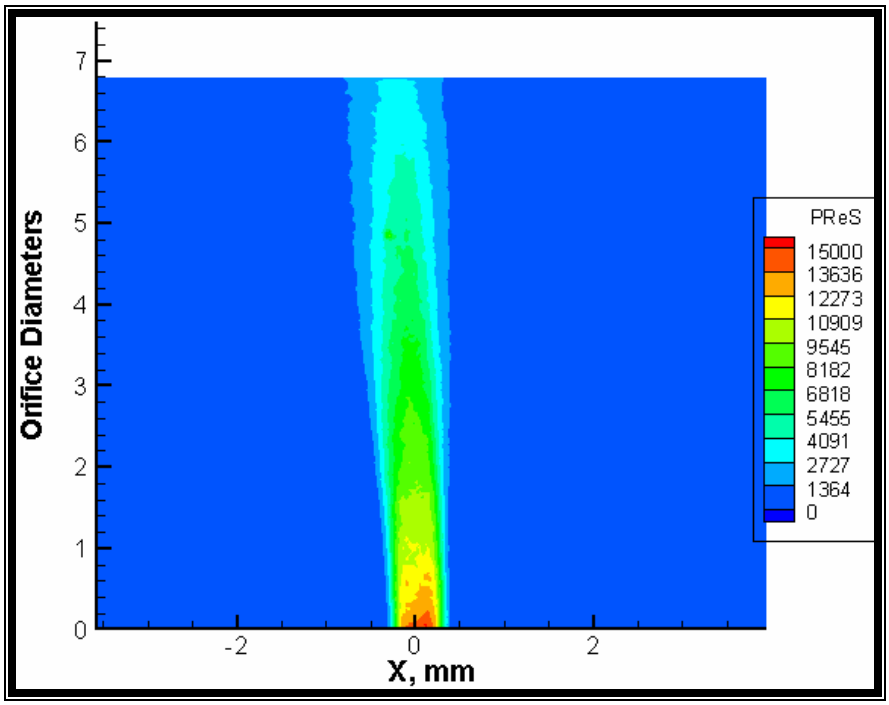

FIGURE 6.2.1.3.2. Principal Reynolds stress (PReS) field for the 800 µm round orifice jet. PReS units are dyn/cm^2. PRes magnitudes are color coded according to the legend.

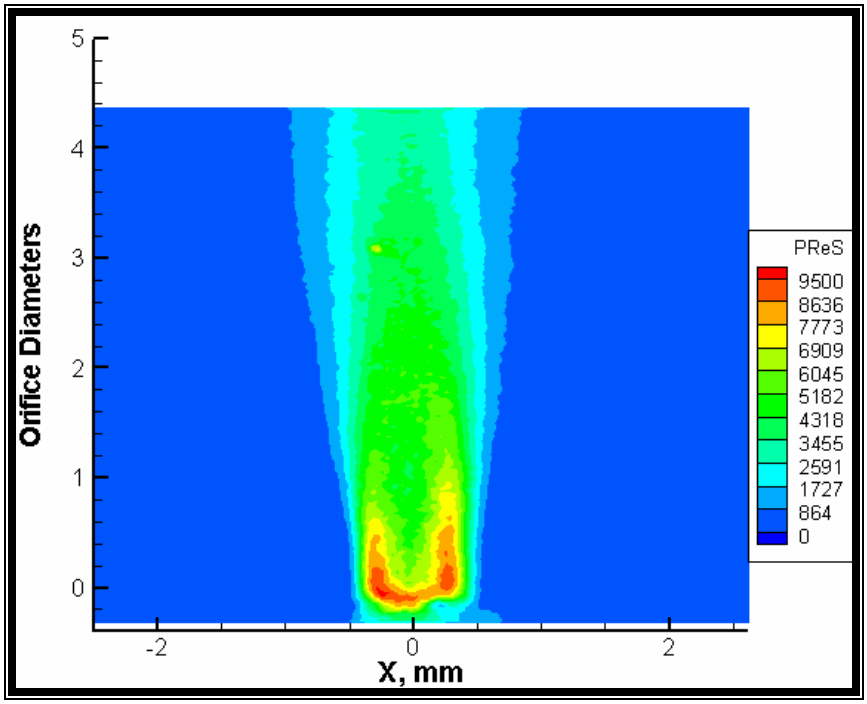

FIGURE 6.2.1.3.3. Principal Reynolds stress (PReS) field for the 1200 µm round orifice jet. PReS units are dyn/cm^2. PRes magnitudes are color coded according to the legend.

The PReS field for the 1200 μm round orifice jet in Figure 6.2.1.3.3 is slightly different from those for the smaller round jets. Instead of the peak PReS being concentrated in the jet core, they are on either side of the core near the orifice. In addition, the peak values are lower than they are for the 800 μm round orifice jet at 9,500 dyn/cm^2.

6.2.1.4. Shear stress fields

The shear stress (SS) fields corresponding to the jet average velocity fields presented in the previous section will be shown in this section. These plots give an indication of the magnitude of the velocity gradients between the different shear layers in the flow that can cause blood element damage and/or platelet activation. The shear stress fields for the 400, 800, and 1200 μm round orifice jets are shown in Figures 6.2.1.4.1, 6.2.1.4.2, and 6.2.1.4.3, respectively.

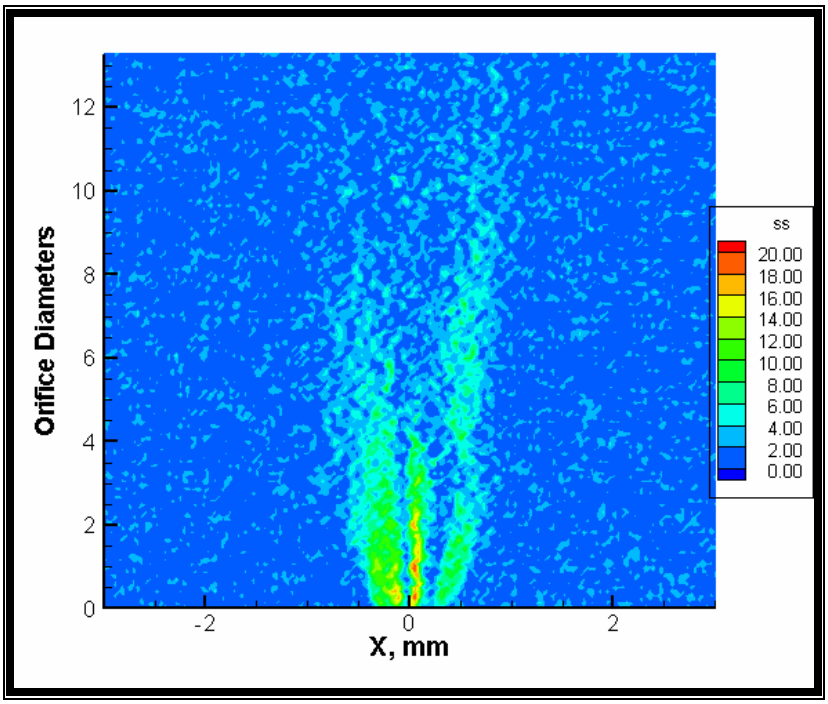

FIGURE 6.2.1.4.1. Shear stress (SS) field for the 400 μm round orifice jet. SS units are dyn/cm^2. SS magnitudes are color coded according to the legend.

Figure 6.2.1.4.1 shows that the highest SS is found on either side of the 400 µm round orifice jet core and has a peak value of approximately 20 dyn/cm^2. The location of these higher SS values coincides with the mixing of the higher velocity jet and the lower velocity recirculation regions near the orifice. Thus, these areas may be vulnerable to inducing platelet activation, and the subsequent recirculation may enable these activated platelets to aggregate.

The SS field for the 800 µm round orifice jet in Figure 6.2.1.4.2 is more homogenous than that for the 400 µm round orifice, and the low flow region has SS values at or near zero. The highest SS is still found on either side of the jet core, but they occur farther downstream of the orifice. Also, the peak value is somewhat higher than that for the 400 µm round orifice jet at 90 dyn/cm^2. respectively. The location of these higher SS values coincides with the mixing of the

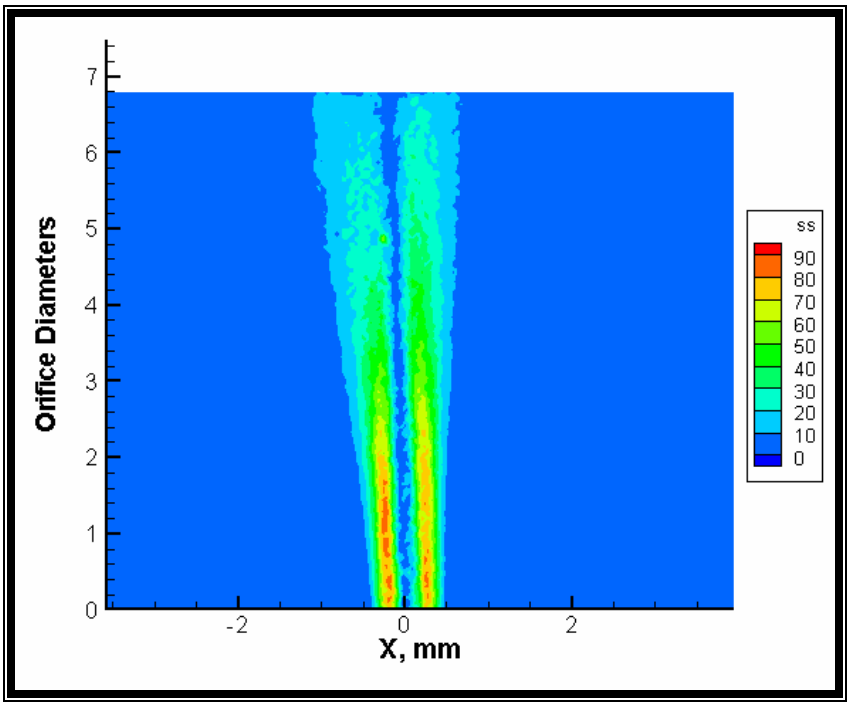

FIGURE 6.2.1.4.2. Shear stress (SS) field for the 800 µm round orifice jet. SS units are dyn/cm^2. SS magnitudes are color coded according to the legend.

The SS field for the 1200 µm round orifice in Figure 6.2.1.3.3 is similar to that for the 800 µm round orifice. However, the peak value for this orifice jet is lower than that for the 800 µm round orifice jet at 80 dyn/cm^2.

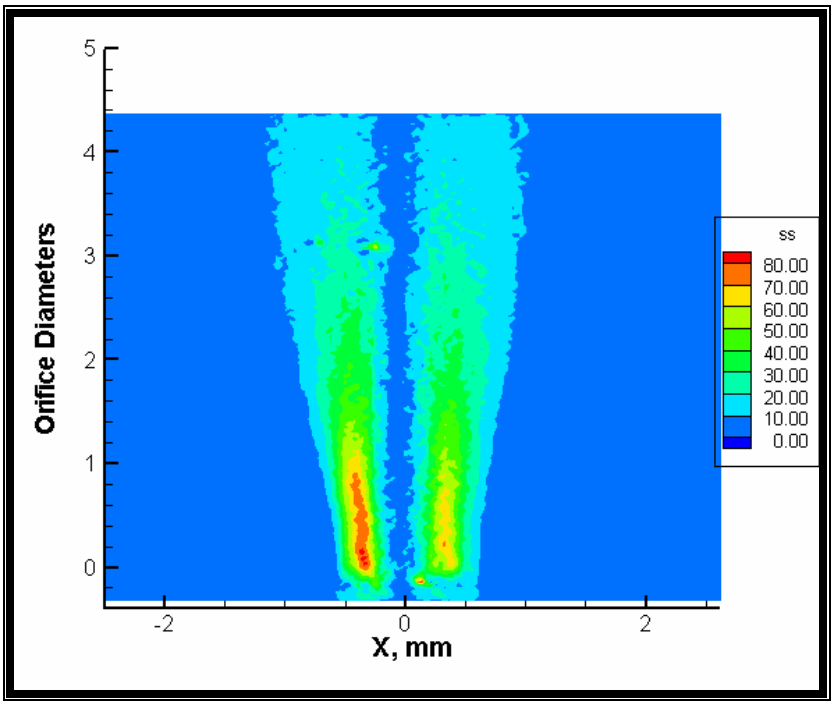

FIGURE 6.2.1.3.3. Shear stress (SS) field for the 1200 µm round orifice jet. SS units are dyn/cm^2. SS magnitudes are color coded according to the legend.

6.2.2. Slit orifice results

The PIV measurements for the slit orifices were taken only at the centerline of the narrow part of the orifice since this narrow cross-section is where the highest Reynolds stresses and shear stresses would be seen. These results are presented below.

6.2.2.1. Average velocity flow fields

The average velocity field for the 200 µm slit orifice with a pulse separation time of 10 µs is shown in Figure 6.2.2.1.1. This pulse separation allows for the tracking of the highest velocity particles that are entrapped in the orifice jet. This jet is similar to those

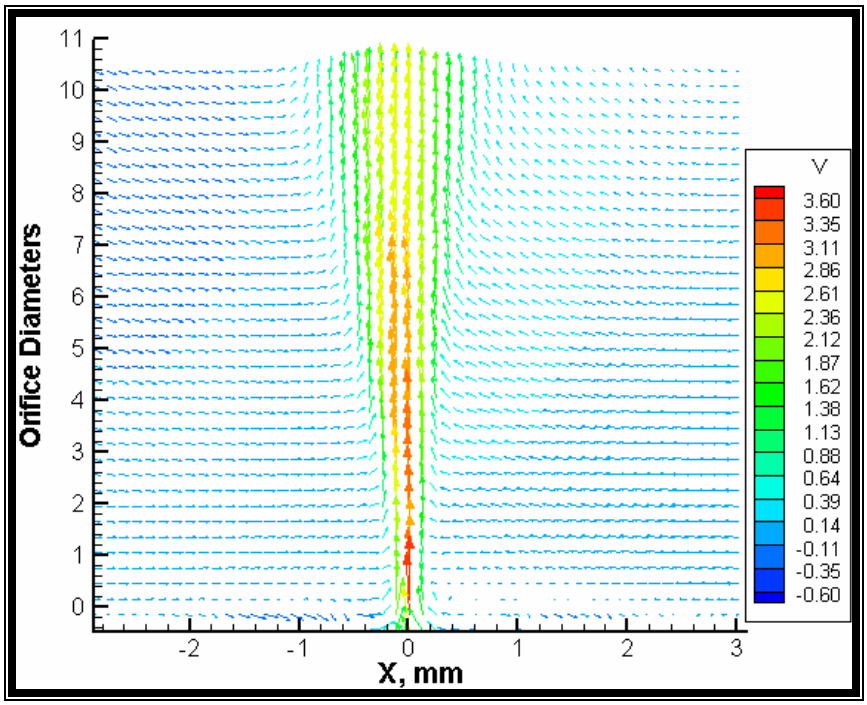

FIGURE 6.2.2.1.1. Average velocity vector field downstream of the 200 μm slit orifice. The pulse separation was 10 μs, and the vector plot is an average of 1000 image pairs. Velocity in m/s is color coded according to the legend.

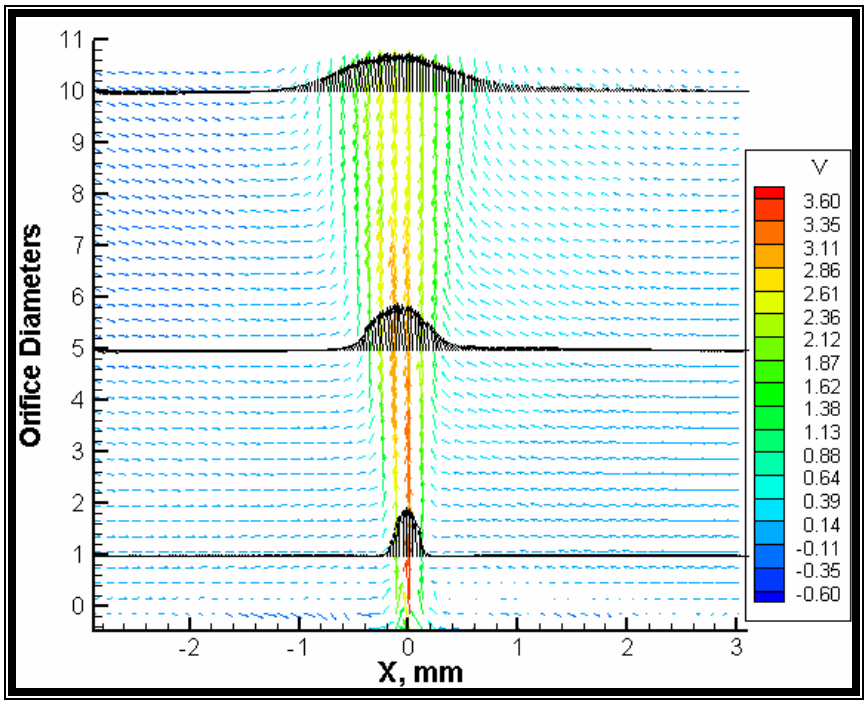

FIGURE 6.2.2.1.2. Flow profiles at 1, 5, and 10 hydraulic diameters downstream of the 200 μm slit orifice. The pulse separation was 10 μs, and the vector plot is an average of 1000 image pairs. Velocity in m/s is color coded according to the legend.

for the 800 and 1200 μm round orifice except that the flow profiles downstream of the jet shown in Figure 6.2.2.1.2 appear to broaden out more quickly than those for the round orifice jets. However, using the hydraulic diameter of 400 μm to characterize the number of diameters downstream of the jet shows that the flow profile at 10 hydraulic diameters downstream still has a Gaussian profile indicating that it has not dissipated.

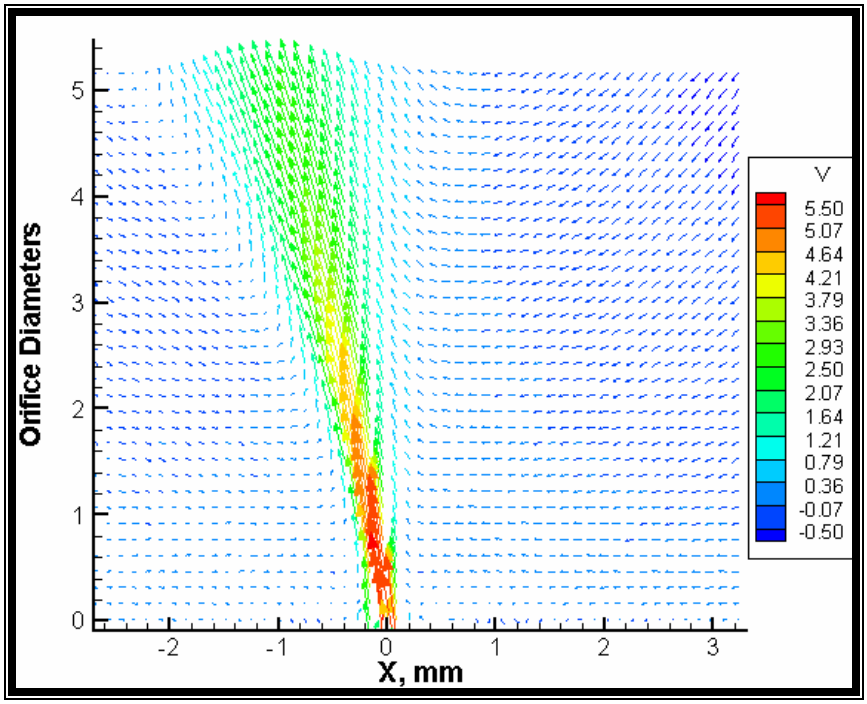

FIGURE 6.2.2.1.3. Average velocity vector field downstream of the 400 μm slit orifice. The pulse separation was 10 μs, and the vector plot is an average of 1000 image pairs. Velocity in m/s is color coded according to the legend.

The average velocity field for the 400 μm slit shown in Figure 6.2.2.1.3 is similar to that for the 200 μm slit orifice except that it is significantly skewed to one side of the chamber. The initial skewing is most likely due to the orifice chamber not being level relative to the camera, but the progressive skewing may be due to excessive curvature of the inlet tubing. Despite the skewing of the jet, comparisons between this and the other jets can still be made. The peak velocity in this jet is approximately 35% higher than that

for the 200 μm slit orifice jet at 5.5 m/s. Similar recirculation regions are present, and this jet also appears to broaden quickly as it progresses downstream of the orifice. Figure 6.2.2.1.4 show the flow profiles at 1, 3 and 5 hydraulic diameters downstream of the orifice. This plot indicates that at 5 diameters downstream of the orifice, the profile is almost the same as that 10 diameters downstream of the 200 μm slit orifice. Thus, this jet appears to dissipate more rapidly than the narrower jet. This dissipation may be due to the higher velocity recirculation regions for the 400 μm slit orifice jet which had a peak reverse velocity of -0.5 m/s compared to -0.35 for the 200 μm slit orifice jet.

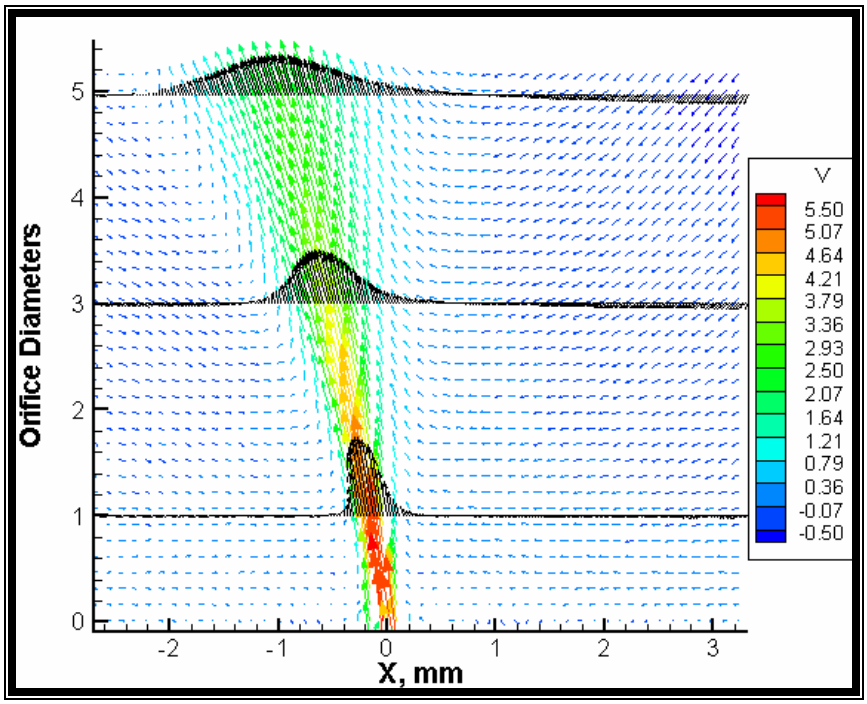

FIGURE 6.2.2.1.4. Flow profiles at 1, 3, and 5 hydraulic diameters downstream of the 400 μm slit orifice. The pulse separation was 10 μs, and the vector plot is an average of 1000 image pairs. Velocity in m/s is color coded according to the legend.

The average velocity field for the 800 μm slit shown in Figure 6.2.2.1.5 is similar to that for the other slit orifice jets. The peak velocity of 4.8 m/s falls between those for the other two slit orifice jets, and the flow profiles shown in Figure 6.2.2.1.6 broaden

quickly as the jet flows downstream of the orifice indicating rapid dissipation. The more rapid dissipation of the slit orifice jets into the bulk flow as compared to the round orifice jets is most likely due to the narrowing of the chamber downstream of the orifice plate. Since the slit orifice jet is much wider in one direction than in the other, and this width is

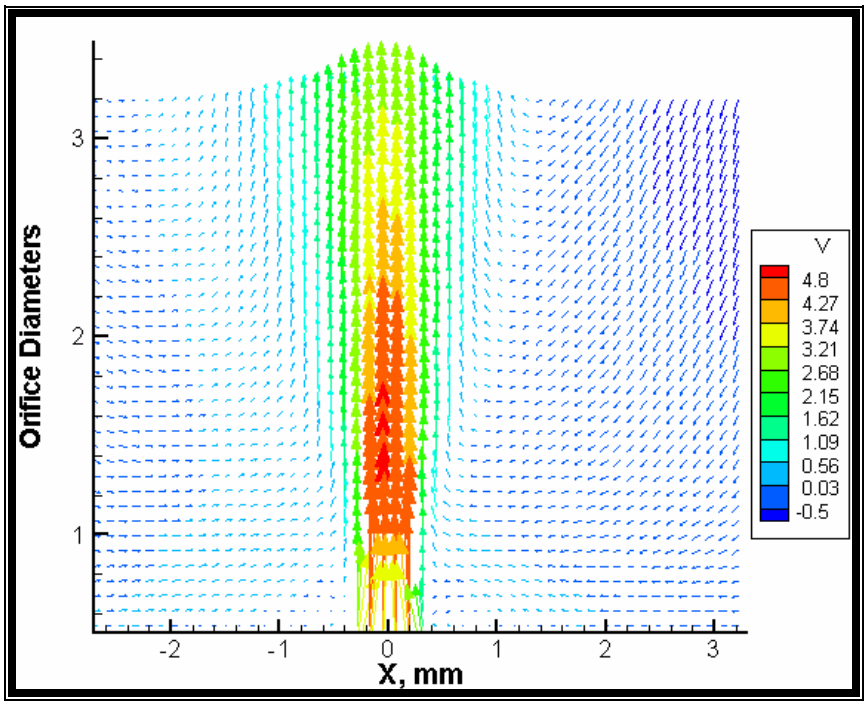

FIGURE 6.2.2.1.5. Average velocity vector field downstream of the 800 μm slit orifice. The pulse separation was 10 μs, and the vector plot is an average of 1000 image pairs. Velocity in m/s is color coded according to the legend.

wider than the neck of the chamber, the jet flow impinges on the chamber wall inducing high velocity recirculation regions. In contrast, the recirculation regions for the round orifice have a maximum reverse velocity of -0.18 m/s. These higher velocity recirculation regions dissipate the jet more rapidly as well as transport activated platelets away from the orifice plate before they can aggregate.

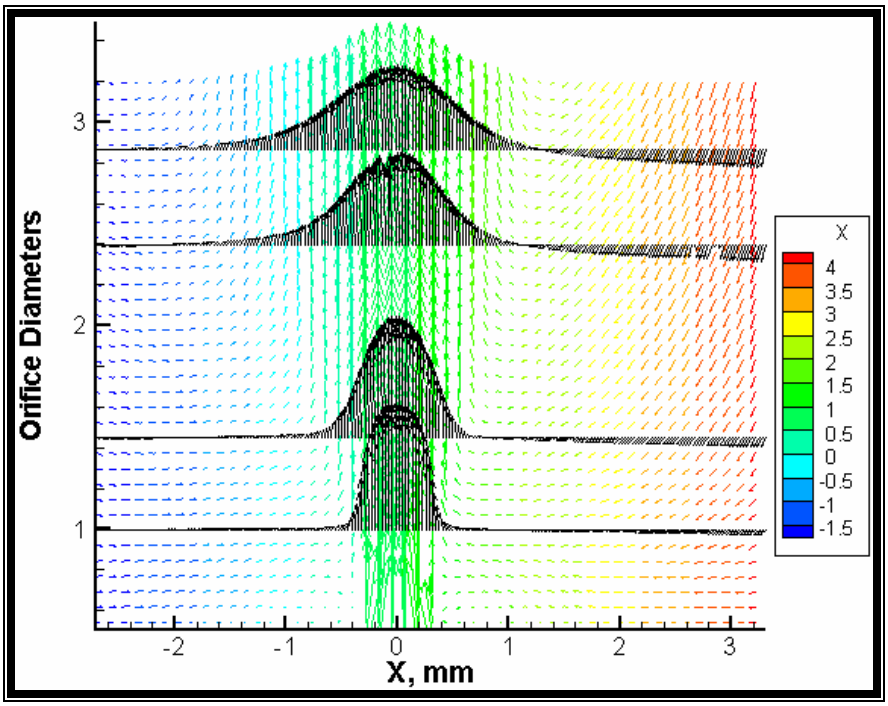

FIGURE 6.2.2.1.6. Flow profiles at 0.5, 1, 2, and 2.5 hydraulic diameters downstream of the 800 μm slit orifice. The pulse separation was 10 μs, and the vector plot is an average of 1000 image pairs. Velocity in m/s is color coded according to the legend.

6.2.2.2. V_{RMS} fields

The V_{RMS} fields corresponding to the jet average velocity fields presented in the previous section will be shown in this section. These plots show the magnitude of the velocity fluctuations present in the jets. The V_{RMS} fields for the 200, 400, and 800 μm slit orifice jets are shown in Figures 6.2.2.2.1, 6.2.2.2.2, and 6.2.2.2.3, respectively. Figure 6.2.2.2.1 shows that the highest V_{RMS} values are found in the core of the 200 μm slit orifice jet near the orifice and has a peak value of approximately 3.4 m/s. This peak value is as high as those for the 800 and 1200 μm round orifices. However, unlike the round orifice jets, these V_{RMS} values decay rapidly, which corresponds to the rapid dissipation evident in the average velocity fields presented in the previous section.

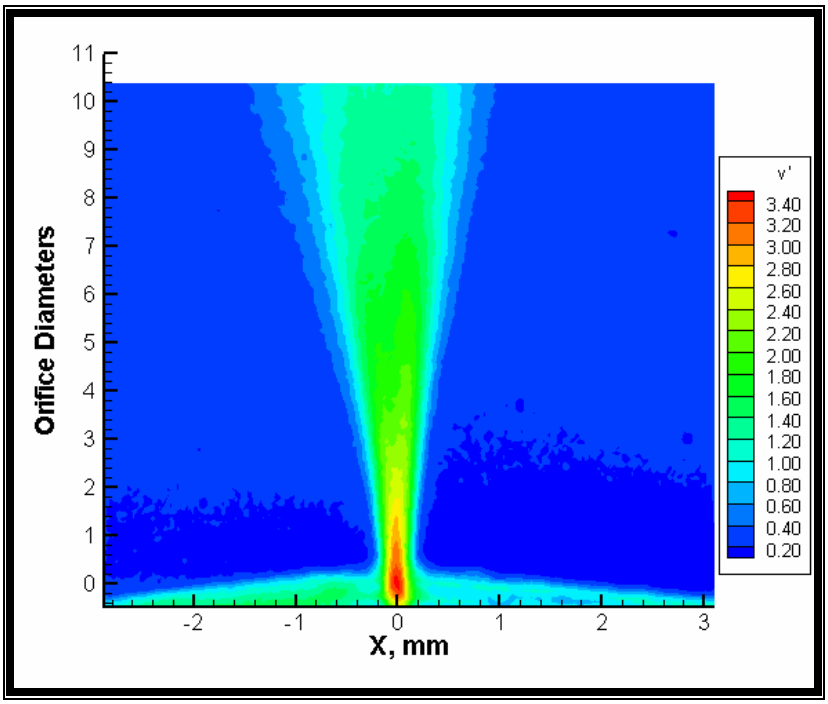

FIGURE 6.2.2.2.1. V_{RMS} field for the 200 μm slit orifice jet. V_{RMS} units are m/s. V_{RMS} magnitudes are color coded according to the legend.

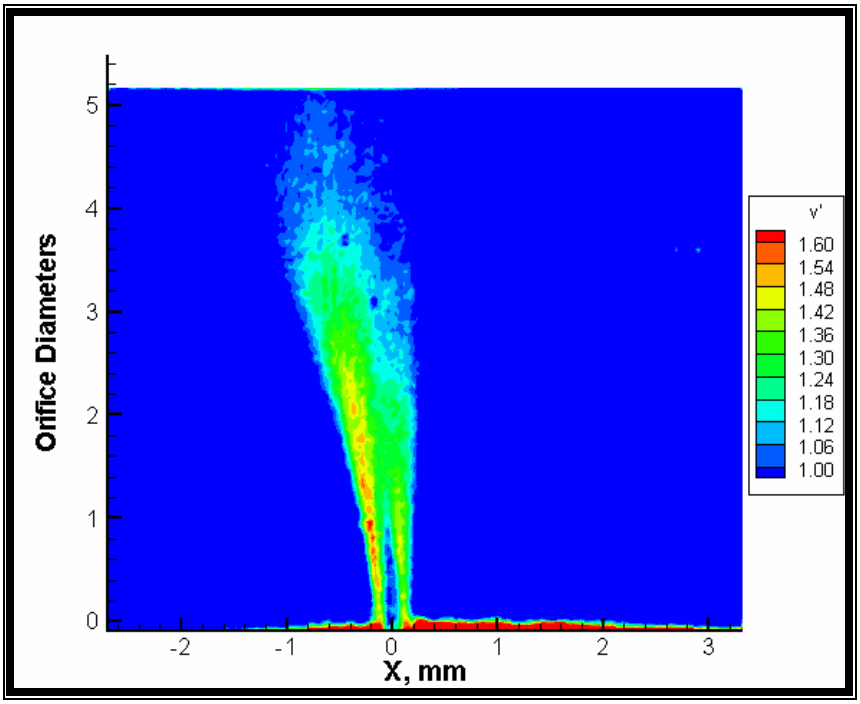

FIGURE 6.2.2.2.2. V_{RMS} field for the 400 μm slit orifice jet. V_{RMS} units are m/s. V_{RMS} magnitudes are color coded according to the legend.

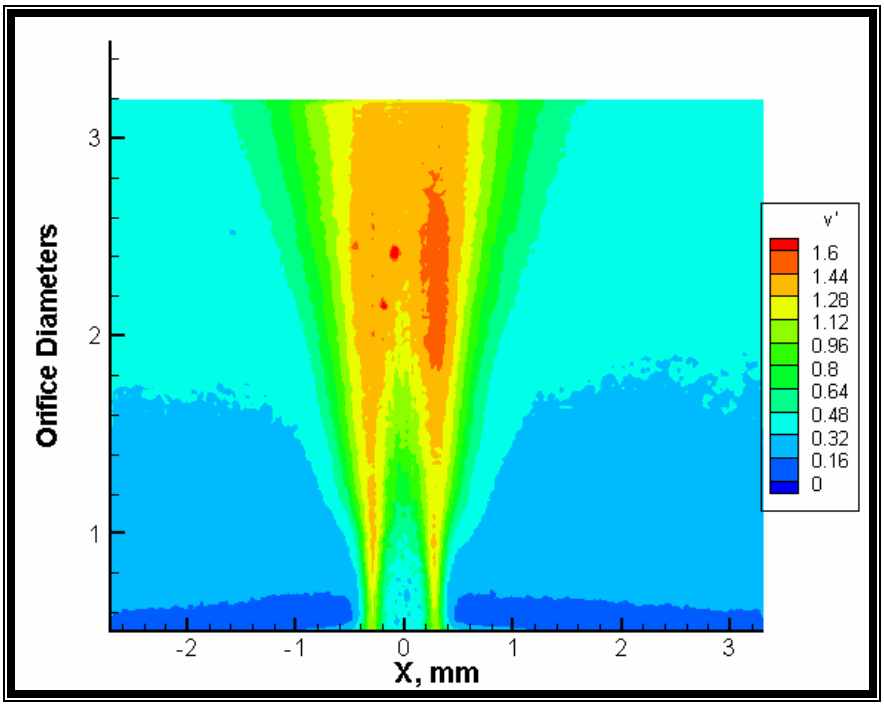

FIGURE 6.2.1.2.3. V_{RMS} field for the 800 µm slit orifice jet. V_{RMS} units are m/s. V_{RMS} magnitudes are color coded according to the legend.

The V_{RMS} field for the 400 µm slit orifice jet in Figure 6.2.2.2.2 is skewed in the same manner as the velocity field. The highest V_{RMS} is found on one side of the jet with a peak value of only 1.6 m/s. The V_{RMS} field for the 800 µm slit orifice jet in Figure 6.2.2.2.3 is more homogenous than that for the 400 µm slit orifice. The peak PReS values are located symmetrically on either side of the jet core downstream of the orifice. The peak values are also approximately 1.6 m/s. However, relatively high V_{RMS} values (0.5 m/s) extend out to the edges of the measurement plane.

6.2.2.3. Reynolds stress fields

The principal Reynold stress (PReS) fields corresponding to the jet average velocity fields presented in the previous section will be shown in this section. These plots give an indication of the velocity fluctuations that can cause blood element damage

and/or platelet activation. The Reynolds stress fields for the 200, 400, and 800 µm round orifice jets are shown in Figures 6.2.2.3.1, 6.2.2.3.2, and 6.2.2.3.3, respectively.

Figure 6.2.2.3.1 shows that the highest PReS is found in the core of the 200 µm slit orifice jet near the orifice and has a peak value of approximately 12,500 dyn/cm^2. This peak value is somewhat less than that for the 800 µm round orifice. However, unlike the round orifice jets, these PReS values decay rapidly, which corresponds to the rapid dissipation evident in the average velocity fields in the previous section.

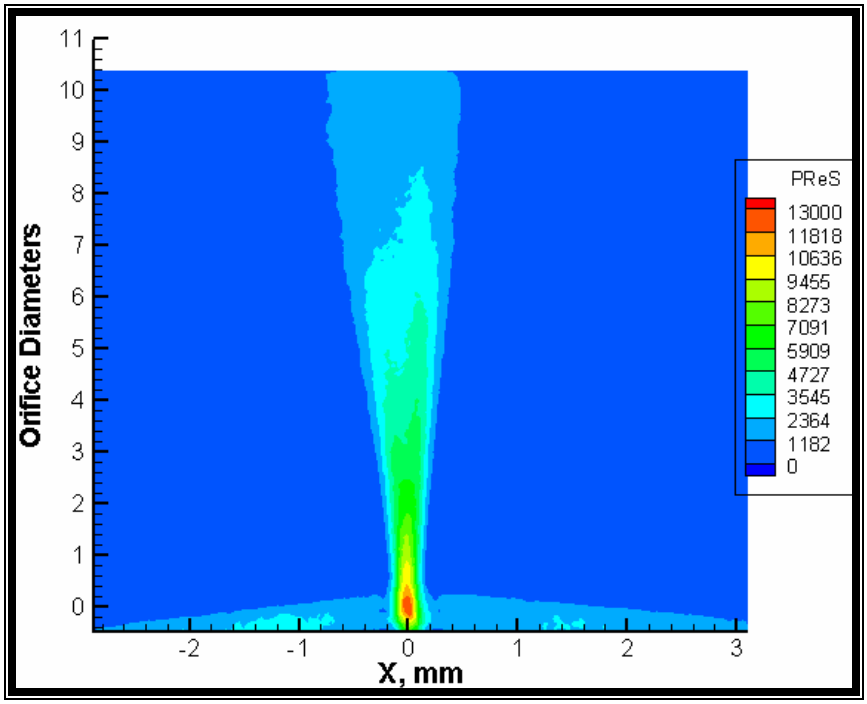

FIGURE 6.2.2.3.1. Principal Reynolds stress (PReS) field for the 200 µm slit orifice jet. PReS units are dyn/cm^2. PRes magnitudes are color coded according to the legend.

The PReS field for the 400 µm slit orifice jet in Figure 6.2.2.3.2 is skewed and has relatively high PReS values in the low flow region between 750 and 1000 dyn/cm^2 with rough contours and asymmetry. The highest PReS is found on only one side of the jet with a peak value of only 3000 dyn/cm^2. The PReS field for the 800 µm slit orifice jet in Figure 6.2.2.3.3 is more homogenous than that for the 400 µm slit orifice. The peak PReS

values are located symmetrically on either side of the jet core downstream of the orifice. The peak values are also approximately 3000 dyn/cm^2.

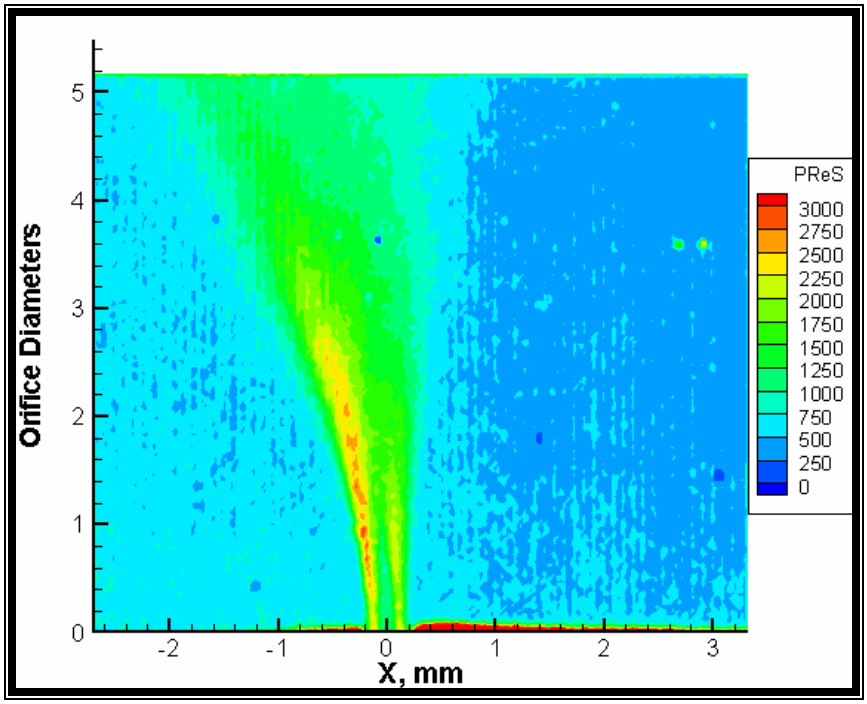

FIGURE 6.2.2.3.2. Principal Reynolds stress (PReS) field for the 400 µm slit orifice jet. PReS units are dyn/cm^2. PRes magnitudes are color coded according to the legend.

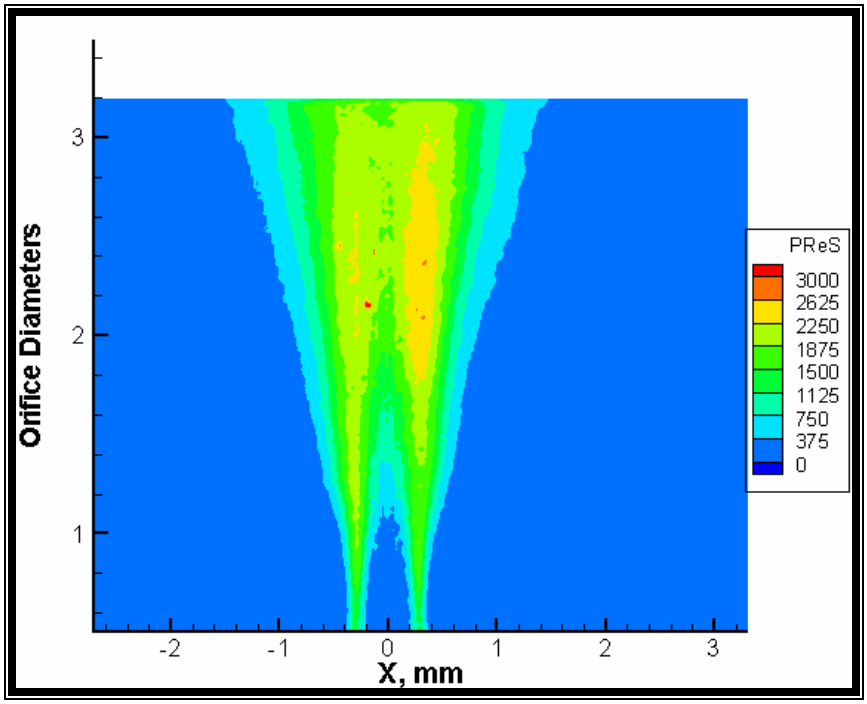

FIGURE 6.2.2.3.3. Principal Reynolds stress (PReS) field for the 800 µm slit orifice jet. PReS units are dyn/cm^2. PRes magnitudes are color coded according to the legend.

6.2.2.4. Shear stress fields

The shear stress (SS) fields corresponding to the jet average velocity fields presented in the previous section are shown in this section. These plots give an indication of the magnitude of the velocity gradients between the different shear layers in the flow that can cause blood element damage and/or platelet activation. The shear stress fields for the 200, 400, and 800 μm slit orifice jets are shown in Figures 6.2.2.4.1, 6.2.2.4.2, and 6.2.2.4.3, respectively. Figures 6.2.2.4.1 shows that the highest SS levels for the 200 μm slit orifice jet are found on either side of the jet core and have peak values of approximately 75 dyn/cm^2. The location of these higher SS values coincides with the mixing of the higher velocity jet and the lower velocity recirculation regions near the orifice. The SS field for the 400 μm slit orifice jet in Figure 6.2.2.4.2 is skewed but like the 200 μm slit orifice, the highest SS values are still found on either side of the jet core. However, the peak SS values on either side of this jet are 140 and 180 dyn/cm^2. This inequality in the magnitude of these SS values indicates that the skewing of the jet induces more interaction between the shear layers on the side that the jet is leaning towards. The SS field for the 800 μm slit orifice in Figure 6.2.2.4.3 is similar to that for the other slit orifices. However, the peak SS values have moved farther downstream of the orifice, which corresponds approximately to the same amount of hydraulic diameters downstream of the orifice as the other slit orifices. The peak SS values are about 130 dyn/cm^2. For all of the slit orifice jets, the location of the higher SS values coincides with the mixing of the higher velocity jet and the lower velocity recirculation regions as the jet begins to dissipate downstream of the orifice. The main difference between SS fields for the slit orifice jets and the round orifice jets is that the high SS regions for the slit orifice

jets diverge more than those for the round orifice jets, which corresponds to the more rapid broadening of the flow profiles downstream of the slit orifices.

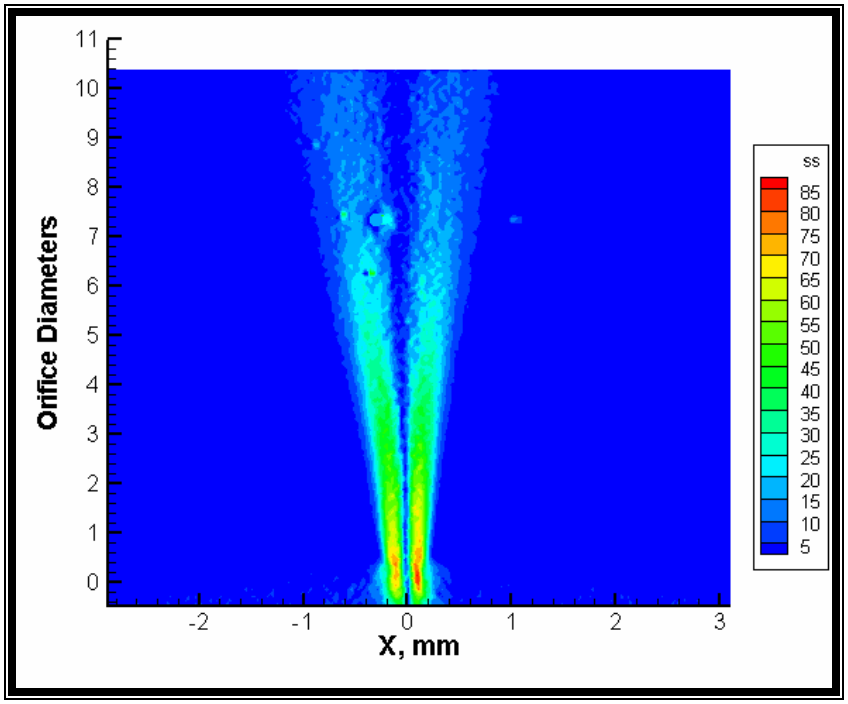

FIGURE 6.2.2.4.1. Shear stress (SS) field for the 200 μm slit orifice jet. SS units are dyn/cm^2. SS magnitudes are color coded according to the legend.

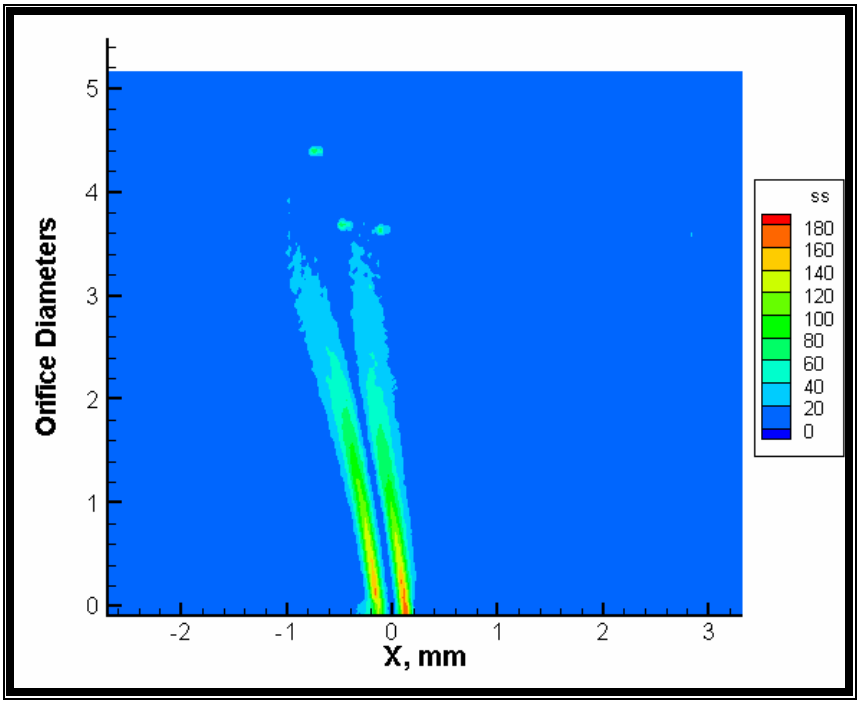

FIGURE 6.2.2.4.2. Shear stress (SS) field for the 400 μm slit orifice jet. SS units are dyn/cm^2. SS magnitudes are color coded according to the legend.

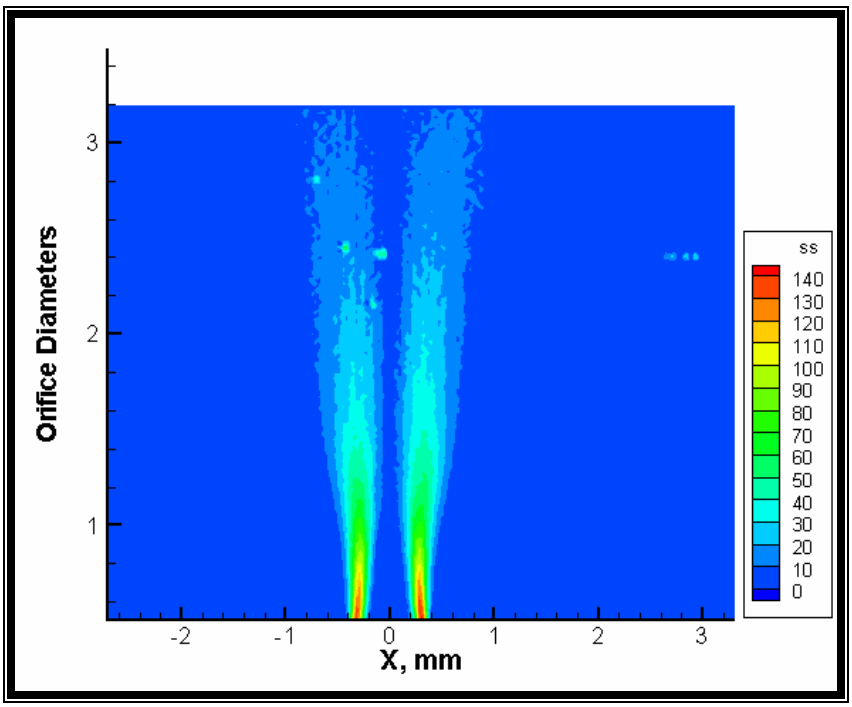

FIGURE 6.2.2.4.3. Shear stress (SS) field for the 800 μm slit orifice jet. SS units are dyn/cm^2. SS magnitudes are color coded according to the legend.

6.2.3. Channel results

PIV was not performed with the channels with a smallest diameter of 400 μm because the seed particles aggregated and occluded the orifice. Thus, the following section includes PIV data only for Channels 2, 4, 6, and 8 (minimum diameter of 800 μm).

6.2.3.1. Average velocity flow fields

The average velocity field for Channel 2 with a pulse separation time of 10 μs is shown in Figure 6.2.3.1.1. The flow field looks similar to that for the 800 μm round orifice with the same peak velocity of 6 m/s. Figure 6.2.3.1.2 shows the velocity profiles at 1, 3, 5, and 7 diameters downstream of Channel 2. These flow profiles show the decay of the jet as the flow moves downstream of the orifice. Since the field of view does not

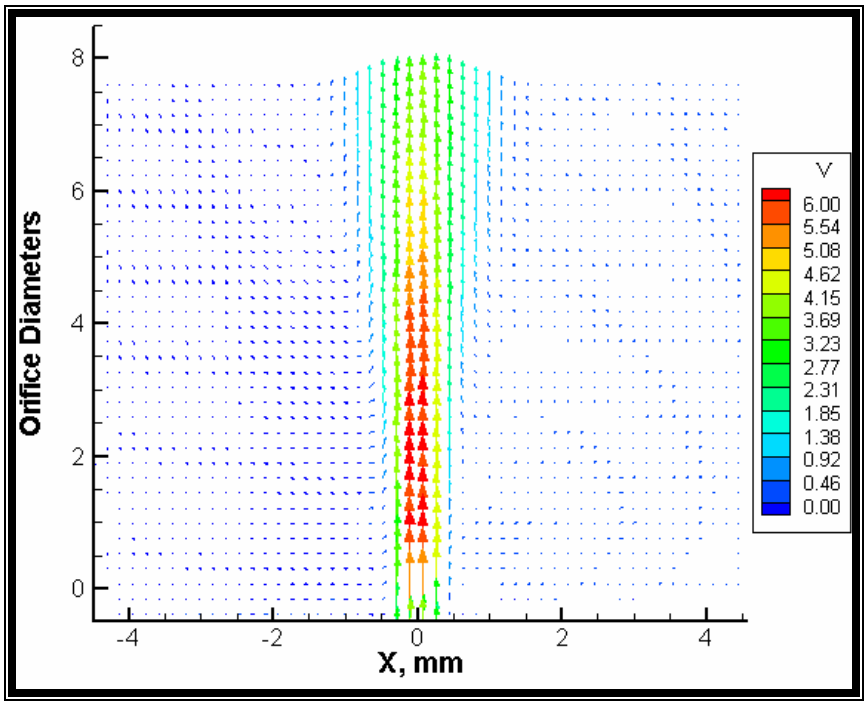

FIGURE 6.2.3.1.1. Average velocity vector field downstream of Channel 2. The pulse separation was 10 μs, and the vector plot is an average of 1000 image pairs. Velocity in m/s is color coded according to the legend.

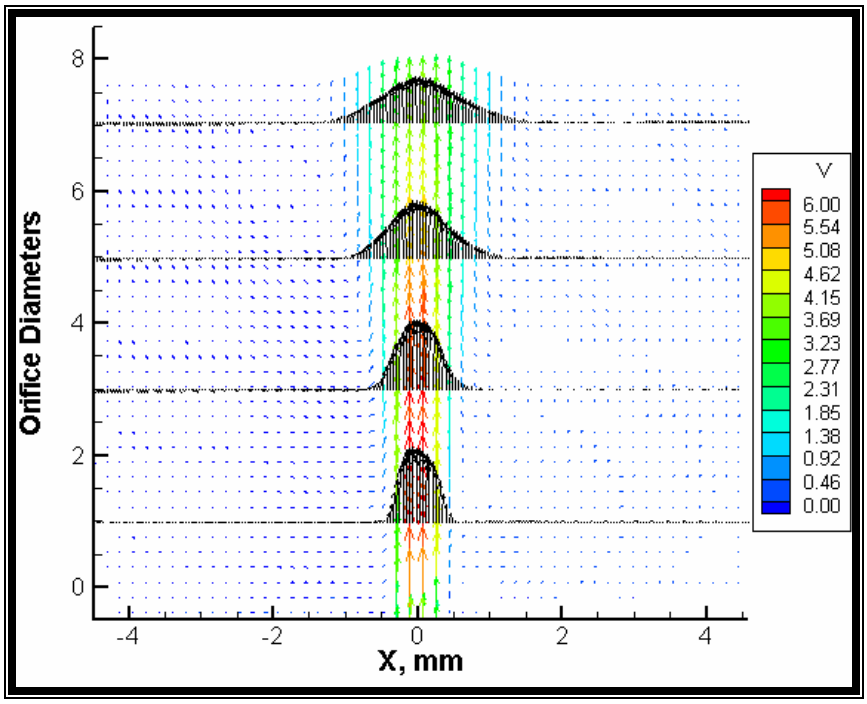

FIGURE 6.2.3.1.2. Flow profiles at 1, 3, 5, and 7 diameters downstream of Channel 2. The pulse separation was 10 μs, and and the vector plot is an average of 1000 image pairs. Velocity in m/s is color coded according to the legend.

extend beyond 7 diameters, the fully developed, self-similar, jet profile cannot be seen in this plot. However, it is evident from this plot that the profile flattens out very quickly indicating that the jet dissipates very rapidly. These jet profiles appear to be similar to those for the 800 μm round orifice.

The average velocity field for Channel 4 with a pulse separation time of 10 μs is shown in Figure 6.2.3.1.3. The flow field also looks similar to that for the 800 μm round

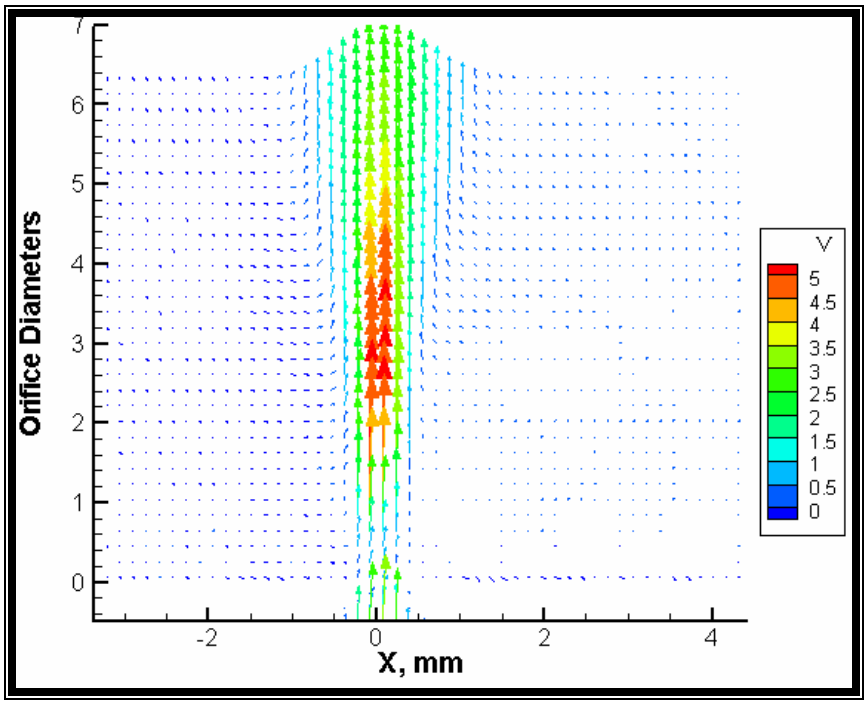

FIGURE 6.2.3.1.3. Average velocity vector field downstream of Channel 4. The pulse separation was 10 μs, and the vector plot is an average of 1000 image pairs. Velocity in m/s is color coded according to the legend.

orifice except that the peak velocity of 5 m/s is somewhat lower. This decrease corresponds to the lower flow rate through Channel 4 that may be due to the more abrupt geometry of Channel 4. Figure 6.2.3.1.4 shows the velocity profiles at 1, 3, and 6 diameters downstream of Channel 4. These flow profiles show the decay of the jet as the flow moves downstream of the orifice. Since the field of view does not extend beyond 6 diameters, the fully developed, self-similar, jet profile cannot be seen in this plot.

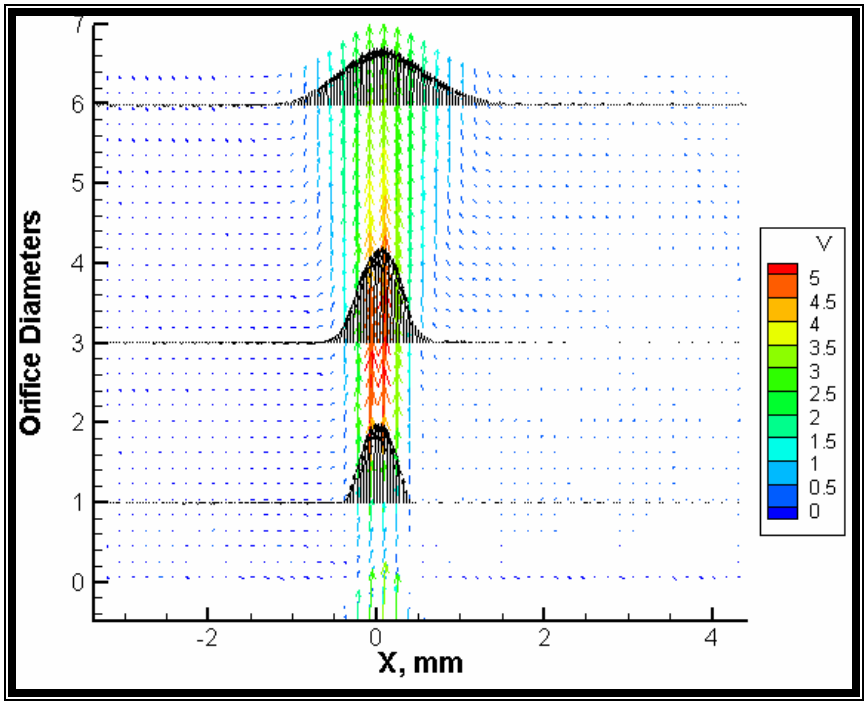

FIGURE 6.2.3.1.4. Flow profiles at 1, 3, and 6 diameters downstream of Channel 4. The pulse separation was 10 μs, and the vector plot is an average of 1000 image pairs. Velocity in m/s is color coded according to the legend.

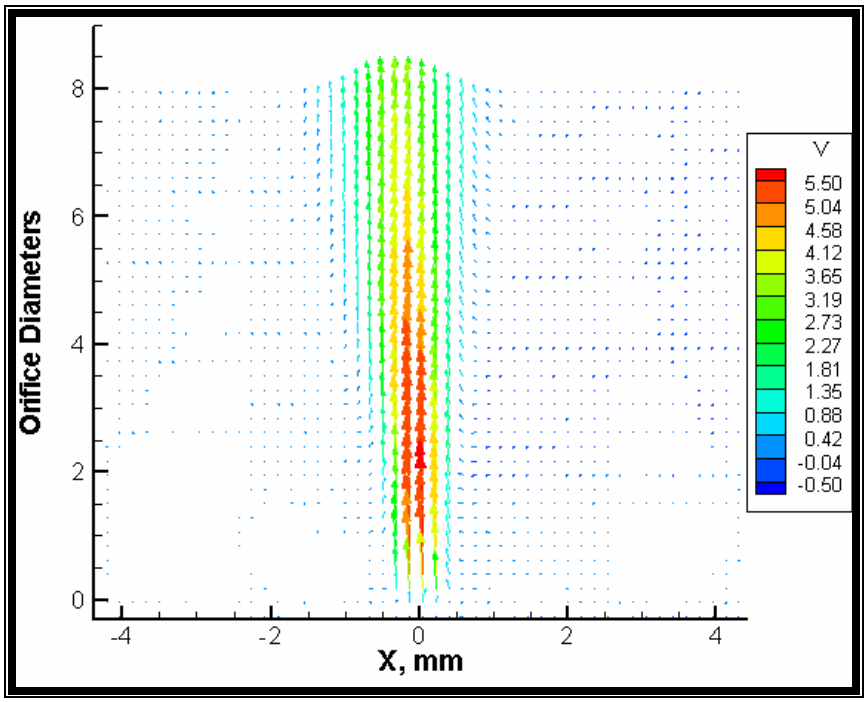

FIGURE 6.2.3.1.5. Average velocity vector field downstream of Channel 6. The pulse separation was 10 μs, and the vector plot is an average of 1000 image pairs. Velocity in m/s is color coded according to the legend.

However, it is evident from this plot that the profile flattens out very quickly indicating that the jet dissipates very rapidly. These jet profiles appear to flatten out more quickly than those for the 800 μm round orifice and Channel 2, which may indicate that the Channel 4 jet dissipates more rapidly, perhaps because of the lower core velocity.

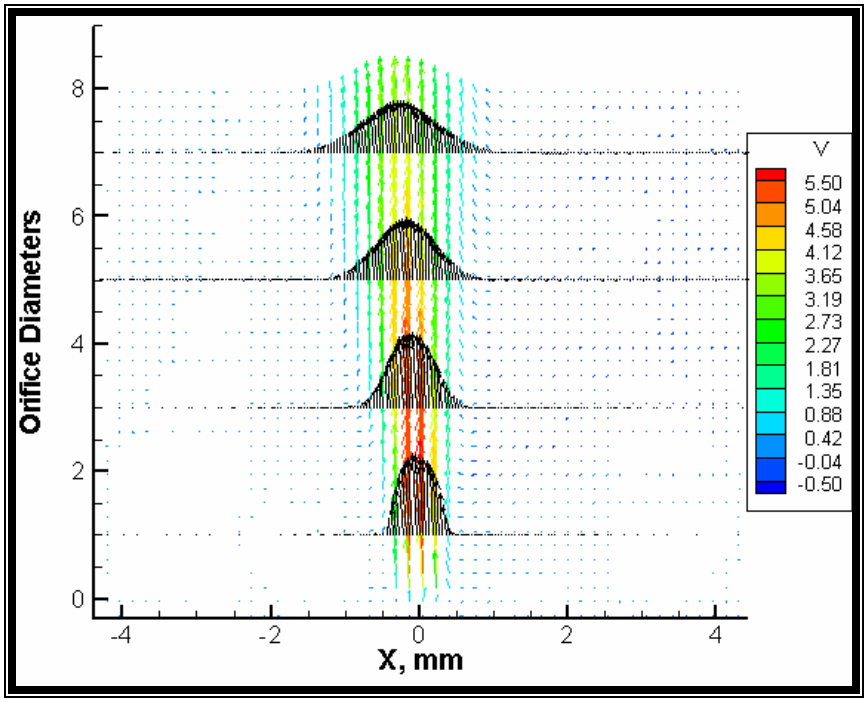

FIGURE 6.2.3.1.6. Flow profiles at 1, 3, 5, and 7 diameters downstream of Channel 6. The pulse separation was 10 μs, and the vector plot is an average of 1000 image pairs. Velocity in m/s is color coded according to the legend.

The average velocity field for Channel 6 with a pulse separation time of 10 μs is shown in Figure 6.2.3.1.5. The flow field looks similar to that for the 800 μm round orifice with a same peak velocity of 5.5 m/s, which is between that of Channels 2 and 4. Figure 6.2.3.1.6 shows the velocity profiles at 1, 3, 5, and 7 diameters downstream of Channel 6. These flow profiles show the decay of the jet as the flow moves downstream of the orifice. Since the field of view does not extend beyond 7 diameters, the fully developed, self-similar, jet profile cannot be seen in this plot. However, it is evident from

this plot that the profile flattens out very quickly indicating that the jet dissipates very rapidly. These jet profiles appear to be similar to those for the 800 µm round orifice and Channel 2.

The average velocity field for Channel 8 with a pulse separation time of 10 µs is shown in Figure 6.2.3.1.7. The flow field spreads out much more quickly than that for any of the other channels or for the 800 µm round orifice. Additionally, the peak velocity of 3.6 m/s is lower than that for the Channels 2 and 6, which have a smoother geometry, and for the 800 µm round orifice. It is also lower than that for Channel 4, which has a larger exterior diameter compared to the larger internal diameter of Channel 8. This larger internal diameter may influence the jet flow due to recirculation regions inside the channel. The jet is also skewed, which may indicate that the chamber was not level relative to the camera.

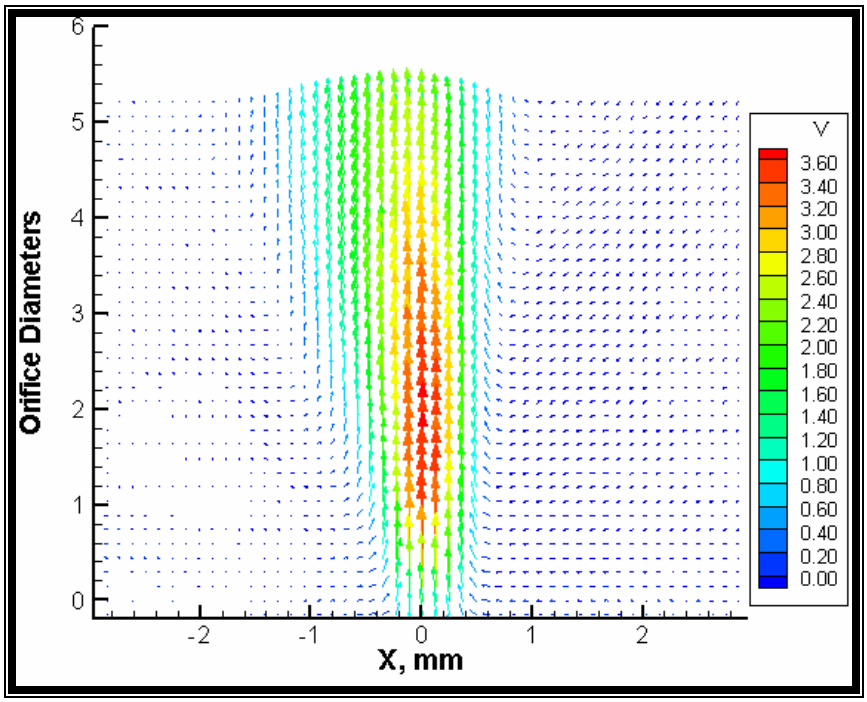

FIGURE 6.2.3.1.7. Average velocity vector field downstream of Channel 8. The pulse separation was 10 µs, and the vector plot is an average of 1000 image pairs. Velocity in m/s is color coded according to the legend.

Figure 6.2.3.1.8 shows the velocity profiles at 1, 3, 5 diameters downstream of Channel 8. These flow profiles show the decay of the jet as the flow moves downstream of the orifice. Since the field of view does not extend beyond 5 diameters, the fully developed, self-similar, jet profile cannot be seen in this plot. However, it is evident from this plot that the profile flattens out very quickly indicating that the jet dissipates very rapidly. These jet profiles appear flatten out more quickly than those for the other channels or the 800 μm round orifice. The Channel 8 jet may dissipate more quickly because of the lower velocity and recirculation regions inside the channel.

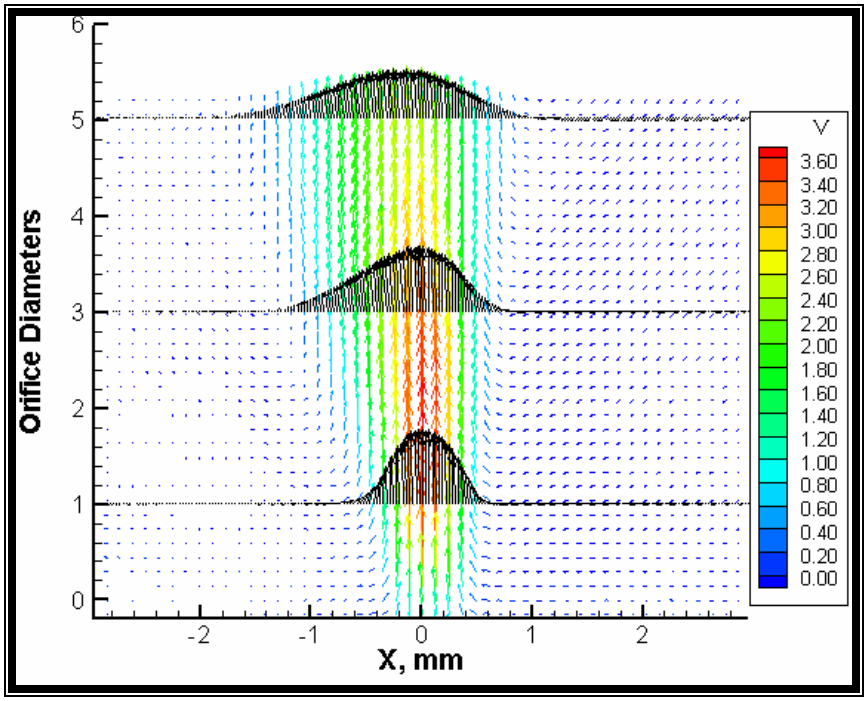

FIGURE 6.2.3.1.8. Flow profiles at 1, 3, and 5 diameters downstream of Channel 8. The pulse separation was 10 μs, and the vector plot is an average of 1000 image pairs. Velocity in m/s is color coded according to the legend.

6.2.3.2. V_{RMS} fields

The V_{RMS} fields corresponding to the channel jet average velocity fields presented in the previous section will be shown in this section. These plots show the magnitude of

the velocity fluctuations present in the jets. The V_{RMS} for the Channel 2, 4, 6, and 8 jets are shown in Figures 6.2.3.2.1, 6.2.3.2.2, 6.2.3.2.3 and 6.2.3.2.4, respectively.

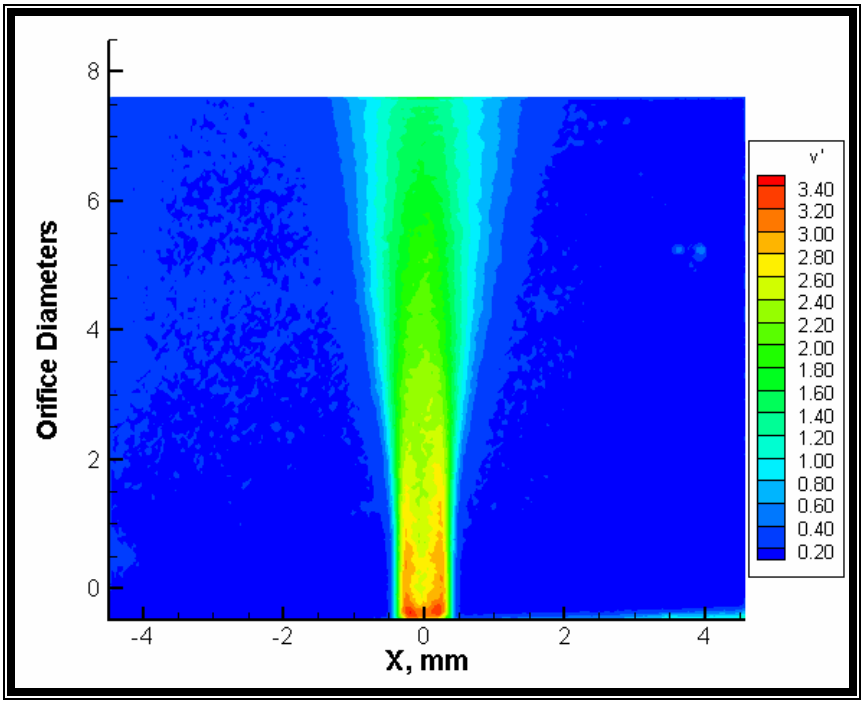

FIGURE 6.2.3.2.1. V_{RMS} field for the Channel 2 jet. V_{RMS} units are m/s. V_{RMS} magnitudes are color coded according to the legend.

The Channel 2 jet V_{RMS} field in Figure 6.2.3.2.1 is similar to that for the 800 μm round orifice jet except that the peak values are distributed on either side of the jet core instead of concentrated in the center. The peak V_{RMS} value for the Channel 2 jet is approximately 3.4 m/s compared to 3.5 m/s for the 800 μm round orifice jet. The V_{RMS} field for the Channel 4 jet in Figure 6.2.3.2.2 is similar to that for Channel 2 and the 800 μm round orifice jets. The peak value of 3 m/s is lower than that for Channel 2 and the 800 μm round orifice. The peak V_{RMS} values are also concentrated in the core of the jet as they are for the 800 μm round orifice indicating that the abrupt transition to the larger exit diameter of Channel 4 may concentrate these velocity fluctuations in the jet core whereas the smoother transition in Channel 2 may spread out these fluctuations thus stabilizing

the jet core. This result corresponds with the flatter jet profile downstream of Channel 4 compared to Channel 2.

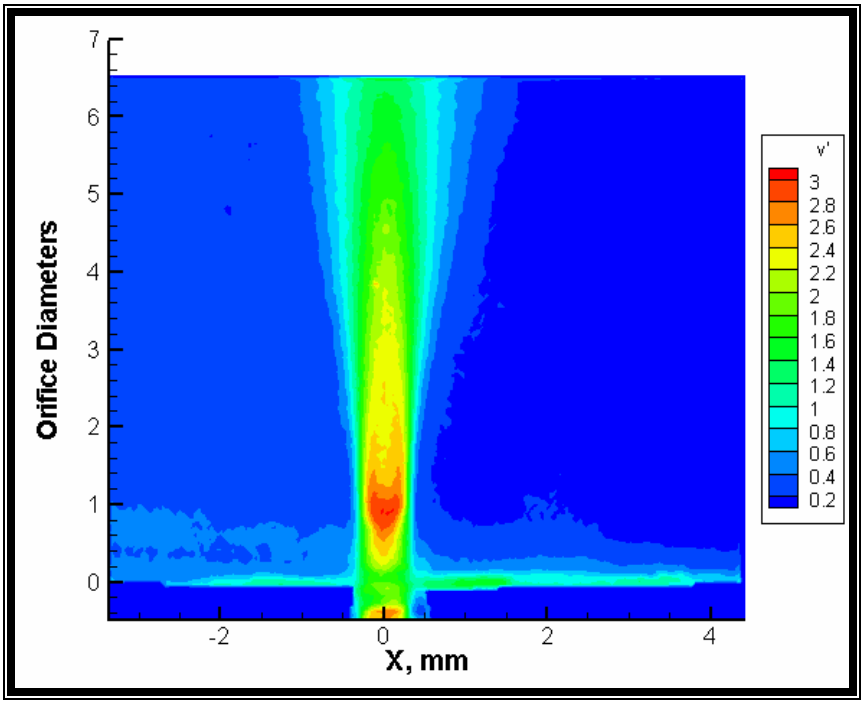

FIGURE 6.2.3.2.2. V_{RMS} field for the Channel 4 jet. V_{RMS} units are m/s. V_{RMS} magnitudes are color coded according to the legend.

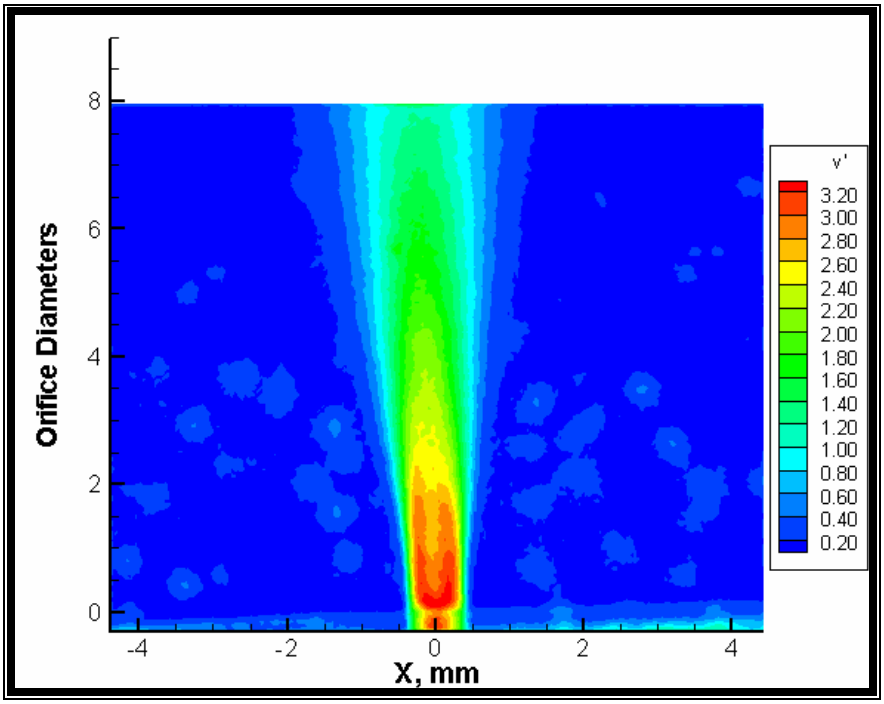

FIGURE 6.2.3.2.3. V_{RMS} field for the Channel 6 jet. V_{RMS} units are m/s. V_{RMS} magnitudes are color coded according to the legend.

The Channel 6 jet V_{RMS} field in Figure 6.2.3.2.3 is similar to that for the 800 µm round orifice jet. Like the 800 µm round orifice jet peak values are concentrated in the core of the jet; however, higher V_{RMS} values also extend to either side of the jet core. The peak V_{RMS} value for the Channel 6 jet is approximately 3.2 m/s compared to 3.5 m/s for the 800 µm round orifice jet and 3.4 m/s for the Channel 2 jet. The V_{RMS} field for the Channel 8 jet in Figure 6.2.3.2.4 is similar to that for the Channel 4 and the 800 µm round orifice jets. The peak value of 2.6 m/s is lower than that for the other channels. The peak V_{RMS} values are also concentrated in the core of the jet as they are for the 800 µm round orifice.

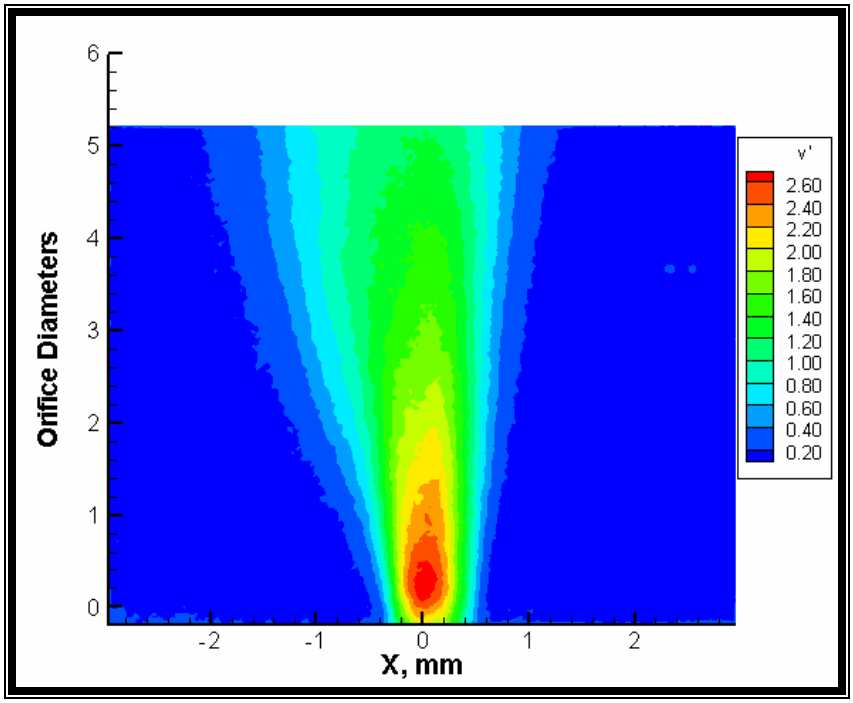

FIGURE 6.2.3.2.4. V_{RMS} field for the Channel 8 jet. V_{RMS} units are m/s. V_{RMS} magnitudes are color coded according to the legend.

6.2.3.3. Reynolds stress fields

The principal Reynold stress (PReS) fields corresponding to the jet average velocity fields presented in the previous section will be shown in this section. These plots give an indication of the velocity fluctuations that can cause blood element damage and/or platelet activation. The Reynolds stress fields for the Channel 2, 4, 6, and 8 jets are shown in Figures 6.2.3.3.1, 6.2.3.3.2, 6.2.3.3.3 and 6.2.3.3.4, respectively.

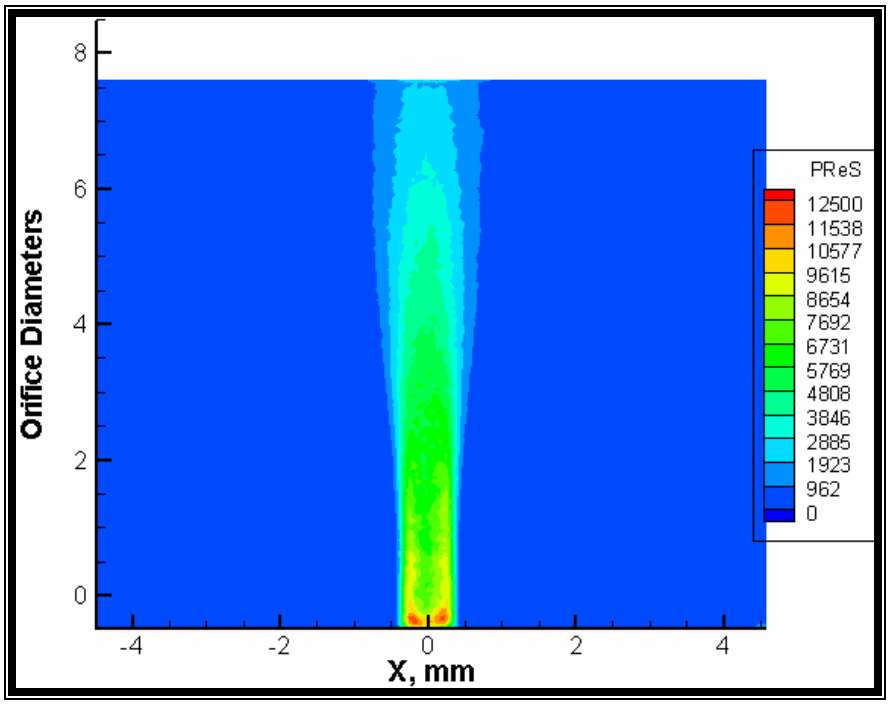

FIGURE 6.2.3.3.1. Principal Reynolds stress (PReS) field for the Channel 2 jet. PReS units are dyn/cm^2. PRes magnitudes are color coded according to the legend.

The Channel 2 jet PReS field in Figure 6.2.3.3.1 is similar to that for the 800 µm round orifice jet except that the peak values are distributed on either side of the jet core instead of concentrated in the center. The peak PReS value for the Channel 2 jet is approximately 12,500 dyn/cm^2 compared to 15,000 dyn/cm^2 for the 800 µm round orifice jet. The PReS field for the Channel 4 jet in Figure 6.2.3.3.2 is similar to that for Channel 2 and the 800 µm round orifice jets. The peak value of 10,000 dyn/cm^2 is lower due to the lower jet

velocity. The peak PReS values are also concentrated in the core of the jet as they are for the 800 µm round orifice indicating that the abrupt transition to the larger exit diameter of Channel 4 may concentrate these stresses in the jet core whereas the smoother transition in Channel 2 may spread out these stresses thus stabilizing the jet core. This result corresponds with the flatter jet profile downstream of Channel 4 compared to Channel 2.

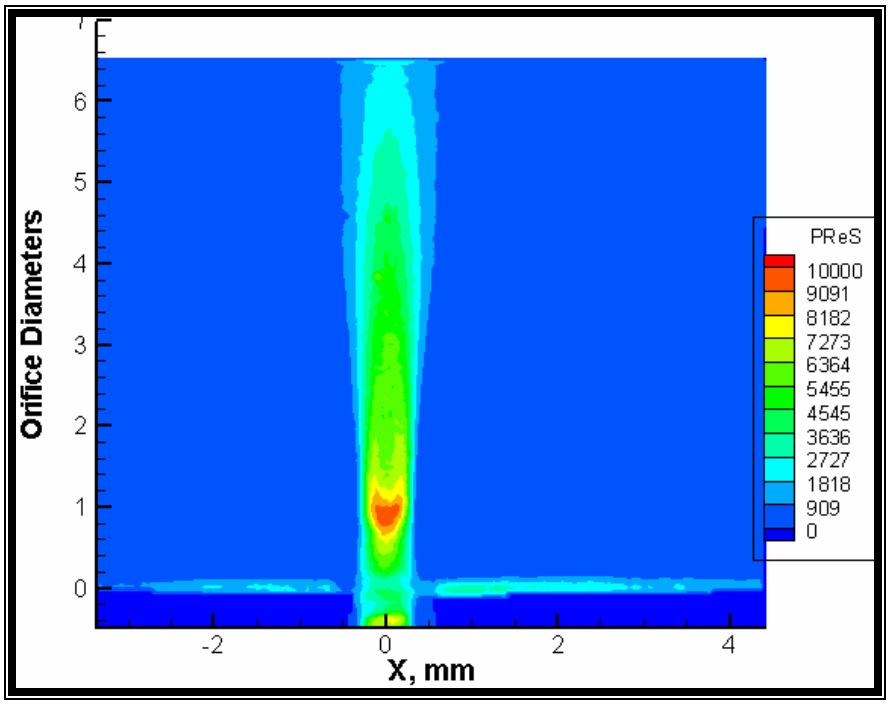

FIGURE 6.2.3.3.2. Principal Reynolds stress (PReS) field for the Channel 4 jet. PReS units are dyn/cm^2. PRes magnitudes are color coded according to the legend.

The Channel 6 jet PReS field in Figure 6.2.3.3.3 is similar to that for the 800 µm round orifice jet. Like the 800 µm round orifice jet peak values are concentrated in the core of the jet; however, higher PReS values also extend to either side of the jet core. The peak PReS value for the Channel 6 jet is approximately 12,000 dyn/cm^2 compared to 15,000 dyn/cm^2 for the 800 µm round orifice jet and 12,5000 for the Channel 2 jet. The PReS field for the Channel 8 jet in Figure 6.2.3.3.4 is similar to that for the Channel 4 and the 800 µm round orifice jets. The peak value of 7,800 dyn/cm^2 is lower due to the lower jet

velocity. The peak PReS values are also concentrated in the core of the jet as they are for the 800 μm round orifice.

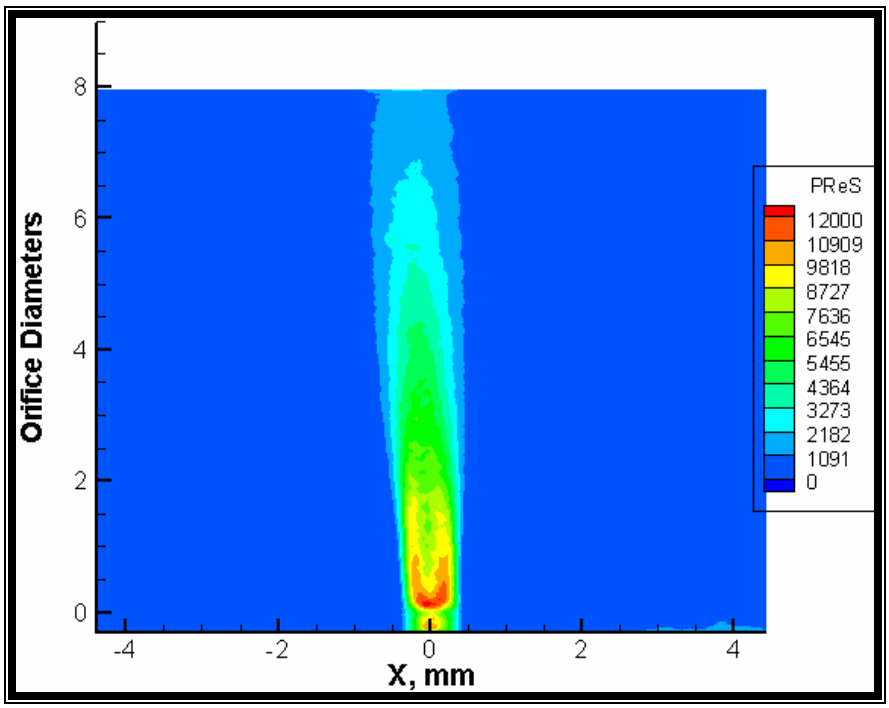

FIGURE 6.2.3.3.3. Principal Reynolds stress (PReS) field for the Channel 6 jet. PReS units are dyn/cm^2. PRes magnitudes are color coded according to the legend.

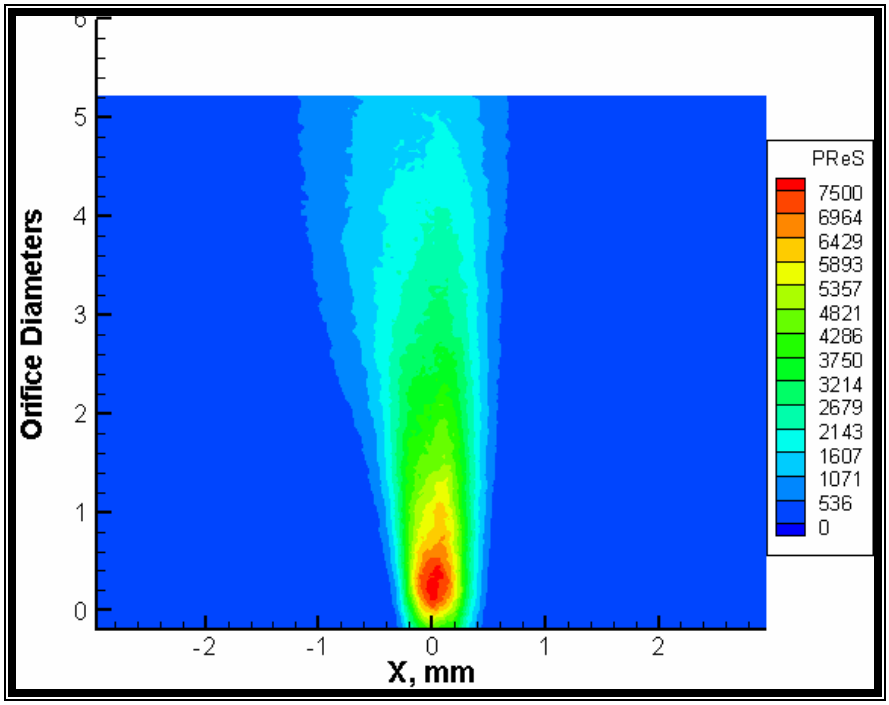

FIGURE 6.2.3.3.4. Principal Reynolds stress (PReS) field for the Channel 8 jet. PReS units are dyn/cm^2. PRes magnitudes are color coded according to the legend.

6.2.3.4. Shear stress fields

The shear stress (SS) fields corresponding to the jet average velocity fields presented in the previous section will be shown in this section. These plots give an indication of the magnitude of the velocity gradients between the different shear layers in the flow that can cause blood element damage and/or platelet activation. The SS fields for the Channel 2, 4, 6, and 8 jets are shown in Figures 6.2.3.4.1, 6.2.3.4.2, 6.2.3.4.3 and 6.2.3.4.4, respectively.

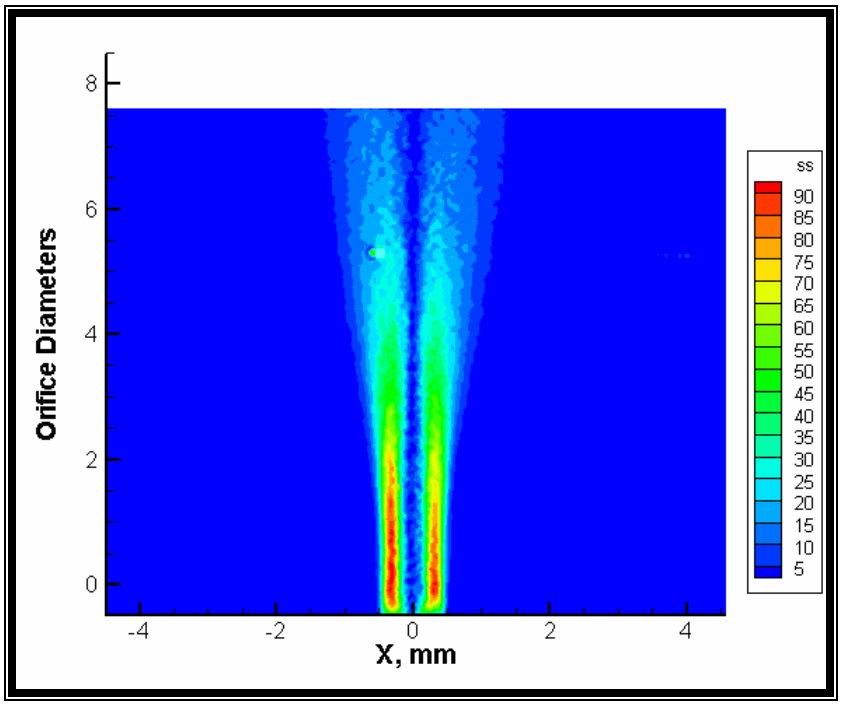

FIGURE 6.2.3.4.1. Shear stress (SS) field for the Channel 2 jet. SS units are dyn/cm^2. SS magnitudes are color coded according to the legend.

Figure 6.2.3.4.1 shows that the highest SS values for the Channel 2 jet are found on either side of the jet core and have a peak value of approximately 90 dyn/cm^2. The location of these higher SS values coincides with the mixing of the higher velocity jet and the lower velocity recirculation regions near the orifice. Thus, these areas may be vulnerable to inducing platelet activation, and the subsequent recirculation may enable

these activated platelets to aggregate. This SS field looks similar to that for the 800 μm round orifice jet except that this jet had concentrations of high SS values at the orifice, and these concentrations are absent for the Channel 2 jet. This may indicate that the smoother exit of Channel 2reduces the shear layers in this region.

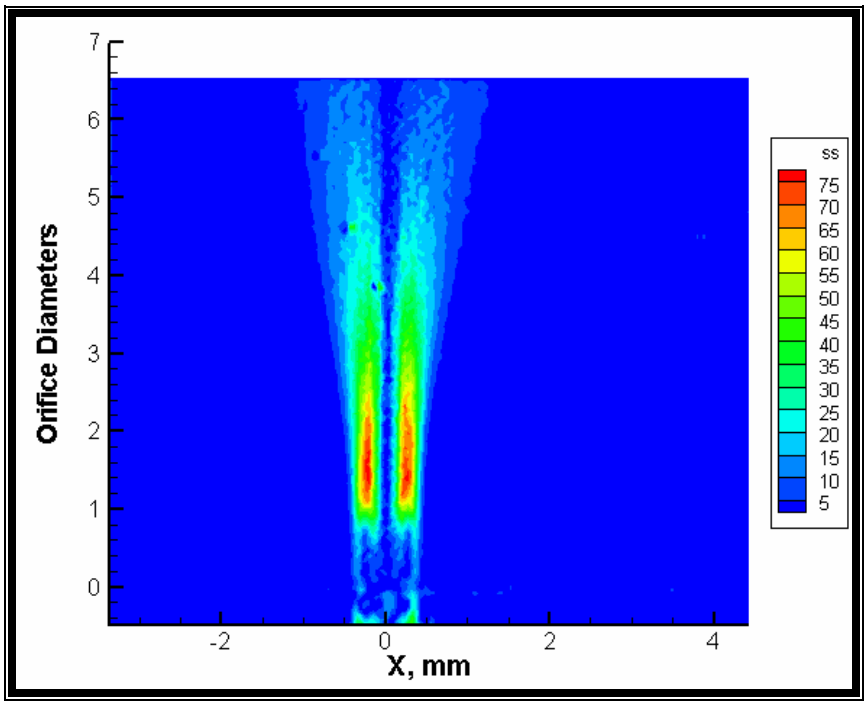

FIGURE 6.2.3.4.2. Shear stress (SS) field for the Channel 4 jet. SS units are dyn/cm^2. SS magnitudes are color coded according to the legend.

The SS field for the Channel 4 jet in Figure 6.2.3.4.2 is similar to that for the Channel 2 jet. However, the peak SS value is somewhat lower than that for the Channel 2 jet at 75 dyn/cm^2. The SS field for the Channel 6 jet in Figure 6.2.3.4.3 is similar to that for the 800 μm round orifice but with a lower peak SS values of 75 dyn/cm^2. The SS field for the Channel 8 jet in Figure 6.2.3.4.4 is similar to that for the Channel 2 and 4 jets. However, the peak value is lower than those for the other channel jets at 45dyn/cm^2. The skewing of the jet is evidenced by the asymmetry of the SS field. The side that the jet is skewed

towards has higher magnitude SS values as well as a more rapid decrease in these values showing the instability of this side of the jet compared to the other side.

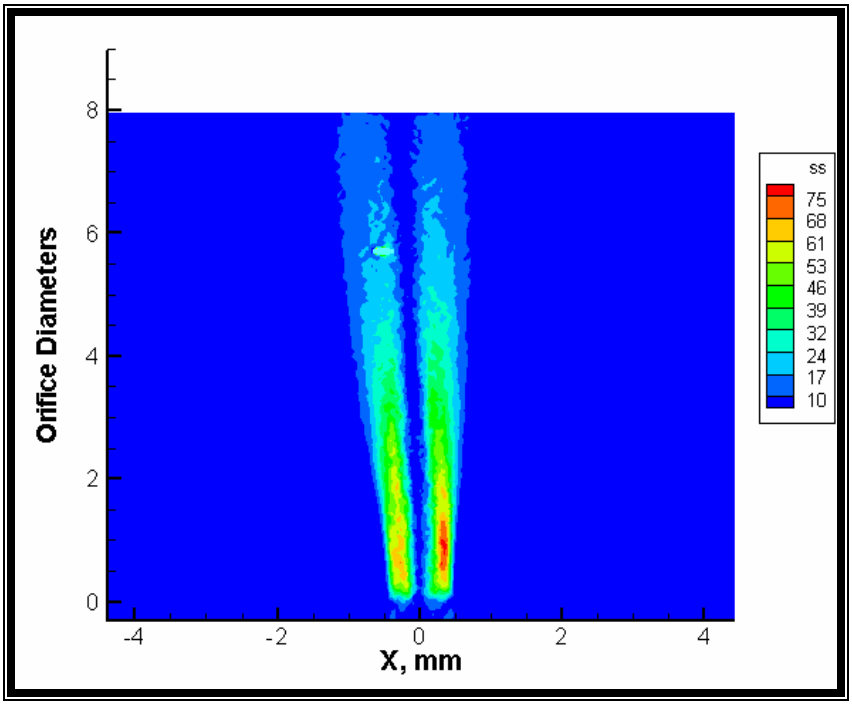

FIGURE 6.2.3.4.3. Shear stress (SS) field for the Channel 6 jet. SS units are dyn/cm^2. SS magnitudes are color coded according to the legend.

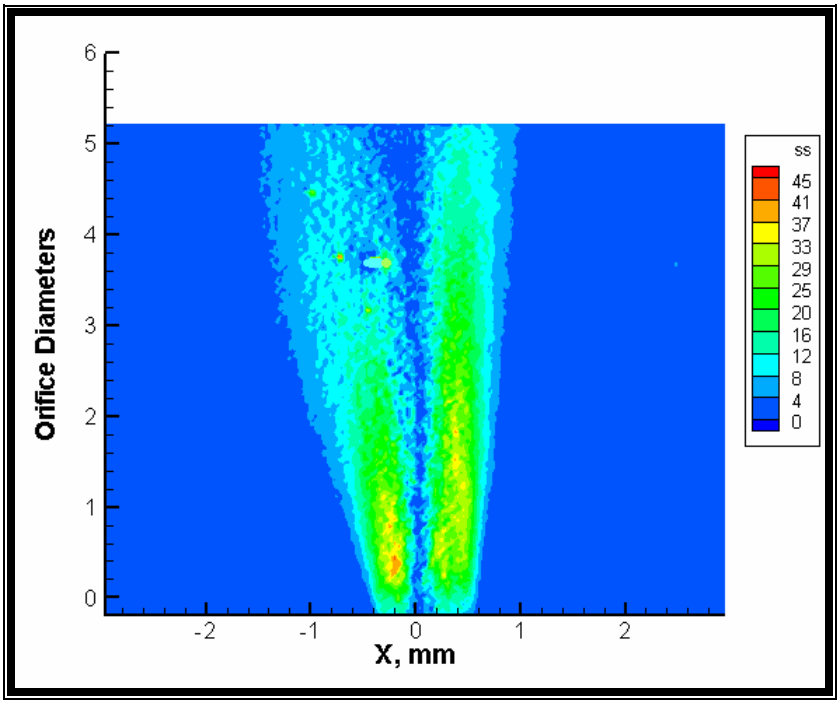

FIGURE 6.2.3.3.4. Shear stress (SS) field for the Channel 8 jet. SS units are dyn/cm^2. SS magnitudes are color coded according to the legend.

6.3. Wall Shear Stress Calculations

The wall shear stresses for the round and slit orifices were calculated using approximations for laminar pipe entrance flows. The wall shear stress for the round orifices was calculated as the dynamic viscosity, ν, times the magnitude of the partial derivative with respect to the radial direction, *r*, of the laminar pipe entrance velocity profile [54] in Equation 5.1.5.1. For the slit orifices, the wall shear stress was calculated as the dynamic viscosity, ν, times the magnitude of the partial derivative with respect to the transverse direction, *y*, of the laminar parallel plate channel velocity profile [54] in Equation 5.1.5.3. For all of the wall shear stress (WSS) calculations, the derivative was calculated 50 μm downstream of the orifice inlet at x=50 μm. WSS was also calculated for the low and high flow rate experiments with the 800 μm round orifice. These wall shear stress WSS values are presented in Table 6.3.1 along with the jet Reynolds numbers, flow rates for the orifices, and estimated bulk velocities.

TABLE 6.3.1. Flow rate, bulk velocity, Reynolds number (Re=aU/ν for the round orifices, Re= hU/ν for the slit orifices), and estimated wall shear stress for the orifices used in this study. Bulk velocity was calculated based on the cross-sectional area and measured flow rate, and wall shear stress was estimated using a laminar pipe entrance flow profile for the round orifices and a parallel plate channel entrance flow profile for the slit orifices 50 μm downstream of the inlet.

	Flow rate (L/min)	**Bulk Velocity (U) through orifice (m/s)**	**Reynolds number**	**Estimated Wall Shear Stress Magnitude (dynes/cm^2)**
200 μm round orifice	0.01	5.31	150	21,700
400 μm round orifice	0.045	5.97	340	19,100
800 μm round orifice-low flow	0.09	3.0	340	5,300
800 μm round orifice-normal	0.15	5.0	570	9,200
800 μm round orifice-high flow	0.19	6.6	750	12,400
1200 μm round orifice	0.32	4.72	810	6,000
200 μm slit orifice	0.90	5.91	170	24,200
400 μm slit orifice	1.7	5.58	320	21,100
800 μm slit orifice	3.06	5.02	570	15,800

6.4. Baboon ex vivo shunt studies

The original purpose of these studies was to establish a relationship between slit size and platelet deposition. However, since only the 800 μm slit orifice was used in the *ex vivo* shunt, this relationship could not be established. However, by repeating the experiments with the 800 μm slit orifice, a reproducible protocol was established for these experiments so that future studies can investigate this connection. Figure 6.4.1 shows the non-normalized results for all the *ex vivo* experiments. These results show that both the cumulative platelet deposition and the platelet deposition rate are dependent upon another factor that was not controlled in the experiments.

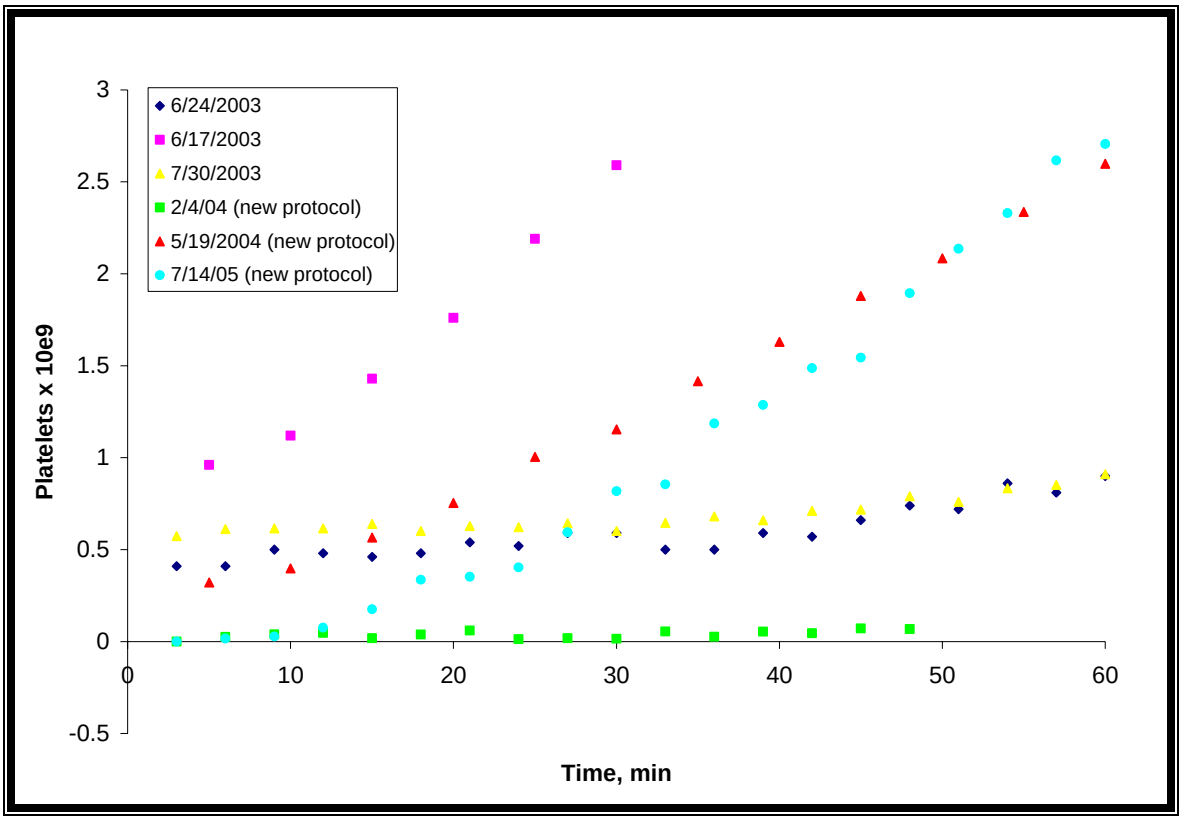

FIGURE 6.4.1. Platelet count over time for the baboon *ex vivo* shunt experiments.

Using the 'new protocol,' the administration of heparin was controlled so that the APTT clotting time was maintained between 95 and 125 seconds. However, even with the new protocol there was still an unacceptable level of variability. Thus, it was determined that initial platelet count was the controlling factor for these experiments. Figure 6.4.2 shows onlydata from experiments with initial platelet counts above 380. The APTT times, initial platelet count, and initial flow rate for each experiment are given in Table 6.4.1. These results show that by controlling the initial platelet count using more stringent animal selection, reproducibility of the platelet deposition rate is achieved. Thus, a protocol that dictates an initial platelet count above 380 and a starting APTT above 95 seconds is able to deliver more reproducible results.

TABLE 6.4.1. Important values for each of the *ex vivo* experiments. (*=same animal). Highlighted experiments had similar platelet deposition rate values.

Date	APTT at t=0, seconds	End APTT, seconds	Initial platelet count, platelets*10^{11}	Initial flow rate, ml/min	Platelet deposition rate, platelets*10^{9}/min
6-17-03*	95	109	412	187	0.067
6-24-03*	167	150	339	203	0.0074
7-30-03	78	94	308	204	0.0048
2-5-04	173	230	242	160	0.0009
5-19-04	132	125	407	260	0.043
7-14-05	105	132	380	200	0.050

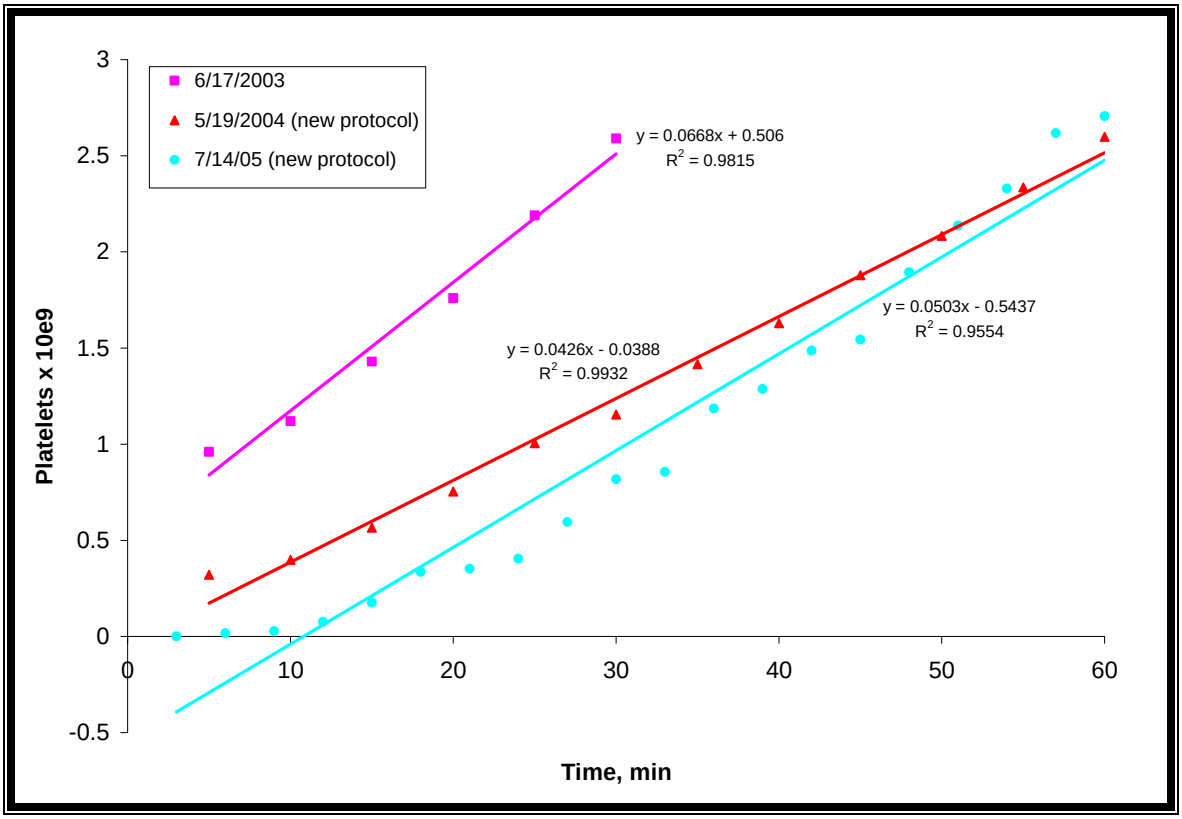

FIGURE 6.4.2. Platelet count over time for the baboon *ex vivo* shunt experiments with initial platelet counts within the newly established limits. Trendlines show the platelet deposition rate. These experiments with similar initial platelet counts had similar platelet deposition rates as shown in Table 7.2.1.

Images of the orifice from 7/14/05 were taken after the experiment and are shown in Figure 6.4.3. The proximal image represents the upstream side of the orifice, and the distal image represents the downstream side. The corresponding platelet count on these

sides of the orifice was $3.89x10^9$ platelets and $0.54x10^9$ platelets for the distal and proximal side, respectively.

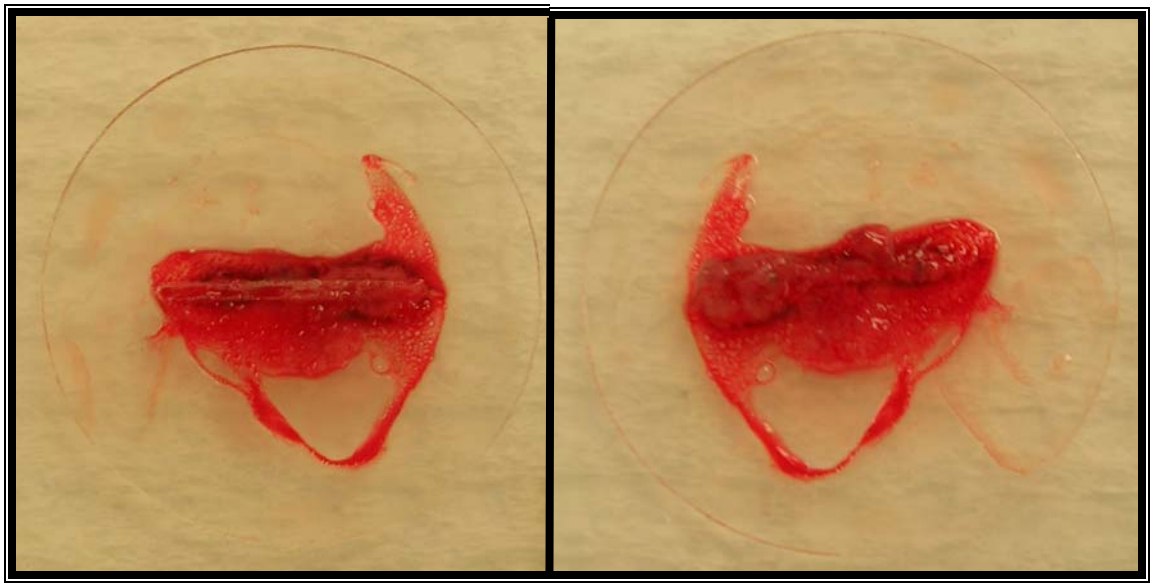

FIGURE 6.4.3. Photographs of the proximal and distal sides of the 800 μm slit orifice after the 7/14/05 baboon *ex vivo* shunt experiment. The distal side appears to have more thrombus growth than the proximal side.

CHAPTER 7

DISCUSSION

In the past, the study of shear-activated platelet aggregation (SIPA) and activation (SIPAct) has been isolated mainly to cone and plate viscometer and parallel plate flow chamber studies in which the parameters are not strictly physiological in nature [39] [40] [42]. Furthermore, many of these studies have been conducted in the presence of collagen, vWF, or fibrin, which promote platelet aggregation thus biasing the results by artificially inducing thrombus formation [57]. The present system enables coagulation in a dynamic steady flow environment in which different orifices and channels as well as mechanical heart valves can be introduced to investigate the effect of different shapes and sizes that induce different flow fields and shear stresses on platelet activation and procoagulant potential. The discussion section is divided into four sections: recalcification system development, the round and slit orifice experiments, the channel experiments, and the MHV experiments. These sections address the specific aims of this study. The first of these aims was to develop an *in vitro* system in which coagulation can occur in response to an external agonist, shear stress in particular. This system was then used to investigate platelet activation and coagulation initiated by flow through different channels designed to approximate the hinge region of various bileaflet MHVs. These flow fields were also validated using DPIV to detail the differences in them that may make a specific geometry more susceptible to thromboemboli formation than another. Lastly, MHVs were used in the *in vitro* system to examine the effect of hinge gap width and hinge geometry on these parameters.

7.1. Recalcification system development

One of the specific aims of this research was to develop a system in which thrombus formation could be reproducibly initiated by shear stress activation of platelets. Initial experiments were performed under low shear stress conditions with a glass tube as an agonist. A continuous infusion of calcium chloride served to partially reverse the anticoagulant effect of the sodium citrate. This system of recalcification proved to be successful in these experiments and in the later experiments with the orifices, channels, and MHVs that did impart high shear stresses on the blood elements. Indeed, experiments with the 400 μm round orifice without calcium chloride infusion showed that calcium infusion was necessary to produce significant TAT generation and clotting in the loop in a reproducible fashion. Although some TAT was formed in the non-calcium infused experiments (Figure 6.1.4.1.1), most likely due to the shear-induced calcium efflux from activated platelets enabling the propagation of the coagulation cascade, it was not significant or reproducible. Thus, a key finding of the study was that calcium may be infused into citrated blood in vitro to greatly enhance the haemostatic and procoagulant potential of citrated recirculating blood. Thus, the method may be attractive for sensitive evaluation of the thrombus forming potential of other surfaces and devices, the effects of antithrombotic strategies, and the role of important variables. Indeed, this method clearly documents the role of platelet concentration for catalyzing coagulation reactions leading to the formation of TAT.

Additional experiments were performed to investigate the role of platelets in the thrombus formation using platelet depleted blood. The purpose of these experiments was to show that thrombus formation in this system was dependent upon initiation of the

coagulation cascade by the activation of platelets. The significantly lower TAT increases seen with platelet depleted blood and the 400 μm orifice compared to the normal runs with this orifice (Figure 6.1.4.1.1), indicate that TAT generation in this system can be attributed predominantly to platelet activation which markedly enhances coagulation reactions. Platelet depleted blood still contains approximately 15% of the platelets found in normal whole blood (85% platelet removal efficiency); thus, the small amount of TAT formed in the platelet depleted experiments is consistent with the TAT increase demonstrated in the experiments with normal whole blood. Indeed, at 45 and 60 minutes the TAT concentrations for the platelet depleted experiments were 13% and 18%, respectively, of the TAT concentrations for the normal experiments at these sample times. This percentage correlates directly with the average percentage of remaining platelets in the depleted blood of 15%. Thus, TAT generation and therefore coagulation are directly dependent upon platelet count.

Hemolysis occurred on a statistically insignificant scale (Figures 6.1.1.2.1 and 6.1.2.2.1), but may have been sufficient to release ADP to further activate the platelets that were present. Platelet aggregates in whole blood have been shown to be more stable than those formed in platelet rich plasma, implying that RBCs play a role in clot formation [58]. Further, RBCs can adhere independently to activated platelets and fibrin under low shear rates instead of just being passively entrapped in clots [59]. Thus, the low shear rates present upstream and downstream of the orifices may have allowed the RBCs to aid in coagulation even when the platelet concentration was markedly reduced. However, because hemolysis was minimal, clotting was most likely due to shear-induced activation of the platelets and not to the release of ADP by damaged RBCs. Additionally,

the importance of circulating tissue factor in the plasma cannot be ruled out. Studies have suggested that this circulating tissue factor may be incorporated into thrombi in a shear-dependent manner [60], although the importance of this pathway in the absence of tissue injury remains unclear.

These experiments with platelet-depleted blood did show the importance of platelets in the thrombus formation in this system; however, the role of shear stress was still not documented. Thus, experiments with Aggrastat and the AN51 antibody were performed to block the GPIIb/IIIa and GPIb platelet receptors, respectively. In particular the GPIb has been implicated in shear activated platelet aggregation as shown in the diagram in Figure 7.1.1. The TAT results for the 400 μm round orifice experiments with Aggrastat and AN51 antibody addition (Figure 6.1.4.1.1) show that the independent inhibition of both the GPIIb/III and GPIb platelet receptors suppresses TAT formation in this shear-activated system. However, the trendlines in Figure 6.1.4.1.2 and the rates of TAT increase in Table 6.1.4.1.1 show that Aggrastat is moderately more effective than AN51 at suppressing TAT formation. This difference in effectiveness can be explained by a two step mechanism for SIPA [40] in which rapid binding of vWF to GPIb tethers platelets, and subsequent binding of fibrinogen to both GPIb and GPIIb/IIIa stabilizes the thrombus. Furthermore, the GPIIb/IIIa receptor on activated platelets can bind with at least four different ligands (fibrinogen, vWF, fibronectin, and vitronectin) and only with immobilized fibrinogen when not activated. However, the GPIb receptor can bind with only soluble vWF in the presence of shear stress and with immobilized vWF in the absence of shear stress [35]. Based on this knowledge, it is apparent that these two platelet receptors represent different pathways of platelet activation and aggregation

under shear stress conditions, and that the GPIIb/IIIa receptor is more versatile and has increased functionality compared to the GPIb receptor. Active GPIIb/IIIa receptors are critical to platelet recruitment in thrombus formation [61]. In the presence of Aggrastat, platelets can be immobilized in a transient manner, but further platelet recruitment is not possible without functional GPIIb/IIIa receptors. However, even in the absence of functional GPIb receptors, platelet aggregation and subsequent platelet recruitment may be possible in low flow regions where activated platelets mingle for sufficient residence times for fibrinogen to bind to activated GPIIb/IIIa receptors. In this system, activated platelets generally move too quickly for this to occur, but we did observe some TAT formation in the AN51 experiments that was above baseline levels showing that some thrombus formation did occur.

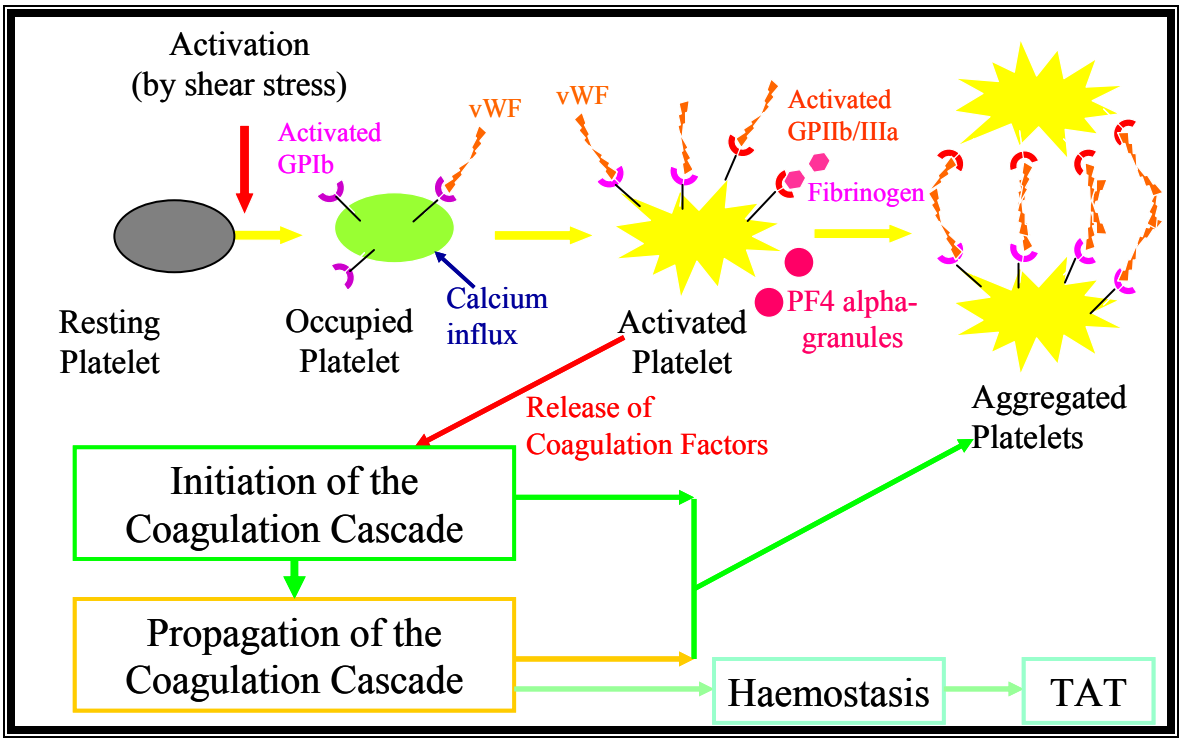

FIGURE 7.1.1. Diagram of the pathway from shear activation of platelets to activation of the coagulation cascade and platelet aggregation.

There is also evidence that vWF and fibrin have a cooperative effect on platelet adhesion and aggregation under high shear conditions. These studies indicate that resting platelets under flow conditions at high shear stresses adhere to immobilized vWF via the GPIb platelet receptor and are consequently slowed down and activated. This activation turns on the GPIIb/IIIa receptor and allows it to bind to vWF, since this adhesive reaction appears to take longer than the reaction between vWF and GPIb. This step is necessary for thrombus formation, since a fast dissociation rate and reversible bonds characterize the vWF-GPIb interaction, while the vWF-GPIIb/IIIa interaction is irreversible. After immobilization by the vWF-GPIIb/IIIa interaction, fibrinogen binding to the GPIIb/IIIa receptor may function to recruit more platelets and to stabilize the thrombus [39-42]. Thus, the vWF-GPIb interaction is crucial to initiating platelet arrest and activation, but the vWF-GPIIb/IIIa interaction is necessary for permanent thrombus formation and increasing the size of the thrombus. In addition to simple development of the thrombus by fibrinogen binding to GPIIb/IIIa, fibrinogen may also gradually replace the vWF that initially constructed the thrombi under high flow conditions [43].

Histological observations also support a two-step mechanism for SIPA and subsequent thrombus formation. In the initial stages, the thrombus increases in height and volume with flow and under the adhesive power of vWF [43]. However, over time the vWF must be replaced by fibrinogen in order to stabilize the thrombus.

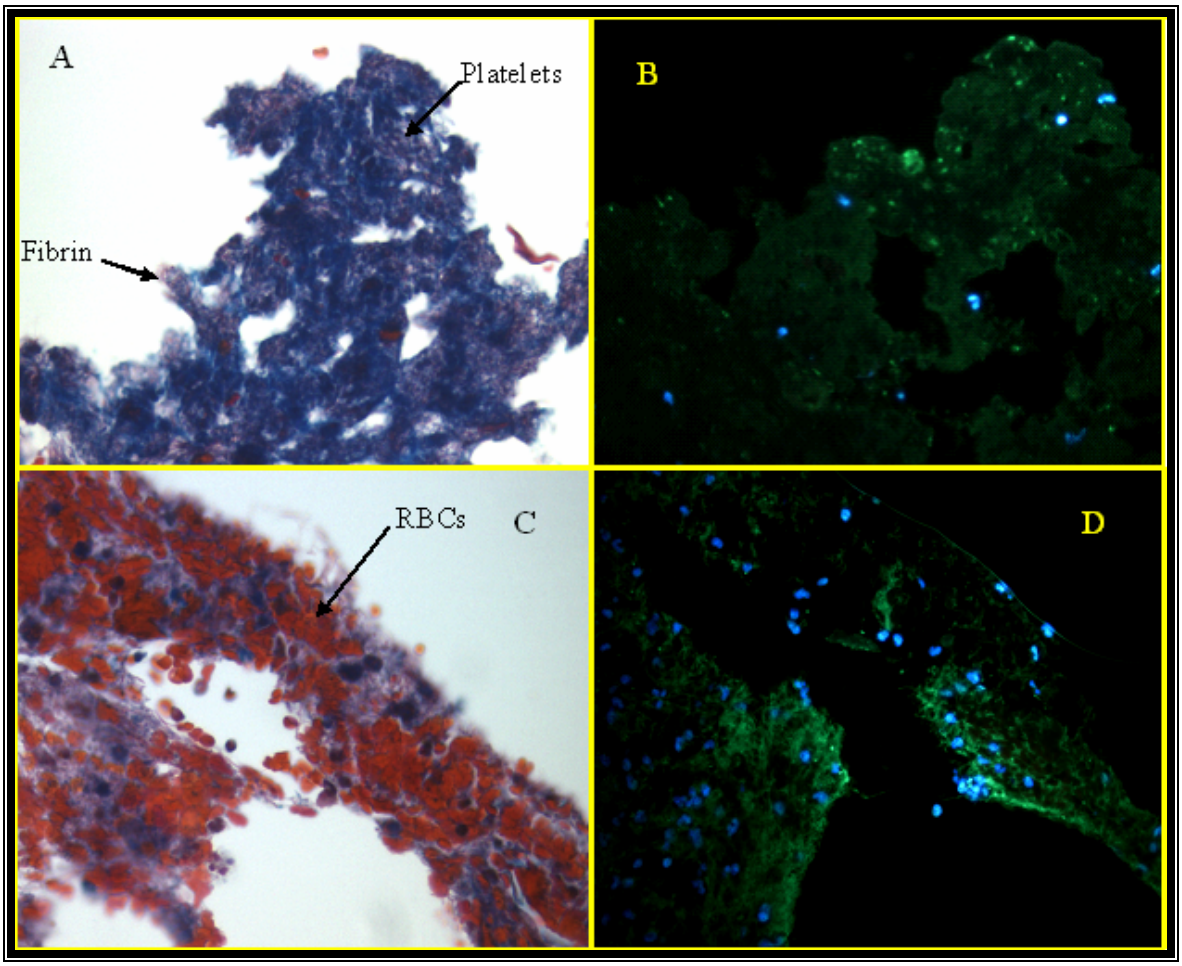

FIGURE 7.1.2. Carstairs and vWF immunofluorescence staining of two clots upstream and downstream of the orifice under normal conditions. (A) Carstairs stain of downstream clot. The dark blue areas indicate a concentration of platelets, and the orange-red cells are RBCs. Fibrin is shown by the red strands surrounding the clot. (B) anti-vWF stain of downstream clot. Bright green denotes vWF, and bright blue is RBCs. (C) Carstairs stain of upstream clot. This thrombus is composed mainly of RBCs with some platelets and fibrin enmeshed. (D) anti-vWF stain of upstream clot. In Carstairs stain navy blue is platelets, red is fibrin and orange-red is RBCs. In anti-vWF stain blue is RBCs and nuclei and bright green is vWF.

This difference in morphology can be observed in the differences between the upstream and downstream thrombi in one of the experiments. The downstream thrombus (Figure 7.1.2A, B) has a more dense construction of mostly platelets and fibrin, whereas the upstream thrombus (Figure 7.1.2C, D) has a looser construction with an abundance of RBCs and vWF as well as some fibrin and platelets. Thus, the downstream thrombus

most likely occurred first and has already transitioned to mostly fibrinogen, while the upstream thrombus was probably still forming when the experiment was stopped.

Platelet activation also seemed to be affected by the addition of Aggrastat and AN51. This study shows an increase in platelet activation in the AN51 experiments over the normal and Aggrastat experiments (Figure 6.1.4.2.2). Conversely, the Aggrastat experiments appeared to produce moderately less platelet activation. Thus, although neither Aggrastat nor AN51 appear to inhibit initial SIPAct, Aggrasat may attenuate further feedback activation by preventing fibrinogen binding to the GPIIb/IIIa receptor. AN51, however, does not inhibit this feedback activation and may even induce PF4 release by its binding to the GPIb receptor.

Previous cone and plate viscometer studies using the AN51 antibody to the GPIb platelet receptor showed a significant reduction in Annexin V expression, which is also a measure of platelet activation [37]. In the current study the measure of platelet activation was PF4, which has previously been shown to be a more sensitive measure of platelet activation than Annexin V expression, which indicates mechanical changes in the platelet membrane Travis [62]. Annexin V expression on the external cell membrane is a positive sign that phosphatidyl serine (PS) has moved from the inside to the outside of the platelet cell membrane. The mechanism behind this transmembrane redistribution is unknown. PF4 release occurs as a result of platelet activation by many different pathways via α-granules released from activated platelets. It is not clear whether PS redistribution or PF4 release occurs first. Thus, PF4 release may occur even in the absence of Annexin V expression. The suppression of Annexin V expression but not PF4 release by the AN51 antibody indicates that PF4 release must occur via a different pathway than PS

translocation. However, since there was not a concomitant increase in TAT production, the release of PF4 observed in the AN51 experiments may not indicate a calcium influx. This calcium influx is necessary for complete shear activated platelet activation and the subsequent release of factors to initiate the coagulation cascade. Thus, this PF4 release may only indicate a conformational change in the GPIb receptor that induced PF4 release without the initiation of a calcium influx that customarily follows binding of GPIb to vWF.

7.2. Round and slit orifice experiments

The round and slit orifice models used in this study, particularly the 400 μm orifice, model the hinge region and the B-datum line of a closed bileaflet MHV, respectively. These are the two regions through which blood flows during the leakage phase of the cardiac cycle, and the resulting flow fields have been shown to impart considerable shear stresses on the blood. Studying these two geometries independently from the complexity of the bileaflet MHV has enabled us to better characterize the clot propensity of these sizes and shapes of orifices without the complications of moving leaflets and the presence of both leakage areas.

These experiments showed a considerable increase in TAT concentration over time for the 200 and 400 μm orifices, but not for the 800 μm or 1200 μm orifices (Figures 6.1.1.1.2 and 6.1.1.1.3). The absence of a significant increase in TAT formation with the 800 μm and 1200 μm orifice confirmed that coagulation was not induced by the flow loop alone. Thus, the TAT increase can be attributed to the platelet activation incurred as the blood flowed through the 200 μm and 400 μm orifices in combination

with the stagnation regions downstream of the smaller orifices. Additionally, since TAT concentration increased dramatically below an orifice size of 800 μm, there is most likely a critical orifice size threshold between 400 and 800 μm that induces thrombus formation.

Surprisingly, TAT levels for the 200 μm orifices were not significantly larger than those for the 400 μm orifices. One explanation for this lack of an increase in the circulating TAT concentration may be that there is a limit for circulating TAT in the flow loop. An apparent leveling off of the TAT concentration at 60 minutes supports this explanation. Another interesting result is that the increase in TAT concentration at 15 minutes is significantly higher for the 400 μm orifice than for the 200 μm orifice (Figure 6.1.1.1.4). This could be due to the fact that the 400 μm orifice has a larger internal circumferential surface area on which a thrombus could form. This behavior also implicates a dependence of TAT formation in this system on the number of times that a blood volume passes through the orifice. At 15 minutes the estimated number of times that a blood volume passes through the 200 μm round orifice is 2, and the number of 'passes' through the 400 μm round orifice at 15 minutes is 10. Thus, after only 2 passes through the system, the platelets may not be sufficiently primed for propagation of the coagulation cascade. This priming of the platelets may occur via exposure to the pump or to the foreign materials in the flow loop as well as via subsequent passes through the orifice. Although mechanical platelet activation via shear stress has been shown to occur in response to a single instance of shear stress, continuous exposure to the conditions in this steady flow loop may activate the GPIb platelet receptors without inducing complete platelet activation. Thus, after a certain amount of exposure, the platelets may be primed

to bind with vWF in an opportunistic fashion if they encounter a stagnation or circulation region.

Shankaran et al [37] showed, using Annexin V binding to GPIb on platelets as a marker, that shear stress induced platelet aggregation (SIPA) is dependent on the shear stress level but not on the shear rate. They found a threshold shear stress for whole blood to undergo SIPA of 83 dyn/cm^2. Zhang et al [63] found that SIPA and subsequent platelet aggregation is increased when there is a small interval (2.5 sec) of high shear (100 dyn/cm^2) followed by a constant application of low shear (5 dyn/cm^2) as opposed to a constant application of high shear. In the current study the average shear stresses experienced by the blood as it passed through the different orifices is estimated to be more than 100 dyn/cm^2, and this high shear is transient followed by regions of stagnation and recirculation. However, there was an indication of significant coagulation in only the two smallest round orifices corresponding to the most pronounced recirculation zones. Thus, the high shear stresses may have activated the platelets, but the recirculation regions and subsequent longer residence times downstream of the orifice plate appear to have been key for inducing and accumulating thrombosis.

Another interpretation for TAT formation in this loop could be the different residence times for the different orifices resulting in flow stagnation and subsequent thrombin formation. Since the smaller orifices have lower flow rates, the residence times in the orifice chamber and the rest of the loop is higher. To investigate these residence times, flow visualization with dye injection was performed for the round orifices since they had the longest residence times. The flow fields for the round orifices were all similar with regions of recirculation both upstream and downstream of the orifice plate.

Upstream of the orifice plate, the flow that did not go through the orifice impinged upon the orifice plate and was directed in two counter-rotational recirculation regions on either side of the chamber. Similarly, downstream of the orifice plate, as the jet expanded, flow at the edges of the jet impinged on the chamber walls at the throat and was directed in two counter-rotational recirculation regions on either side of the jet. In general the residence times upstream of all the round orifices were relatively long ranging from 3 to 5 seconds for the 1200 μm round orifice to 16 to 18 seconds for the 200 μm orifice. If the particles became entrapped in a recirculation region, the residence time was even longer. The residence times downstream of the orifices were not nearly as long ranging from 1.3 to 2.6 seconds for the 200 μm round orifice to less than 0.2 seconds for the 1200 μm orifice. However, if the particles became entrapped in a downstream region of recirculation this residence time could be much longer with observed entrapment times of up to 38 seconds for the 200 μm orifice and 9 seconds for the 400 μm. In general, however, the jet was mixed with the bulk flow efficiently.

Detailing the kinetics of thrombus formation is critical in determining whether or not a thrombus will form under various flow conditions, especially in regions of high velocity such as mechanical heart valve leakage jets. Studies done using a 10-micron filter to retain platelet aggregates while applying a predetermined pressure leading to elevated shear stress have shown that activation and aggregation can occur within 8 ms [64]. Thus, activated platelets, if brought together, could aggregate in a very short time period. Another study that investigated the cytosolic calcium flux that occurs with platelet activation and subsequent thrombus formation found that interactions between a resting and a pre-formed thrombus, which contains activated platelets undergoing

sustained calcium flux oscillations, must occur within a temporal window of less than 0.6 seconds in order for the signal to be propagated [46]. This activation was dependent upon the platelets coming into contact when the activated cell was expressing its peak calcium flux. Therefore, calcium flux propagation appears to be dependent upon timely and intimate platelet interactions between activated and resting platelets. At the location in the flow loop just downstream of the orifice, at least some of the platelets have been activated by the shear stress both inside and at the orifices. With a time of 0.6 seconds between initial platelet activation by shear and subsequent activation of adjacent platelets by communication of a calcium flux via contact with the activated platelet [46], the residence times downstream of the orifice, especially if the platelet is entrapped in a vortice, are crucial to propagation of platelet activation. Once the blood leaves the chamber it is mixed in the centrifugal pump with platelets that are most likely no longer activated or at least beyond the stage at which they can propagate activation. Thus, if platelet aggregation is to occur it is dependent upon activated platelets propagating a calcium flux to other platelets within 0.6 seconds of initial activation.

Although these different residence times must play a part in the thrombus formation in this system, other evidence does not imply that TAT would be formed in the absence of the high shear stresses imparted during flow through the smaller orifices. To test whether the blood was in an artificially thrombogenic state after the addition of the calcium, the blood was sampled at the end of the experiments and placed in glass test tubes to measure the whole blood clotting times. However, in every case the clotting time was infinite. These results are contrary to what was seen in bench tests at higher citrate to Ca^{2+} ratios in which the blood did clot after an average of 200 seconds. Thus, it appears

that contact activation has a higher Ca^{2+} requirement than does shear stress-mediated platelet activation and subsequent thrombus formation.

The role of residence time and varying shear stress with the same size orifice was investigated using the 800 μm round orifice at both higher and lower flow rates than the normal 800 μm round orifice experiments. At the higher flow rate, the pump speed had to be increased to increase the flow rate. The higher pump RPMs resulted in unacceptable temperature increases (up to 104 ° F) and consequent high levels of hemolysis (Figure 6.1.3.2.1). Thus, these results were not considered valid to show the effect of elevated shear stress with the same orifice size. However, the low flow rate experiments were successful, and these results showed that decreasing the flow rate did not increase the TAT levels compared to the 800 μm round orifice normal shear stress experiments (Figure 6.1.3.1.1). This result shows that it was not only the lower flow rate and consequent lower Reynolds number for the 400 μm round orifice that caused significant TAT production compared to the 800 μm round orifice. The 400 μm round orifice had higher WSS (Table 6.3.1) than either the normal or low flow 800 μm round orifice experiments with estimated values of 19,100 dyn/cm^2, 9,200 dyn/cm^2, and 6,000 dyn/cm^2 for the 400 μm round, 800 μm round normal, and 800 μm round low flow experiments, respectively. This WSS for the 400 μm round orifice is nearly twice that for the 800 μm round orifice under normal conditions with similar durations of exposure for the individual platelets. Thus, the TAT formation resulting from flow through the 400 μm round orifice is most likely a combination of the resulting high WSS and downstream stagnation regions.

Because of the short exposure time of the platelets to these high WSS of approximately 0.1 ms for each pass through the orifice, it may not be reasonable to assume that they are being activated by shear stress alone. In addition, the dependence upon passes discussed earlier for the 200 μm round orifice experiments implies that the flow loop itself may be responsible for placing the platelets in a state in which they are primed for activation due to the action of the centrifugal pump and the presence of foreign materials. In this primed state, the platelets can aggregate in response to stagnation regions thus propagating the coagulation cascade. In this system the addition of Ca^{2+} provides the final stimulus to enable coagulation and TAT formation. Although this contact activation of the platelets is not the effect that was initially desired, it may be similar to what is happening *in vivo* due to the implantation of foreign materials in the form of MHVs or other vascular devices.

However, in discussing the possibility for the steady flow loop to place the platelets in a primed state, the cumulative effect of exposure to the wall shear stresses and Reynolds stresses encountered by the platelets as they pass through the orifices cannot be ignored. The cumulative exposure times for the different orifices are 0.8 ms, 3.5 ms, 11.7 ms, and 24.9 ms for the 200 μm, 400 μm, 800 μm, and 1200 μm round orifices, respectively. These cumulative exposure times, especially for the larger orifices with higher flow rates, are sufficient to completely activate the platelets at the WSS and RSS levels present in these experiments. Control experiments without an orifice demonstrated a cumulative PF4 concentration of approximately 220 ng/ml. When compared to the cumulative PF4 levels found for the 400 μm and 1200 μm round orifices of 480 ng/ml and 990 ng/ml, respectively, it is evident that the although the pump and the rest of the

steady flow loop contribute to platelet activation in this system, they are not the dominant factor. Also, because of the larger volume of the pump head compared to the orifice plate, the exposure time in the pump is approximately 65% of the time that the blood spends in the steady flow loop. Thus, a larger contribution to platelet activation would be expected if the pump appreciably activates the platelets. For the control experiments at a flow rate of 3.4 l/min, the estimated amount of passes through the pump for each platelet at the end of the experiment was greater that 2500. Thus, when normalized by passes, the cumulative PF4 release for the control experiment and the 400 μm and 1200 μm round orifice experiments was 0.088 ng/ml*pass, 13.7 ng/ml*pass, and 4.0 ng/ml*pass, respectively. This implies that the flow through the orifice has a substantially greater contribution to platelet activation than flow through the pump head.

The result that the slit orifices did not produce a measurable increase in TAT concentration (Figure 6.1.2.1.1) contradicts a leakage jet study from Travis et al in which higher RSSs were measured in the jets through the B-datum line than through the hinge [17]. The analysis by Travis et al indicated that planar free jets may be more unstable than other leakage jets (round free jets and wall jets) based on its transitionally turbulent nature leading to faster spreading of the jet and thus more damaging to blood elements [17]. However the planar jets in the current study did not exhibit more instability than the round jets. The planar jets studied in Travis et al also differed in size and shape from the slit orifice jets and had different maximum velocities. The two planar jets were 4 mm x 1 mm with a maximum velocity of 0.41 m/s and 2.8 mm x 0.8 mm with a maximum velocity of 0.78 m/s. Both of these jets had Reynolds numbers above 30. The maximum velocities of the jets in the current study were between 5 and 8 m/s with Reynolds

numbers above 160. These higher jet Reynolds numbers indicate that the slit jets in the current study are turbulent jets and are not directly comparable to the transitional jets from Travis et al. Furthermore, higher RSS values are not the only factor taken into consideration for propagation of the coagulation cascade. The presence of stagnation or circulation regions downstream of the high RSSs are also necessary.

DPIV was used to further investigate these flow fields and to illuminate the important differences between these different flow fields that could result in TAT formation for the smaller orifices but not for the larger orifices. These measurements showed that the 400 μm round orifice jet had a lower velocity than the 800 and 1200 μm jets and dissipated more rapidly (Figures 6.2.1.1.1, 6.2.1.1.4, and 6.2.1.1.8). Also, the flow field appeared to be more unstable, although this could have been due to problems with the DPIV measurements since the particles had a tendency to aggregate and occlude the 400 μm round orifice. To alleviate the orifice occlusion, the particle number and size were decreased, which resulted in a non-optimal seeding density for the cross-correlation scheme. The filter settings for the post-processing had to be relaxed to allow for the calculation of vectors from only one or a few particles in the flow. Thus, more noise was introduced into the measurements for the 400 μm round orifice DPIV experiments. Averaging the image pairs did help to remove some of the noise, but in doing so, low velocity vectors, which may or may not have been real or may not have been in the jet centerplane, were included in the averaged velocity field.

One important difference between the 400 μm round orifice jet and the 800 μm round orifice jets is the velocities in the recirculation regions on either side of the jet (Figures 6.2.1.1.2 and 6.2.1.1.5). The reverse velocity magnitudes in this region for the

800 µm round orifice jet were twice that for the 400 µm round orifice (-0.09 m/s versus -0.18 m/s) Thus, as was shown qualitatively in the flow visualization studies discussed earlier, platelets that become entrapped in these regions will remain in them longer for the 400 µm round orifice than for the large orifices. Stream traces placed in the flow for both of these orifice jets shown in Figure 7.2.1 demonstrate the potential entrapment pathways for these platelets. Vortices are also evident downstream of the jet where platelets can become entrapped and aggregate. These aggregates can travel through the flow loop and then become lodged in the orifice where they have the potential to grow into the larger thrombi that were seen at the end of the experiments.

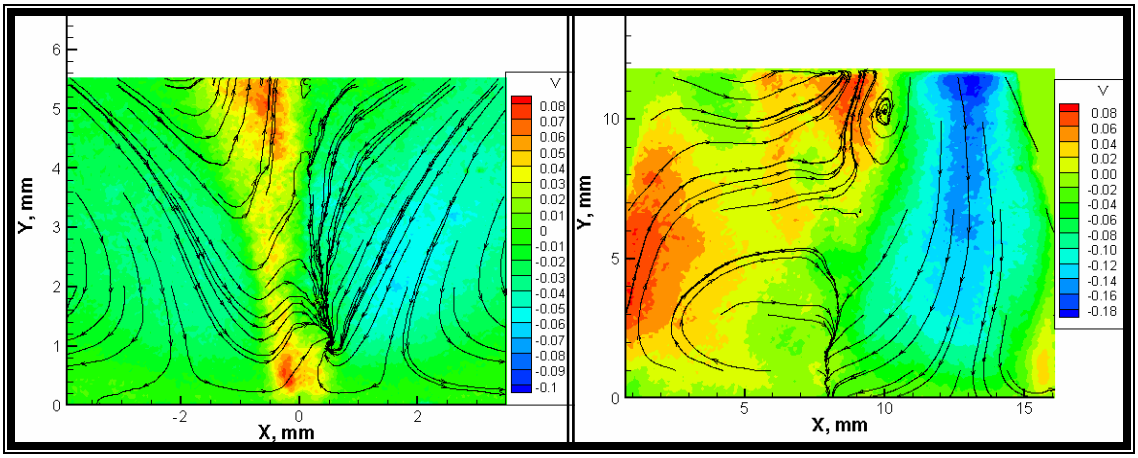

FIGURE 7.2.1. Stream traces for the 400 and 800 µm round orifice jet recirculation regions. These traces show where platelets travel from different origin points in the flow field. For both orifices, traces show a trend for the flow to impinge upon the chamber throat and return to the jet where Reynolds and shear stresses are high. There are also stagnation regions downstream of the orifice.

These pathways, in addition to bringing activated platelets together to aggregate, also potentially expose platelets repeatedly to the high Reynolds stresses (Figures 6.2.1.3.1 and 6.2.1.3.2) and high shear stresses (Figures 6.2.1.4.1 and 6.2.1.4.2) at edges of the jets. This repeated exposure, even at low levels of shear stress, can result in cumulative platelet activation.

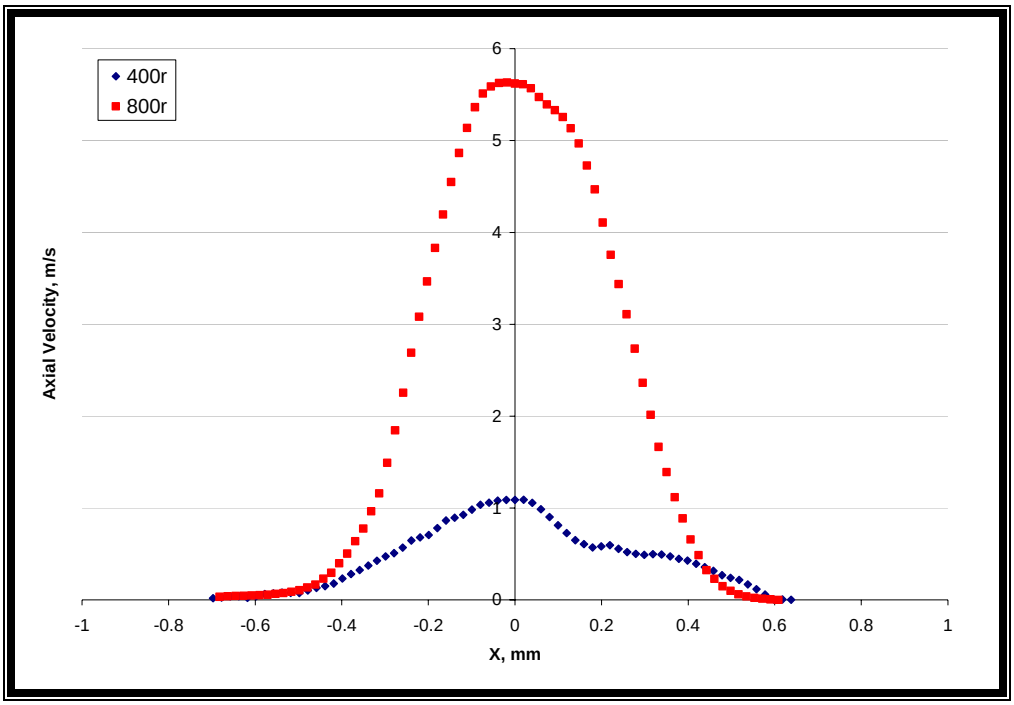

FIGURE 7.2.2. Axial profiles of streamwise velocity 1 diameter downstream of the 400 and 800 µm round orifices. The 800 µm round orifice jet appears to have a more Gaussian profile characteristic of a turbulent jet.

To better understand the differences in the 400 µm and 800 µm round orifice jet flow fields, velocity cross-sections at 1 and 6 diameters downstream of the two orifices are shown in Figures 7.2.2 and 7.2.3. Besides the considerable difference in the peak centerline velocities between the two orifices, there is also a difference in the shape of the curves. The 800 µm round orifice jet exhibits a more Gaussian type curve that is more characteristic of a turbulent jet, whereas the 400 µm round orifice has a flatter profile that appears to dissipate rapidly only 6 diameters from the orifice.

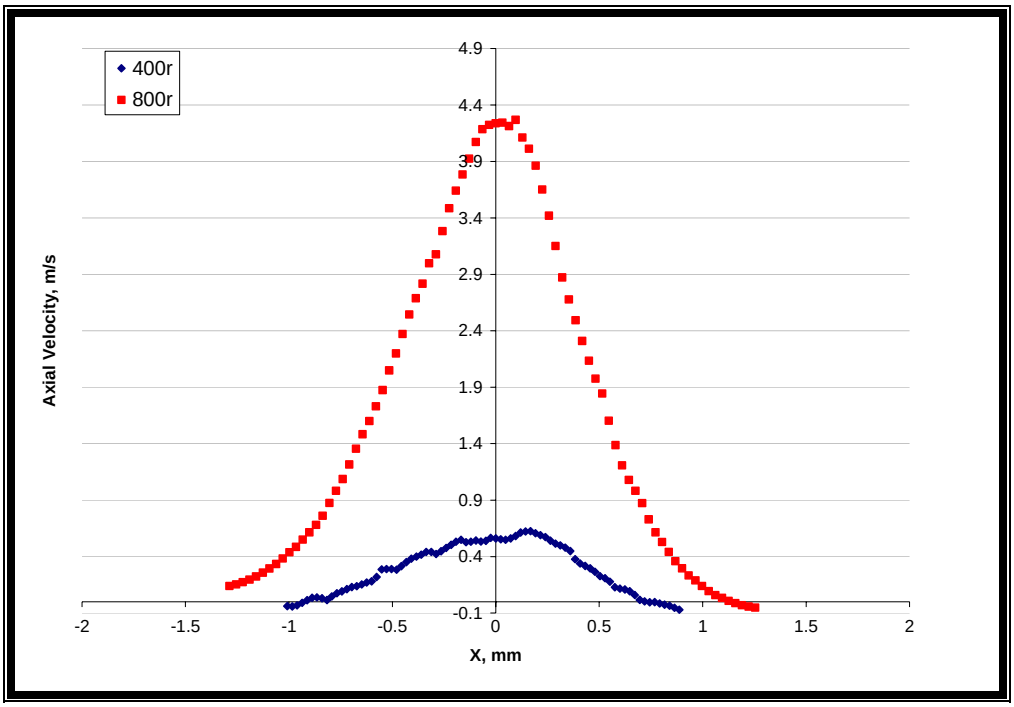

FIGURE 7.2.3. Axial profiles of streamwise velocity 6 diameters downstream of the 400 and 800 μm round orifices. The 800 μm round orifice jet appears to have a more Gaussian profile characteristic of a turbulent jet.

This dissipation can be more clearly seen in Figure 7.2.4. This plot shows the centerline velocities for the 400 and 800 μm round orifice jets as a function of the axial direction. The trendline is the mean centerline velocity decay for a self preserving round turbulent jet given by Equation 7.2.1 [65]:

$$\frac{V}{V_c} = a\left(\frac{Y - Y_o}{D}\right)^{-1} \qquad \text{Equation 7.2.1}$$

where V is the average centerline velocity at Y, Y_o is the jet origin (orifice plate location), V_c is the average centerline velocity at Y_o, D is the orifice diameter, and *a* is a constant for the type of jet. This constant has values of 5.6 and 6.5 for nozzle and pipe jets, respectively. Values of the decay constant that deviate from these accepted values can give important insight into the decay behavior of the jet. A previous study of a turbulent jet issuing into a more viscous fluid than the jet fluid has shown a dependence

of the decay constant, *a*, on entrainment [66]. This study showed that increased entrainment of the relatively stagnant fluid by the jet results in a lower jet decay constant, and, consequently, the jet decays more quickly than expected. This faster decay is due to the higher laminar shear stresses that cause the jet decay to deviate from the normal behavior of a turbulent jet. Increased entrainment is an indication that more mixing is occurring. In the case of activated platelets issuing into a relatively stagnant pool of resting platelets, increased mixing can increase the probability for propagation of platelet activation and, consequently, the coagulation cascade.

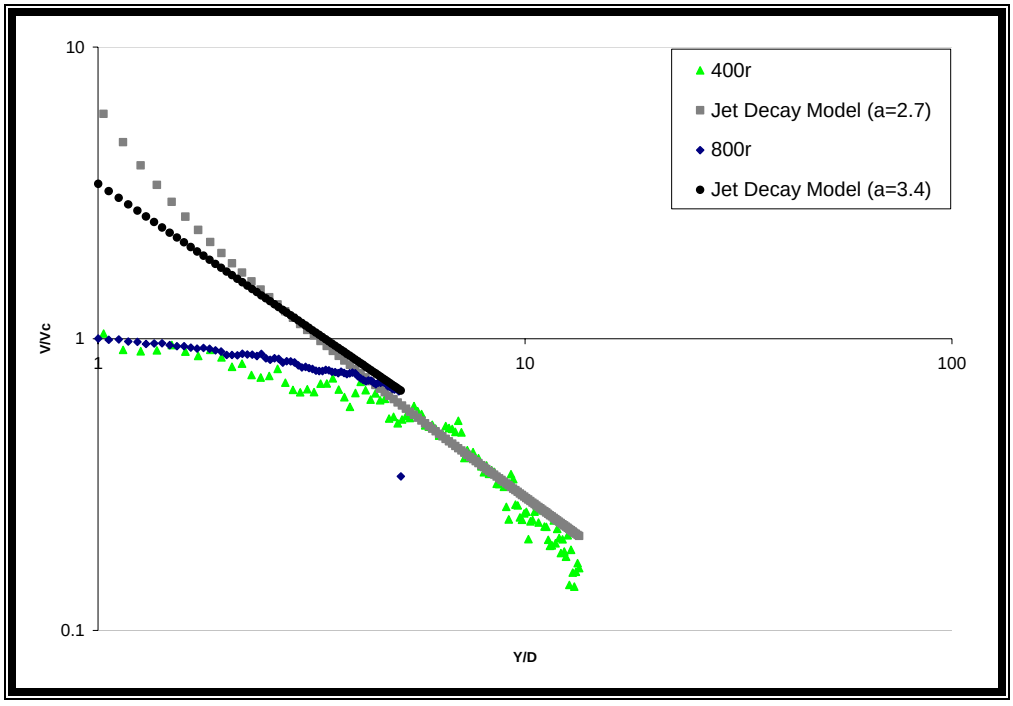

FIGURE 7.2.4. Axial centerline jet profiles for the 400 and 800 μm round orifice jets plotted with the jet decay model for self-similar round turbulent jets.

Figure 7.2.4 shows that at approximately 5 diameters, the 800 μm round orifice jet has still not entered the self-similar region. Figure 7.2.5 shows the axial centerline velocity for the 800 μm round orifice jet even farther downstream, and when it reaches 10

diameters it clearly fits this model for a self-similar turbulent jet with a decay constant of 6, which is between that for nozzle and pipe jets. The 400 μm round orifice has the correct slope for a turbulent jet between 5 and 11 diameters downstream of the orifice. However, the decay constant is lower than that for a turbulent jet. Thus, the 400 μm round orifice jet appears to entrain more of the chamber fluid than the larger jets resulting in a lower decay constant and faster decay rate. This behavior may explain its rapid dissipation since the entrainment disrupts the orderly jet structure relatively quickly. Entrainment of the relatively still chamber fluid would introduce platelets to the higher stresses in the jet potentially activating more of the platelets than if entrainment was not as prevalent. This increase in entrainment may also explain why the 400 μm round orifice jet induces TAT formation, while the 800 μm round orifice does not, even at lower Reynolds numbers.

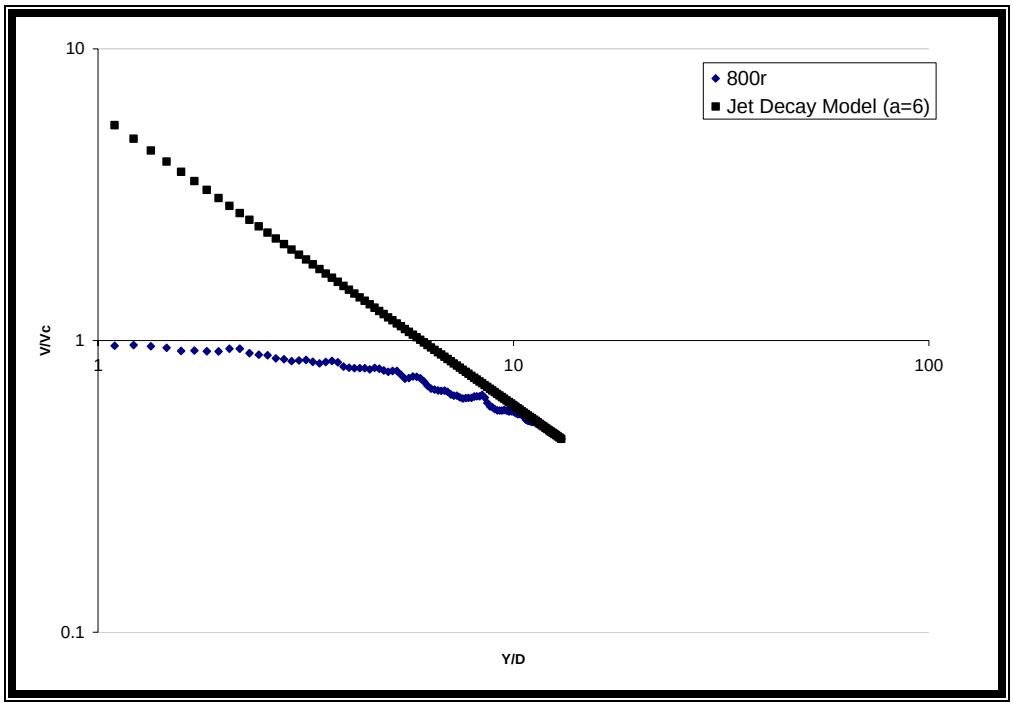

FIGURE 7.2.5. Axial centerline jet profiles beyond 10 diameters downstream for the 800 μm round orifice jets plotted with the jet decay model for self-similar turbulent jets. The 800 μm round orifice jet does correlate with the model using a constant between that for nozzle and pipe jets (5.6 and 6.5, respectively).

Figure 7.2.6 shows the centerplane jet velocities plotted versus the axial direction for the 800 μm round orifice jets under normal and low flow rate conditions. These two jets have almost the same decay curves, and the decay constants are 4.0 and 4.1 for the low and normal shear stress cases, respectively. Despite the different Reynolds numbers (570 and 340 for the normal and low flow rate cases, respectively), and consequent different velocities and shear stresses, the universal jet properties are still the same. Therefore, it may be orifice size, and not the flow rate through the orifice that determines these jet properties at the Reynolds numbers tested in this study. This similarity in these jets may explain why there was no difference in TAT formation between the normal and low flow rate experiments with the 800 μm round orifice.

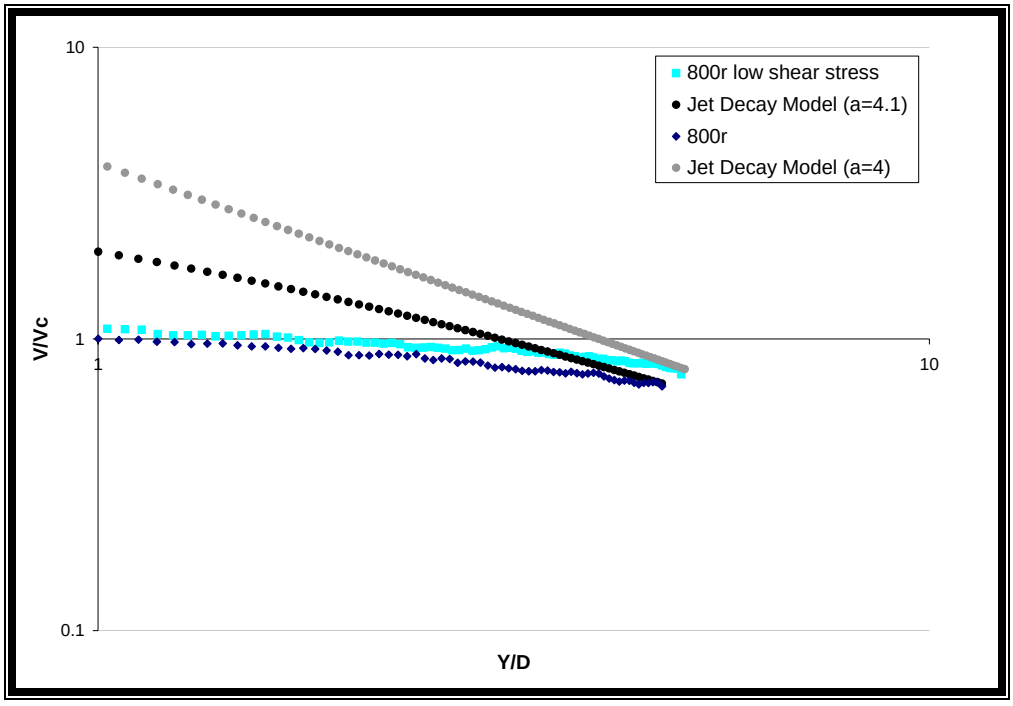

FIGURE 7.2.6. Axial centerline jet profiles for the 800 μm round low and normal shear stress orifice jets plotted with the jet decay model for round self-similar turbulent jets.

Despite the lower flow rate, the low flow rate jet did not demonstrate the rapid dissipation resulting from the increased entrainment that was seen in the 400 μm round orifice jet. It is this greater mixing of the jet flow with the relatively stagnant chamber fluid that appears to be key for inducing thrombus formation in this system.

7.3. Channel experiments

The channels used in this study model the geometrical features of the hinge region of various bileaflet MHVs (Figure 6.1.5.1). For the smaller channels with a minimum diameter of 400 μm, there was no significant difference in TAT formation. Thus, for this diameter, size was more important than the geometry in initiating coagulation resulting in subsequent thrombus formation. Since the minimum diameter of these smaller channels were the same as that of the 400 μm round orifice, the resulting TAT formation is most likely due to the same mechanism as that for the 400 μm round orifice. However, the elevated TAT levels for the larger channels indicates that there must be a difference either in the jets or in the internal channel fluid dynamics that results in an increased propensity for thromboemboli formation for some of the channels. The PF4 results (Figure 6.1.5.2.1) showed that there was no significant difference in platelet activation between the different channels, and PF4 release for all of the channels was above 400 ng/ml, which shows that platelets were mechanically activated above the baseline level (7 ng/ml) for all of the channels. Furthermore, PIV results for the larger channels showed similar flow fields (Figures 6.2.3.1.2, 6.2.3.1.4, 6.2.3.1.6, and 6.2.3.1.8) and similar Reynolds stress (Figures 6.2.3.3.1-6.2.3.3.4) and shear stress levels (Figures 6.2.3.4.1-6.2.3.4.4). To further investigate the differences in the jet flow fields, the flow profiles 1

diameter and 5 diameters downstream of the channel exit were plotted for all of the channels (Figures 7.3.1 and 7.3.2). Although the centerline velocities were not the same for all of the channels due to the different flow rates through the channels (Table 7.3.1), the shape of the profile did fit with the expected Gaussian profile for turbulent jets. The velocities for Channels 4 and 8 were lower than expected from the estimated values, which indicates that the actual profile was flatter than the parabolic profile used to estimate the velocities. The Channel 8 profile 5 at diameters downstream of the channel was noticeably flatter than the other profiles at this point.

TABLE 7.3.1. Flow rates and estimated centerline velocities for the large channels.

Channel	Flow Rate, l/min	Estimated Velocity, m/s
2	0.17	5.6
4	0.14	4.6
6	0.15	5.0
8	0.12	4.0

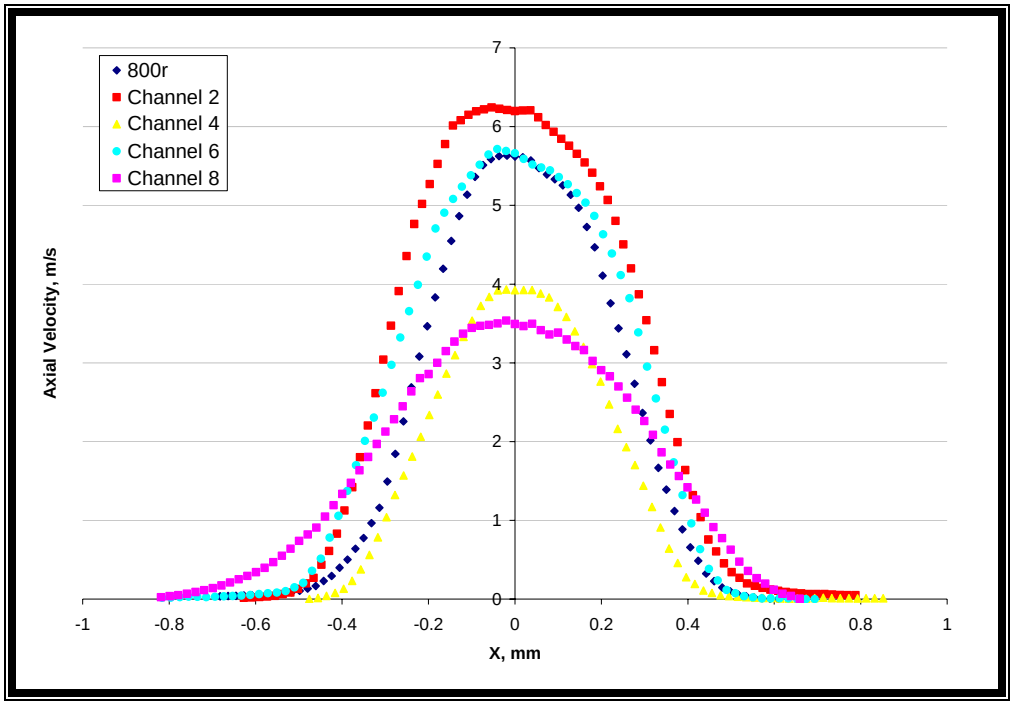

FIGURE 7.3.1. Axial profiles of streamwise velocity 1 diameter downstream of Channels 2, 4, 6, and 8 Although the velocities differ, the shapes of the flow profiles are similar and have a Gaussian profile.

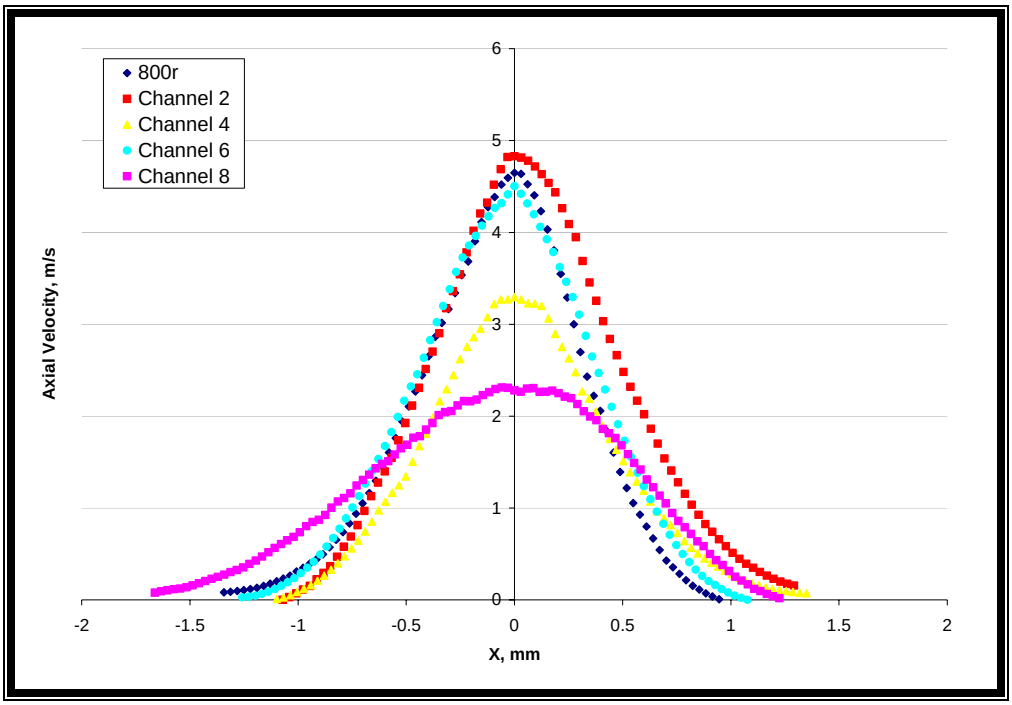

FIGURE 7.3.2. Axial profiles of streamwise velocity 5 diameter downstream of Channels 2, 4, 6, and 8 Although the velocities differ, the shapes of the flow profiles are similar and have a Gaussian profile.

The jet decay for these channel jets was investigated further by fitting Equation 7.2.1 to the log-log plots of the normalized centerline velocity versus the axial direction normalized by the minimum channel diameter. Figures 7.3.3, 7.3.4, 7.3.5, and 7.3.6 show these plots for Channels 2, 4, 6, and 8, respectively. At locations greater than 5 diameters downstream of the channel exit, the Channel 2 and Channel 6 jets correlated well with the jet decay model with decay constants, *a*, of 4.3 for both of them, which is close to the accepted literature values between 5 and 6. However, Channels 4 and 8 had decay constants of 2.6 and 2.75, respectively, indicating that these jets may have had more entrainment of the chamber fluid, which caused the jet to dissipate more rapidly. This entrainment may result in increased interaction between the activated platelets thus increasing the chance for propagation of platelet activation and the coagulation cascade. Since all other flow parameters were maintained the same except for the channel

geometry, the internal sharp edges in Channels 4 and 8 are responsible for this increase in entrainment indicated by the decrease in the decay constant. Thus, the sharper edges may increase the jet's propensity for entrainment making it more vulnerable to mixing of the relatively stagnant chamber fluid with the jet flow and consequent rapid dissipation.

Since PF4 release (Figure 6.1.5.2.1) was similar for all of the channel experiments showing comparable levels of platelet activation, this greater amount of mixing for the channels with sharper edges appears to be instrumental in enabling propagation of the coagulation cascade as demonstrated by greater TAT formation for these channels. Thus, an increase in TAT production for Channels 4 and 8 versus Channels 2 and 6 (Figure 6.1.5.1.2) is dependent upon differences in the flow fields for these different jets. Significantly more entrainment for the Channel 4 and 8 jets relative to the Channel 2 and 6 jets indicates a greater amount of mixing of the fluid in the chamber and thus more stagnation. A lower jet decay constant also implies that the jet has been hampered in its development compared to the jets with higher jet decay constants and has thus been unable to develop into a characteristic turbulent round free jet. This behavior suggests that the internal geometry of Channels 4 and 8 induces flow fields inside the channel that affect the jet character. These internal flow fields may also enable coagulation to be initiated within the channels that is propagated as the jet exits. In this case, mixing of the jet downstream of the channel would amplify this effect resulting in increased TAT formation.

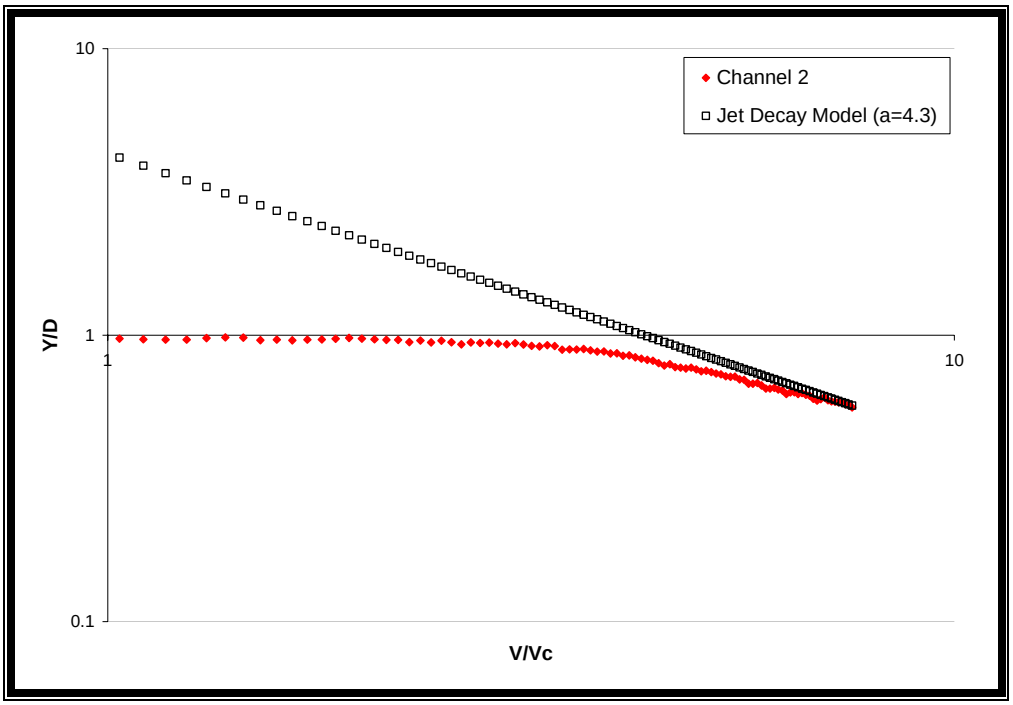

FIGURE 7.3.3. Axial centerline jet profiles for Channel 2 plotted with the jet decay model for round self-similar turbulent jets. The correlation with the turbulent decay model is good beyond 6 diameters downstream of the channel with a jet decay constant of 4.3, which is close to the accepted values of 5 to 6 for a round turbulent jet.

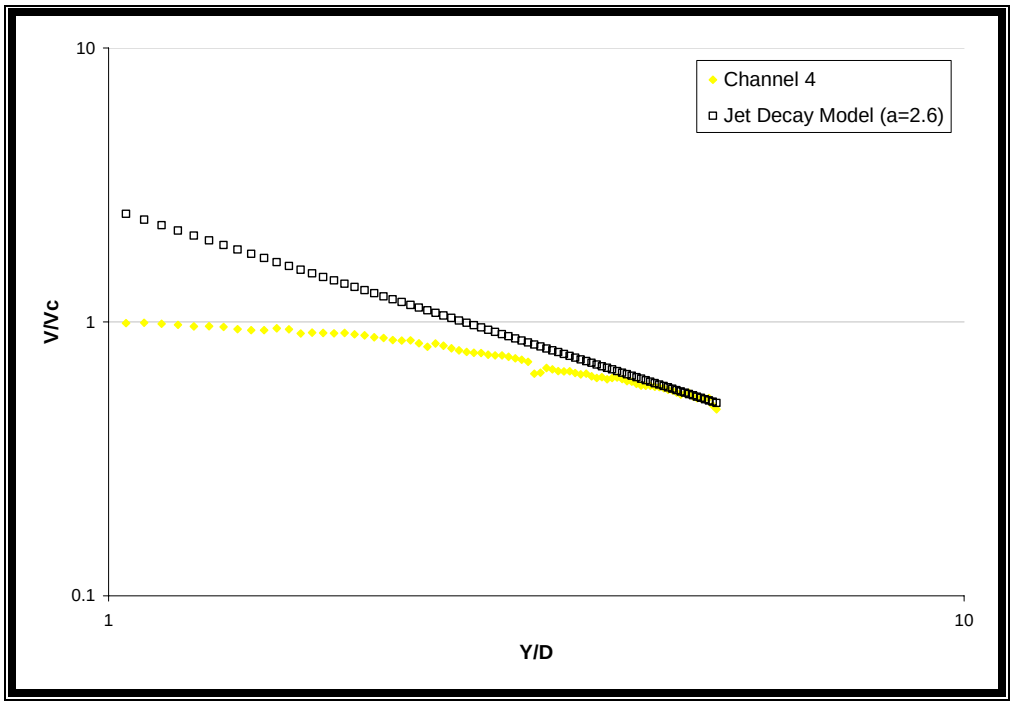

FIGURE 7.3.4. Axial centerline jet profiles for Channel 4 plotted with the jet decay model for round self-similar turbulent jets. The decay function has the same slope as that for a round turbulent jet, but the decay constant (a=2.6) is much lower than the accepted values for a round jet indicating that there may be a significant amount of entrainment.

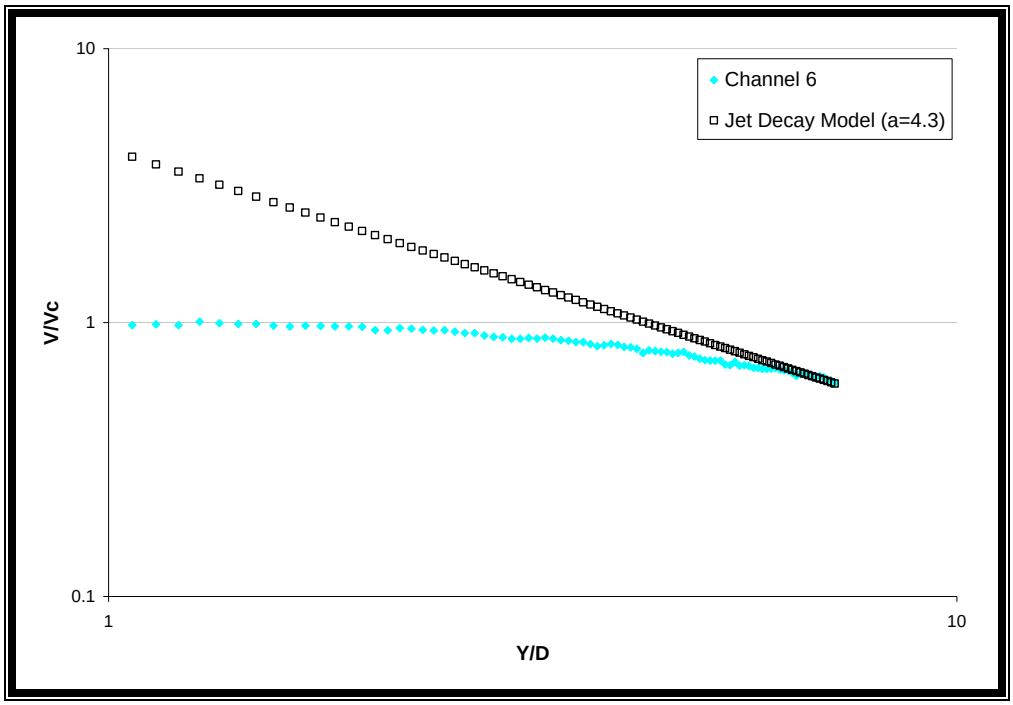

FIGURE 7.3.5. Axial centerline jet profiles for Channel 6 plotted with the jet decay model for round self-similar turbulent jets. The correlation with the turbulent decay model is good beyond 6 diameters downstream of the channel with a jet decay constant of 4.3, which is close to the accepted values of 5 to 6 for a round turbulent jet.

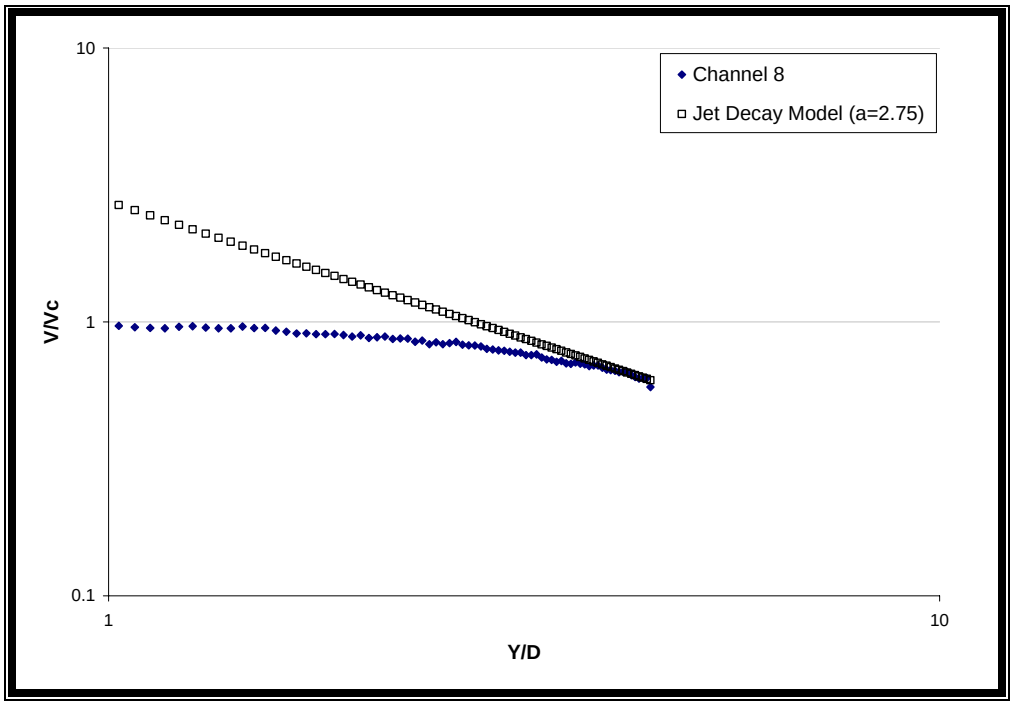

FIGURE 7.3.6. Axial centerline jet profiles for Channel 8 plotted with the jet decay model for round self-similar turbulent jets. The decay function has the same slope as that for a round turbulent jet, but the decay constant (a=2.75) is much lower than the accepted values for a round jet indicating that there may be a significant amount of entrainment.

Animations of instantaneous vorticity measurements (movies 7.3.1, 7.3.2, 7.3.3, and 7.3.4 for Channels 2, 4, 6, and 8, respectively) also show the susceptibility of the Channel 4 and 8 jets to entrainment compared to the Channel 2 and 6 jets. Although all of these jets demonstrate significant vorticity and transverse movement of the jet, the Channel 4 and 8 jets begin to expand at locations nearer to the jet origin than do the Channel 2 and 6 jets. The vortices on either side of the Channel 4 and 8 jets appear to infiltrate theses jets closer to the jet origin than is the case for the Channel 2 and 6 jets.

7.4. Mechanical heart valve experiments

Previous *in vitro* blood studies with bileaflet MHVs have been isolated to the assessment of platelet activation [49] or damage, and most of these used only platelets [50] or porcine blood [16], not whole human blood. However, no other *in vitro* human blood studies have been performed to investigate the procoagulant potential of different bileaflet MHVs. Thus, one of the aims of this study was to show *in vitro* that hinge gap width and the hinge geometry affect both platelet activation and the propensity for coagulation. Both of these factors did in fact affect platelet activation and coagulation.

In the experiments to assess the affect of hinge gap width, both the high leaker and the low leaker prototype valves induced significantly more PF4 release than the SJM Standard valve (Figures 6.1.6.2.2 and 6.1.6.2.3). The hinge geometry of these valves does not differ significantly, thus the only difference was the hinge gap width, which was estimated to be 80 μm, 100 μm, and 230 μm for the low leaker, the SJM Standard, and the high leaker valves, respectively (Table 5.1.7.1.). Previous fluid dynamics studies with LDV [25] have shown than the flow fields through the low and high leaker valves and the

SJM Standard valve differ mainly in the leakage jet size as shown in Figure 7.4.1. The high leaker valve has the largest leakage jets, thus, more platelets may be exposed to

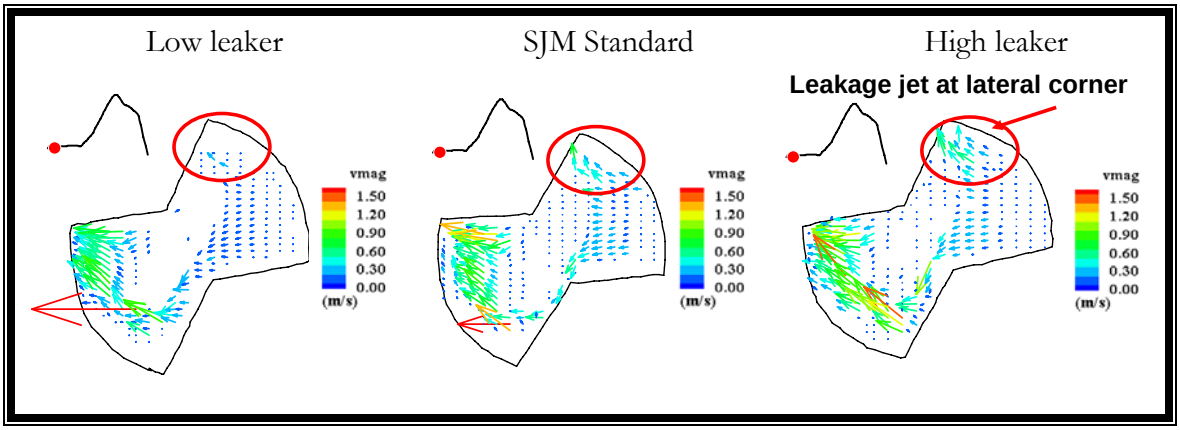

FIGURE 7.4.1. Flow fields for the the low leaker prototypw, SJM Standard, and high leaker prototype valves acquired via LDV. These flow fields show the leakage jet at the lateral corner, which is the main difference between the valve leakage flow fields [25].

the high shear stresses in the hinge region. Additionally, the low leaker valve is subject to higher viscous stresses and more stagnation due to the smaller hinge gap and decreased flow through the hinge region. Gap width was also shown in this study to affect TAT formation, or the procoagulant potential of the valve. The low leaker prototype valve demonstrated significantly greater TAT formation (Figures 6.1.6.1.2 and 6.1.6.1.3) than the SJM Standard valve. This valve had lower flow rates through the hinge region, thus as was the case for the smaller round orifices, the recirculation regions after the valve may have had lower velocities giving the activated platelets more time to mingle and aggregate. Figure 7.4.1 does show lower flow in the area of the leakage jet at the lateral corner of the hinge compared to the SJM Standard and high leaker prototype valves, thus, this region may be vulnerable to thrombus formation. Additionally, estimation of the viscous shear stresses through these hinge areas assuming Newtonian flow through a long narrow channel show yield values for the viscous shear stresses in the high and low

leaker hinge gaps of 470 and 9450 dyn/cm^2, respectively [49]. These high estimated viscous stresses for the low leaker valve may explain the significant amount of PF4 release compared to the SJM Standard valve despite the smaller leakage jet. The estimated viscous shear stress value for the SJM Standard valve was 1080 dyn/cm^2, which is considerable less than that for the low leaker valve. Thus, the SJM Standard hinge gap size provides a balance between the high and low leaker hinge gap width that minimizes leakage volume without inducing excessive viscous stresses and enabling the formation of stagnation regions.

This study also showed that hinge geometry affects procoagulant potential but not platelet activation. The MP valve was used as an extreme example of an unfavorable hinge geometry, and this valve was compared to the SJM Standard valve, which has a very smooth hinge geometry with minimal change in hinge diameter (Figure 2.3.2). Figure 7.4.2 shows the exact geometry of the MP hinge channel as measured by the LDV probe volume [15]. In the current study the MP valve demonstrated significantly

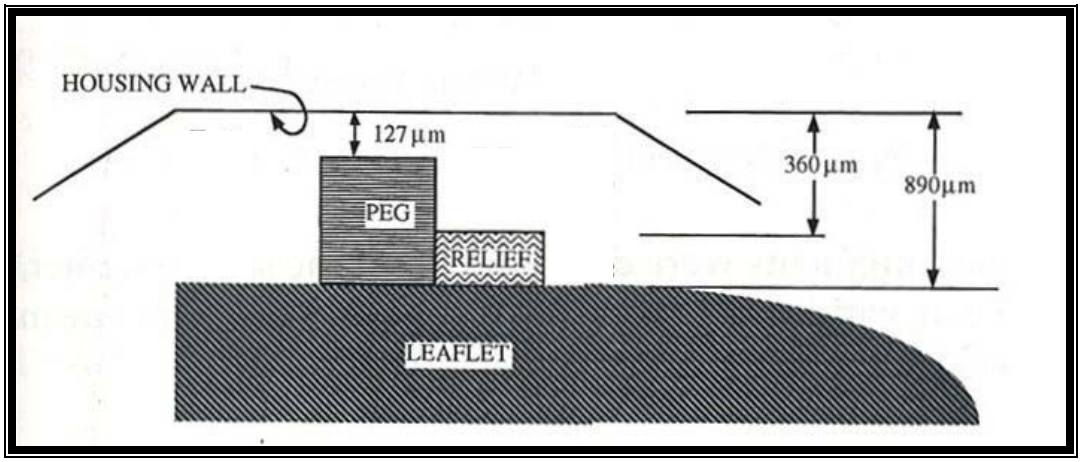

FIGURE 7.4.2. Diagram of the MP valve hinge. The peg and the relief are the mechanism by which the leaflet opens and closes in the hinge recess [15].

higher TAT formation (Figures 6.1.6.1.2 and 6.1.6.1.3) than the SJM Standard valve without higher levels of PF4 release (Figures 6.1.6.2.2 and 6.1.6.2.3). However both the SJM Standard and the MP valves did exhibit PF4 levels greater than 300 ng/ml, which is an order of magnitude higher than the clinical baseline level (20 ng/ml) indicating mechanical platelet activation. Thus, the multiple steps in diameter with 90 degree angles present in the MP hinge region must engender flow conditions that are conducive to flow stasis and recirculation that enables platelet aggregation and subsequent thromboemboli formation. This valve was in fact removed from the market during clinical trials because of excessive thromboembolic complication rates, and hemodynamic studies of the hinge region [23] [15] detailing the MP valve leakage flow fields have shown vortical flow patterns and stagnation regions. These leakage flow fields measured with LDV are shown

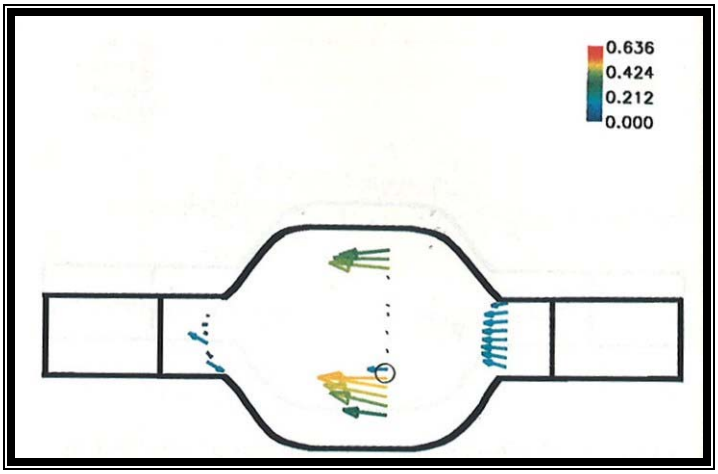

FIGURE 7.4.3. LDV measurements of leakage flow within the hinge of the MP valve. Vector colors indicate velocity (m/s). The central region is characterized by a stagnation region with low flow, and the vectors at the outflow region indicate vortice formation. High velocity vectors are present at the top and bottom flowing around the peg [15].

in Figure 7.4.3. In this figure the velocity vectors along the inflow channel suggest a vortical flow pattern, and the reverse velocities near the center were only 0.05 m/s, which is essentially stagnant flow where activated platelets can aggregate. Higher velocity flow

is directed over the peg resulting in laminar shear stresses of about 200 dynes/cm^2, which is sufficient for platelet activation. The converging flow at the outlet provides another region where activated platelets can interact. Flow visualization studies by Gross et al (Gross, 1996) with hydrogen bubbles have illuminated these flow pathways even more. The schematic in Figure 7.4.4 shows that there in the stagnation region downstream of the peg, there is significant recirculation and unstable flow patterns where activated platelets may be entrapped and propagate the coagulation cascade. Computational fluid dynamics (CFD) was also performed to investigate these flow patterns, and these studies gave similar results as shown in Figure 7.4.5 [23]. The flow patterns in the hinge of the SJM Standard valve do not exhibit this type of unstable behavior since the blood is able to flow over the hinge protrusion with minimal impedance.

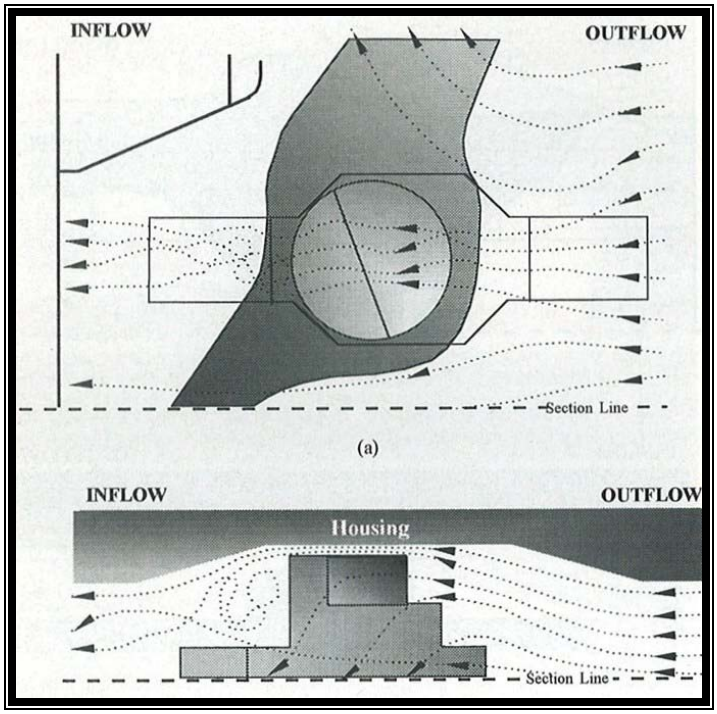

FIGURE 7.4.4. Schematic of leakage flow fields through the MP valve visualized using hydrogen bubbles. Vortice formation is evident downstream of the peg [23].

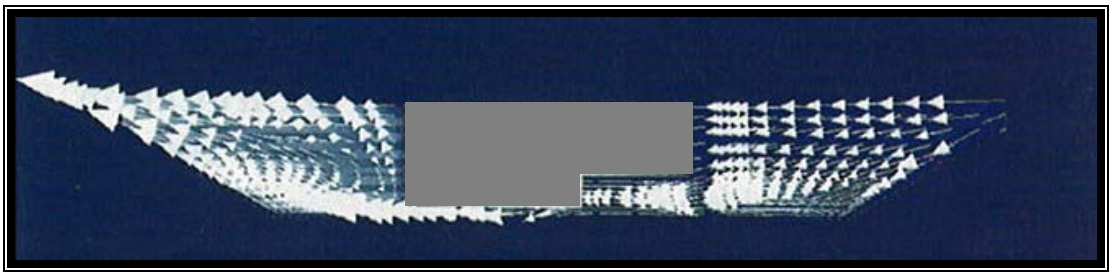

FIGURE 7.4.5. Leakage flow fields through the MP valve simulated using CFD. Vortice formation is evident downstream of the peg [23].

The platelet activation results for the high leaker prototype valve are corroborated by previous studies with the same valves that also used PF4 as an endpoint [49]. Figure 7.4.6 shows the PF4 results from the previous study. In this study, there appears to be a plateau in the PF4 values after 60 minutes, which may indicate that the PF4 concentration has reached a limiting value in the flow loop. The values for the previous study at 60 minutes, at which point significance was nearly reached with a p-value of 0.083, are similar to those from the present study as shown in Figure 7.4.7.

In addition to illuminating the importance of the hinge geometry and gap width on platelet activation and propensity for thromboemboli formation, this study also describes a system that can be used to investigate these parameters for other vascular devices that expose the blood to high or varying shear stresses. This methodology has the sensitivity to detect changes in both platelet activation and thromboembolic potential based on changes in the hinge geometry. It also has a small volume requiring only relatively small amounts of human blood that can be drawn from one donor. Thus, this study provides a simple yet powerful methodology to investigate various vascular devices for both platelet activation and thromboembolic potential.

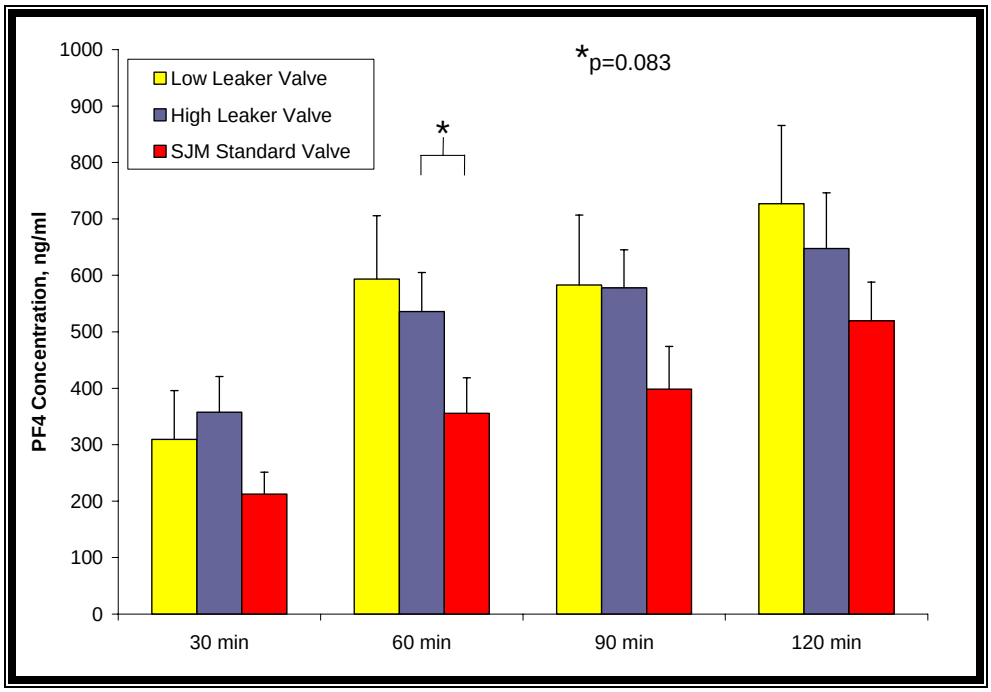

FIGURE 7.4.6. Data from a previous in vitro steady flow study using the SJM Standard valve, low leaker prototype valve, and high leaker prototype valve [49].

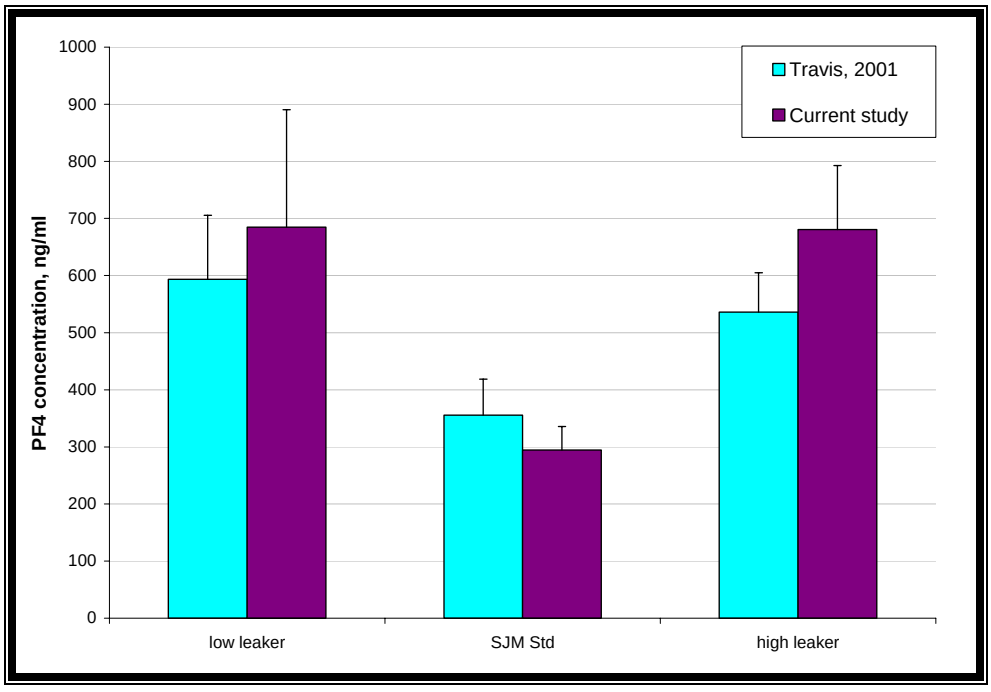

FIGURE 7.4.7. Combined PF4 data for the current study and Travis et al at 60 minutes. This time represented the endpoint for the current study, but only the midpoint for Travis et. al. Values are similar and there was a plateau around these values for Travis et al.

CHAPTER 8

STUDY LIMITATIONS

8.1. Blood experiments

The blood studies have certain limitations because of the *in vitro* nature of the experiments and because whole blood was used with as little manipulation as possible. The goal of the study was to characterize coagulation in response to flow through small orifices while maintaining the blood in as close to a normal state as possible. In doing this, the blood was not manipulated to keep RBC and platelet counts constant. However, these were measured and the deviations from the average values were less than 15% between different donors. Continuous recalcification was performed to slowly reverse the effect of the sodium citrate, but it was not possible to bring the blood back to normal clotting times without resulting in gross thrombosis of the entire flow loop. To further maintain this normal state of the blood, it was used within 3 hours of being drawn from the donor to ensure that haemostasis factors would not degrade. To make this possible the duration of the experiments was kept at 60 minutes. However, in comparing these results to others by Travis et al, this duration appears to be sufficient for reproducible results. Beyond 60 minutes there appears to be a leveling off of PF4 concentrations indicating the platelets may be refractory at this point. Also, in this study TAT concentration began to level off between 45 and 60 minutes indicating that the haemostasis factors may be beginning to break down. Another limitation was that experiments were performed at room temperature. However, although SIPA has been shown to increase significantly at

temperatures below 37 °C, there was not a concomitant increase platelet activation [67] or in the haemostasis factors that indicate thrombus formation [68]. Thus, since these experiments serve to compare outcomes between different geometries under the same conditions, temperature was not considered a factor that would alter these comparative results. Also absent are factors associated with blood vessels and blood vessel injury, as well as filtration, dilution, and inactivation mechanisms as occur *in vivo*.

This study also has certain limitations due to the simplicity of the orifice model for the MHV geometry. Because the aim was to isolate the hinge region and b-datum line there are no moving parts. Consequently, the intentional washing of the hinge area that occurs each time the leaflets open and close is not present. This washing is meant to sweep any aggregating platelets from the hinge area before a clot can form. Another limitation is that flow through the model is steady instead of pulsatile. The absence of pulsatile flow means that there is no change in the flow field as there is *in vivo*.

8.2. DPIV experiments

The limitations of the DPIV studies were mainly due to the small size of the orifices relative to the particle size. The orifices and channels with diameters of 400 μm or less were prone to occlusion due to aggregation of the 1-20 μm fluorescent particles over time resulting in a decrease in the flow rate until it became zero. Smaller 1-2 μm glass microbeads were tried, but they did not emit enough light to be imaged using the zoom lens. Smaller 1 μm fluorescent particles were also used, but they were also not bright enough to be used with the zoom lens. The final solution, which was adequate for the 400 μm round orifice was to filter the larger fluorescent particles with a 5 μm filter so that

they would be between 1 and 5 μm in diameter. This solution did, however, result in lower particle density. Thus, the measurements for the 400 μm round orifice may not have been as accurate as those for the larger orifices and channels.

Another limitation of the DPIV study was that we were duplicating the flow loop used in the blood studies. Thus, the entrance length was not sufficient to assume a fully-developed flow profile at the inlet. This assumption is necessary for the jet calculations used in the discussion. However, since the orifices were quite small compared to the chamber diameter ($D_{chamber}/D_{orifice}<0.05$), this probably did not greatly influence the calculations.

Another limitation was introduced by the laser light arm that was used to transport the laser sheet to the experimental setup. As the laser beam traveled through this arm, small errors in the mirror positions at each bend were propagated resulting in an enlargement of the laser spot diameter at the outlet of the laser arm. Thus, the laser sheet was limited to a thickness of 0.8 to 1 mm. For the 400 μm round orifice, this resulted in low velocity out of plane particles being included in the jet flow field. These lower velocity particles may have biased the velocity measurements so that the average centerline velocity was lower than anticipated by the measured flow rate. This behavior was not seen for the larger orifices.

CHAPTER 9

CONCLUSIONS

This study describes the development of a system to recalcify citrated human blood to assess the thrombogenic potential of different devices in an in vitro steady flow loop. The significant findings were that: 1) recalcification of recirculating citrated blood markedly increases the magnitude of thrombus forming reactions and the sensitivity for their detection; 2) a shear-dependent threshold for thrombin generation and coagulation exists, suggesting that thrombosis in a MHV is most likely due to leakage flow through the hinge area and not through the B-datum line; 3) platelet activation, and the presence of adequate platelet numbers, may be essential for the activation of coagulation under conditions of high shear; and 4) coagulation can be inhibited by blocking the platelet receptors that facilitate platelet aggregation.

The shear-induced nature of the system was confirmed by the inhibition of thrombus formation by blocking two platelet receptors, GPIIb/IIIa and GPIb, that are crucial to shear-induced platelet activation and aggregation. Histological results further showed the evolving morphology of the formed thrombus under the high shear flow conditions. Based on these results this system can be used to assess differences in procoagulant potential of various geometries under steady flow conditions. Even though the specific application for this study is MHV hinge geometries, it can also be used to study the procoagulant potential of other medical devices that are exposed to blood under varying shear conditions such as stents, septal devices, and vascular grafts.

The results from the DPIV studies give some insight into why the different channels resulted in varying propensities for thrombosis as measured by TAT concentration. The channel geometries that induced significantly higher levels of thrombosis also formed jets that were subject to increased entrainment of the stagnant fluid in the chamber. Entrainment enables more mixing of the shear-activated platelets with the surrounding flow, which can propagate the coagulation cascade, thus increasing the chance for thrombus formation. The channel geometries that produced these less stable jets had abrupt changes in diameter with 90 degree angles. Thus, these abrupt changes in diameter engender flow fields that are more favorable for coagulation.

The influence of abrupt changes in diameter was also evident in the human blood studies designed to investigate the effect of MHV hinge geometry. The MP valve, which has a tortuous pathway through the hinge channel induced significantly more TAT formation than the SJM Standard valve with a smoother hinge channel. This increased propensity for coagulation by the MP valve was not accompanied by an increase in platelet activation relative to the SJM Standard valve. Thus, although platelet activation was similar for both of the valves, coagulation was not. This result shows that it is not necessarily platelet activation that is important in determining whether or not a valve will induce thrombosis *in vivo*. It is the subsequent flow fields after platelet activation has occurred that determine procoagulant potential. Nevertheless this study does show that MHV hinge geometry should be as smooth and free of diameter changes as possible to eliminate circulation and stagnation regions that enable activated platelets to congregate and propagate the coagulation cascade.

Leakage gap width also had a significant effect not only on procoagulant potential but also on platelet activation. Both the low and high leaker prototype valves had significantly higher levels of platelet activation compared to the SJM Standard valve, but only the low leaker valve demonstrated a higher propensity for coagulation. Since it is important to minimize both platelet activation and thromboemboli formation, an optimal gap width should be maintained for BMHVs that is similar to that of the SJM Standard valve to minimize both of these parameters.

Cumulatively, these results imply that the designers of BMHVs should endeavor to minimize areas of high shear stress followed by stagnation regions. This can be accomplished by expanding hinge channels using smooth transitions to the larger diameter. Right angles should be avoided as well as expansion regions that are enclosed on both sides by contraction regions. Additionally, hinge channel size should be optimized to expose the smallest blood volume possible to the high shear stresses in the channel without exposing the blood to high viscous stresses resulting from flow through smaller hinge gap widths, such as those in the low leaker valve, that may induce excessive platelet activation and blood element damage as well as enable stagnation regions to form. Based on the estimated viscous shear stresses in the SJM Standard valve, this objective can be achieved by designing the hinge channel with viscous shear stresses of between 1000 and 1100 dyn/cm^2.

CHAPTER 10

RECOMMENDATIONS

This study shows that this recalcification methodology can be used to investigate the procoagulant potential of BMHVs and geometries to mimic the BMHV hinge region. However, the slits used in this study may not have been small enough to accurately predict coagulation induced by jets through the B-datum line of BMHVs or around the periphery of the valve between the leaflet and the valve housing. Thus, in the future smaller slits could be used to investigate the effects of these jets. Also, in the future this system could also be utilized to investigate the thrombus-forming potential of other vascular devices besides BMHVs. This methodology has the necessary sensitivity to investigate the effect of small nuances in geometry and relate these to procoagulant potential. Thus, it could be used to look at different stent or ventricular patch designs.

In addition to investigating other types of vascular devices, this recalcification system can also be used to elucidate the mechanism behind the thrombus formation that occurs in response to high shear stress regions followed by recirculation and stagnation regions. Platelet activation induces a calcium influx that in turn propagates the coagulation cascade. Using fluorescently labeled Ca^{2+} as the infusion medium, this influx could be observed in real time with confocal microscopy. Aggregation of these fluorescently labeled platelets would yield a better understanding of the flow field properties necessary to enable platelet aggregation and subsequent thrombus formation. Coupled with inhibition strategies to block different pathways in the coagulation cascade

and platelet activation and aggregation, this system could be a powerful tool to engender a better understanding of shear-activated thrombus formation.

Despite its success at measuring thromboembolic potential, this system may not be optimal for detecting the influence of small changes in geometry on platelet activation. Significant differences were detected based on hinge gap width, but there was no difference in PF4 release between the orifices or channels. Also, PF4 release was not suppressed significantly by either Aggrastat or AN51, and it was significantly increased by AN51 addition. This increase occurred without a concomitant increase in TAT formation, which would be expected if the platelets were actually activated. Thus, PF4 may not be the best indication platelet activation in this system. Future work could be focused on developing a better marker for platelet activation.

These results could also be used to develop a CFD model to predict thromboembolic potentials for different flow fields. The flow fields in the current study are well-defined and simple to duplicate in CFD because of there symmetric nature. The experimental conditions were also well-controlled. Thus, these TAT and PF4 results can be used in conjunction with the flow fields to develop and validate this code. This CFD code could then be used to predict these endpoints for other more complex geometries such as the MHV hinge area and other vascular devices.

The DPIV used in this study could also be improved by using smaller fluorescent particles with increased brightness compared to the 1 μm particles that were used for some of these experiments. If the particles emitted more light in response to the laser, the zoom lens would be better able to detect these particles and track them using the DPIV software. Another method to improve the DPIV results would be to use particle tracking

software instead of DPIV software. Although it would not enable the quantitative measurements that can be achieved with DPIV, it would allow for better tracking of lone particles that are lost in DPIV processing. Particle tracking would also provide a history of what is happening to a single platelet in the flow field.

Another area of this research that has room for further study are the *ex vivo* baboon experiments. The preliminary research performed in this area shows that reproducible results can be obtained by controlling the initial platelet count of the animal used in the studies. Thus, the protocol developed in this research can be used to investigate the smaller slit orifices and perhaps a larger slit orifice. The platelet deposition rates found in these studies would provide insight into the influence of slit size on thrombus formation in a more physiological environment than was present in the *in vitro* studies.

APPENDIX A

BLOOD EXPERIMENTAL PROTOCOLS

A.1. PF4 Sample collection Protocol

Solution recipes:

ACD
Acid Citrate Dextrose solution is available from the pharmacy or can be prepared as follows:
2.45g Dextrose
2.2g Sodium Citrate (dihydrate)
0.75g Citric Acid (anhyrous)
Make up to 100mL with distilled water.
Filter sterilize and store at 4°C

ASA
Acetylsalicylic acid (Sigma)
Weigh out 1.8g and dissolve in 10mL absolute ethanol
Store at room temperature.

PGE1
Prostaglandin E1 (Sigma)
Stock solution - 1mg/mL
Add 1mL absolute ethanol to 1mg vial.
Store at -20°C
Working solution - 100µg/mL
Dilute stock solution 1:10 in absolute ethanol
Store at -20°C

Blood collection:

Cocktail is prepared just before the blood collection and kept on ice.
Collect blood up to 1mL in the following mixture:
200µL ACD
16µL ASA
2µL PGE1

Keep the blood chilled on ice for at least 5min but less than 30min.
Ideally the blood should be centrifuged at 48000g for 20min at 4°C.
Remove 200µL of the top plasma and store at -20°C or colder until assay time.
It is important not to remove plasma to close to the cell layer since even a single platelet can cause a substantial increase in the PF4 levels.

A.2. TAT ELISA Protocol

Note: All determinations should be performed in duplicate. A reference curve must be established for each series of measurements using the standards found in the test kit. All samples and standards must be pipetted into the 96-well plate within 5 minutes. The incubation period begins when the plate is placed in the water bath.

1. Into each well of the 96-well plate pipette 50 µl of Sample Buffer. To each well then add 50 µl standard, control, or sample. After filling the test plates, shake briefly to ensure thorough mixing.
2. Cover with self-adhesive foil and incubate for 15 minutes at 37 °C.
3. Remove the foil, use a pipette to empty the contents of the wells and fill them with 0.3 ml diluted washing solution. Remove the washing solution with a pipette then refill with 0.3 ml diluted washing solution. Remove the washing solution then wash and remove with the pipette once more for a total of 3 washing steps. Expel any remaining washing solution by knocking the test plate on a paper towel.
4. Pipette 100 µl of Working Conjugate Solution into each well, taking care not to wet the edges of the wells.
5. Cover with fresh self-adhesive foil and incubate for 15 minutes at 37 °C.
6. Prepare the Working Chromogen Solution shortly before the end of the incubation period by adding 10 ml Buffer/Substrate POD into a vial of Chromogen POD and shake to dissolve.
7. Remove the foil, use a pipette to empty the contents of the wells and fill them with 0.3 ml diluted washing solution. Remove the washing solution with a pipette then refill with 0.3 ml diluted washing solution. Remove the washing solution then wash and remove with the pipette once more for a total of 3 washing steps. Expel any remaining washing solution by knocking the test plate on a paper towel.
8. To each well add 100 µl of the freshly prepared Working Chromogen Solution.
9. Cover with fresh self-adhesive foil and incubate at 20 to 25 °C protected from light for 30 minutes.
10. Remove the foil and add 100 µl of Stopping Solution POD, keeping to the same timing as for the dispensing of the Working Chromogen Solution.
11. Within one hour read against distilled water at a measurement wavelength of 492 nm.
12. After calculating the mean absorbance values of the standards plot the reference curve on log-log graph paper (abscissa: concentration, ordinate: absorbance). From this standard curve you can get the concentrations of the other samples.

A.3. PF4 ELISA Protocol

1. Into each well of the 96-well plate pipette 50 µl of Sample Buffer. To each well then add 50 µl standard, control, or sample. After filling the test plates, shake briefly to ensure thorough mixing.
2. Cover with self-adhesive foil and incubate for 15 minutes at 37 °C.
3. Remove the foil, use a pipette to empty the contents of the wells and fill them with 0.3 ml diluted washing solution. Remove the washing solution with a pipette then refill with 0.3 ml diluted washing solution. Remove the washing solution then wash and remove with the pipette once more for a total of 3 washing steps. Expel any remaining washing solution by knocking the test plate on a paper towel.
4. Pipette 100 µl of Working Conjugate Solution into each well, taking care not to wet the edges of the wells.
5. Cover with fresh self-adhesive foil and incubate for 15 minutes at 37 °C.
6. Prepare the Working Chromogen Solution shortly before the end of the incubation period by adding 10 ml Buffer/Substrate POD into a vial of Chromogen POD and shake to dissolve.
7. Remove the foil, use a pipette to empty the contents of the wells and fill them with 0.3 ml diluted washing solution. Remove the washing solution with a pipette then refill with 0.3 ml diluted washing solution. Remove the washing solution then wash and remove with the pipette once more for a total of 3 washing steps. Expel any remaining washing solution by knocking the test plate on a paper towel.
8. To each well add 100 µl of the freshly prepared Working Chromogen Solution.
9. Cover with fresh self-adhesive foil and incubate at 20 to 25 °C protected from light for 30 minutes.
10. Remove the foil and add 100 µl of Stopping Solution POD, keeping to the same timing as for the dispensing of the Working Chromogen Solution.
11. Within one hour read against distilled water at a measurement wavelength of 492 nm.
12. After calculating the mean absorbance values of the standards plot the reference curve on log-log graph paper (abscissa: concentration, ordinate: absorbance). From this standard curve you can get the concentrations of the other samples.

A.4. Deparaffinization Protocol

Purpose: Removal of paraffin from tissue sections prior to staining.
References: Leica Autostainer Manual
Microtomy: 5 um sections.
Fixation: Neutral buffered formalin (formalin saline recommended).
QC: Clotted blood or thrombus.
Hazards: Alcohol is highly flammable.

Method:

1. Xylene substitutes, 3 stations, 5 min each.
2. 100% alcohol, twice, 2 min each.
3. 95% alcohol, twice, 2 min each.
4. 75%, 2 min.
5. Wash in water for 2 minutes.

Regents and Solutions:

Alcohol: EMD#65347/85
Xylene substitute:EMD#XX0060-4

A.5. Hematoxylin and Eosin Stain Protocol

Purpose: Detection of cell nuclei and membranes.
References: Leica Autostainer Manual.
Microtomy: 5 um sections.
Fixation: Neutral buffered formalin (formalin saline recommended).
QC: Clotted blood or thrombus.
Hazards: Xylene and alcohol are highly flammable.

Method:

1. Deparaffinized slides are stained in Hematoxylin for 30 seconds;
2. Rinse in DI water.
3. Dip in acid alcohol.
4. Rinse in DI water.
5. Place in Scott's solution for 30 seconds.
6. Rinse in DI water.
7. Wash in 95% alcohol for 1 min.
8. Stain in alcoholic Eosin for 30 seconds.
9. Dehydrate through ascending grades of alcohol and clear to xylene. Mount in a permanent mounting media.

Regents and Solutions:

Hematoxylin:Dilute Gill's hematoxylin no.2 (Polysciences #04570) one to one with dH2O before use.
Acid alcohol:2ml HCl (Fisher #A144s) in 198 ml of 70% ethanol.
Eosin: EM Science #588X
Scott's solution: NaHCO3: 2g, MgSO4.7H2O : 20g, dH2O : 1000ml. Mix until dissolved.
Xylene:EMD#XX0060-4

Results:

Membranes_____red
Cell nuclei_____blue

A.6. Carstair's Stain Protocol

Purpose: Detection of fibrin and platelets.
References: Sheehan's Theory and Practice of Histotechnology, 2nd edition.
Microtomy: 5 um sections.
Fixation: Neutral buffered formalin (formalin saline recommended).
QC: Clotted blood or thrombus.
Hazards: Picric acid is highly explosive when dry. Wipe lids after use and tighten to prevent drying of solutions. Xylene and alcohol are highly flammable.

Method:

1. Deparaffinze and rehydrate to distilled water.
2. Rinse well in distilled water.
3. Mordant sections in 5% ferric alum for 10 minutes and then rinse in tap water.
4. Stain with Harris' hematoxylin for 5 minutes and rinse in tap water. If necessary, differentiate in 0.25% acid alcohol.
5. Stain in picric acid-orange G solution for 30 minutes (up to 1 hour).
6. Rinse once in distilled water.
7. Stain in ponceau fuchsin for 5 minutes.
8. Rinse once in distilled water.
9. Differentiate with 1% phosphotungstic acid for 2 minutes. Rinse well in water if checking microscopically.
10. Stain with aniline blue solution for 10 minutes (up to 1 hour).
11. Rinse sections in several changes of distilled water.
12. Dehydrate, clear, and mount.

Results:

Fibrin_____red
Muscle_____red
Platelets gray-blue to navy
Collagen_____bright blue
Rbc's_____clear yellow

Reagents and Solutions:

Picric Acid-Orange G

Saturated picric acid	20ml	
Saturate picric acid in isopropanol	80ml	
Orange-G (CI 16230)	0.2g	

Ponceau-fuchsin

Acid fuchsin (CI 42685)	0.5g	
Ponceau 2R	0.5g	
Glacial acetic acid		1ml
Distilled water	99ml	

1% Aniline Blue

Aniline blue (CI 42755)	1g

1% acetic acid	100ml

5% Ferric Alum
1% Phosphotungstic acid

A.7. vWF Immunohistochemistry Protocol Using Avidin D Fluorochrome Conjugates

Purpose: Detection of vWF.
Microtomy: 5 um sections.
Fixation: Neutral buffered formalin (formalin saline recommended).
QC: Clotted blood or thrombus.

Hazards: None

Please note: All antibodies and related reagents are temperature sensitive. Please keep at 4 deg C or on ice at all times. This will maintain the longevity of the reagents and limit antibody or reagent-related problems with experiments.

1. Deparaffinize embedded tissue and rehydrate in descending grades of alcohol. Wash sections in 1X PBS for 4 minutes.
2. Perform antigen retrieval by incubating in protease for 10 minutes at room temperature.
3. Wash slides in 1X PBS twice for 4 minutes each.
4. Block tissue using 1% gelatin/PBS mixture for 20 minutes at room temp.
5. Prepare the working dilution of the vWF antibody (Sigma), 1/600, in 1% BSA in 1X PBS. Blot off gelatin/PBS and apply primary antibody. Incubate sections in a humid chamber for 1 hour at room temp.
6. Blot off excess antibody and wash slides in 1X PBS twice for 4 minutes each.
7. Prepare working dilution of the biotinylated secondary antibody in 1% BSA in 1X PBS and add 2% of normal serum from the source animal of the seconday antibody. Prepare secondary antibody at 1/400 dilution. Apply antibody and incubate 30 minutes at room temp in a humid chamber.
8. Blot off excess antibody and wash slides in 1X PBS twice for 4 minutes each.
9. Incubate sections with fluorochrome conjugated avidin D for 30 minutes in the dark. Prep 1/100 in BSA/PBS Avidin-D-FITC.
10. Blot off excess solution and wash slides in 1X PBS twice for 4 minutes each in the dark.
11. Mount with vectashield mounting media with nuclear counterstain. Store slides in the dark at 4 deg C.

Regents and Solutions:

Avidin D Fluorochrome conjugated: Texas red (Vector A-2006), Fluoroscein (Vector A-2001)
1% BSA/PBS: 1 g fraction V BSA (Sigma A2153) in 100 ml 1X PBS
10 mM Citrate buffer, pH 6.0 (500 ml): Solution A: 9 ml, Solution B: 41 ml, dH_2O: 450 ml. Adjust pH to 6.0. Bring up to 500 ml. Final concentrations are 1.96 mM citric acid and 8.2 mM sodium citrate.
Solution A, Citric acid (109 mM): Citric acid: 4.2 g, dH_2O: 200 ml
Solution B, Sodium citrate (100 mM): Sodium citrate: 14.7 g, dH_2O: 500 ml
10X PBS: Boehringer Mannheim 1666789

Protease: Dissolve protease (Sigma P-8038) in PBS for a stock concentration of 100 mg/ml. Store at -20 °C.
Proteinase K: Dissolve proteinase K (Sigma P-4914) in dH_2O for a stock concentration of 20 mg/ml. Store at -20 °C.
Secondary antibodies, avidn D conjugates, and normal animal serum: Vector laboratories, Inc. 30 Ingold Road, Burlingame, CA 94010
Vectashield Hardset Mountant with DAPI (nuclear counterstain): Vector H-1500

A.8. vWF Immunohistochemistry Protocol Using ABC-Peroxidase

Purpose: Detection of vWF.
Microtomy: 5 um sections.
Fixation: Neutral buffered formalin (formalin saline recommended).
QC: Clotted blood or thrombus.
Hazards: ***DAB is a carcinogen, use protective measures to prevent exposure.***

Please note: All antibodies and related reagents are temperature sensitive. Please keep at 4 deg C or on ice at all times. This will maintain the longevity of the reagents and limit antibody or reagent-related problems with experiments.

1. Deparaffinize embedded tissue and rehydrate in descending grades of alcohol. Wash sections in 1X PBS for 4 minutes.
2. Perform antigen retrieval by incubating in protease for 10 minutes at room temperature.
3. Wash slides in 1X PBS twice for 4 minutes each.
4. Block endogenous peroxidase using 3% H_2O_2 in methanol for 15 min. at room temperature (dilute 1.5 ml of 30% H_2O_2 in 150 ml methanol).
5. Rehydrate sections in 1X PBS twice for 5 min. each at room temp.
6. Block tissue using 1% gelatin/PBS mixture for 20 minutes at room temp.
7. Prepare the working dilution of the vWF antibody (Sigma), 1/600, in 1% BSA in 1X PBS. Blot off gelatin/PBS and apply primary antibody. Incubate sections in a humid chamber for 1 hour at room temp.
8. Blot off excess antibody and wash slides in 1X PBS twice for 4 minutes each.
9. Prepare working dilution of the biotinylated secondary antibody in 1% BSA in 1X PBS and add 2% of normal serum from the source animal of the seconday antibody. Prepare secondary antibody at 1/400 dilution. Apply antibody and incubate 30 minutes at room temp in a humid chamber.
10. Prepare the working solution of ABC-peroxidase complex from the Vectastain Elite ABC kit (PK-6100). Mix 5 ml of 1X PBS, 2 drops reagent A, and 2 drops reagent B. *Allow to sit for* ***30 minutes*** *prior to use*.
11. Blot off excess antibody and wash slides in 1X PBS twice for 4 minutes each.
12. Apply prepared ABC mixture to each slide. Incubate in humid chamber for 1 hour at room temp.
13. Blot off excess solution and wash slides in 1X PBS twice for 4 minutes each, followed by one wash in sterile deionized/distilled water for 5 min.
14. Make up substrate solution, diaminobenizidine (DAB), immediately before use. **DAB is a carcinogen so wear gloves, goggles, work on a diaper, and save liquid waste to be disposed of with chemical waste.** In order, add: 15 ml of TBS, pH 7.6, 1 tablet DAB (10 mg), and 12 µl of 30% H_2O_2. Mix to dissolve tablet. Filter using Whatman #1. Apply filtered solution to each section. Incubate slides in the dark up to 10 min., checking color periodically. Stop reaction by blotting off substrate and rinsing in 1X PBS 3 times for 4 minutes each.
15. Lightly counterstain with hematoxylin. Rinse slides well in water until water is clear. Dehydrate through graded alcohols, then xylene and coverslip for viewing.

Regents and Solutions:

1% BSA/PBS: 1 g fraction V BSA (Sigma A2153) in 100 ml 1X PBS
10 mM Citrate buffer, pH 6.0 (500 ml): Solution A: 9 ml, Solution B: 41 ml, dH_2O: 450 ml. Adjust pH to 6.0. Bring up to 500 ml. Final concentrations are 1.96 mM citric acid and 8.2 mM sodium citrate.
Solution A, Citric acid (109 mM): Citric acid: 4.2 g, dH_2O: 200 ml
Solution B, Sodium citrate (100 mM): Sodium citrate: 14.7 g, dH_2O: 500 ml
Diaminobenzidine Tetrahydrochloride (DAB): Sigma D-5905, 10 mg tablets X 50 tablets
Elite ABC-Peroxidase Kit: Vector PK-6100
10X PBS: Boehringer Mannheim 1666789
Protease: Dissolve protease (Sigma P-8038) in PBS for a stock concentration of 100 mg/ml. Store at -20 °C.
Proteinase K: Dissolve proteinase K (Sigma P-4914) in dH_2O for a stock concentration of 20 mg/ml. Store at -20 °C.
Secondary antibodies, avidn D conjugates, and normal animal serum: Vector laboratories, Inc. 30 Ingold Road, Burlingame, CA 94010
TBS: Tris base: 12.1 g, Sodium chloride: 8.77g, dH_2O to l l. (pH to 7.6)

A.9. Hematoxylin Counterstaining Protocol

Purpose:	Counterstain cell nuclei to identify cells after performing ABC-peroxidase immunohistochemcistry.
Microtomy:	5 um sections.
Fixation:	Neutral buffered formalin (formalin saline recommended).
QC:	Clotted blood or thrombus.
Hazards:	Xylene and alcohol are highly flammable.

Method:

1. Hematoxylin for 10 seconds.
2. Rinse in tap water until clear.
3. Dip once in 1% acid alcohol.
4. Rinse in water.
5. Scott's solution for 20 seconds.
6. Rinse in water.
7. Dehydrate through graded alcohols then xylene.
8. Coverslip.

Regents and solutions:

Hematoxylin: Dilute Gill's hematoxylin no.2 (Polysciences #04570) one to one with dH2O before use.
1% Acid Alcohol: 2ml HCl (Fisher #A144s) in 198 ml of 70% ethanol.
Scott's Solution: NaHCO3: 2g, MgSO4.7H2O : 20g, dH2O : 1000ml. Mix until dissolved.

A.10. SEM Preparation Protocol

Purpose: Prepare samples for viewing with SEM.
Microtomy: 5 um sections.
Fixation: Neutral 2.5% glutaraldehyde.
QC: Clotted blood or thrombus.
Hazards: Xylene and alcohol are highly flammable.

Method:

1. Harvest tissue and rinse briefly in 0.2M sodium cacodylate buffer, pH 7.2.
2. Fix tissue in 2.5% glutaraldehyde in cacodylate buffer, pH 7.2 for 1-2 hours. Dilute the stock of 8% glutaraldehyde using 0.2M cacodylate buffer, pH 7.2 immediately before use.
3. Rinse in 0.2M cacodylate buffer, pH 7.2, 3 x 10 minutes.
4. Dehydrate tissue sample using the following schedule, each for 0.5-1 hour: 25% alcohol, 50%, 70%, 90% x 2, 100% x 2.
5. In place of critical point drying, dry the sample using hexamethyldisilazane. Use one of the following schedules (if the sample is of animal origin, use schedule a or b):
6. Ratio 100% ethanol:HMDS starting from 100% ethanol going to 100% HMDS, each step for 30 min.
    a. 100% Ethanol =>2:1, 1:1, 1:2 => 100% HMDS
    b. 100% Ethanol =>3:1, 1:1, 1:3 => 100% HMDS
7. Rinse in 3 changes of 100% HMDS.
8. Dry from the last 100% HMDS. The level of HMDS should just cover the tissue sample. Leave the tube containing the sample open in the fume hood and allow the HMDS to evaporate and thus dry the tissue. Depending on sample size, drying should occur overnight.
9. Adhere the sample to an aluminum stub using conductive, double sided carbon adhesive tape.
10. Sputter-coat the sample using gold to a thickness of approx. 100 Angstroms. Desiccate sample until ready to analyze (in MSE lab).
11. Keep tissue in desiccators (vacuum oven) before viewing under microscope.

Reagents and supplies:

8% Glutaraldehyde: Electron Microscopy Sciences #16019
16% Paraformaldehyde: Electron Microscopy Sciences #15710
0.2M cacodylate buffer, pH 7.4: Electron Microscopy Sciences # 11652
Hexamethyldisilazane: Electron Microscopy Sciences #16700
Aluminum stubs for the Hitachi S-800: SPI #01506-BA (table dia.12.7mm, pin dia. 3.2mm, pin length 8.0mm)
Conductive, double sided carbon adhesive tape: SPI #05081-AB (6 mm x 20 feet)

APPENDIX B

BLOOD EXPERIMENTAL DATA

B.1. TAT ELISA assays – Raw data

Orifice TAT Data:

200um round		Raw data, TAT concentration (ng/ml)						Initial value subtracted, adjusted for dilution (ng/ml)			
date		0 min	15 min	30 min	45 min	60 min		15 min	30 min	45 min	60 min
12/19/2003		0.00	0.00	47.67	109.75	110.68		0.00	48.36	112.98	115.63
12/19/2003		0.00	4.53	11.10	62.74	103.74		4.53	11.26	64.58	108.39
1/5/2004		0.00	0.00	43.70	112.24	115.54		0.00	44.34	115.54	120.71
01/06/04		37.12	22.15	111.79	115.39	118.86		-14.97	76.28	81.66	87.06
01/14/04		10.00	8.12	na	32.35	19.49		-1.88	na	23.30	10.37
	average	9.42	6.96	53.56	86.49	93.66	average	-2.46	45.06	79.61	88.43
	std dev	16.08	9.15	42.13	37.20	41.85	std deviation	7.38	26.64	38.09	45.49
							std error	3.30	13.32	17.04	20.34

400um round		Raw data, TAT concentration (ng/ml)						Initial value subtracted, adjusted for dilution (ng/ml)			
date		0 min	15 min	30 min	45 min	60 min		15 min	30 min	45 min	60 min
7/8/2004		25.99	50.33	41.65	36.29	34.51		24.33	16.49	11.77	10.66
7/8/2004		25.99	34.87	57.12	95.70	113.25		8.88	32.27	73.59	94.29
8/25/2004		0.19	47.32	80.74	85.55	82.38		47.13	82.15	88.82	87.30
8/30/2004		0.39	8.19	30.59	81.39	77.15		7.80	30.81	84.30	81.54
8/30/2004		0.39	9.74	25.40	79.19	87.15		9.34	25.51	82.01	92.17
9/2/2004		0.06	0.08	1.23	1.17	17.24		0.02	1.19	1.16	18.25
9/30/2004		1.40	1.88	123.89	139.24	134.23		0.48	124.95	143.49	141.16
9/30/2004		0.87	22.04	130.26	142.21	138.09		21.17	131.98	147.11	145.79
8/6/2003		0.00	3.24	33.02	81.58	164.32		3.24	33.49	83.98	171.68
8/20/2003		0.00	67.45	105.08	162.20	194.39		67.45	106.60	166.97	203.10
11/11/03		0.00	0.00	22.78	58.04	96.71		0.00	23.11	59.75	101.04
09/24/03		1.07	63.91	26.04	24.60	52.18		62.84	25.35	24.25	53.44
09/25/03		3.75	26.98	26.74	27.97	30.75		23.23	23.38	25.04	28.38
10/01/03		0.00	32.27	55.60	70.58	81.09		32.27	56.41	72.66	84.72
	average	4.293129	26.30695	54.29491	77.55088	93.102421	average	22.013817	50.9771183	76.06389796	93.82292653
	std dev	9.245708	23.80126	40.45622	47.07355	51.713205	std deviation	6.1102725	11.4120902	13.56769962	15.15778452
							std error	1.633039	3.0500094	3.62612025	4.051088316

800um round		Raw data, TAT concentration (ng/ml)						Initial value subtracted, adjusted for dilution (ng/ml)			
date		0 min	15 min	30 min	45 min	60 min		15 min	30 min	45 min	60 min
9/24/2003		1.07	2.83	3.12	30.31	27.64		1.76	2.09	30.13	27.81
10/1/2003		0.00	2.50	15.91	19.94	13.92		2.50	16.14	20.53	14.54
10/15/2003		0.09	0.00	0.00	1.96	8.08		-0.09	-0.09	1.93	8.36
10/16/2003		0.00	0.00	0.58	0.00	0.38		0.00	0.59	0.00	0.40
1/9/2004		0.00	11.87	33.79	46.00	52.82		11.87	34.28	47.35	55.19
1/14/2004		10.00	6.61	8.32	12.04	17.64		-3.39	-1.56	2.39	8.43
	average	1.86	3.97	10.29	18.37	20.08	average	2.11	8.58	17.06	19.12
	std dev	4.01	4.57	12.96	17.63	18.47	std deviation	5.20	14.15	19.16	19.89
							std error	2.12	5.78	7.82	8.12

1200um round		Raw data, TAT concentration (ng/ml)						Initial value subtracted, adjusted for dilution (ng/ml)			
date		0 min	15 min	30 min	45 min	60 min		15 min	30 min	45 min	60 min
9/2/2004		48.08	40.40	137.13	138.87	132.98		-7.68	91.77	96.42	93.16
9/15/2004		20.44	8.65	41.70	91.51	81.60		-11.79	22.08	74.78	66.22
8/7/2003		0.00	0.00	0.00	0.00	0.00		0.00	0.00	0.00	0.00
8/20/2002		0.00	3.52	2.23	10.39	0.00		3.52	2.26	10.69	0.00
9/4/2003		0.00	0.00	0.00	0.00	0.00		0.00	0.00	0.00	0.00
9/25/2003		3.75	3.00	29.79	21.51	20.68		-0.75	26.47	18.39	17.86
10/2/2003		10.35	13.79	11.36	17.16	14.63		3.43	1.17	7.31	4.93
10/9/2003		0.00	4.11	6.76	8.30	10.18		4.11	6.85	8.55	10.64
	average	10.33	9.18	28.62	35.97	32.51	average	-1.14	18.83	27.02	24.10
	std dev	16.89	13.42	46.38	51.05	48.75	std deviation	5.72	31.23	37.09	35.61
							std error	2.02	11.04	13.11	12.59

200um slit		Raw data, TAT concentration (ng/ml)						Initial value subtracted, adjusted for dilution (ng/ml)			
date		0 min	15 min	30 min	45 min	60 min		15 min	30 min	45 min	60 min
10/22/2003		0.18	0.05	0.22	3.97	0.00		-0.12	0.05	3.91	4.83
10/23/2003		0.00	0.11	0.00	0.00	0.00		0.11	0.00	0.00	0.00
11/12/2003		0.00	0.00	0.00	0.00	0.00		0.00	0.00	0.00	0.00
	average	0.06	0.05	0.07	1.32	0	average	0.00	0.02	1.30	1.61
	std dev	0.10	0.06	0.13	2.29	0	std deviation	0.12	0.03	2.26	2.79
							std error	0.07	0.02	1.30	1.61

400um slit		Raw data, TAT concentration (ng/ml)						Initial value subtracted, adjusted for dilution (ng/ml)			
date		0 min	15 min	30 min	45 min	60 min		15 min	30 min	45 min	60 min
10/22/2003		0.18	0.40	0.27	2.44	2.26		0.23	0.10	2.34	2.19
10/23/2003		0.00	0.27	0.00	0.51	0.11		0.27	0.00	0.52	0.11
10/30/2003		9.52	11.63	8.57	6.63	9.97		2.12	-0.82	-2.69	0.90
	average	3.23	4.10	2.95	3.19	4.12	average	0.87	-0.24	0.06	1.07
	std dev	5.44	6.52	4.87	3.13	5.19	std deviation	1.08	0.50	2.54	1.05
							std error	0.62	0.29	1.47	0.60

800um slit		Raw data, TAT concentration (ng/ml)						Initial value subtracted, adjusted for dilution (ng/ml)			
date		0 min	15 min	30 min	45 min	60 min		15 min	30 min	45 min	60 min
11/3/2003		0.00	0.66	1.66	1.55	0.24		0.66	1.68	1.60	0.26
11/11/2003		0.00	0.00	0.00	1.95	0.07		0.00	0.00	2.01	0.07
11/12/2003		0.00	0.00	0.00	0.00	0.00		0.00	0.00	0.00	0.00
	average	0.00	0.22	0.55	1.17	0.11	average	0.22	0.56	1.20	0.11
	std dev	0.00	0.38	0.96	1.03	0.13	std deviation	0.38	0.97	1.06	0.13
							std error	0.22	0.56	0.61	0.08

400um pf		Raw data, TAT concentration (ng/ml)						Initial value subtracted, adjusted for dilution (ng/ml)			
date		0 min	15 min	30 min	45 min	60 min		15 min	30 min	45 min	60 min
2/16/2004		0.28	0.06	12.05	19.97	20.03		-0.22	11.95	20.28	20.65
3/17/2004		0.00	0.00	0.63	6.03	10.48		0.00	0.64	6.21	10.95
3/25/2004		8.17	9.82	14.74	29.20	57.38		1.65	6.78	21.89	51.78
3/26/2004		0.72	0.92	0.77	2.04	1.02		0.20	0.07	1.38	0.35
4/9/2004		3.16	3.22	2.71	2.83	3.78		0.05	-0.42	-0.25	0.79
	average	2.47	2.80	6.18	12.02	18.54	average	0.34	3.80	9.90	16.90
	std dev	3.43	4.14	6.71	12.03	22.92	std deviation	0.75	5.41	10.50	21.21
							std error	0.34	2.42	4.69	9.48

pf = experiments with platelet removal

400um no ca2+		Raw data, TAT concentration (ng/ml)						Initial value subtracted, adjusted for dilution (ng/ml)			
date		0 min	15 min	30 min	45 min	60 min		15 min	30 min	45 min	60 min
1/28/2004		0.64	0.00	0.00	8.38	2.68		-0.64	-0.64	7.98	2.16
1/28/2004		0.64	0.00	45.94	45.36	50.24		-0.64	45.97	46.06	51.85
2/4/2004		0.00	0.00	0.00	0.00	0.00		0.00	0.00	0.00	0.00
2/4/2004		0.00	0.00	0.00	4.13	0.00		0.00	0.00	4.25	0.00
2/25/2004		0.00	0.00	0.00	1.31	4.50		0.00	0.00	1.35	4.70
2/25/2004		0.00	11.71	47.37	68.79	88.59		11.71	48.05	70.82	92.55
	average	0.21	1.95	15.55	21.33	24.33	average	1.74	15.56	21.74	25.21
	std dev	0.33	4.78	24.10	28.81	37.00	std deviation	4.90	24.37	29.61	38.65
							std error	2.00	9.95	12.09	15.78

no ca2+ = experiments with no added Ca^{2+}

400um 18g Agg		Raw data, TAT concentration (ng/ml)						Initial value subtracted, adjusted for dilution (ng/ml)			
date	nd flow (lpn	0 min	15 min	30 min	45 min	60 min		15 min	30 min	45 min	60 min
6/30/2004	0.03	14.47	9.09	21.13	20.61	34.50		-5.38	7.08	6.98	22.17
6/30/2004	0.03	14.47	12.15	9.02	29.98	29.15		-2.32	-5.27	16.72	16.49
	average	14.47	10.62	15.08	25.30	31.83	average	-3.85	0.91	11.85	19.33

18g Agg = experiments with 18µg added Aggrastat

400um 180g Agg		Raw data, TAT concentration (ng/ml)						Initial value subtracted, adjusted for dilution (ng/ml)			
date	nd flow (lpn	0 min	15 min	30 min	45 min	60 min		15 min	30 min	45 min	60 min
6/24/2004	0.06	1.86	3.45	4.95	10.70	18.55		1.59	3.18	9.27	17.83
6/24/2004	0.01	1.86	2.28	2.06	2.27	3.23		0.42	0.24	0.50	1.57
7/20/2004	0	0.84	1.35	2.34	3.04	clotted		0.51	1.55	2.32	na
7-20-04b	0.02	0.84	2.29	2.63	3.63	1.65		1.45	1.84	2.94	0.91
7/23/2004	0.03	0.14	3.96	3.11	3.27	3.87		3.82	3.03	3.26	3.97
7/23/2004	0.02	0.14	0.27	0.62	0.63	0.54		0.13	0.49	0.51	0.43
	Average	0.95	2.27	2.62	3.92	5.57	average	1.32	1.72	3.13	4.94
	std dev	0.77	1.35	1.42	3.49	7.37	std deviation	1.36	1.23	3.23	7.33
							std error	0.55	0.50	1.32	2.99

180g Agg = experiments with 180µg added Aggrastat

400um 125 ul AN51		Raw data, TAT concentration (ng/ml)						Initial value subtracted, adjusted for dilution (ng/ml)			
date	nd flow (lpn	0 min	15 min	30 min	45 min	60 min		15 min	30 min	45 min	60 min
1/19/2005	0.01	2.84	1.01	0.92	0.85	0.99		-1.84	-1.90	-1.96	-1.79
1/19/2005	0.03	2.84	1.25	0.62	0.83	0.84		-1.59	-2.21	-1.98	-1.95
1/20/2005	0.06	0.59	2.98	48.01	79.23	92.90		2.39	48.37	81.85	98.08
1/20/2005		0.59	0.45	0.60	0.57	0.37		-0.14	0.02	0.00	-0.20
1/21/2005		1.26	1.82	4.41	3.59	3.32		0.55	3.23	2.47	2.26
1/21/2005		1.26	4.47	2.37	2.93	4.46		3.21	1.16	1.79	3.47
	Average	1.57	2.00	9.49	14.67	17.15	average	0.43	8.11	13.69	16.65
	std dev	1.03	1.49	18.93	31.65	37.15	std deviation	2.06	19.82	33.44	39.95
	std error	0.42	0.61	7.73	12.92	15.17	std error	0.84	8.09	13.65	16.31

125 ul AN51 = experiments with 125 µl AN51 antibody

		Raw data, TAT concentration (ng/ml)						Initial value subtracted, adjusted for dilution (ng/ml)			
		Passes						Passes			
800r low		0	25	50	75	100		25	50	75	100
7/29/2005		6.70	11.51	5.56	6.80	11.94		4.81	-1.07	0.30	5.77
8/3/2005		5.98	40.49	26.91	43.04	51.73		34.51	21.32	38.32	48.06
7/21/2005		0.34	0.41	0.81	2.76	1.85		0.07	0.49	2.50	1.60
7/15/2005		1.07	4.09	2.18	9.03	43.30		3.02	1.14	8.22	44.16
7/28/2005		2.53	2.72	9.42	8.63	11.41		0.19	7.03	6.36	9.39
7/27/2005		1.33	0.47	0.83	1.03	4.92		-0.86	-0.49	-0.27	3.81
	average	2.99	9.95	7.62	11.88	20.86	average	6.96	4.74	9.24	18.80
	std dev	2.70	15.51	10.02	15.60	21.17	std deviation	13.66	8.63	14.63	21.35
							std error	5.58	3.52	5.97	8.71
		Raw data, TAT concentration (ng/ml)						Initial value subtracted, adjusted for dilution (ng/ml)			
800r high		0	25	50	75	100		25	50	75	100
7/29/2005		6.70	4.99	3.49	3.03	1.51		-1.72	-3.17	-3.59	-5.13
7/21/2005		0.34	0.46	4.94	36.85	62.88		0.12	4.67	37.54	65.22
7/28/2005		1.33	0.56	1.74	5.66	20.19		-0.77	0.44	4.48	19.72
8/3/2005		5.98	12.40	13.05	11.28	10.49		6.42	7.25	5.61	4.95
	average	3.59	4.60	5.81	14.20	23.77	average	1.01	2.30	11.01	21.19
	std dev	3.22	5.61	5.00	15.48	27.17	std deviation	3.68	4.60	18.16	31.08
							std error	1.84	2.30	9.08	15.54
		Raw data, TAT concentration (ng/ml)						Initial value subtracted, adjusted for dilution (ng/ml)			
800r norm		0	25	50	75	100		25	50	75	100
7/13/2005		1.42	2.07	1.32	3.31	13.66		0.65	-0.07	2.03	13.09
9/24/2003		1.07	2.83	3.12	30.31	27.64		1.76	2.11	30.47	28.29
10/1/2003		0.00	2.50	15.91	19.94	13.92		2.50	16.22	20.75	14.78
10/15/2003		0.09	0.00	0.00	1.96	8.08		-0.09	-0.09	1.96	8.49
10/16/2003		0.00	0.00	0.58	0.00	0.38		0.00	0.59	0.00	0.41
1/9/2004		0.00	11.87	33.79	46.00	52.82		11.87	34.47	47.86	56.10
1/14/2004		10.00	6.61	8.32	12.04	17.64		-3.39	-1.51	2.53	8.74
	average	1.80	3.70	9.01	16.22	19.16	average	1.90	7.39	15.08	18.56
	std dev	3.66	4.23	12.30	17.08	17.03	std deviation	4.78	13.39	18.58	18.60
							std error	1.81	5.06	7.02	7.03

800r low = low flow rate experiments with the 800 μm round orifice
800r high = high flow rate experiments with the 800 μm round orifice
800r normal = standard flow rate experiments with the 800 μm round orifice

		Raw data, TAT concentration (ng/ml)						Initial value subtracted, adjusted for dilution (ng/ml)			
control		0 min	15 min	30 min	45 min	60 min		15 min	30 min	45 min	60 min
7/13/2005		1.42	1.54	8.07	9.97	11.77		0.12	6.81	8.96	11.08
5/24/2005		2.59	3.03	3.14	1.51	2.48		0.43	0.61	-1.02	0.04
	average	2.01	2.28	5.61	5.74	7.12	average	0.28	3.71	3.97	5.56

Channel TAT data:

Channel 1		Raw data, TAT concentration (ng/ml)						Initial value subtracted, adjusted for dilution (ng/ml)			
date		0 min	15 min	30 min	45 min	60 min		15 min	30 min	45 min	60 min
11/14/03		2.21	9.56	69.77	114.13	120.89		7.35	68.57	115.28	124.10
11/21/03		2.01	0.00	20.99	32.40	44.59		-2.01	19.28	31.34	44.58
11/24/03		0.00	0.00	0.50	5.09	6.73		0.00	0.51	5.24	7.03
3/24/2003		0.07	3.63	65.84	109.43	114.35		3.56	66.72	112.58	119.40
5/14/2004		1.10	1.17	20.54	50.39	81.62		0.08	19.75	50.78	84.18
6/1/2005		5.83	23.14	43.26	41.50	59.30		17.31	38.29	37.36	57.15
	average	1.87	6.25	36.82	58.83	71.25	average	4.38	35.52	58.76	72.74
	std dev	2.15	9.02	27.58	43.77	43.47	std deviation	7.14	27.61	45.23	45.39
							std error	2.92	11.27	18.47	18.53

Channel 2		Raw data, TAT concentration (ng/ml)						Initial value subtracted, adjusted for dilution (ng/ml)			
date		0 min	15 min	30 min	45 min	60 min		15 min	30 min	45 min	60 min
11/14		2.21	2.47	20.46	32.38	5.81		0.26	18.55	31.12	3.87
11/24		0.00	10.21	10.75	9.57	10.68		10.21	10.90	9.85	11.16
11/25-B		0.40	7.75	5.40	4.49	6.13		7.35	5.08	4.22	6.01
3/24/2004		0.07	45.40	83.05	98.14	95.45		45.33	84.18	100.96	99.65
5/14/2004		1.10	9.89	13.47	13.40	13.86		8.79	12.57	12.70	13.38
6/1/2005		5.83	9.29	6.15	4.33	6.52		3.46	0.41	-1.37	0.99
	average	1.60	14.17	23.21	27.05	23.08	average	12.57	21.95	26.25	22.51
	std dev	2.23	15.56	29.82	36.33	35.59	std deviation	16.46	31.12	38.23	38.07
							std error	6.72	12.71	15.61	15.54

Channel 3		Raw data, TAT concentration (ng/ml)						Initial value subtracted, adjusted for dilution (ng/ml)			
date		0 min	15 min	30 min	45 min	60 min		15 min	30 min	45 min	60 min
5/27/2004		10.05	7.87	11.21	18.28	28.59		-2.18	1.38	8.97	20.32
5/26/2003		3.97	4.81	5.88	11.76	13.31		0.83	2.02	8.26	10.16
5/24/2003		2.47	3.26	4.36	7.69	9.81		0.79	1.98	5.53	7.95
6/16/2004		3.45	3.43	9.13	16.42	20.23		-0.01	5.87	13.64	18.04
5/19/2004		3.43	2.18	5.20	51.99	104.77		-1.25	1.88	50.67	107.85
9/15/2004		20.44	12.01	86.92	140.48	140.55		-8.44	68.20	125.73	128.83
9/20/2004		1.19	4.79	117.51	140.43	135.39		3.59	118.66	144.93	142.60
	Average	6.43	5.48	34.32	55.29	64.66	average	-0.95	28.57	51.11	62.25
	std dev	6.79	3.40	47.28	59.94	59.57	std deviation	3.77	46.66	59.81	61.02
							std error	1.43	17.64	22.61	23.06

Channel 4		Raw data, TAT concentration (ng/ml)						Initial value subtracted, adjusted for dilution (ng/ml)			
date		0 min	15 min	30 min	45 min	60 min		15 min	30 min	45 min	60 min
5/27/2004		10.05	10.80	21.97	31.22	43.74		0.75	12.35	22.44	36.40
5/26/2003		3.97	6.48	35.22	116.48	108.20		2.51	31.95	117.23	110.95
5/24/2003		2.47	7.33	17.25	37.50	44.60		4.86	15.13	36.56	44.91
6/16/2004		3.45	26.17	31.16	36.23	38.72		22.72	28.34	34.25	37.67
5/20/2004		4.76	9.99	9.44	15.36	24.42		5.23	4.86	11.22	21.18
5/19/2004		3.43	0.93	1.36	17.81	14.51		-2.50	-2.04	15.10	11.98
9/9/2004		48.08	20.66	80.56	132.90	142.98		-27.42	34.08	90.21	103.77
9/20/2004		0.17	1.19	2.88	5.33	9.87		1.02	2.77	5.38	10.31
	Average	9.55	10.44	24.98	49.10	53.38	average	0.90	15.93	41.55	47.15
	std dev	15.82	8.89	25.60	48.13	47.30	std deviation	13.77	14.00	40.47	39.20
							std error	4.87	4.95	14.31	13.86

Channel 5		Raw data, TAT concentration (ng/ml)						Initial value subtracted, adjusted for dilution (ng/ml)			
date		0 min	15 min	30 min	45 min	60 min		15 min	30 min	45 min	60 min
12/6/2004		0.00	0.00	1.63	5.55	8.88		0.00	1.66	5.78	9.43
12/8/2004		24.68	67.30	82.80	83.10	115.03		42.62	59.76	61.79	97.49
12/13/2004		0.00	0.00	1.63	5.55	8.88		0.00	1.66	5.78	9.43
12/22/2004		0.00	0.00	28.90	103.05	109.97		0.00	29.47	107.23	116.80
1/12/2005		1.21	115.03	66.45	93.97	83.10		113.82	66.56	96.57	87.04
1/14/2005		0.00	88.83	90.29	90.56	89.33		88.83	92.09	94.23	94.88
12/6/2004		28.07	26.56	31.95	39.61	na		-1.51	4.52	13.14	na
12/8/2004		20.25	17.34	27.03	44.70	36.05		-2.91	7.31	26.26	18.03
	Average	9.28	39.38	41.33	58.26	64.46	average	30.10	32.88	51.35	61.87
	std dev	12.65	45.12	34.53	39.69	45.79	std deviation	46.94	35.42	43.68	47.31
							std error	16.59	12.52	15.44	16.73

Channel 6		Raw data, TAT concentration (ng/ml)						Initial value subtracted, adjusted for dilution (ng/ml)			
date		0 min	15 min	30 min	45 min	60 min		15 min	30 min	45 min	60 min
10/15/2004		0.83	0.89	3.35	5.49	9.22		0.06	2.59	4.88	8.97
11/5/2004		1.74	10.46	9.11	14.44	19.82		8.72	7.54	13.28	19.30
10/26/2004		0.00	17.16	15.72	16.06	17.19		17.16	16.03	16.72	18.26
11/17/2004		2.62	6.09	46.29	73.31	82.61		3.47	44.59	73.66	85.12
11/19/2004		2.95	2.69	3.24	2.56	14.14		-0.25	0.35	-0.29	12.07
11/22/2004		0.94	109.97	2.32	0.44	0.51		109.03	1.43	-0.48	-0.40
11/17/2004		2.62	6.09	46.29	73.31	82.61		3.47	44.59	73.66	85.12
	Average	1.67	21.91	18.05	26.52	32.30	average	20.24	16.73	25.92	32.63
	std dev	1.12	39.20	19.85	32.48	34.93	std deviation	39.61	19.75	33.24	36.44
							std error	14.97	7.46	12.56	13.77

Channel 7		Raw data, TAT concentration (ng/ml)						Initial value subtracted, adjusted for dilution (ng/ml)			
date		0 min	15 min	30 min	45 min	60 min		15 min	30 min	45 min	60 min
12/8/2004		24.68	66.45	93.97	1.21	2.38		41.77	71.16	-23.42	-22.15
12/22/2004		0.00	2.32	0.44	0.51	0.94		2.32	0.45	0.53	1.00
1/12/2005		1.21	2.38	83.01	97.07	104.83		1.17	83.45	99.79	110.12
1/14/2005		0.00	102.03	103.58	105.22	117.82		102.03	105.64	109.48	125.14
1/24/2005		1.00	1.19	0.95	0.67	0.62		0.19	-0.03	-0.30	-0.34
	Average	5.38	34.87	56.39	40.94	45.32	average	29.50	52.13	52.38	58.98
	std dev	10.80	46.79	51.36	55.04	60.43	std deviation	44.19	48.98	62.39	69.17
							std error	19.76	21.91	31.19	34.59

Channel 8		Raw data, TAT concentration (ng/ml)						Initial value subtracted, adjusted for dilution (ng/ml)			
date		0 min	15 min	30 min	45 min	60 min		15 min	30 min	45 min	60 min
10/15/2004		0.83	1.29	9.88	12.26	12.73		0.46	9.25	11.93	12.69
11/12/2004		0.00	13.56	17.13	19.24	21.55		13.56	17.47	20.02	22.89
11/5/2004		1.74	4.36	33.82	57.74	62.71		2.62	32.75	58.34	64.86
11/17/2004		2.62	22.59	60.97	69.73	72.08		19.97	59.56	69.93	73.93
11/22/2004		0.94	0.77	0.63	5.16	84.53		-0.17	-0.30	4.43	88.83
10/26/2004		0.00	56.74	41.55	36.08	54.83		56.74	42.37	37.54	58.23
	Average	1.02	16.55	27.33	33.37	51.40	average	15.53	26.85	33.70	53.57
	std dev	1.02	21.41	22.35	25.94	28.46	std deviation	21.74	22.27	26.28	29.73
							std error	8.87	9.09	10.73	12.14

Valve TAT data:

low leaker		Raw data, TAT concentration (ng/ml)						Initial value subtracted, adjusted for dilution (ng/ml)			
date		0 min	15 min	30 min	45 min	60 min		15 min	30 min	45 min	60 min
7/29/2004		0.24	0.79	clotted	na	na		0.55	na	na	na
7/30/2004		2.09	0.07	3.36	2.85	3.14		-2.01	1.44	0.85	1.19
8/18/2004		39.70	76.10	84.49	82.93	90.76		36.39	44.79	43.23	51.06
9/10/2004		0.00	6.46	6.68	5.95	3.56		6.46	6.68	5.95	3.56
12/15/2004		18.96	0.08	na	na	na		-18.88	na	na	na
1/10/2005		0.00	24.68	67.30	82.80	na		24.68	67.30	82.80	na
7/22/2005		1.32	2.61	7.20	21.58	52.79		1.29	5.88	20.26	51.47
7/12/2005		1.85	2.16	15.65	87.88	99.99		0.31	13.80	86.03	98.14
	Average	8.02	14.12	30.78	47.33	50.05	average	6.10	23.31	39.85	41.08
	std dev	14.30	26.35	35.60	41.29	46.15	std deviation	17.07	26.63	37.53	40.19
							std error	6.04	10.87	15.32	17.98

high leaker		Raw data, TAT concentration (ng/ml)						Initial value subtracted, adjusted for dilution (ng/ml)			
date		0 min	15 min	30 min	45 min	60 min		15 min	30 min	45 min	60 min
7/28/2004		0.24	2.12	2.91	4.43	4.19		1.88	2.67	4.19	3.95
8/23/2004		1.24	2.02	2.04	2.43	2.34		0.78	0.80	1.19	1.10
8/2/2004		9.31	11.92	9.96	10.38	14.98		2.61	0.65	1.07	5.66
9/27/2004		15.76	30.96	32.50	37.61	33.98		15.20	16.74	21.85	18.21
12/20/2004		0.77	0.63	5.16	84.53	112.07		-0.15	4.38	83.75	111.29
1/27/2005		0.51	0.82	0.92	0.92	0.80		0.31	0.42	0.41	0.29
5/26/2005		25.26	19.71	21.06	23.41	22.88		-5.55	-4.20	-1.85	-2.38
	Average	7.59	9.74	10.65	23.39	27.32	average	2.16	3.07	15.80	19.73
	std dev	9.77	11.79	11.87	30.04	39.29	std deviation	6.33	6.58	31.00	40.92
							std error	2.39	2.49	11.72	15.47

SJM Std		Raw data, TAT concentration (ng/ml)						Initial value subtracted, adjusted for dilution (ng/ml)			
date		0 min	15 min	30 min	45 min	60 min		15 min	30 min	45 min	60 min
8/25/2004		0	2.24	1.45	1.95	3.19		2.24	1.45	1.95	3.19
9/8/2004		0	0.14	0.74	0.74	2.36		0.14	0.74	0.74	2.36
10/11/2004		0	1.59	1.19	1.23	2.22		1.59	1.19	1.23	2.22
11/10/2004		0	2.67	2.41	3.05	2.77		2.67	2.41	3.05	2.77
7/20/2005		0	2.34	3.98	3.32	2.63		2.34	3.98	3.32	2.63
	Average	0	1.79	1.95	2.06	2.63	average	1.79	1.95	2.06	2.63
	std dev	0	1.00	1.29	1.12	0.38	std deviation	1.00	1.29	1.12	0.38
							std error	0.45	0.58	0.50	0.17

MP		Raw data, TAT concentration (ng/ml)						Initial value subtracted, adjusted for dilution (ng/ml)			
date		0 min	15 min	30 min	45 min	60 min		15 min	30 min	45 min	60 min
9/22/2004		0.70	2.31	4.53	6.06	6.40		1.61	3.83	5.37	5.70
9/29/2004		0.87	1.46	1.73	2.97	30.84		0.59	0.86	2.10	29.97
10/8/2004		0.00	6.74	3.96	5.73	6.95		6.74	3.96	5.73	6.95
10/14/2004		0.00	0.00	18.46	44.03	63.24		0.00	18.46	44.03	63.24
10/25/2004		0.00	2.91	5.36	5.88	9.83		2.91	5.36	5.88	9.83
11/23/2004		0.08	0.00	0.00	28.90	103.05		-0.08	-0.08	28.82	102.97
12/3/2004		0.00	0.00	0.00	0.00	18.96		0.00	0.00	0.00	18.96
	Average	0.24	1.92	4.86	13.37	34.18	average	1.68	4.63	13.13	33.95
	std dev	0.38	2.44	6.37	16.51	36.37	std deviation	2.48	6.46	16.64	36.45
							std error	0.94	2.44	6.29	13.78

B.2. PF4 ELISA assays – Raw data

Orifice PF4 Data:

	Raw data, PF4 concentration (ng/ml)						Initial value subtracted, adjusted for dilution and multiplied by 100 to obtain concentration in flow loop			
400r Norm	0 min	15 min	30 min	45 min	60 min		15 min	30 min	45 min	60 min
7/8/2004	3.35	3.84	4.31	4.33	3.43		48.63	104.56	115.48	28.80
7/8/2004	3.35	7.00	11.30	12.36	10.72		365.40	817.83	950.70	803.75
8/25/2004	1.29	9.70	11.97	7.30	8.49		840.78	1091.18	630.00	772.14
8/30/2004	1.03	6.55	10.92	9.52	9.07		551.82	1010.29	887.36	859.40
8/30/2004	1.03	6.07	8.55	9.35	na		503.83	768.31	869.38	na
9/2/2004	0.99	1.82	2.15	2.36	1.96		83.08	121.06	147.21	109.51
9/30/2004	0.70	1.81	2.38	2.67	3.78		110.22	171.87	207.09	331.39
9/30/2004	0.70	3.05	5.11	4.38	5.06		234.72	450.83	385.49	466.95
						average	342.31	566.99	524.09	481.71
						std deviation	277.20	406.56	353.17	369.26
						std error	98.00	143.74	124.86	139.57

400r Norm = Standard experiments with the 400 μm round orifice

	Raw data, PF4 concentration (ng/ml)						Initial value subtracted, adjusted for dilution and multiplied by 100 to obtain concentration in flow loop			
400r Agg (18)	0 min	15 min	30 min	45 min	60 min		15 min	30 min	45 min	60 min
6/30	4.10	10.54	15.51	19.03	14.44		429.82	781.70	1047.30	749.24
6/30	4.10	12.14	15.08	14.95	12.27		536.56	752.21	763.91	596.02
						average	483.19	766.96	905.60	672.63

Agg (18) = experiments with 18μg added Aggrastat

	Raw data, PF4 concentration (ng/ml)						Initial value subtracted, adjusted for dilution and multiplied by 100 to obtain concentration in flow loop			
400r Agg (180)	0 min	15 min	30 min	45 min	60 min		15 min	30 min	45 min	60 min
6/24	0.90	4.65	1.60	2.00	2.28		249.87	49.17	78.61	101.41
6/24	0.90	9.78	8.46	6.89	7.98		592.00	515.14	418.45	505.33
7/20	1.21	5.09	5.65	6.88			388.38	456.03	594.93	na
7/20	1.21	4.83	4.74	6.31	5.58		362.21	362.49	536.04	471.86
7/23	0.52	2.46	2.89	3.34	2.97		194.50	242.82	295.73	263.68
7/23	0.52	1.41	1.52	1.81	1.72		89.07	103.00	136.72	130.90
						average	312.67	288.11	343.41	294.63
						std deviation	175.57	189.04	210.29	187.68
						std error	71.67	77.17	85.85	83.93

Agg (180) = experiments with 180μg added Aggrastat

	Raw data, PF4 concentration (ng/ml)						Initial value subtracted, adjusted for dilution and multiplied by 100 to obtain concentration in flow loop			
400r AN51 (125 ul)	0 min	15 min	30 min	45 min	60 min		15 min	30 min	45 min	60 min
1/19/2005	1.54	3.11	3.89	5.19	6.67		156.53	242.47	386.52	554.28
1/19/2005	1.54	3.44	4.98	7.24	9.80		189.73	354.33	599.09	886.39
1/20/2005	0.96	4.30	8.49	14.45	12.50		334.31	769.38	1407.23	1231.95
1/20/2005	0.96	5.23	8.11	9.98	11.24		427.32	731.27	942.23	1098.10
1/21/2005	1.53	7.52	14.92	15.19	12.32		598.97	1368.32	1427.57	1155.08
1/21/2005	1.53	9.37	7.67	11.95	11.16		784.09	629.34	1090.78	1032.30
						average	415.16	682.52	975.57	993.02
						std deviation	242.61	396.09	422.79	244.87
						std error	99.04	161.70	172.60	99.97

AN51 (125 ul) = experiments with 125 μl added AN51 antibody

	Raw data, PF4 concentration (ng/ml)						Initial value subtracted, adjusted for dilution and multiplied by 100 to obtain concentration in flow loop			
1200r Norm	0 min	15 min	30 min	45 min	60 min		15 min	30 min	45 min	60 min
9/2/2004	0.99	5.00	8.22	11.64	10.41		401.32	739.94	1113.00	1006.78
9/9/2004	2.18	5.80	8.59	6.34	5.28		361.87	658.05	440.95	342.58
9/15/2004	0.87	5.33	11.70	13.14	16.17		445.69	1106.44	1279.97	1629.90
						average	402.96	834.81	944.64	993.09
						std deviation	41.93	238.78	444.13	643.77
						std error	24.21	137.86	256.42	371.68

1200r Norm = Standard experiments with the 1200 μm round orifice

	Raw data, PF4 concentration (ng/ml)						Initial value subtracted, adjusted for dilution and multiplied by 100 to obtain concentration in flow loop			
800r norm	0 min	15 min	30 min	45 min	60 min		15 min	30 min	45 min	60 min
7/13/2005	1.05	2.52	4.18	3.97	5.50		147.40	321.30	307.65	479.05
	Raw data, PF4 concentration (ng/ml)						Initial value subtracted, adjusted for dilution and multiplied by 100 to obtain concentration in flow loop			
800r high	0 min	15 min	30 min	45 min	60 min		15 min	30 min	45 min	60 min
7/29/2005	2.50	5.81	5.45	5.54	4.81		330.26	305.60	326.37	260.58
7/21/2005	0.61	6.15	4.51	6.66	7.89		553.90	398.54	631.22	776.19
7/22/2004	10.36	5.11	4.38	5.97	9.18		-525.07	-589.49	-414.93	-60.56
7/28/2005	1.11	10.64	9.78	5.59	8.85		953.81	886.79	471.07	829.68
8/3/2005	2.88	9.01	8.60	10.04	11.82		613.57	589.67	756.60	967.43
						average	385.29	318.22	354.07	554.66
						std deviation	555.78	553.97	459.52	435.91
						std error	277.89	276.98	229.76	217.96
	Raw data, PF4 concentration (ng/ml)						Initial value subtracted, adjusted for dilution and multiplied by 100 to obtain concentration in flow loop			
800r low	0 min	17.5 min	35 min	52.5 min	70 min		15 min	30 min	45 min	60 min
7/29/2005	2.50	2.41	3.01	3.52	5.15		-9.29	57.01	116.04	296.71
8/3/2005	2.88	4.68	4.98	6.27	5.78		180.51	220.47	364.14	326.39
7/21/2005	0.61	3.92	7.08	5.27	10.17		330.64	660.61	487.23	1018.51
7/28/2005	1.11	4.78	5.94	7.96	6.63		366.99	495.13	718.12	593.14
7/27/2005	2.26	2.69	4.12	6.29	4.20		43.76	194.30	428.35	220.60
7/15/2005	2.67	4.60	5.72	8.03	8.61		193.37	316.64	569.32	648.36
						average	184.33	324.03	447.20	517.28
						std deviation	149.74	219.76	203.39	299.09
						std error	61.13	89.72	83.03	122.10

800r low = low flow rate experiments with the 800 μm round orifice
800r high = high flow rate experiments with the 800 μm round orifice
800r normal = standard flow rate experiments with the 800 μm round orifice

Channel PF4 data:

	Raw data, PF4 concentration (ng/ml)						Initial value subtracted, adjusted for dilution and multiplied by 100 to obtain concentration in flow loop			
Channel 1	0 min	15 min	30 min	45 min	60 min		15 min	30 min	45 min	60 min
6/1/2005	3.69	4.80	4.07	13.25	11.85		110.94	46.40	1010.03	889.61

	Raw data, PF4 concentration (ng/ml)						Initial value subtracted, adjusted for dilution and multiplied by 100 to obtain concentration in flow loop			
Channel 2	0 min	15 min	30 min	45 min	60 min		15 min	30 min	45 min	60 min
6/1/2005	3.69	4.09	15.50	8.90	10.63		40.60	1212.23	557.09	760.59

	Raw data, PF4 concentration (ng/ml)						Initial value subtracted, adjusted for dilution and multiplied by 100 to obtain concentration in flow loop			
Channel 3	0 min	15 min	30 min	45 min	60 min		15 min	30 min	45 min	60 min
5/19	0.21	5.33	11.98	7.78	9.21		340.99	800.48	525.36	638.06
5/20	1.37	5.97	3.08	4.37	4.62		306.63	117.82	211.94	235.46
5/24	0.67	3.55	8.05	4.73	5.85		191.95	502.89	283.25	369.64
5/26	1.02	3.34	8.99	10.49	10.41		154.28	542.79	659.26	668.79
6/16	0.96	10.85	9.87	15.70	11.27		659.64	607.23	1025.10	734.35
9/15/2004	0.87	6.26	8.90	7.95	10.56		538.90	820.92	739.68	1033.97
9/20/2004	1.57	6.11	7.97	7.71	12.83		453.41	656.13	645.40	1205.34
						average	377.97	578.32	584.28	697.95
						std deviation	183.50	235.98	277.06	341.03
						std error	69.35	89.19	104.72	128.90

	Raw data, PF4 concentration (ng/ml)						Initial value subtracted, adjusted for dilution and multiplied by 100 to obtain concentration in flow loop			
Channel 4	0 min	15 min	30 min	45 min	60 min		15 min	30 min	45 min	60 min
5/19	0.21	0.66	5.74	9.97	1.82		29.63	376.42	677.77	114.49
5/20	1.37	3.52	4.62	10.32	17.41		143.30	222.58	624.53	1141.40
5/24	0.67	2.64	6.18	4.84	5.22		131.21	375.93	291.24	325.34
5/26	1.02	4.75	10.98	9.31	8.77		248.75	678.12	577.52	552.50
6/16	0.96	4.85	10.26	16.07	10.13		259.52	634.10	1050.84	653.73
9/9/2004	2.18	16.95	12.15	17.12	18.04		1476.30	1021.29	1563.43	1697.59
9/20/2004	1.57	8.75	19.60	18.74	19.54		718.18	1842.26	1792.43	1918.10
						average	429.56	735.81	939.68	914.73
						std deviation	511.77	554.00	555.00	690.18
						std error	193.43	209.39	209.77	260.86

	Raw data, PF4 concentration (ng/ml)						Initial value subtracted, adjusted for dilution and multiplied by 100 to obtain concentration in flow loop			
Channel 5	0 min	15 min	30 min	45 min	60 min		15 min	30 min	45 min	60 min
1/14/2005	1.00	9.44	10.37	11.30	10.99		844.20	957.11	1076.17	1066.91
1/12/2005	0.92	10.82	11.63	11.92	13.91		990.07	1094.34	1148.37	1385.23
12/13/2005	2.82	9.77	12.28	13.27	12.89		694.94	970.62	1098.53	1086.48
12/22/2004	0.09	1.54	3.94	5.95	6.49		145.07	392.99	610.70	680.69
						average	668.57	853.76	983.45	1054.83
						std deviation	369.21	313.33	250.32	288.84
						std error	184.61	156.66	125.16	144.42

	Raw data, PF4 concentration (ng/ml)						Initial value subtracted, adjusted for dilution and multiplied by 100 to obtain concentration in flow loop			
Channel 6	0 min	15 min	30 min	45 min	60 min		15 min	30 min	45 min	60 min
10/15/2004	2.01	8.94	8.01	7.98	6.92		693.57	616.56	629.41	534.42
10/26/2004	1.83	3.41	5.98	5.50	5.84		158.25	426.99	388.78	436.89
11/5/2004	1.72	13.07	12.54	14.66	14.60		1134.94	1107.06	1353.26	1379.04
						average	662.25	716.87	790.49	783.45
						std deviation	489.10	350.95	502.01	518.10
						std error	282.38	202.62	289.83	299.12

	Raw data, PF4 concentration (ng/ml)						Initial value subtracted, adjusted for dilution and multiplied by 100 to obtain concentration in flow loop			
Channel 7	0 min	15 min	30 min	45 min	60 min		15 min	30 min	45 min	60 min
1/14/2005	1.00	11.82	10.24	10.42	11.58		1081.50	944.82	984.76	1130.00
1/12/2005	0.92	1.67	2.73	2.45	4.06		75.06	186.44	163.16	339.19
12/13/2004	2.82	2.67	3.87	7.15	11.30		-15.28	112.93	461.73	918.15
12/22/2004	0.09	2.87	2.28	2.86	6.24		278.08	223.46	288.96	653.60
1/24/2005	0.14	0.59	0.92	0.85	0.64		44.94	79.80	74.05	53.22
						average	292.86	309.49	394.53	618.83
						std deviation	454.43	359.71	360.65	433.08
						std error	203.23	160.87	161.29	193.68

	Raw data, PF4 concentration (ng/ml)						Initial value subtracted, adjusted for dilution and multiplied by 100 to obtain concentration in flow loop			
Channel 8	0 min	15 min	30 min	45 min	60 min		15 min	30 min	45 min	60 min
10/15/2004	2.01	6.22	7.14	7.21	6.80		421.22	527.52	550.08	521.90
10/26/2004	1.83	8.70	9.54	11.06	10.62		687.20	789.92	967.82	944.48
11/5/2004	1.72	7.53	5.85	6.18	6.55		581.09	425.19	471.88	523.92
11/12/2004	2.95	4.86	5.95	4.55	4.76		190.53	312.09	178.05	210.34
6-10-05 b	2.56	6.27	9.93	9.57	10.06		371.11	757.55	740.46	812.91
						average	450.23	562.45	581.66	602.71
						std deviation	192.24	207.69	295.92	286.22
						std error	85.97	92.88	132.34	128.00

Valve PF4 data:

	Raw data, PF4 concentration (ng/ml)						Initial value subtracted, adjusted for dilution and multiplied by 100 to obtain concentration in flow loop			
low leaker	0 min	15 min	30 min	45 min	60 min		15 min	30 min	45 min	60 min
7/29/2004	2.03	5.96	na	na	na		415.08	na	na	na
7/30/2004	1.07	1.74	2.22	2.16	2.50		73.72	125.50	121.81	159.90
8/18/2004	1.00	0.02	9.88	13.82	14.63		-98.08	934.92	1361.29	1461.68
9/10/2004	1.28	1.72	2.30	2.31	2.45		50.48	112.90	116.04	133.28
10/1/2004	1.03	5.08	9.12	11.08	10.05		424.13	852.56	1068.35	970.34
1/10/2005	0.94	5.58	9.95	13.03	na		484.54	948.27	1283.87	na
12/15/2005	0.80	6.04	na	na	na		546.58	na	na	na
7/22/2005	0.89	2.69	4.48	6.26	6.78		190.11	380.61	572.86	634.51
7/12/2005	2.96	5.64	4.29	10.44	9.78		289.32	153.83	808.22	748.48
						average	263.99	501.23	761.78	684.70
						std deviation	222.47	395.51	514.84	504.25
						std error	74.16	149.49	194.59	205.86

	Raw data, PF4 concentration (ng/ml)						Initial value subtracted, adjusted for dilution and multiplied by 100 to obtain concentration in flow loop			
SJM Std	0 min	15 min	30 min	45 min	60 min		15 min	30 min	45 min	60 min
8/25/2004	0.58	2.21	6.62	4.23	4.96		172.04	635.93	389.21	471.89
9/8/2004	0.51	8.11	1.90	2.12	2.84		790.35	148.46	173.25	252.54
11/15/2004	0.95	2.14	2.92	3.35	3.06		126.38	210.65	258.56	231.58
10/11/2004	0.57	1.60	1.90	2.16	2.32		108.49	141.82	170.88	190.55
11/10/2004	0.44	2.36	2.92	4.31	3.60		201.40	261.74	412.07	340.62
7/22/2005	1.35	2.42	3.07	3.57	3.89		115.77	185.97	242.80	280.23
						average	252.40	264.10	274.46	294.57
						std deviation	265.97	187.38	104.24	100.32
						std error	108.58	76.50	42.56	40.96

	Raw data, PF4 concentration (ng/ml)						Initial value subtracted, adjusted for dilution and multiplied by 100 to obtain concentration in flow loop			
high leaker	0 min	15 min	30 min	45 min	60 min		15 min	30 min	45 min	60 min
7/28/2004	0.81	1.79	2.09	2.98	3.29		104.69	138.08	234.28	270.19
8/2/2004	1.81	3.36	5.53	4.63	7.21		166.87	397.92	308.45	588.47
8/23/2004	1.00	2.11	7.01	10.09	7.16		119.03	633.84	966.60	664.35
1/27/2005	0.94	2.86	7.09	8.36	8.37		202.96	648.72	790.60	799.64
9/27/2004	2.30	2.32	3.26	4.83	5.81		11.18	111.82	281.33	390.98
12/20/2005	2.09	6.77	10.29	11.48	12.35		492.77	868.19	1005.12	1109.72
5/26/2005	1.05	4.01	6.08	9.35	9.80		311.29	532.05	883.67	941.05
						average	201.25	475.80	638.58	680.63
						std deviation	158.37	278.27	347.66	296.43
						std error	59.86	105.18	131.40	112.04

	Raw data, PF4 concentration (ng/ml)						Initial value subtracted, adjusted for dilution and multiplied by 100 to obtain concentration in flow loop			
MP	0 min	15 min	30 min	45 min	60 min		15 min	30 min	45 min	60 min
9/22/2004	0.90	3.08	5.16	5.09	5.67		229.50	450.28	448.17	515.10
12/3/2004	3.04	2.09	3.65	4.09	5.51		-87.28	78.29	128.19	284.09
9/29/2004	1.49	2.14	3.78	3.32	4.62		72.70	247.16	202.10	343.48
10/8/2004	1.25	2.54	3.31	3.93	4.83		138.09	221.10	289.90	390.00
10/14/2004	1.55	3.01	3.97	6.23	5.39		156.95	260.94	503.05	420.35
10/25/2004	0.51	1.60	2.21	3.33	3.86		115.31	180.43	300.65	360.62
10/27/2004	2.21	4.93	5.85	7.23	7.00		290.49	392.06	543.41	526.19
						average	130.82	261.47	345.07	405.69
						std deviation	120.52	125.61	156.75	89.11
						std error	45.55	47.47	59.25	33.68

B.3. Plasma hemoglobin assays – Raw data

Orifice Hemolysis Data:

200um round		Raw data, Hemoglobin concentration (mg/ml)						Initial value subtracted, adjusted for dilution and multiplied by 100 to obtain concentration in flow loop (mg/ml)			
date		0 min	15 min	30 min	45 min	60 min		15 min	30 min	45 min	60 min
12/19/2003		1.64	4.28	6.25	5.37	7.51		2.64	4.70	3.89	6.21
12/19/2003		1.64	7.46	6.05	6.80	8.34		5.83	4.50	5.37	7.08
1/5/2004		1.32	2.89	4.05	4.40	4.48		1.57	2.79	3.21	3.36
01/06/04		2.55	4.02	4.69	6.98	5.04		1.46	2.21	4.64	2.71
01/06/04		2.55	4.76	6.51	na	na		2.21	4.05	na	na
	average	1.94	4.68	5.26	5.89	6.34	average	2.74	3.65	4.28	4.84
	std dev	0.57	1.70	1.06	1.23	1.88	std deviation	1.79	1.10	0.93	2.13
							std error	0.80	0.49	0.42	0.95

400 um round		Raw data, Hemoglobin concentration (mg/ml)						Initial value subtracted, adjusted for dilution and multiplied by 100 to obtain concentration in flow loop (mg/ml)			
date		0 min	15 min	30 min	45 min	60 min		15 min	30 min	45 min	60 min
7/8/2004		2.08	3.11	3.18	3.61	2.39		1.03	1.14	1.64	0.42
7/8/2004		2.08	4.30	4.71	6.51	7.52		2.21	2.72	4.69	5.91
7/22/2004		2.14	5.87	4.27	6.79	9.55		3.73	2.19	4.85	7.84
7/23/2004		1.67	5.23	4.44	4.59	5.15		3.56	2.85	3.10	3.80
7/23/2004		1.67	1.79	2.12	2.13	2.04		0.12	0.49	0.54	0.50
8/25/2004		1.90	2.82	3.89	3.41	4.30		0.91	2.06	1.65	2.67
8/30/2004		1.21	3.10	3.82	3.91	4.07		1.89	2.68	2.85	3.11
8/30/2004		1.21	2.49	3.05	3.44	2.03		1.28	1.89	2.37	0.95
9/2/2004		1.52	5.81	7.76	13.68	14.30		4.29	6.40	12.72	13.67
9/2/2004		1.52	1.97	1.99	2.00	1.61		0.45	0.51	0.56	0.19
08/06/03		2.91	2.67	3.15	5.39	3.31		-0.24	0.29	2.64	0.56
8/20/2003		2.76	4.36	6.14	6.86	7.06		1.60	3.46	4.30	4.61
9/4/2003		1.94	3.46	4.08	na	2.97		1.51	2.19	na	1.16
9/24/2003		1.80	2.87	3.45	3.48	3.54		1.08	1.70	1.79	1.91
9/25/2003		2.81	2.61	3.02	2.91	3.76		-0.20	0.25	0.18	1.12
10/1/2003		1.81	2.98	3.55	3.41	3.49		1.17	1.79	1.70	1.84
10/16/2003		1.88	2.70	2.95	8.55	3.53		0.83	1.12	6.92	1.81
	average	1.94	3.42	3.86	5.04	4.43	average	1.48	1.98	3.28	3.06
	std dev	0.50	1.25	1.41	2.96	3.29	std deviation	1.32	1.49	3.10	3.45
							std error	0.32	0.36	0.77	0.84

800um round		Raw data, Hemoglobin concentration (mg/ml)						Initial value subtracted, adjusted for dilution and multiplied by 100 to obtain concentration in flow loop (mg/ml)			
date		0 min	15 min	30 min	45 min	60 min		15 min	30 min	45 min	60 min
9/22/2003		1.88	3.77	4.14	4.20	4.20		1.90	2.32	2.44	2.51
9/24/2003		1.80	4.46	4.56	6.85	5.78		2.67	2.83	5.25	4.24
10/1/2003		1.81	3.79	4.36	4.32	4.33		1.98	2.61	2.63	2.71
10/15/2003		2.18	5.40	5.03	5.24	4.89		3.22	2.92	3.21	2.92
10/16/2003		1.88	2.64	3.04	2.77	2.61		0.76	1.21	0.97	0.85
1/9/2004		0.00	4.43	5.66	7.39	7.41		4.43	5.74	7.60	7.74
							average	2.49	2.94	3.69	3.49
							std deviation	1.26	1.51	2.37	2.34
							std error	0.51	0.61	0.97	0.96

1200um new setup		Raw data, Hemoglobin concentration (mg/ml)						Initial value subtracted, adjusted for dilution and multiplied by 100 to obtain concentration in flow loop (mg/ml)			
date		0 min	15 min	30 min	45 min	60 min		15 min	30 min	45 min	60 min
8/7/2003		1.77	2.38	3.45	3.44	3.30		0.61	1.75	1.81	1.73
8/20/2003		2.82	3.68	4.21	4.15	5.06		0.86	1.48	1.50	2.55
9/4/2003		1.94	2.33	2.56	2.77	2.82		0.38	0.66	0.91	1.00
9/25/2003		2.81	2.67	2.63	3.42	2.79		-0.15	-0.14	0.70	0.10
10/2/2003		1.74	3.48	3.30	3.39	3.56		1.74	1.60	1.74	1.98
10/9/2003		1.91	2.86	2.77	2.93	2.77		0.95	0.91	1.11	0.98
9/2/2004		1.58	1.97	1.99	2.00	1.61		0.38	0.43	0.48	0.10
9/9/2004		1.48	5.51	6.79	8.87	12.06		4.03	5.41	7.65	11.12
9/15/2004		1.21	2.12	2.55	3.14	3.78		0.92	1.38	2.03	2.74
	average	1.92	3.00	3.36	3.79	4.19	average	1.08	1.50	1.99	2.48
	std dev	0.56	1.11	1.44	1.99	3.09	std deviation	1.22	1.59	2.19	3.38
							std error	0.41	0.53	0.73	1.13

200um slit		Raw data, Hemoglobin concentration (mg/ml)						Initial value subtracted, adjusted for dilution and multiplied by 100 to obtain concentration in flow loop (mg/ml)			
date		0 min	15 min	30 min	45 min	60 min		15 min	30 min	45 min	60 min
10/22/2003		1.98	3.67	4.03	4.66	4.47		1.68	2.11	2.81	2.69
11/12/2003		1.36	2.54	2.80	2.88	2.85		1.18	1.48	1.60	1.62
	average	1.67	3.10	3.42	3.77	3.66	average	1.43	1.79	2.21	2.15
							std deviation	0.35	0.44	0.85	0.75
							std error	0.25	0.31	0.60	0.53

400um slit		Raw data, Hemoglobin concentration (mg/ml)						Initial value subtracted, adjusted for dilution and multiplied by 100 to obtain concentration in flow loop (mg/ml)			
date		0 min	15 min	30 min	45 min	60 min		15 min	30 min	45 min	60 min
10/22/2003		1.98	3.70	3.98	4.27	4.50		1.72	2.06	2.42	2.72
10/30/2003		1.39	2.02	3.11	3.23	3.15		0.62	1.76	1.93	1.90
							average	1.17	1.91	2.17	2.31
							std deviation	0.77	0.21	0.34	0.58
							std error	0.55	0.15	0.24	0.41

800um slit		Raw data, Hemoglobin concentration (mg/ml)						Initial value subtracted, adjusted for dilution and multiplied by 100 to obtain concentration in flow loop (mg/ml)			
date		0 min	15 min	30 min	45 min	60 min		15 min	30 min	45 min	60 min
11/3/2003		1.10	1.78	2.00	1.89	2.07		0.69	0.93	0.85	1.06
11/11/2003		0.00	2.49	2.88	3.28	4.07		2.49	2.93	3.38	4.25
11/12/2003		1.36	2.70	3.08	2.91	2.94		1.34	1.76	1.64	1.71
	average	0.82	2.32	2.65	2.70	3.03	average	1.51	1.87	1.96	2.34
	std dev	0.72	0.48	0.57	0.72	1.01	std deviation	0.91	1.00	1.29	1.69
							std error	0.53	0.58	0.75	0.97

400um pf		Raw data, Hemoglobin concentration (mg/ml)						Initial value subtracted, adjusted for dilution and multiplied by 100 to obtain concentration in flow loop (mg/ml)			
date		0 min	15 min	30 min	45 min	60 min		15 min	30 min	45 min	60 min
2/16/2004		0.94	2.62	3.55	3.69	3.63		1.68	2.66	2.86	2.86
3/17/2004		1.97	1.89	2.04	2.27	2.45		-0.08	0.10	0.37	0.59
3/18/2004		3.82	4.53	5.37	6.43	6.66		0.71	1.63	2.81	3.15
3/25/2004		1.45	4.57	6.21	6.93	6.78		3.12	4.86	5.69	5.63
3/26/2004		3.28	2.11	2.48	3.30	3.14		-1.18	-0.77	0.12	-0.01
4/9/2004		1.23	1.65	1.88	1.83	1.60		0.42	0.68	0.66	0.45
	average	2.29	3.14	3.93	4.53	4.53	average	0.78	1.53	2.08	2.11
	std dev	1.22	1.31	1.81	2.04	2.04	std deviation	1.48	2.02	2.14	2.17
							std error	0.61	0.83	0.88	0.89

pf = experiments with platelet removal

400um no ca2+		Raw data, Hemoglobin concentration (mg/ml)						Initial value subtracted, adjusted for dilution and multiplied by 100 to obtain concentration in flow loop (mg/ml)			
date		0 min	15 min	30 min	45 min	60 min		15 min	30 min	45 min	60 min
1/28/2004		1.33	3.05	3.76	2.92	3.69		1.72	2.48	1.67	2.53
1/28/2004		1.33	2.00	3.07	2.93	3.08		0.67	1.78	1.68	1.89
2/4/2004		1.34	3.71	4.80	4.76	5.21		2.37	3.53	3.56	4.10
2/4/2004		1.34	3.31	3.96	3.95	4.66		1.96	2.68	2.73	3.52
2/25/2004		2.59	5.28	6.62	7.07	7.35		2.69	4.12	4.68	5.09
2/25/2004		2.59	4.26	5.40	7.06	7.50		1.67	2.88	4.67	5.24
	average	1.76	3.60	4.60	4.78	5.25	average	1.85	2.91	3.17	3.73
	std dev	0.65	1.12	1.28	1.90	1.84	std deviation	0.70	0.82	1.37	1.35
							std error	0.28	0.33	0.56	0.55

no ca2+ = experiments with no added Ca^{2+}

400um 18g Agg		Raw data, Hemoglobin concentration (mg/ml)						Initial value subtracted, adjusted for dilution and multiplied by 100 to obtain concentration in flow loop (mg/ml)			
date		0 min	15 min	30 min	45 min	60 min		15 min	30 min	45 min	60 min
6/30/2004		4.93	2.90	2.86	2.44	3.19		-2.02	-2.01	-2.39	-1.54
6/30/2004		4.93	2.84	2.16	3.14	2.54		-2.08	-2.72	-1.65	-2.22
	average	4.93	2.87	2.51	2.79	2.87		-2.05	-2.37	-2.02	-1.88

18g Agg = experiments with 18µg added Aggrastat

400um 180g Agg		Raw data, Hemoglobin concentration (mg/ml)						Initial value subtracted, adjusted for dilution and multiplied by 100 to obtain concentration in flow loop (mg/ml)			
date		0 min	15 min	30 min	45 min	60 min		15 min	30 min	45 min	60 min
7/20/2004		2.32	2.80	3.72	4.38	na		0.47	1.47	2.23	na
7-20-04b		2.32	3.68	3.99	4.93	3.08		1.35	1.75	2.80	0.95
	Average	2.32	3.24	3.86	4.65	3.08		0.91	1.61	2.52	0.95

180g Agg = experiments with 180µg added Aggrastat

400um 125 ul AN51		Raw data, Hemoglobin concentration (mg/ml)						Initial value subtracted, adjusted for dilution and multiplied by 100 to obtain concentration in flow loop (mg/ml)			
date		0 min	15 min	30 min	45 min	60 min		15 min	30 min	45 min	60 min
1/19/2005		1.84	2.28	2.02	2.39	2.33		0.43	0.22	0.65	0.63
1/19/2005		1.84	1.98	2.18	2.95	3.54		0.14	0.38	1.23	1.92
1/20/2005		1.67	2.79	3.59	4.57	5.02		1.11	1.99	3.08	3.65
1/20/2005		1.67	2.56	2.73	2.50	2.51		0.89	1.11	0.93	0.99
1/21/2005		1.62	2.06	2.26	2.41	2.92		0.44	0.69	0.89	1.48
1/21/2005		1.62	2.99	2.31	2.69	2.33		1.37	0.74	1.18	0.86
	Average	1.71	2.44	2.52	2.92	3.11	average	0.73	0.85	1.33	1.59
	std dev	0.10	0.41	0.58	0.84	1.04	std deviation	0.47	0.64	0.89	1.11
	std error	0.04	0.17	0.24	0.34	0.43	std error	0.19	0.26	0.36	0.45

125 ul AN51 = experiments with 125 µl AN51 antibody

		Raw data, Hemoglobin concentration (mg/ml)						Initial value subtracted, adjusted for dilution and multiplied by 100 to obtain concentration in flow loop (mg/ml)			
		Passes						Passes			
800r low		0	25	50	75	100		25	50	75	100
7/29/2005		2.12	2.89	3.26	3.64	2.89		0.77	1.19	1.64	0.90
8/3/2005		1.55	2.38	2.54	3.18	2.90		0.84	1.02	1.73	1.48
7/21/2005		2.06	4.34	4.20	4.77	4.83		2.28	2.20	2.85	2.99
7/15/2005		1.81	2.34	2.91	2.44	5.92		0.53	1.15	0.70	4.37
7/28/2005		2.07	3.76	1.88	2.45	3.13		1.68	-0.16	0.45	1.19
7/27/2005		3.57	4.40	4.42	5.15	3.24		0.83	0.91	1.74	-0.18
	average	2.20	3.35	3.20	3.61	3.82	average	1.16	1.05	1.52	1.79
	std dev	0.70	0.94	0.97	1.15	1.26	std deviation	0.68	0.75	0.86	1.63
							std error	0.28	0.31	0.35	0.66
800r high		0	25	50	75	100		25	50	75	100
7/29/2005		2.12	3.88	3.73	10.75	21.00		1.77	1.67	8.94	19.78
7/21/2005		2.06	6.29	49.53	93.28	112.07		4.23	48.15	93.83	114.78
7/28/2005		2.07	1.43	1.56	23.60	36.73		-0.64	-0.49	22.19	36.23
8/3/2005		0.00	2.54	2.71	3.27	3.62		2.54	2.75	3.37	3.78
	average	1.56	3.54	14.38	32.73	43.35	average	1.97	13.02	32.08	43.64
	std dev	1.04	2.09	23.45	41.23	47.76	std deviation	2.02	23.46	41.92	49.24
							std error	1.01	11.73	20.96	24.62
800r norm		0	25	50	75	100		25	50	75	100
7/13/2005		1.88	3.77	4.14	4.20	4.20		1.90	2.34	2.49	2.58
9/24/2003		1.80	4.46	4.56	6.85	5.78		2.67	2.85	5.33	4.34
10/1/2003		1.81	3.79	4.36	4.32	4.33		1.98	2.63	2.68	2.78
10/15/2003		2.18	5.40	5.03	5.24	4.89		3.22	2.95	3.27	3.01
10/16/2003		1.88	2.64	3.04	2.77	2.61		0.76	1.22	1.00	0.90
1/9/2004		1.32	4.43	5.66	7.39	7.41		3.11	4.45	6.37	6.55
1/14/2004		7.65	6.08	5.55	6.05	6.60		-1.57	-2.00	-1.36	-0.65
	average	2.65	4.37	4.62	5.26	5.12	average	1.72	2.06	2.83	2.79
	std dev	2.22	1.13	0.90	1.63	1.62	std deviation	1.68	2.03	2.58	2.31
							std error	0.63	0.77	0.98	0.87

800r low = low flow rate experiments with the 800 µm round orifice
800r high = high flow rate experiments with the 800 µm round orifice
800r normal = standard flow rate experiments with the 800 µm round orifice

Channel Hemolysis data:

Channel 1		Raw data, Hemoglobin concentration (mg/ml)						Initial value subtracted, adjusted for dilution and multiplied by 100 to obtain concentration in flow loop (mg/ml)			
date		0 min	15 min	30 min	45 min	60 min		15 min	30 min	45 min	60 min
11/14/2003		0.75	1.19	1.12	2.31	2.07		0.44	0.39	1.62	1.41
11/17/2003		0.36	0.67	0.78	0.85	0.91		0.32	0.44	0.52	0.60
11/21/2003		0.52	1.86	3.27	2.59	3.01		1.33	2.80	2.14	2.62
11/24/2003		0.61	2.46	3.34	3.34	3.34		1.85	2.78	2.83	2.88
3/24/2003		1.47	4.00	6.34	6.46	5.36		2.53	4.96	5.18	4.13
3/31/2003		0.00	6.97	8.92	na	na		6.97	9.05	na	na
5/14/2004		1.10	2.04	2.55	2.58	2.92		0.94	1.51	1.58	2.01
	average	0.69	2.74	3.76	3.02	2.94	average	2.06	3.13	2.31	2.27
	std dev	0.48	2.14	2.91	1.87	1.48	std deviation	2.30	3.06	1.60	1.23
							std error	0.87	1.15	0.65	0.50

Channel 2		Raw data, Hemoglobin concentration (mg/ml)						Initial value subtracted, adjusted for dilution and multiplied by 100 to obtain concentration in flow loop (mg/ml)			
date	nd flow (lpm	0 min	15 min	30 min	45 min	60 min		15 min	30 min	45 min	60 min
11/14/2003		0.75	0.86	1.80	1.46	0.85		0.11	1.08	0.75	0.14
11/24/2003		0.61	1.60	2.03	2.60	1.54		1.00	1.45	2.06	1.00
11/25/2003		0.51	0.77	1.23	2.19	2.27		0.27	0.74	1.74	1.86
11/25/2003		0.51	1.09	1.59	1.75	2.06		0.58	1.11	1.30	1.65
3/24/2004		1.47	3.58	4.62	5.41	5.13		2.10	3.22	4.09	3.89
5/14/2004		1.10	2.14	3.31	3.91	4.71		1.04	2.25	2.92	3.82
	average	0.82	1.67	2.43	2.89	2.76	average	0.85	1.64	2.15	2.06
	std dev	0.39	1.06	1.29	1.50	1.75	std deviation	0.72	0.93	1.20	1.51
							std error	0.29	0.38	0.49	0.62

Channel 3		Raw data, Hemoglobin concentration (mg/ml)						Initial value subtracted, adjusted for dilution and multiplied by 100 to obtain concentration in flow loop (mg/ml)			
date		0 min	15 min	30 min	45 min	60 min		15 min	30 min	45 min	60 min
5/19/2004		1.25	4.42	5.11	5.45	6.15		3.18	3.97	4.43	5.29
5/20/2004		1.25	1.78	1.72	1.99	2.15		0.53	0.51	0.83	1.03
9/15/2004		1.21	2.63	3.91	4.82	5.34		1.42	2.78	3.81	4.47
	Average	1.23	2.94	3.58	4.09	4.55	average	1.71	2.42	3.02	3.60
	std dev	0.02	1.35	1.72	1.84	2.12	std deviation	1.35	1.76	1.92	2.26
							std error	0.78	1.02	1.11	1.30

Channel 4		Raw data, Hemoglobin concentration (mg/ml)						Initial value subtracted, adjusted for dilution and multiplied by 100 to obtain concentration in flow loop (mg/ml)			
date		0 min	15 min	30 min	45 min	60 min		15 min	30 min	45 min	60 min
5/20/2004		1.54	3.14	1.57	2.92	4.14		1.60	0.06	1.50	2.86
5/19/2004		1.25	2.61	2.84	3.03	3.24		1.36	1.65	1.91	2.20
9/9/2004		1.48	2.18	2.46	3.21	3.50		0.70	1.03	1.86	2.24
	Average	1.42	2.64	2.29	3.05	3.63	average	1.22	0.91	1.76	2.43
	std dev	0.15	0.48	0.65	0.14	0.46	std deviation	0.47	0.80	0.22	0.37
							std error	0.27	0.46	0.13	0.21

Channel 5		Raw data, Hemoglobin concentration (mg/ml)						Initial value subtracted, adjusted for dilution and multiplied by 100 to obtain concentration in flow loop (mg/ml)			
date		0 min	15 min	30 min	45 min	60 min		15 min	30 min	45 min	60 min
12/6/2004		1.25	2.73	4.38	3.26	2.10		1.48	3.21	2.14	0.98
12/8/2004		1.08	2.34	3.44	4.49	6.24		1.26	2.43	3.60	5.54
12/13/2004		1.22	3.16	4.98	5.29	7.17		1.94	3.86	4.28	6.40
12/22/2004		1.43	2.05	2.71	3.96	4.32		0.62	1.34	2.69	3.16
1/12/2005		1.00	2.82	3.51	3.81	3.91		1.81	2.58	2.96	3.15
1/14/2005		1.42	2.08	2.07	1.90	2.45		0.67	0.69	0.56	1.18
	Average	1.23	2.53	3.52	3.78	4.36	average	1.30	2.35	2.70	3.40
	std dev	0.17	0.45	1.06	1.15	2.02	std deviation	0.56	1.17	1.29	2.21
							std error	0.20	0.41	0.46	0.78

Channel 6		Raw data, Hemoglobin concentration (mg/ml)						Initial value subtracted, adjusted for dilution and multiplied by 100 to obtain concentration in flow loop (mg/ml)			
date		0 min	15 min	30 min	45 min	60 min		15 min	30 min	45 min	60 min
10/15/2004		2.70	4.61	4.93	7.20	2.60		1.91	2.33	4.79	0.06
10/26/2004		1.59	2.56	2.40	3.56	2.86		0.97	0.86	2.11	1.45
11/17/2004		1.63	3.92	5.51	7.57	9.30		2.29	3.99	6.24	8.25
11/19/2004		1.65	2.86	4.18	4.70	3.45		1.21	2.62	3.24	2.02
11/22/2004		1.14	3.55	4.39	5.86	6.97		2.40	3.33	4.96	6.26
	Average	1.74	3.50	4.28	5.78	5.04	average	1.76	2.63	4.27	3.61
	std dev	0.57	0.82	1.17	1.68	2.96	std deviation	0.64	1.18	1.61	3.48
							std error	0.26	0.48	0.66	1.42

Channel 7		Raw data, Hemoglobin concentration (mg/ml)						Initial value subtracted, adjusted for dilution and multiplied by 100 to obtain concentration in flow loop (mg/ml)			
date		0 min	15 min	30 min	45 min	60 min		15 min	30 min	45 min	60 min
12/8/2004		1.08	1.39	1.53	1.94	1.50		0.31	0.48	0.94	0.52
12/13/2004		1.22	1.03	1.86	1.54	1.54		-0.19	0.68	0.38	0.41
12/22/2004		1.43	2.71	2.01	2.01	4.81		1.28	0.62	0.66	3.68
1/12/2005		1.00	1.11	1.17	1.39	1.82		0.11	0.19	0.44	0.93
1/14/2005		1.42	1.85	1.62	1.50	1.59		0.43	0.23	0.14	0.27
1/24/2005		1.62	1.86	1.98	1.85	2.17		0.24	0.39	0.30	0.68
	Average	1.30	1.66	1.69	1.71	2.24	average	0.36	0.43	0.48	1.08
	std dev	0.24	0.62	0.32	0.26	1.28	std deviation	0.50	0.20	0.29	1.29
							std error	0.20	0.08	0.12	0.53

Channel 8		Raw data, Hemoglobin concentration (mg/ml)						Initial value subtracted, adjusted for dilution and multiplied by 100 to obtain concentration in flow loop (mg/ml)			
date		0 min	15 min	30 min	45 min	60 min		15 min	30 min	45 min	60 min
10/15/2004		2.70	3.64	4.73	5.58	4.95		0.94	2.12	3.11	2.56
11/12/2004		1.84	6.24	4.30	8.36	7.58		4.39	2.55	6.86	6.21
11/5/2004		2.66	2.98	4.00	3.63	4.19		0.32	1.42	1.12	1.79
11/17/2004		1.63	3.51	4.90	5.07	7.14		1.88	3.37	3.65	5.95
11/22/2004		1.14	2.00	2.74	3.46	5.10		0.85	1.65	2.46	4.28
10/26/2004		1.59	2.42	2.68	2.22	2.48		0.83	1.15	0.72	1.05
	Average	1.93	3.46	3.89	4.72	5.24	average	1.54	2.04	2.98	3.64
	std dev	0.62	1.50	0.97	2.15	1.89	std deviation	1.49	0.82	2.21	2.17
							std error	0.61	0.33	0.90	0.89

Valve Hemolysis data:

low leaker		Raw data, Hemoglobin concentration (mg/ml)						Initial value subtracted, adjusted for dilution and multiplied by 100 to obtain concentration in flow loop (mg/ml)			
date		0 min	15 min	30 min	45 min	60 min		15 min	30 min	45 min	60 min
7/29/2004		1.77	2.28	na	na	na		0.60	na	na	na
7/30/2004		3.49	1.61	4.68	4.20	4.46		-1.82	1.41	0.96	1.28
8/18/2004		1.45	3.07	4.07	4.45	4.82		1.62	2.62	3.00	3.37
9/10/2004		2.29	1.83	2.23	2.61	2.86		-0.46	-0.06	0.32	0.57
12/15/2004		1.28	2.16	na	na	na		0.88	na	na	na
1/10/2005		1.19	2.01	3.10	4.50	na		0.82	1.91	3.31	na
7/22/2005		1.87	2.26	2.41	3.38	3.14		0.39	0.55	1.51	1.28
7/12/2005		1.54	2.37	3.21	3.01	2.95		0.83	1.67	1.47	1.41
	Average	1.86	2.20	3.29	3.69	3.65	average	0.36	1.35	1.76	1.58
	std dev	0.75	0.43	0.95	0.80	0.92	std deviation	1.05	0.97	1.17	1.05
							std error	0.35	0.37	0.44	0.43

high leaker		Raw data, Hemoglobin concentration (mg/ml)						Initial value subtracted, adjusted for dilution and multiplied by 100 to obtain concentration in flow loop (mg/ml)			
date		0 min	15 min	30 min	45 min	60 min		15 min	30 min	45 min	60 min
7/28/2004		1.76	3.52	4.26	5.68	5.44		1.75	2.49	3.91	3.68
8/23/2004		0.14	1.62	2.29	2.33	2.74		1.47	2.14	2.19	2.60
8/2/2004		1.70	1.52	3.13	2.07	2.44		-0.18	1.43	0.37	0.74
12/20/2004		1.10	1.97	2.68	3.32	4.20		0.87	1.58	2.22	3.10
1/27/2005		1.52	1.78	2.11	2.44	2.97		0.26	0.59	0.92	1.44
	Average	1.25	2.08	2.89	3.17	3.56	average	0.83	1.65	1.92	2.31
	std dev	0.67	0.82	0.86	1.48	1.25	std deviation	0.81	0.73	1.37	1.21
							std error	0.36	0.33	0.61	0.54

SJM std		Raw data, Hemoglobin concentration (mg/ml)						Initial value subtracted, adjusted for dilution and multiplied by 100 to obtain concentration in flow loop (mg/ml)			
date		0 min	15 min	30 min	45 min	60 min		15 min	30 min	45 min	60 min
11/10/2004		1.72	2.66	2.83	3.00	3.45		0.94	1.11	1.28	1.73
11/15/2004		1.50	1.93	2.31	2.53	3.10		0.43	0.81	1.03	1.60
7/20/2005		1.55	2.06	2.59	2.32	2.50		0.51	1.04	0.77	0.95
	Average	1.59	2.22	2.57	2.62	3.02	average	0.63	0.99	1.03	1.43
	std dev	0.11	0.39	0.26	0.35	0.48	std deviation	0.27	0.16	0.26	0.42
							std error	0.16	0.09	0.15	0.24

MP		Raw data, Hemoglobin concentration (mg/ml)						Initial value subtracted, adjusted for dilution and multiplied by 100 to obtain concentration in flow loop (mg/ml)			
date		0 min	15 min	30 min	45 min	60 min		15 min	30 min	45 min	60 min
9/22/2004		1.26	2.17	2.38	2.80	2.91		0.91	1.12	1.54	1.65
10/14/2004		2.40	3.61	4.51	4.83	4.81		1.21	2.11	2.43	2.41
10/25/2004		1.58	1.55	1.61	1.72	2.53		-0.03	0.03	0.14	0.94
10/27/2004		1.57	1.62	1.66	2.10	1.94		0.04	0.09	0.52	0.37
11/23/2004		1.17	1.53	2.57	2.62	3.98		0.37	1.40	1.45	2.81
12/3/2004		1.47	1.93	2.08	2.20	2.96		0.46	0.61	0.72	1.49
	Average	1.58	2.07	2.47	2.71	3.19	average	0.49	0.89	1.13	1.61
	std dev	0.44	0.80	1.07	1.11	1.04	std deviation	0.49	0.81	0.83	0.90
							std error	0.20	0.33	0.34	0.37

B.4. Baboon *ex vivo* experiments – Raw data

6/17/2003 data:

800 um slit

	without background removed					initial	
Rt 30x30 (proximal)		Lft 30x30 (distal)		Ctr 30x30		35 then 92	187
time	platelets	time	platelets	time	platelets	APTT*	flow (ml/min)
5	1.03	5	1.2	5	1.77		
10	1.12	10	1.3	10	1.93		170
15	1.29	15	1.57	15	2.24	94.4	160
20	1.41	20	1.84	20	2.57		130
25	1.63	25	2.19	25	3		
30	1.83	30	2.51	30	3.4	108.9	100
after flush	1.11	after flush	2.24	after flush	2.59		
			background				
	0.72		0.27		0.81		

	with background removed						
Rt 30x30 (proximal)		Lft 30x30 (distal)		Ctr 30x30			
time	platelets	time	platelets	time	platelets	norm (by initial Platelet #)	norm, e11
5	0.31	5	0.93	5	0.96	0.002330097	0.23301
10	0.4	10	1.03	10	1.12	0.002718447	0.271845
15	0.57	15	1.3	15	1.43	0.003470874	0.347087
20	0.69	20	1.57	20	1.76	0.004271845	0.427184
25	0.91	25	1.92	25	2.19	0.005315534	0.531553
30	1.11	30	2.24	30	2.59	0.006286408	0.628641

*APTT was measured prior to heparin addition and then at 15 minute intervals during the experiment

6/24/2003 data:

800 um slit

without background removed

Rt 30x30 (proximal)		Lft 30x30 (distal)		Ctr 30x30				initial 27 then 166.9	175
time	platelets	time	platelets	time	platelets	norm (by initial Platelet #)	norm, e11	APTT*	flow, ml/min
3	0.93	3	1.51	3	2.01	0.005929204	0.59292		203
6	0.95	6	1.52	6	2.01	0.005929204	0.59292		192
9	0.99	9	1.55	9	2.1	0.00619469	0.619469		186
12	1	12	1.55	12	2.08	0.006135693	0.613569		
15	0.97	15	1.55	15	2.06	0.006076696	0.60767	138.9	
18	0.99	18	1.58	18	2.08	0.006135693	0.613569		
21	1	21	1.63	21	2.14	0.006312684	0.631268		196
24	1	24	1.61	24	2.12	0.006253687	0.625369		
27	1.06	27	1.68	27	2.19	0.006460177	0.646018		
30	1	30	1.7	30	2.19	0.006460177	0.646018	144	
33	0.98	33	1.68	33	2.1	0.00619469	0.619469		
36	0.99	36	1.68	36	2.1	0.00619469	0.619469		
39	1	39	1.76	39	2.19	0.006460177	0.646018		
42	0.95	42	1.85	42	2.17	0.00640118	0.640118		
45	1.02	45	1.9	45	2.26	0.006666667	0.666667	146.4	200
48	1.05	48	1.96	48	2.34	0.006902655	0.690265		
51	1.01	51	2.01	51	2.32	0.006843658	0.684366		
54	1.08	54	2.05	54	2.46	0.007256637	0.725664		
57	1.04	57	2.08	57	2.41	0.007109145	0.710914		
60	1.06	60	2.16	60	2.5	0.007374631	0.737463	150.4	
after flush	0.28	after flush	0.9	after flush	0.9				
background									
	0.78		1.26		1.6				

with background removed

Rt 30x30 (proximal)		Lft 30x30 (distal)		Ctr 30x30				
time	platelets	time	platelets	time	platelets	norm (by initial Platelet #)	norm, e11	divide by flow rate (platelets/l/min)
3	0.15	3	0.25	3	0.41	0.00120944	0.120944	2.05
6	0.17	6	0.26	6	0.41	0.00120944	0.120944	2.05
9	0.21	9	0.29	9	0.5	0.001474926	0.147493	2.5
12	0.22	12	0.29	12	0.48	0.001415929	0.141593	2.4
15	0.19	15	0.29	15	0.46	0.001356932	0.135693	2.3
18	0.21	18	0.32	18	0.48	0.001415929	0.141593	2.4
21	0.22	21	0.37	21	0.54	0.00159292	0.159292	2.7
24	0.22	24	0.35	24	0.52	0.001533923	0.153392	2.6
27	0.28	27	0.42	27	0.59	0.001740413	0.174041	2.95
30	0.22	30	0.44	30	0.59	0.001740413	0.174041	2.95
33	0.2	33	0.42	33	0.5	0.001474926	0.147493	2.5
36	0.21	36	0.42	36	0.5	0.001474926	0.147493	2.5
39	0.22	39	0.5	39	0.59	0.001740413	0.174041	2.95
42	0.17	42	0.59	42	0.57	0.001681416	0.168142	2.85
45	0.24	45	0.64	45	0.66	0.001946903	0.19469	3.3
48	0.27	48	0.7	48	0.74	0.002182891	0.218289	3.7
51	0.23	51	0.75	51	0.72	0.002123894	0.212389	3.6
54	0.3	54	0.79	54	0.86	0.002536873	0.253687	4.3
57	0.26	57	0.82	57	0.81	0.002389381	0.238938	4.05
60	0.28	60	0.9	60	0.9	0.002654867	0.265487	4.5

*APTT was measured prior to heparin addition and then at 15 minute intervals during the experiment

7/30/2003 data:

800 um slit

without background removed

Rt 30x30 (proximal)		Lft 30x30 (distal)		Ctr 30x30	
time	platelets	time	platelets	time	platelets
3	0.50	3	0.69	3	0.96
6	0.52	6	0.71	6	1.00
9	0.54	9	0.70	9	1.00
12	0.50	12	0.72	12	1.00
15	0.53	15	0.69	15	1.03
18	0.52	18	0.70	18	0.99
21	0.57	21	0.68	21	1.02
24	0.52	24	0.70	24	1.01
27	0.54	27	0.72	27	1.03
30	0.53	30	0.70	30	0.99
33	0.53	33	0.75	33	1.03
36	0.57	36	0.73	36	1.07
39	0.57	39	0.73	39	1.05
42	0.60	42	0.77	42	1.10
45	0.63	45	0.72	45	1.10
48	0.67	48	0.77	48	1.18
51	0.63	51	0.77	51	1.15
54	0.69	54	0.83	54	1.22
57	0.73	57	0.84	57	1.24
60	0.74	60	0.88	60	1.30
after flush	0.51	after flush	0.61	after flush	0.91

background

0.23088	0.268423	0.38654

with background removed

initial

35.4 then 78

204

Rt 30x30 (proximal)		Lft 30x30 (distal)		Ctr 30x30					
time	platelets	time	platelets	time	platelets	norm (by initial Platelet #)	norm, e11	APTT*	flow, ml/min
3	0.27333	3	0.41792	3	0.57386	0.001863182	0.186318		
6	0.28705	6	0.4385	6	0.61159	0.001985682	0.198568		
9	0.3042	9	0.43164	9	0.61502	0.001996818	0.199682		
12	0.27333	12	0.45565	12	0.61502	0.001996818	0.199682		
15	0.30077	15	0.42135	15	0.63903	0.002074773	0.207477	88.4	
18	0.29391	18	0.42821	18	0.6013	0.001952273	0.195227		
21	0.33507	21	0.41449	21	0.62874	0.002041364	0.204136		
24	0.29391	24	0.43164	24	0.62188	0.002019091	0.201909		
27	0.3042	27	0.44879	27	0.64246	0.002085909	0.208591		
30	0.30077	30	0.43164	30	0.6013	0.001952273	0.195227	84.9	
33	0.29734	33	0.47966	33	0.64589	0.002097045	0.209705		
36	0.3385	36	0.46251	36	0.68019	0.002208409	0.220841		
39	0.33507	39	0.46594	39	0.65961	0.002141591	0.214159		
42	0.36937	42	0.49681	42	0.71106	0.002308636	0.230864		
45	0.39681	45	0.45222	45	0.71792	0.002330909	0.233091	89.4	
48	0.43797	48	0.50367	48	0.78995	0.002564773	0.256477		
51	0.40024	51	0.50024	51	0.75908	0.002464545	0.246455		
54	0.46198	54	0.55855	54	0.83454	0.002709545	0.270955		
57	0.49628	57	0.56884	57	0.85169	0.002765227	0.276523		
60	0.51	60	0.61	60	0.91	0.002954545	0.295455	93.9	

*APTT was measured prior to heparin addition and then at 15 minute intervals during the experiment

2/5/2004 data:

Baboon	23871	**Computer**		NQ		**Plt Cnt Pre**	243		**Whole Blood**	244296			
Date	2/5/2004	**Data Partition**				**Plt Cnt Post**	242		**Plasma**	40120			
		Camera		G E		**WBC**	3.9		**Fraction**	88.5%			
Study Description		**ROI (device)**				**Hct Pre**	29.80%		**Free**	11.5%			
Anna's 800µ slit		**Window**		10%		**Hct Post**	29.50%		**Volume (cc)**	3			
60u/kg bolus heparin + 50u/kg/hr infusion		**Energy**	>	**172**		**Flow (ml/min)**	160 open						
			>	247					**Blood Std CPM**	3126			
		Collimator	>	**low**					**Bkg CPM**	982			
				med					**Bkgd CPM 1**	2144			
Iodine		**Matrix**		word					**CPM In-plts**	1896.8239			
Remarks		256	>	**byte**					**CPM/ml In-plts**	632.27464			
									FINAL	0.0003843			

Time	**ROI** 6.6 x 78.6	**ROI**	**CPM**			norm (by initial Platelet #)		**Time**	**ROI**	**ROI**	**CPM**		
Min	**CPM**	**CPM bkg**	**Thrombus**	**Standard**	**Plts x10^9**		norm, e11	**Min**	**CPM**	**CPM bkg**	**Thrombus**	**Standard**	**Plts x10^9**
3	952	952	0.00	0.000384	**0.00**	0	0	APTT		sec	results (ng/mL)		
6	1018	952	66.00	0.000384	**0.03**	0.000104727	0.010473	Pre		30	3.80		
9	1056	952	104.00	0.000384	**0.04**	0.000165025	0.016502	8min		179.8			
12	1076	952	124.00	0.000384	**0.05**	0.00019676	0.019676	15min		172.9			
15	1001	952	49.00	0.000384	**0.02**	7.77521E-05	0.007775	0time	start of shunt				
18	1053	952	101.00	0.000384	**0.04**	0.000160264	0.016026	15		198	3.9		
21	1109	952	157.00	0.000384	**0.06**	0.000249124	0.024912	30		222	3.80		
24	987	952	35.00	0.000384	**0.01**	5.55372E-05	0.005554	45		238	4.40		
27	1002	952	50.00	0.000384	**0.02**	7.93388E-05	0.007934	60		230	5.00		
30	993	952	41.00	0.000384	**0.02**	6.50579E-05	0.006506						
33	1095	952	143.00	0.000384	**0.05**	0.000226909	0.022691						
36	1021	952	69.00	0.000384	**0.03**	0.000109488	0.010949						
39	1092	952	140.00	0.000384	**0.05**	0.000222149	0.022215						
42	1070	952	118.00	0.000384	**0.05**	0.00018724	0.018724						
45	1137	952	185.00	0.000384	**0.07**	0.000293554	0.029355						
48	1130	952	178.00	0.000384	**0.07**	0.000282446	0.028245						
			0.00		**0.00**						0.00		**0.00**
			0.00		**0.00**						0.00		**0.00**
95			0.00		**0.00**						0.00		**0.00**
100			0.00		**0.00**						0.00		**0.00**
105			0.00		**0.00**						0.00		**0.00**
110			0.00		**0.00**						0.00		**0.00**
115			0.00		**0.00**						0.00		**0.00**
120			0.00		**0.00**						0.00		**0.00**
125			0.00		**0.00**						0.00		**0.00**
130			0.00		**0.00**						0.00		**0.00**
135			0.00		**0.00**						0.00		**0.00**
140			0.00		**0.00**						0.00		**0.00**
145			0.00		**0.00**						0.00		**0.00**
150			0.00		**0.00**						0.00		**0.00**

5/19/2004 data:

Baboon	24080	**Computer**		NQ	**Plt Cnt Pre**	426	**Whole Blood**	818798
Date	5/19/2004	**Data Partition**			**Plt Cnt Post**	407	**Plasma**	48003
		Camera		G E	**WBC**	10.6	**Fraction**	96.1%
Study Description		**ROI (device)**			**Hct Pre**	33.00%	**Free**	3.9%
Anna's 800µ slit		**Window**		10%	**Hct Post**	32.90%	**Volume (cc)**	3
		Energy	>	**172**	**Flow (ml/min)**	260open		
50u/kg bolus heparin + 40u/kg/hr infusion			>	247			**Blood Std CPM**	3625
		Collimator	>	**low**			**Bkg CPM**	292
				med			**Bkgd CPM 1**	3333
Iodine-no		**Matrix**		word			**CPM In-plts**	3202.0813
Remarks			256	> **byte**			**CPM/ml In-plts**	1067.3604
							FINAL	0.0003991

Time	**ROI** 6.6 x 78.6	**ROI**	**CPM**			**Time**	**ROI**	**ROI**	**CPM**			
Min	**CPM**	**CPM bkg**	**Thrombus**	**Standard**	**Plts x10^9**	**Min**	**CPM**	**CPM bkg**	**Thrombus**	**Standard**	**Plts x10^9**
3		952	-952.00	0.000384	**-0.37**	5	1696	893	803.00	0.000399	**0.32**
6		952	-952.00	0.000384	**-0.37**	10	1891	893	998.00	0.000399	**0.40**
9		952	-952.00	0.000384	**-0.37**	15	2311	893	1418.00	0.000399	**0.57**
12		952	-952.00	0.000384	**-0.37**	20	2783	893	1890.00	0.000399	**0.75**
15		952	-952.00	0.000384	**-0.37**	25	3411	893	2518.00	0.000399	**1.00**
18		952	-952.00	0.000384	**-0.37**	30	3786	893	2893.00	0.000399	**1.15**
21		952	-952.00	0.000384	**-0.37**	35	4441	893	3548.00	0.000399	**1.42**
24		952	-952.00	0.000384	**-0.37**	40	4978	893	4085.00	0.000399	**1.63**
27		952	-952.00	0.000384	**-0.37**	45	5602	893	4709.00	0.000399	**1.88**
30		952	-952.00	0.000384	**-0.37**	50	6116	893	5223.00	0.000399	**2.08**
33		952	-952.00	0.000384	**-0.37**	55	6748	893	5855.00	0.000399	**2.34**
36		952	-952.00	0.000384	**-0.37**	60	7405	893	6512.00	0.000399	**2.60**
39		952	-952.00	0.000384	**-0.37**						
42		952	-952.00	0.000384	**-0.37**	Rinsed Static Image					
45		952	-952.00	0.000384	**-0.37**		6512	58	6454.00	0.000399	**2.58**
48		952	-952.00	0.000384	**-0.37**						
			0.00		**0.00**				0.00		**0.00**
			0.00		**0.00**				0.00		**0.00**
95			0.00		**0.00**				0.00		**0.00**
100			0.00		**0.00**				0.00		**0.00**
105			0.00		**0.00**				0.00		**0.00**
110			0.00		**0.00**				0.00		**0.00**
115			0.00		**0.00**				0.00		**0.00**
120			0.00		**0.00**				0.00		**0.00**
125			0.00		**0.00**				0.00		**0.00**
130			0.00		**0.00**				0.00		**0.00**
135			0.00		**0.00**				0.00		**0.00**
140			0.00		**0.00**				0.00		**0.00**
145			0.00		**0.00**				0.00		**0.00**
150			0.00		**0.00**				0.00		**0.00**

7/14/2005 data:

Baboon	24568	**Computer**		NQ	
Date	7/14/2005	**Data Partition**		620	
		Camera		G E	
Study Description		**ROI (device)**			
Anna's 800µ slit		**Window**		10%	
50u/kg heparin + 40u/kg/hr infusion		**Energy**	**>**	**172**	
Heparin started 20min pre shunt			>	247	
		Collimator	**>**	**low**	
				med	
Iodine No		**Matrix**		word	
Remarks		256	**>**	**byte**	

Plt Cnt Pre	364
Plt Cnt Post	380
WBC	7.1
Hct Pre	31.50%
Hct Post	33.90%
Flow (ml/min)	200 open

Whole Blood	342949
Plasma	49231
Fraction	90.2%
Free	9.8%
Volume (cc)	3

Blood Std CPM	1109
Bkg CPM	179
Bkgd CPM 1	930
CPM In-plts	838.55023
CPM/ml In-plts	279.51674
FINAL	0.0013022

3.5cm region 6cm high

Time			CPM			
Min	**CPM**	**CPM bkg**	**Thrombus**	**Standard**	**Plts x10^9**	Plt norm
3	1432	1432	0.00	0.001302	**0.00**	0
6	1446	1433	13.00	0.001302	**0.02**	0.0044542
9	1455	1434	21.00	0.001302	**0.03**	0.0071953
12	1493	1435	58.00	0.001302	**0.08**	0.0198726
15	1571	1436	135.00	0.001302	**0.18**	0.0462553
18	1695	1437	258.00	0.001302	**0.34**	0.0883989
21	1709	1438	271.00	0.001302	**0.35**	0.0928532
24	1749	1439	310.00	0.001302	**0.40**	0.1062158
27	1897	1440	457.00	0.001302	**0.60**	0.1565826
30	2069	1441	628.00	0.001302	**0.82**	0.2151726
33	2099	1442	657.00	0.001302	**0.86**	0.2251089
36	2354	1443	911.00	0.001302	**1.19**	0.3121374
39	2432	1444	988.00	0.001302	**1.29**	0.33852
42	2587	1445	1142.00	0.001302	**1.49**	0.3912853
45	2632	1446	1186.00	0.001302	**1.54**	0.4063611
48	2902	1447	1455.00	0.001302	**1.89**	0.4985289
51	3089	1448	1641.00	0.001302	**2.14**	0.5622584
54	3238	1449	1789.00	0.001302	**2.33**	0.6129679
57	3460	1450	2010.00	0.001302	**2.62**	0.6886895
60	3529	1451	2078.00	0.001302	**2.71**	0.7119884

	ROI	**ROI**			
Time			**CPM**		
Min	**CPM**	**CPM bkg**	**Thrombus**	**Standard**	**Plts x10^9**
post study device	2693	1432	1261.00	0.001302	**1.64**
intact but rinsed					
Disc flat on camera	3478	76	3402.00	0.001302	**4.43**
Disc flat prox side			0.00		
scraped clean	3064	76	2988.00	0.001302	**3.89**
			0.00	0.0001	**0.00**
			0.00	0.0001	**0.00**
			0.00	0.0001	**0.00**
			0.00	0.0001	**0.00**
			0.00	0.0001	**0.00**
			0.00	0.0001	**0.00**
			0.00	0.0001	**0.00**

B.5. Histology images

Hematoxylin & Eosin stain

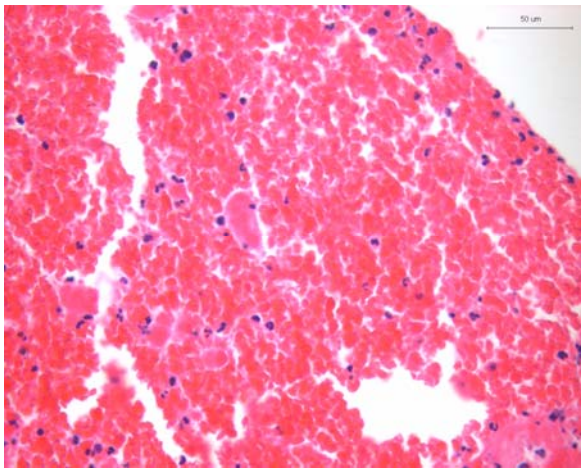

FIGURE B.5.1. Low leaker prototype valve, region 2 of thrombus originating in the hinge region. 40X magnification.

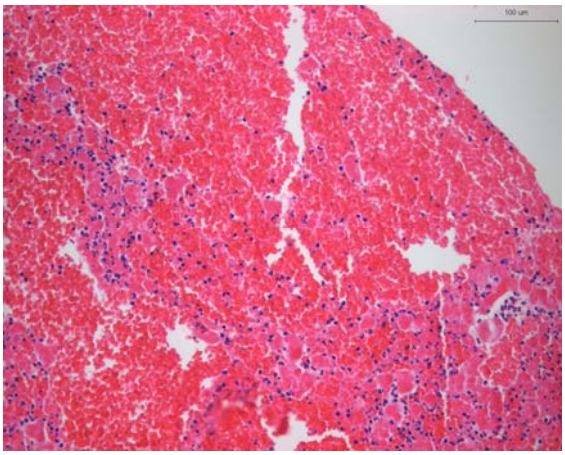

FIGURE B.5.2. Low leaker prototype valve, region 2 of thrombus originating in the hinge region. 20X magnification.

Carstairs stain

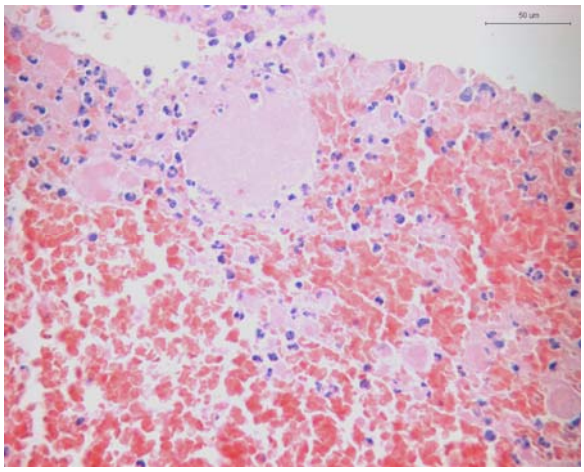

FIGURE B.5.3. Low leaker prototype valve, region 2 of thrombus originating in the hinge region. 40X magnification.

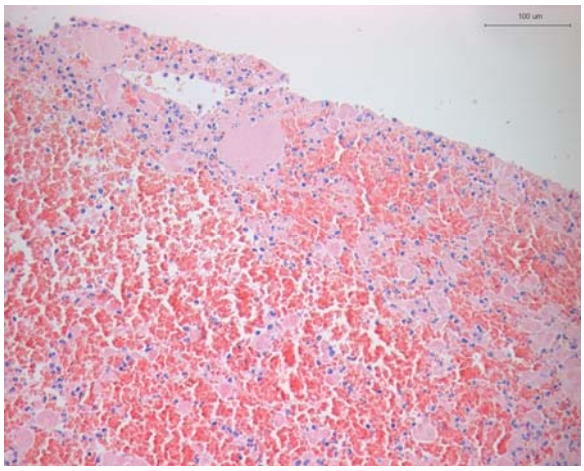

FIGURE B.5.4. Low leaker prototype valve, region 2 of thrombus originating in the hinge region. 20X magnification.

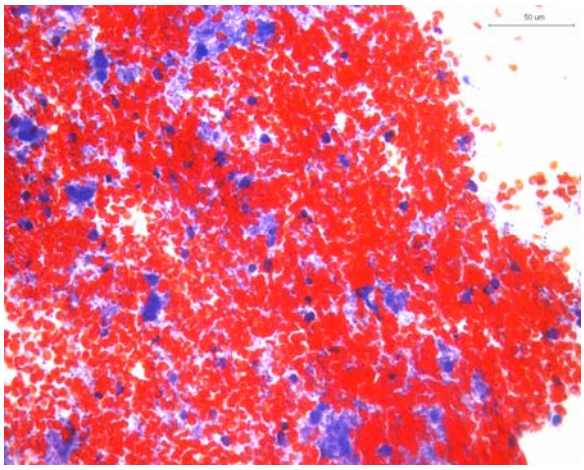

FIGURE B.5.5. 200 µm round orifice. 40X magnification.

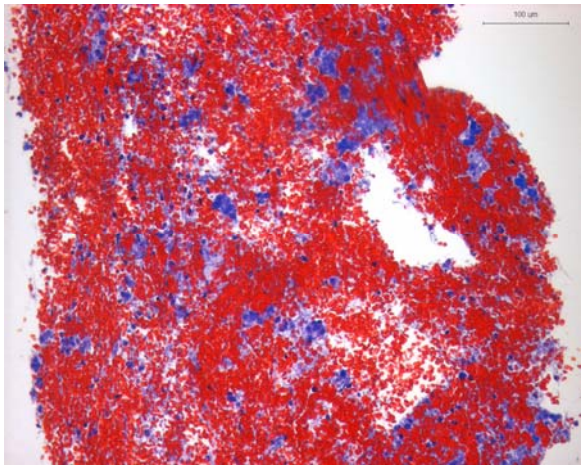

FIGURE B.5.6. 200 µm round orifice. 20X magnification.

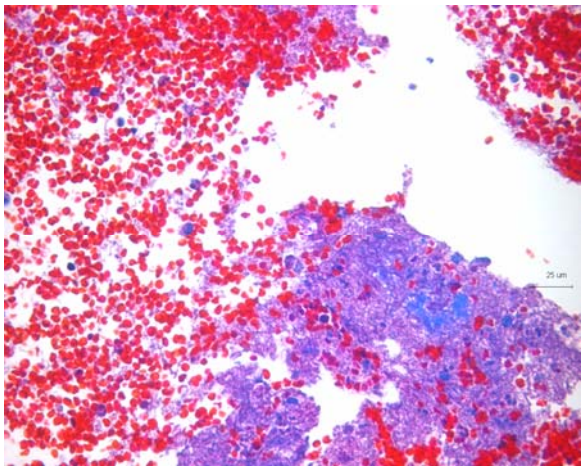

FIGURE B.5.7. Channel 1 thrombus. 40X.

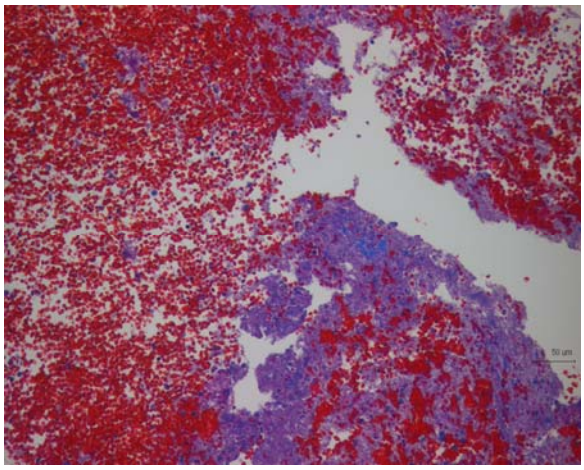

FIGURE B.5.8. Channel 1 thrombus. 20X .

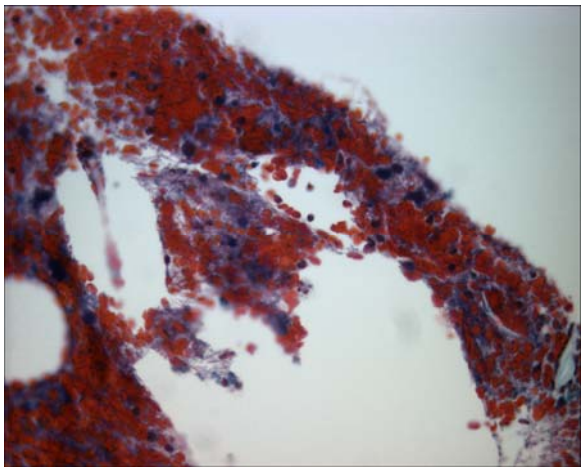

FIGURE B.5.9. Channel 3 upstream thrombus. 40X.

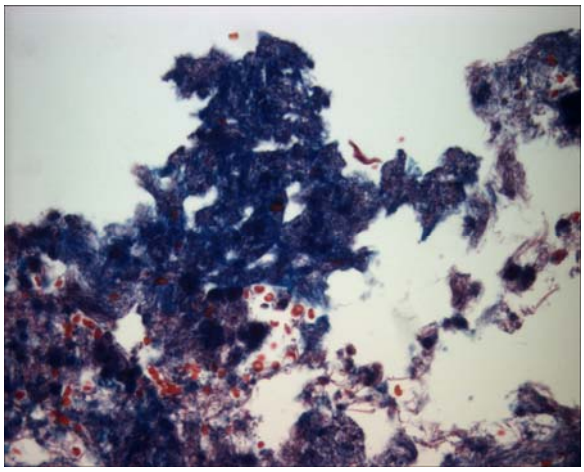

FIGURE B.5.10. Channel 3 downstream thrombus. 40X.

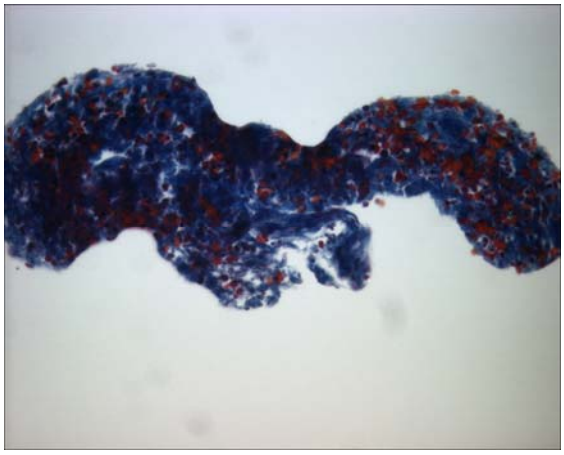

FIGURE B.5.11. Low leaker thrombus, region 3A. 40X.

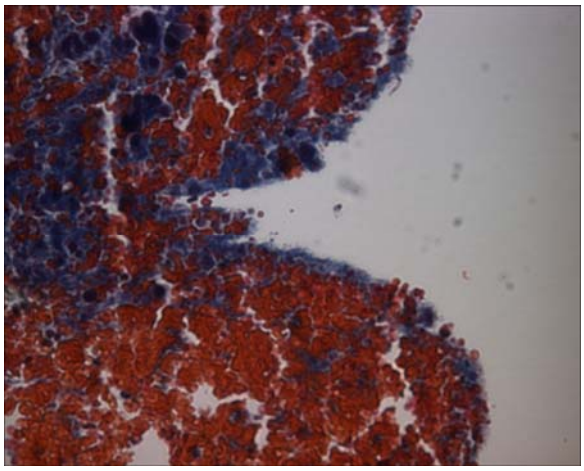

FIGURE B.5.12. Low leaker thrombus, region 3B. 40X

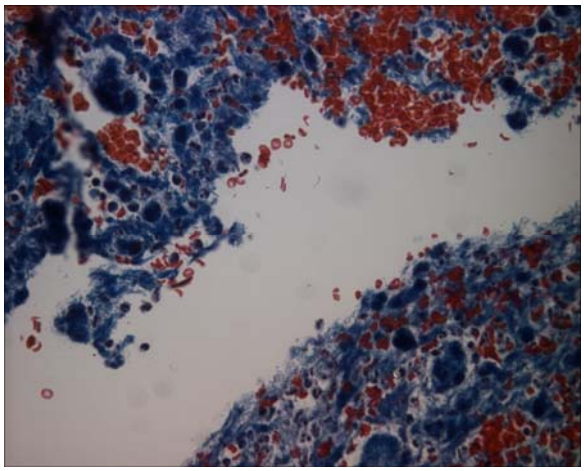

FIGURE B.5.13. Low leaker thrombus, region 1. 40X.

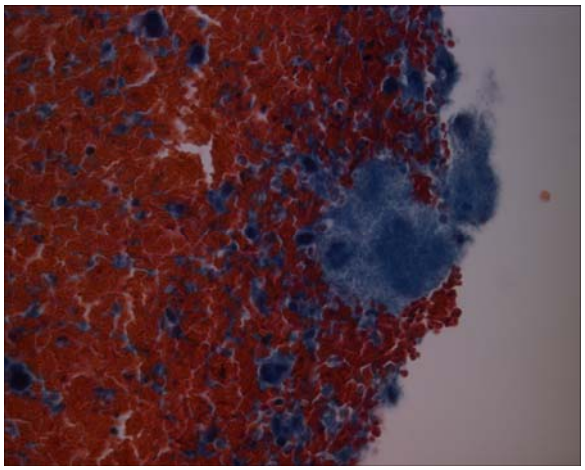

FIGURE B.5.14. Low leaker thrombus, region 2. 40X.

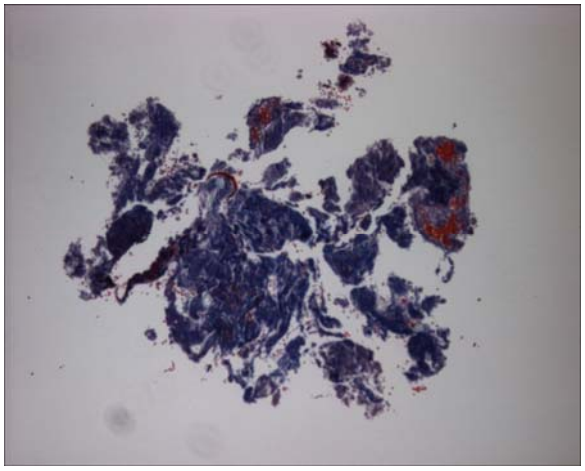

FIGURE B.5.15. Low leaker thrombus, region 4. 10X

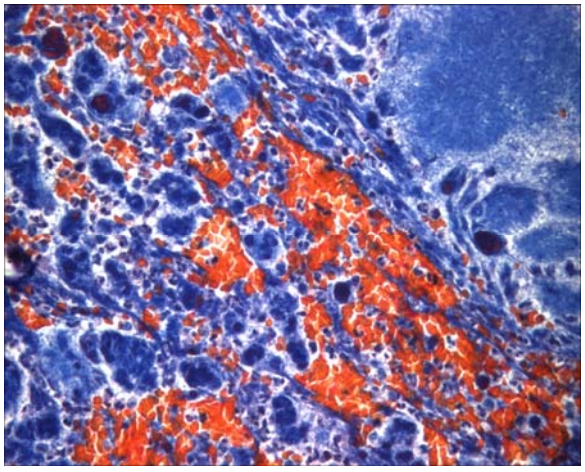

FIGURE B.5.16. Low leaker thrombus, region 1. 40X

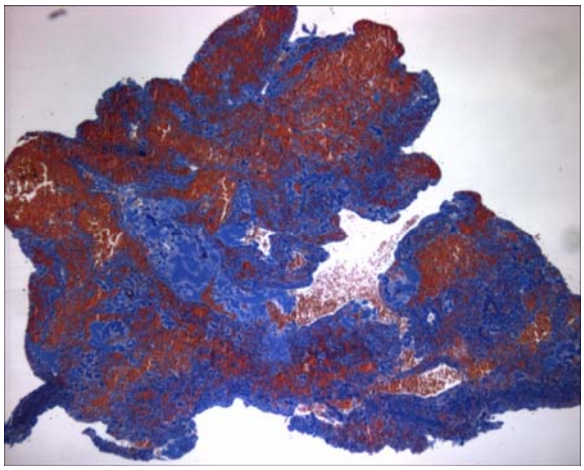

FIGURE B.5.17. Low leaker thrombus, region 1. 4X

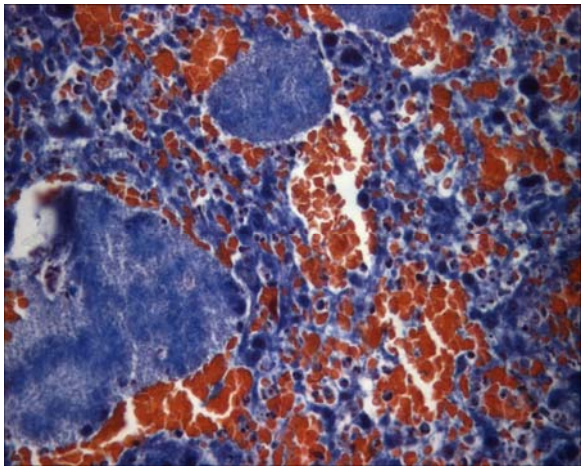

FIGURE B.5.18. Low leaker thrombus, region 1. 40X

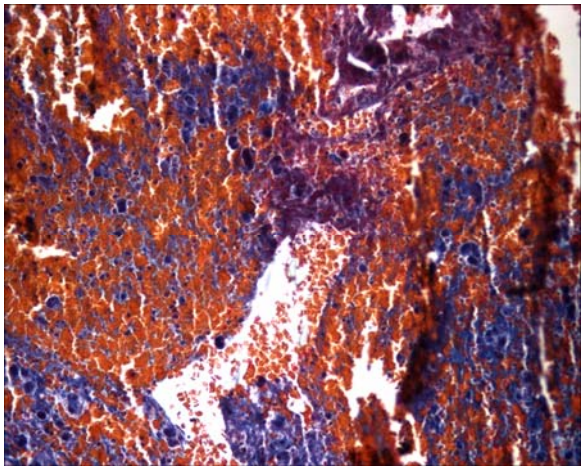

FIGURE B.5.20. Low leaker thrombus, region 1. 20X

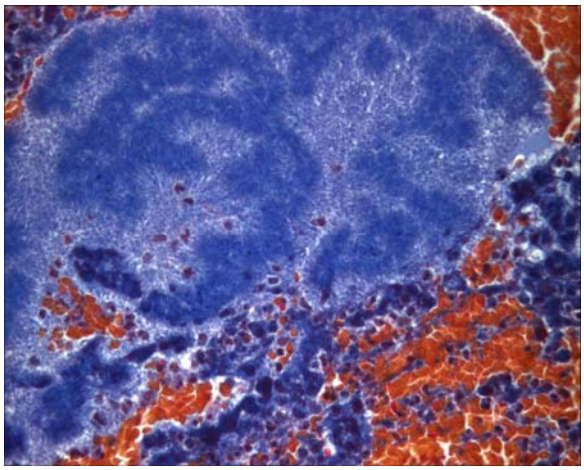

FIGURE B.5.21. Low leaker thrombus, region 2-left. 40X

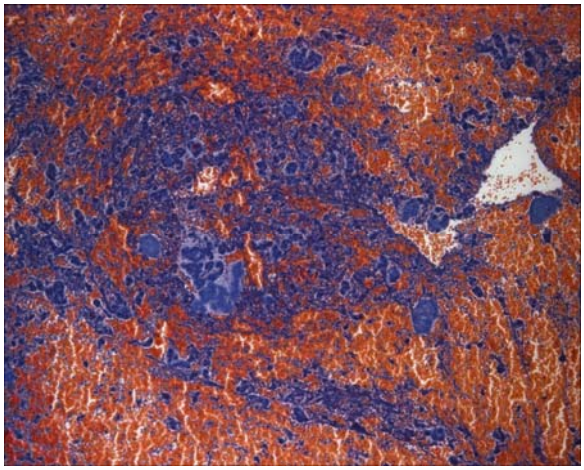

FIGURE B.5.22. Low leaker thrombus, region 2. 10X

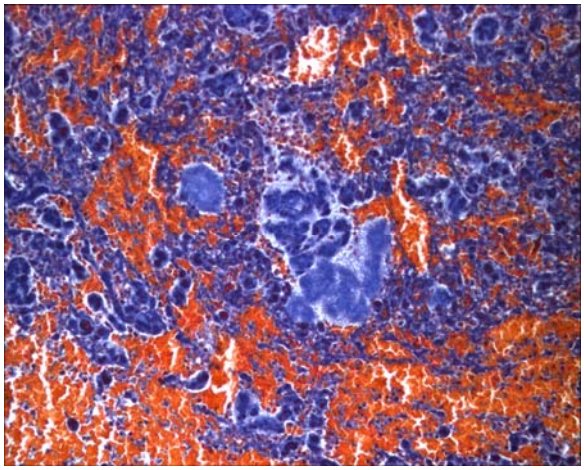

FIGURE B.5.23. Low leaker thrombus, region 2-right. 40X

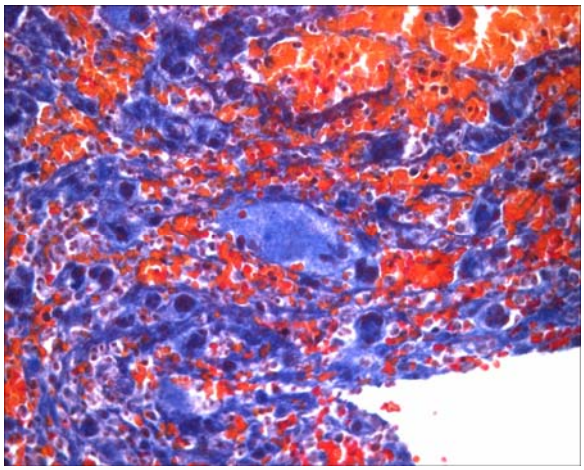

FIGURE B.5.24. Low leaker thrombus, region 2-bottom right. 40X

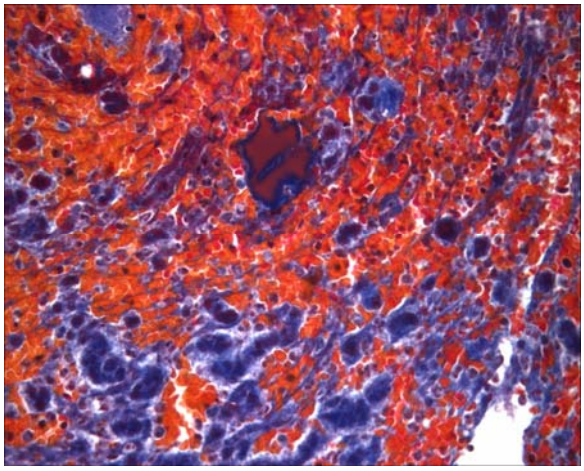

FIGURE B.5.25. Low leaker thrombus, region 2-bottom left. 40X.

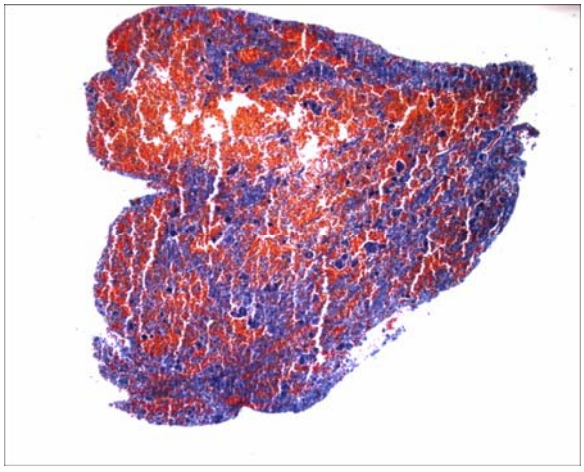

FIGURE B.5.26. Low leaker thrombus, region 3. 10X

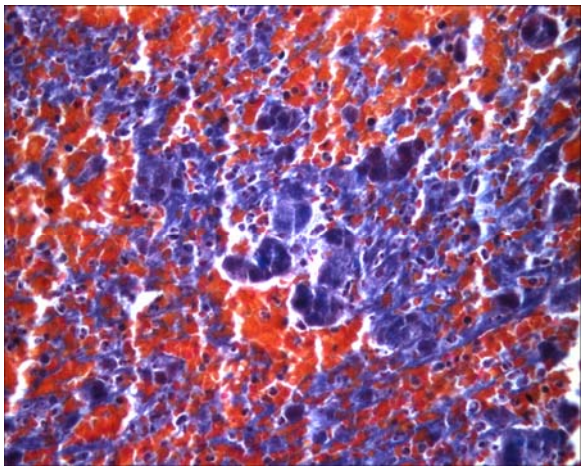

FIGURE B.5.27. Low leaker thrombus, region 3. 40X.

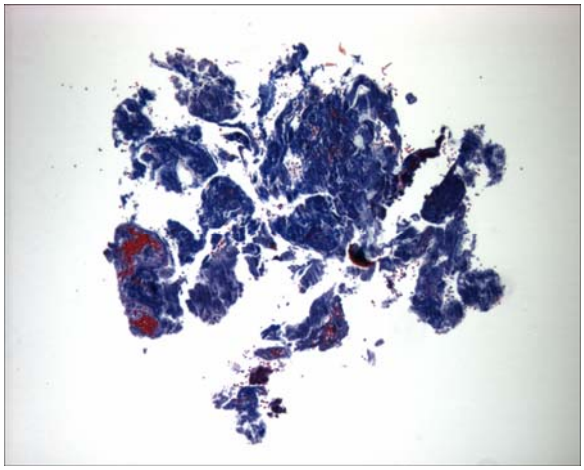

FIGURE B.5.28. Low leaker thrombus, region 4. 10X

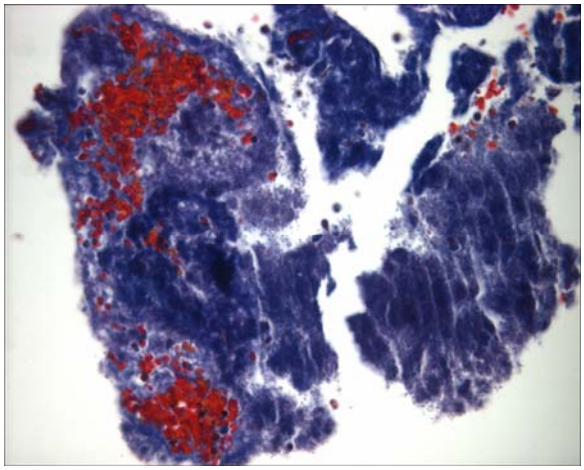

FIGURE B.5.29. Low leaker thrombus, region 4-left. 40X.

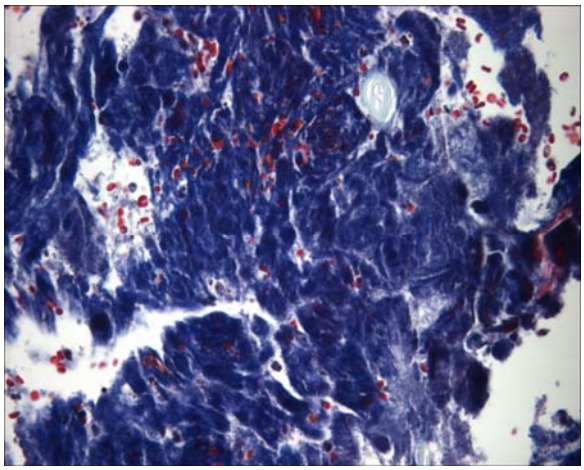

FIGURE B.5.30. Low leaker thrombus, region 4-right. 40X.

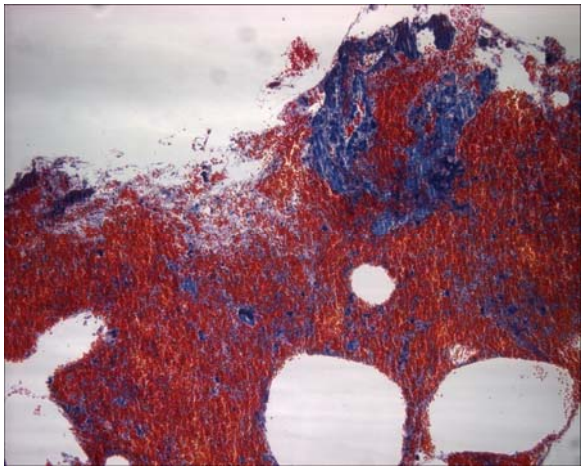

FIGURE B.5.31. Channel 3 thrombus-upstream. 10X

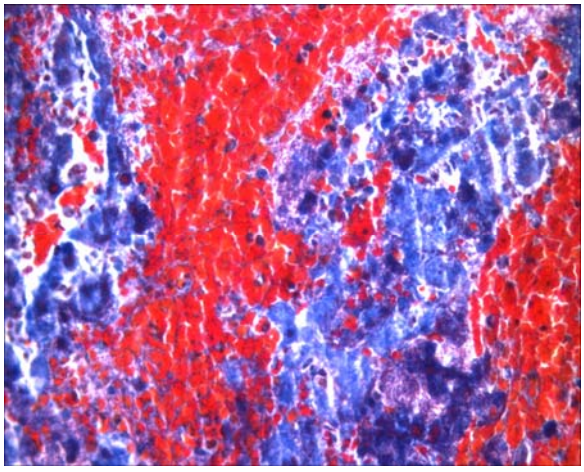

FIGURE B.5.32. Channel 3 thrombus-upstream. 40X

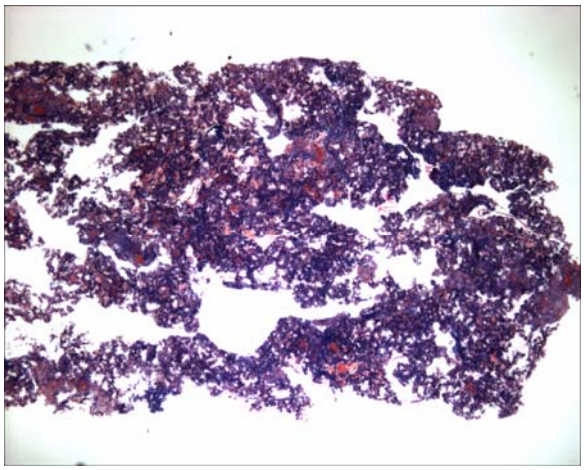

FIGURE B.5.33. Channel 3 thrombus-downstream. 4X

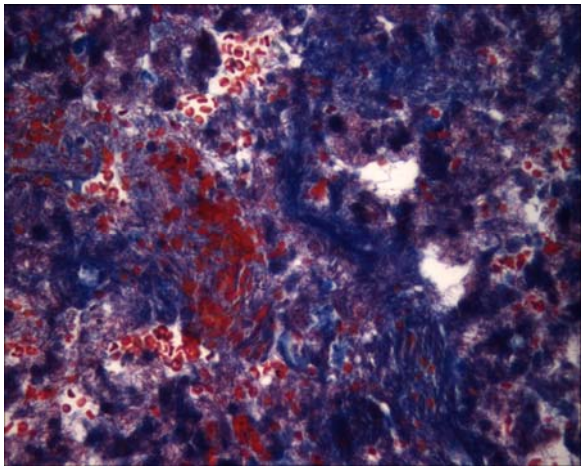

FIGURE B.5.34. Channel 3 thrombus-downstream, top. 40X.

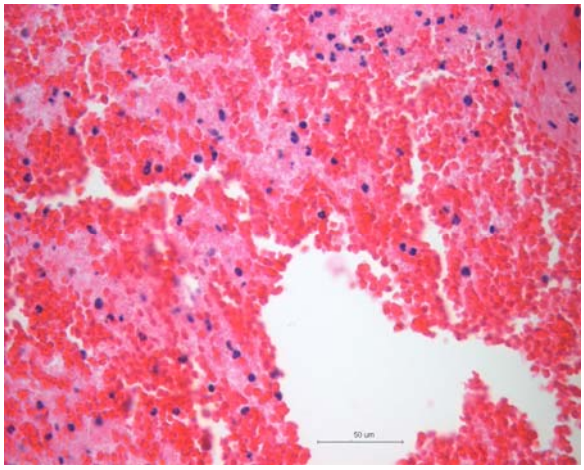

FIGURE B.5.35. Channel 1 thrombus. 40X magnification.

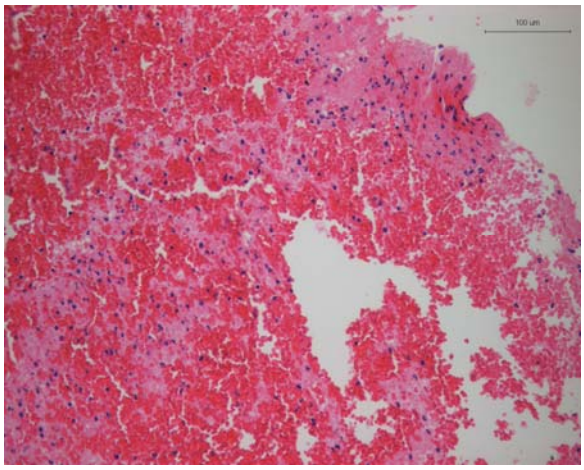

FIGURE B.5.36. Channel 1 thrombus. 20X magnification.

Fluorescent vWF immunostain

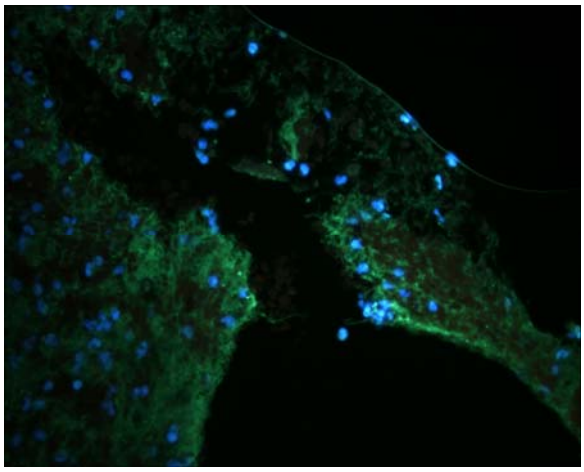

FIGURE B.5.37. Channel 3 upstream thrombus. 40X.

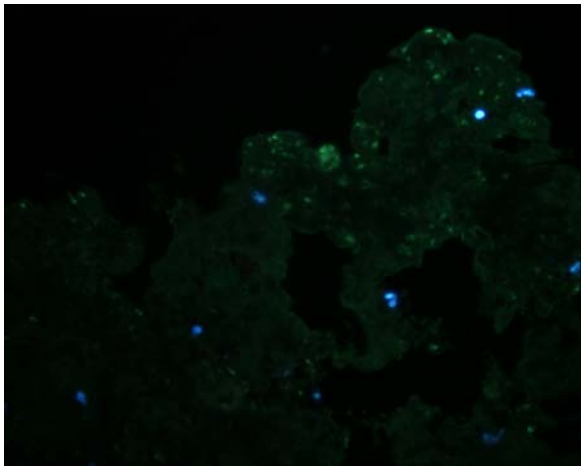

FIGURE B.5.38. Channel 3 downstream thrombus. 40X.

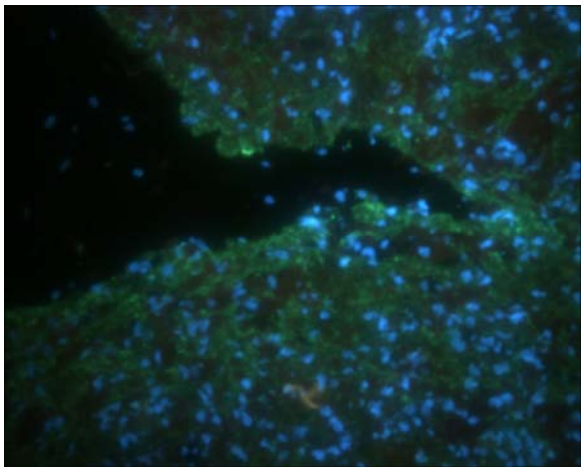

FIGURE B.5.39. Low leaker thrombus, region 3A. 40X.

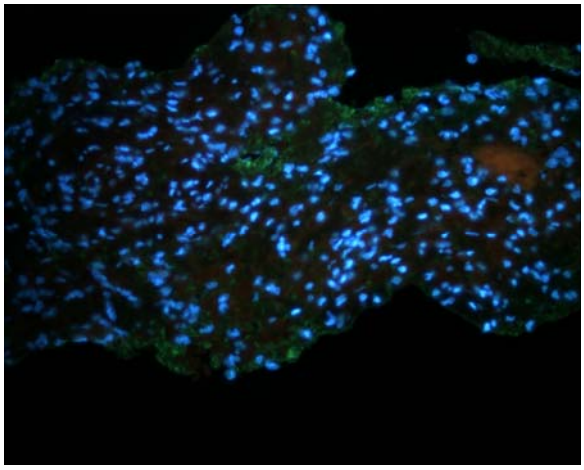

FIGURE B.5.40. Low leaker thrombus, region 3B. 40X

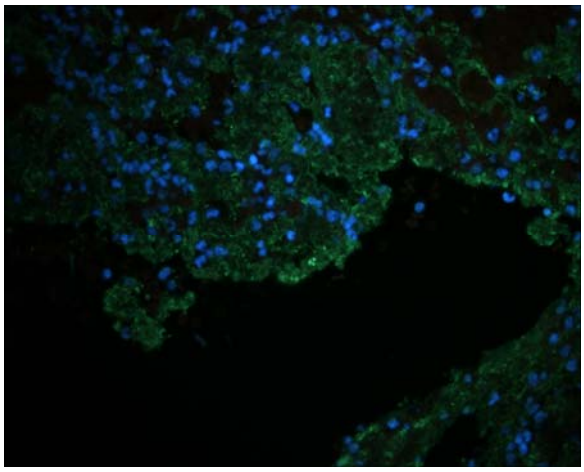

FIGURE B.5.41. Low leaker thrombus, region 1. 40X.

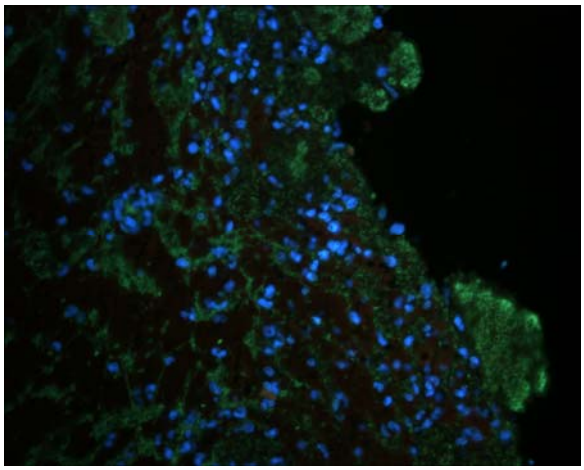

FIGURE B.5.42. Low leaker thrombus, region 2. 40X.

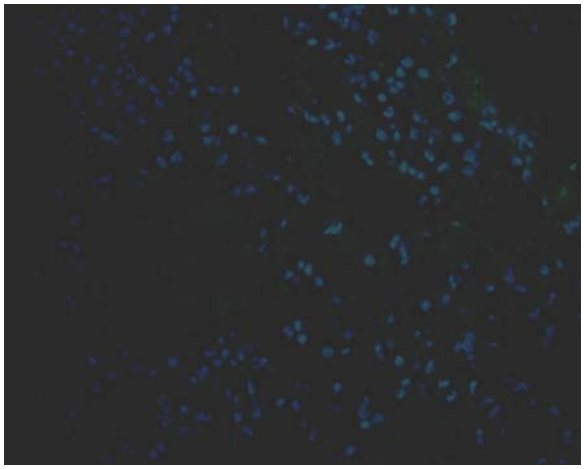

FIGURE B.5.43. Low leaker thrombus, region 1. 40X

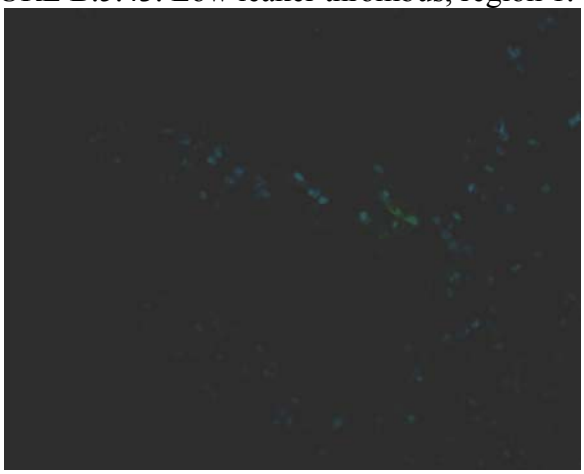

FIGURE B.5.44. Low leaker thrombus, region 1. 40X

FIGURE B.5.45. Low leaker thrombus, region 2. 40X

FIGURE B.5.46. Low leaker thrombus, region 2. 20X.

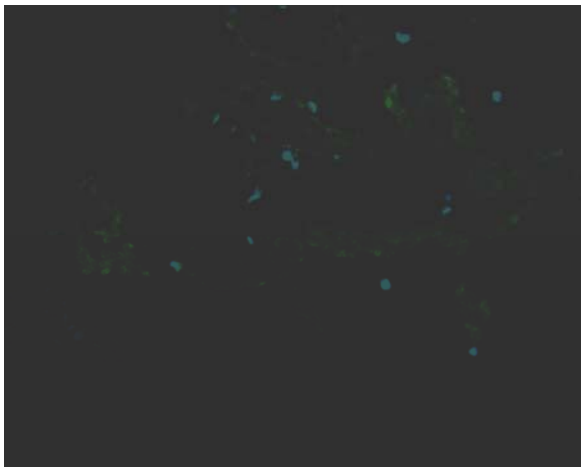

FIGURE B.5.47. Low leaker thrombus, region 4. 40X.

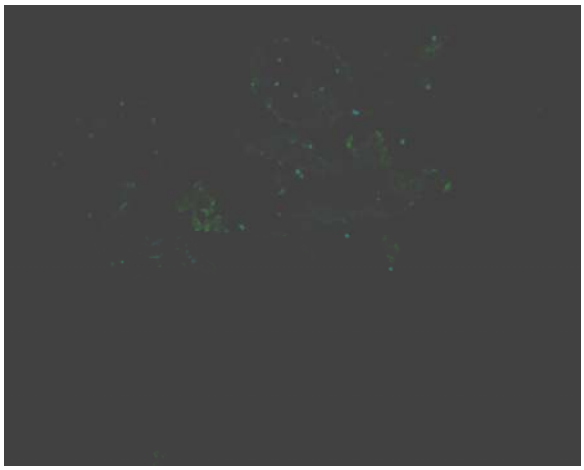

FIGURE B.5.48. Low leaker thrombus, region 4. 20X.

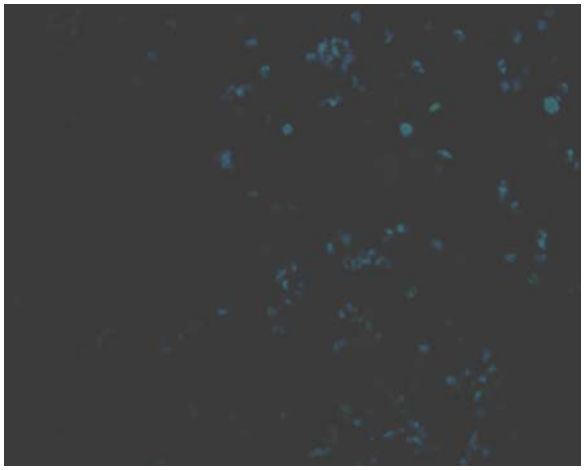

FIGURE B.5.49. Channel 3 thrombus-upstream. 40X

FIGURE B.5.50. Channel 3 thrombus-downstream. 40X.

Colorimetric vWF immunostain

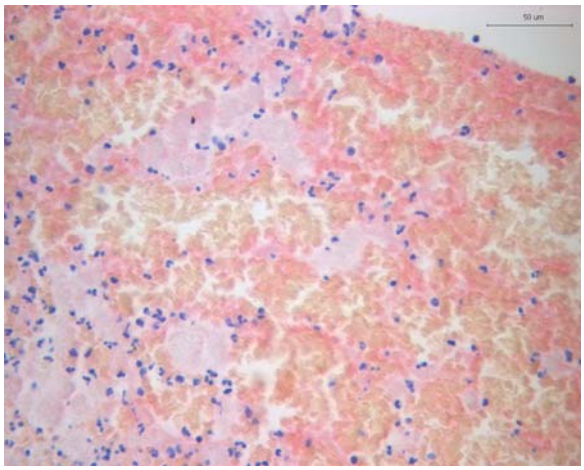

FIGURE B.5.51. Low leaker prototype valve, region 2 of thrombus originating in the hinge region. 40X magnification.

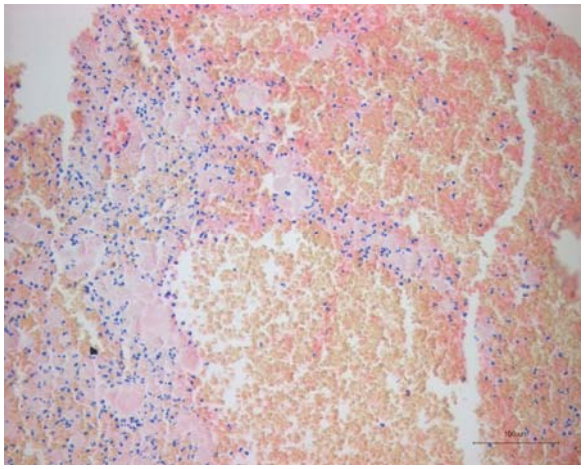

FIGURE B.5.52. Low leaker prototype valve, region 2 of thrombus originating in the hinge region. 20X magnification.

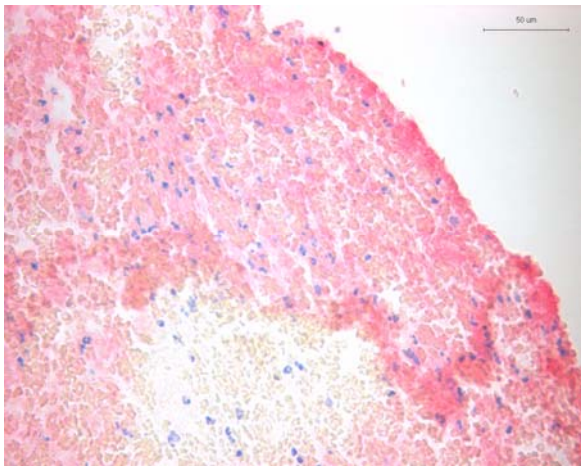

FIGURE B.5.53. 200 μm round orifice. 40X magnification.

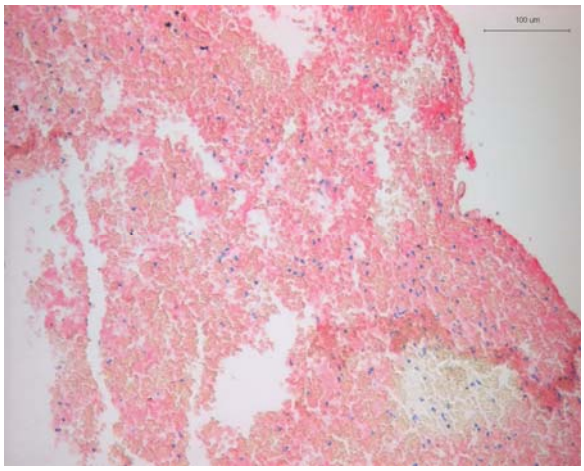

FIGURE B.5.54. 200 μm round orifice. 20X magnification.

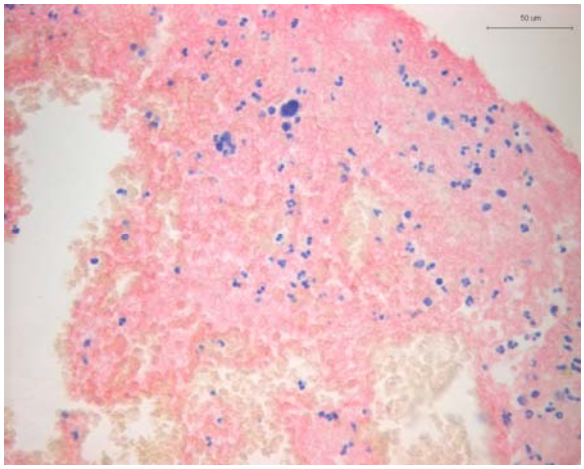

FIGURE B.5.55. Channel 1 thrombus. 40X.

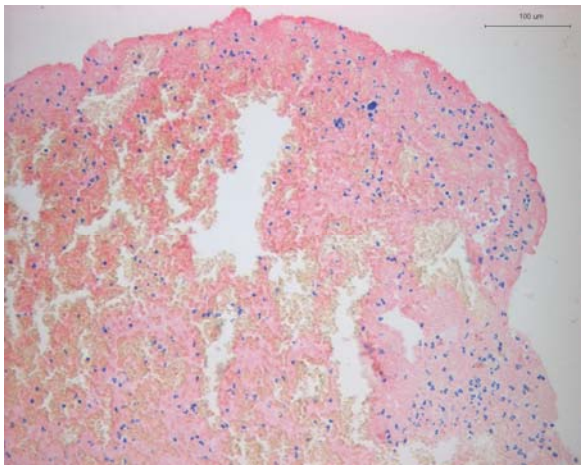

FIGURE B.5.56. Channel 1 thrombus. 20X.

APPENDIX C

DPIV EXPERIMENTAL DATA

C.1. Velocity Vector Plots

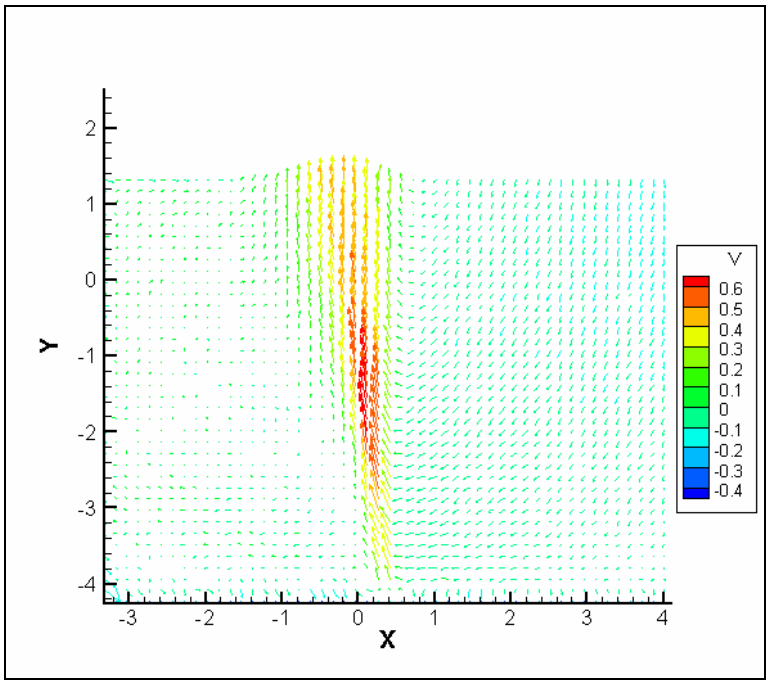

FIGURE C.1.1. Average velocity vector field downstream of the 400 μm round orifice. The pulse separation was 10 μs. Velocity in m/s is color coded according to the legend.

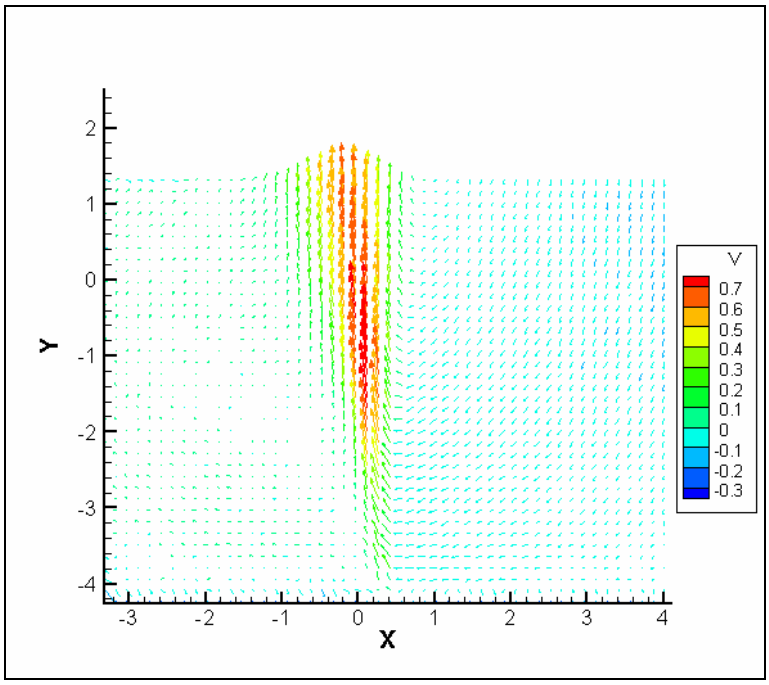

FIGURE C.1.2. Average velocity vector field downstream of the 400 µm round orifice. The pulse separation was 15 µs. Velocity in m/s is color coded according to the legend.

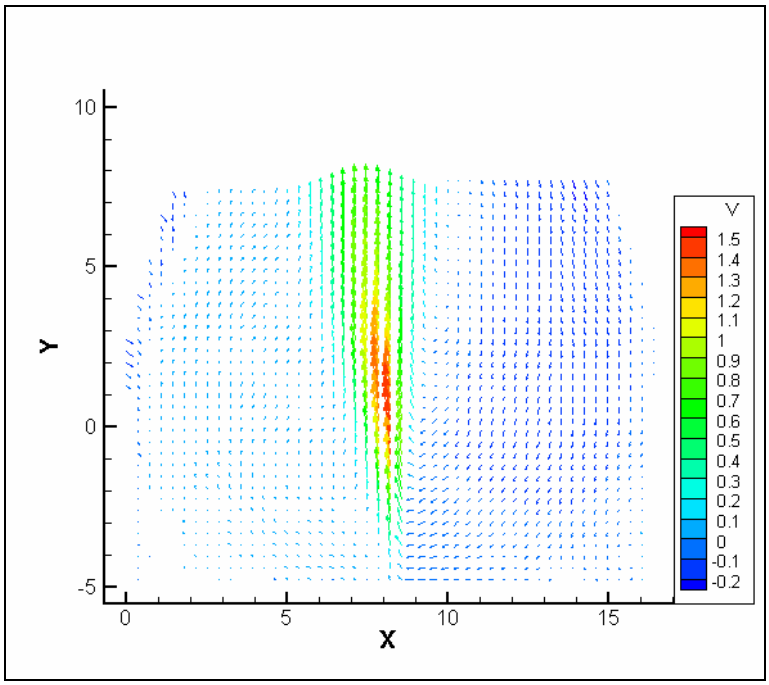

FIGURE C.1.3. Average velocity vector field downstream of the 400 µm round orifice. The pulse separation was 15 µs. Velocity in m/s is color coded according to the legend.

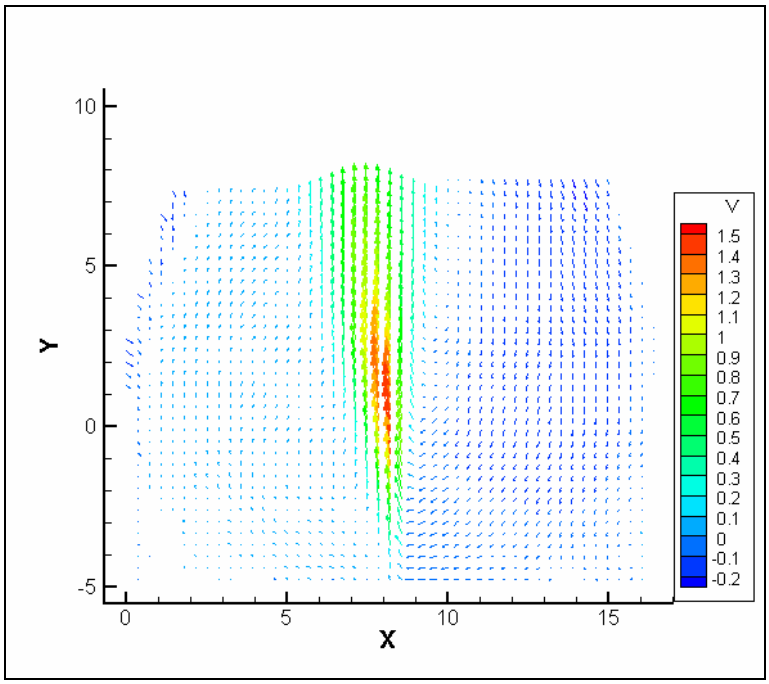

FIGURE C.1.4. Average velocity vector field downstream of the 400 µm round orifice. The pulse separation was 15 µs. Velocity in m/s is color coded according to the legend.

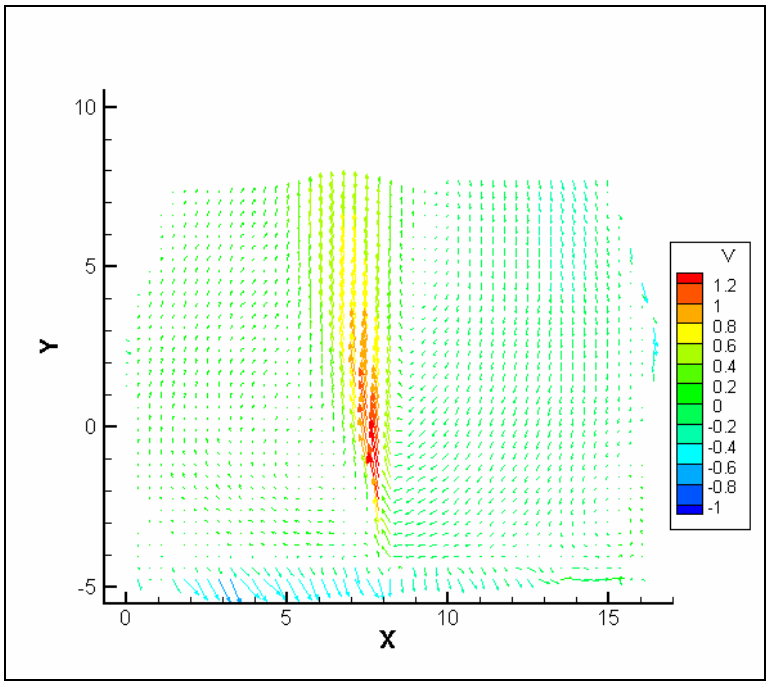

FIGURE C.1.5. Average velocity vector field downstream of the 400 µm round orifice. The pulse separation was 15 µs. Velocity in m/s is color coded according to the legend.

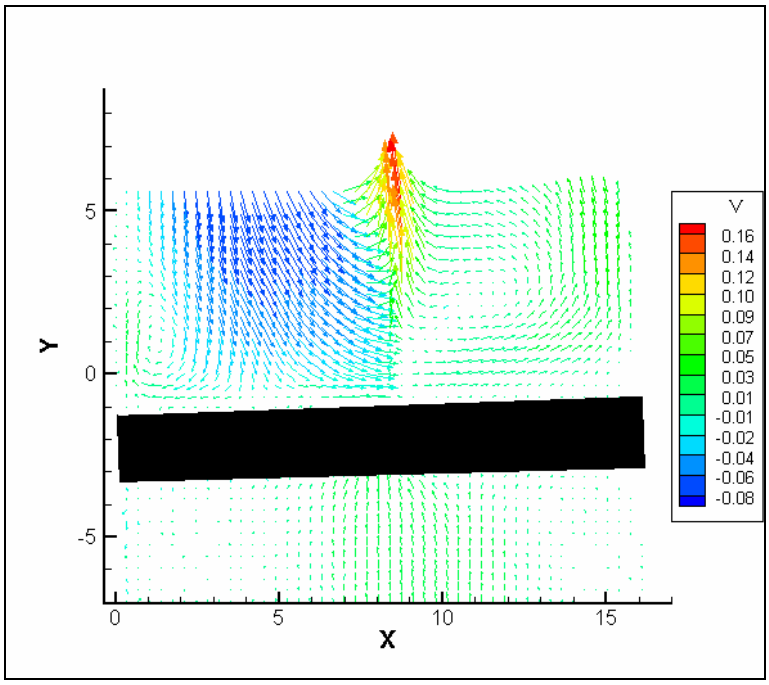

FIGURE C.1.6. Average velocity vector field upstream and downstream of the 400 µm round orifice. The pulse separation was 250 µs. Velocity in m/s is color coded according to the legend.

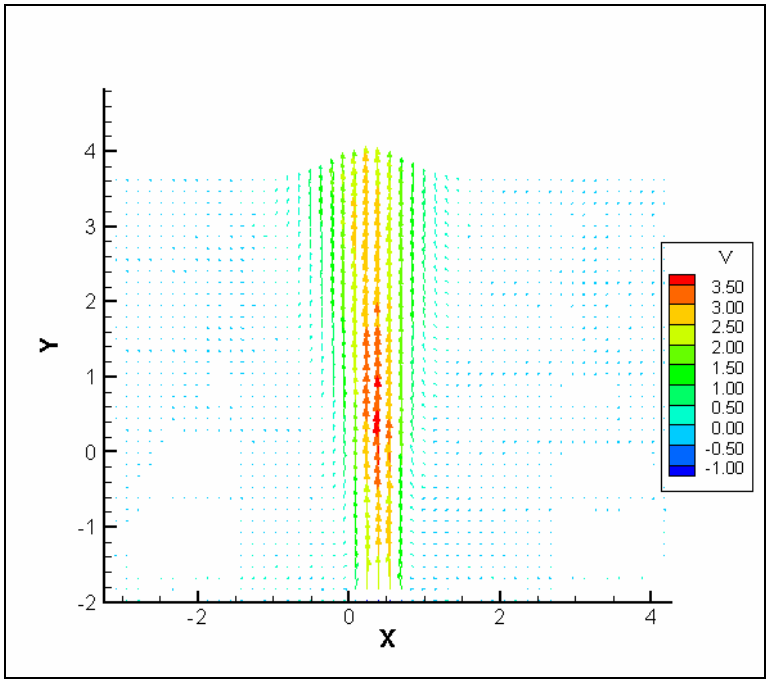

FIGURE C.1.7. Average velocity vector field downstream of the 800 µm round orifice. The pulse separation was 5 µs. Velocity in m/s is color coded according to the legend.

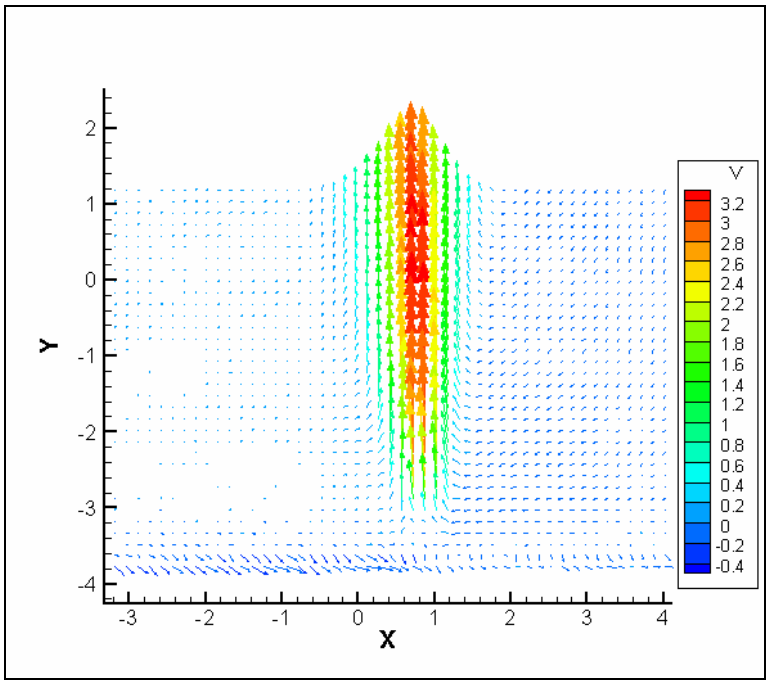

FIGURE C.1.8. Average velocity vector field downstream of the 800 µm round orifice. The pulse separation was 10 µs. Velocity in m/s is color coded according to the legend.

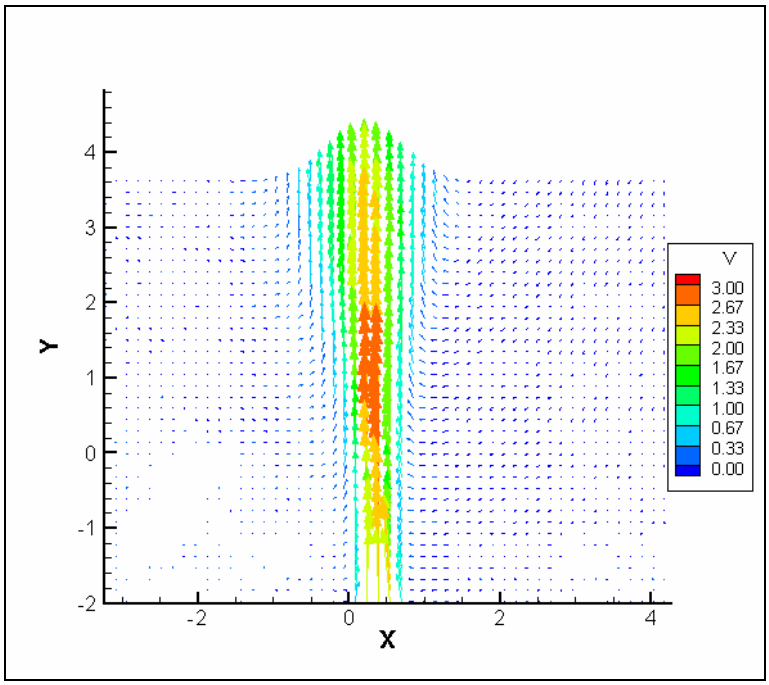

FIGURE C.1.9. Average velocity vector field downstream of the 800 µm round orifice (1500 RPM). The pulse separation was 10 µs. Velocity in m/s is color coded according to the legend.

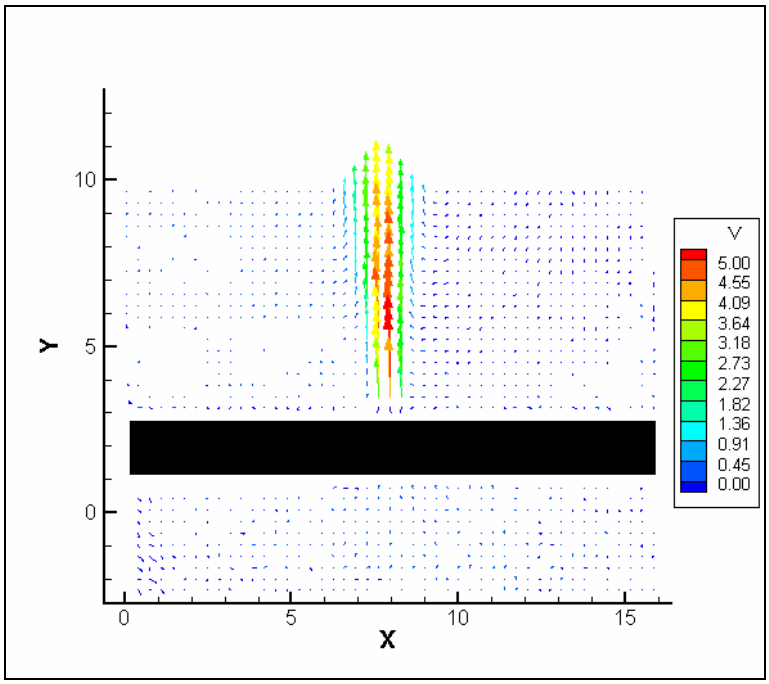

FIGURE C.1.10. Average velocity vector field upstream and downstream of the 1200 µm round orifice. The pulse separation was 10 µs. Velocity in m/s is color coded according to the legend.

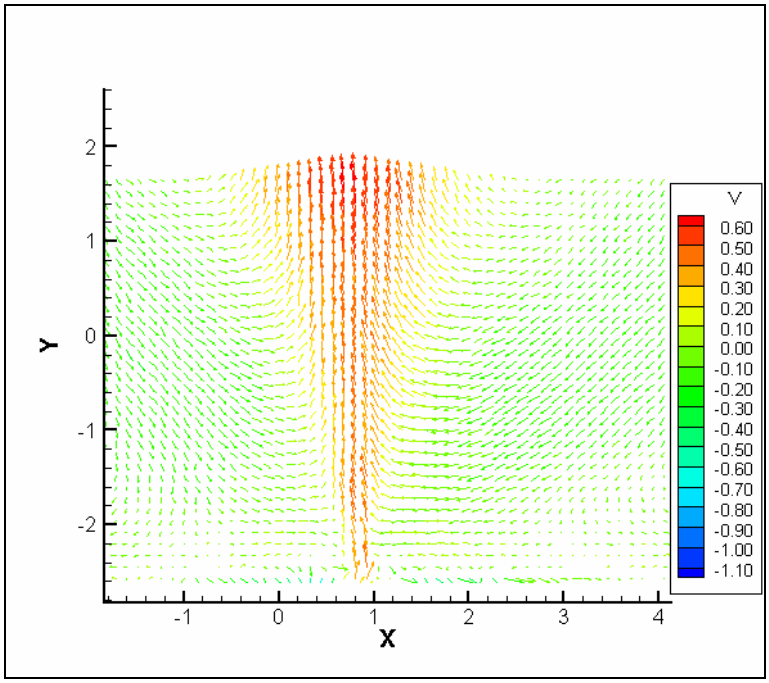

FIGURE C.1.11. Average velocity vector field downstream of the 200 µm slit orifice. The pulse separation was 5 µs. Velocity in m/s is color coded according to the legend.

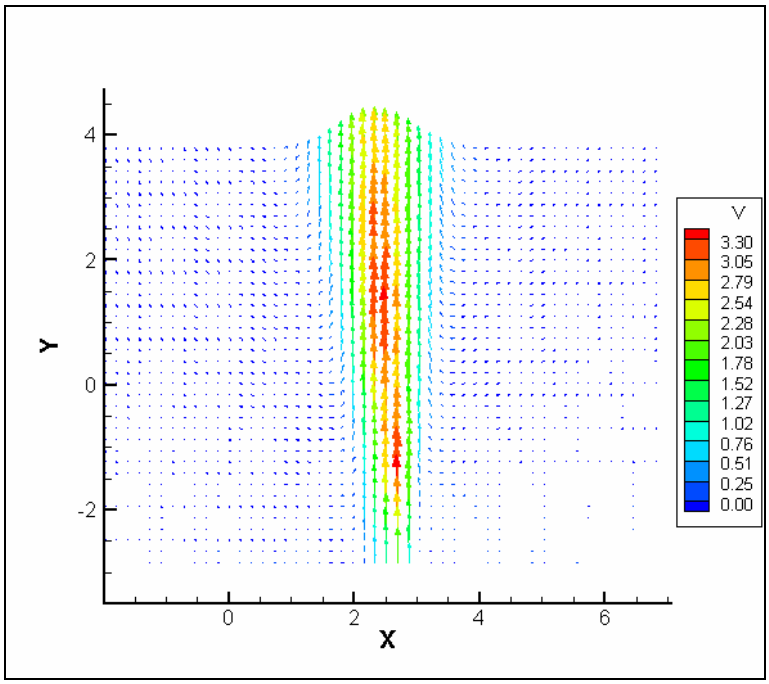

FIGURE C.1.12. Average velocity vector field downstream of Channel 4. The pulse separation was 10 µs. Velocity in m/s is color coded according to the legend.

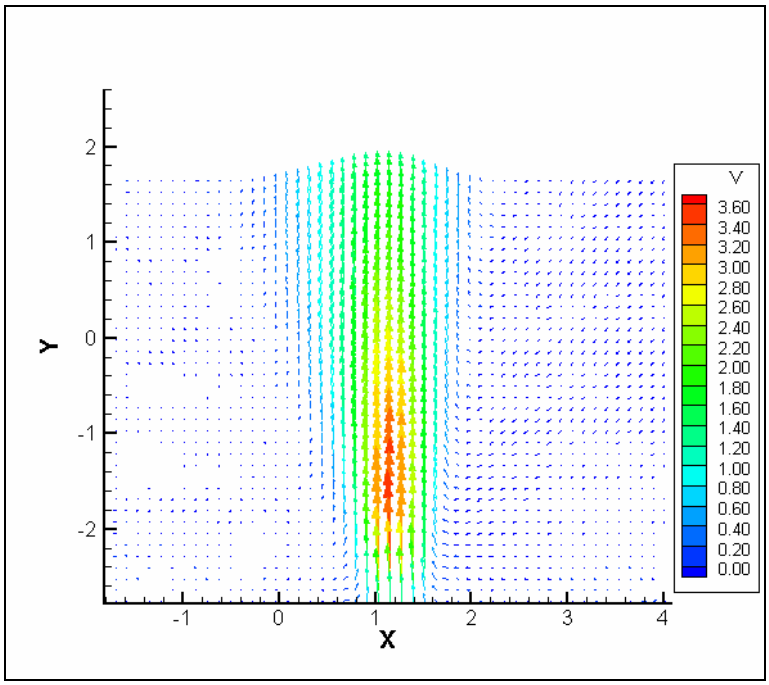

FIGURE C.1.13. Average velocity vector field downstream of Channel 8. The pulse separation was 5 µs. Velocity in m/s is color coded according to the legend.

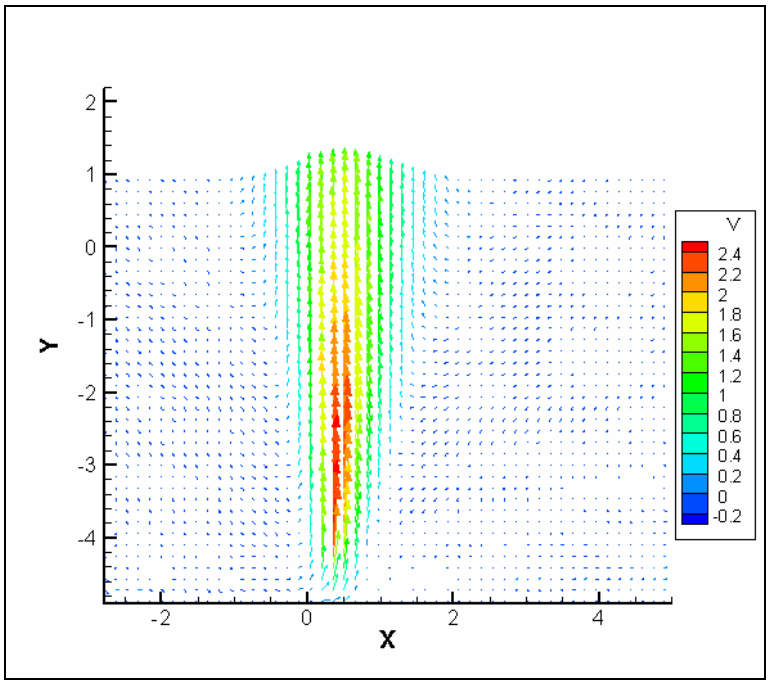

C.1.14. Average velocity vector field downstream of Channel 8. The pulse separation was 10 μs. Velocity in m/s is color coded according to the legend.

C.2. PReS Plots

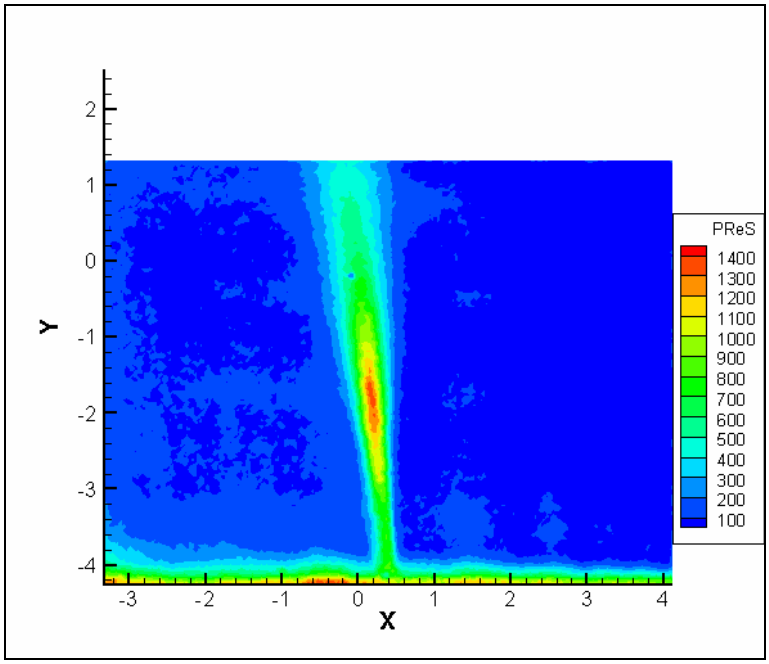

FIGURE C.2.1. Principal Reynolds stress (PReS) field for the 400 µm round orifice jet. Pulse separation was 15 µs. PReS units are dyn/cm^2. PRes magnitudes are color coded according to the legend.

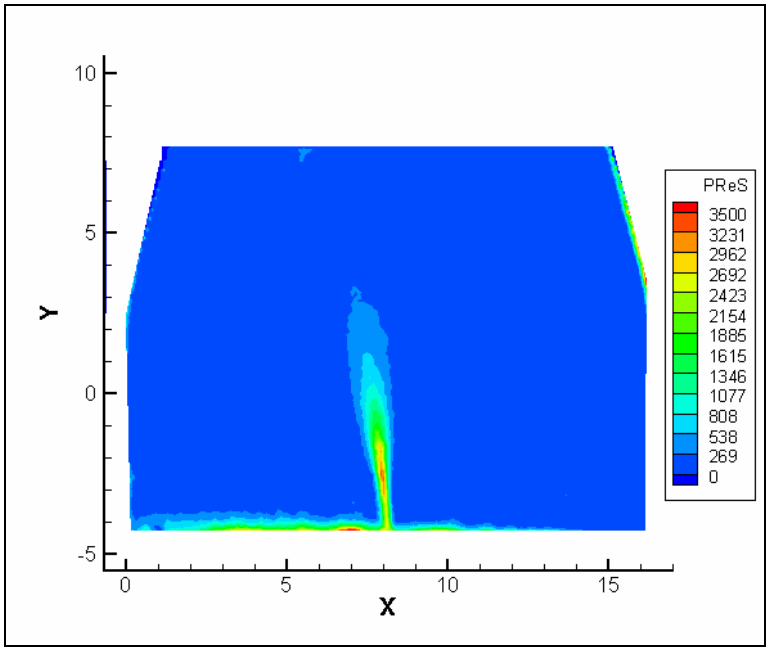

FIGURE C.2.2. Principal Reynolds stress (PReS) field for the 400 µm round orifice jet. Pulse separation was 15 µs. PReS units are dyn/cm^2. PRes magnitudes are color coded according to the legend.

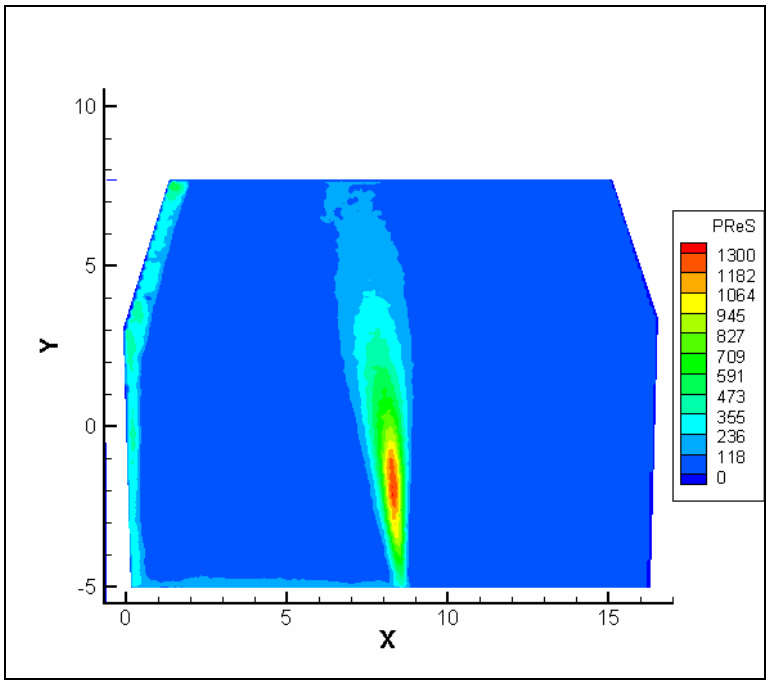

FIGURE C.2.3. Principal Reynolds stress (PReS) field for the 400 µm round orifice jet. Pulse separation was 15 µs. PReS units are dyn/cm^2. PRes magnitudes are color coded according to the legend.

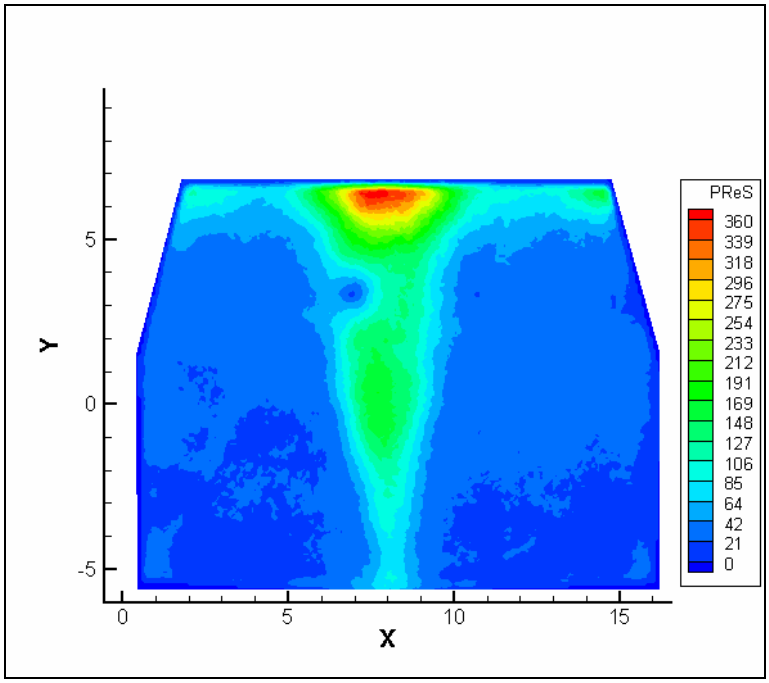

FIGURE C.2.4. Principal Reynolds stress (PReS) field for the 800 µm round orifice jet. Pulse separation was 400 µs. PReS units are dyn/cm^2. PRes magnitudes are color coded according to the legend.

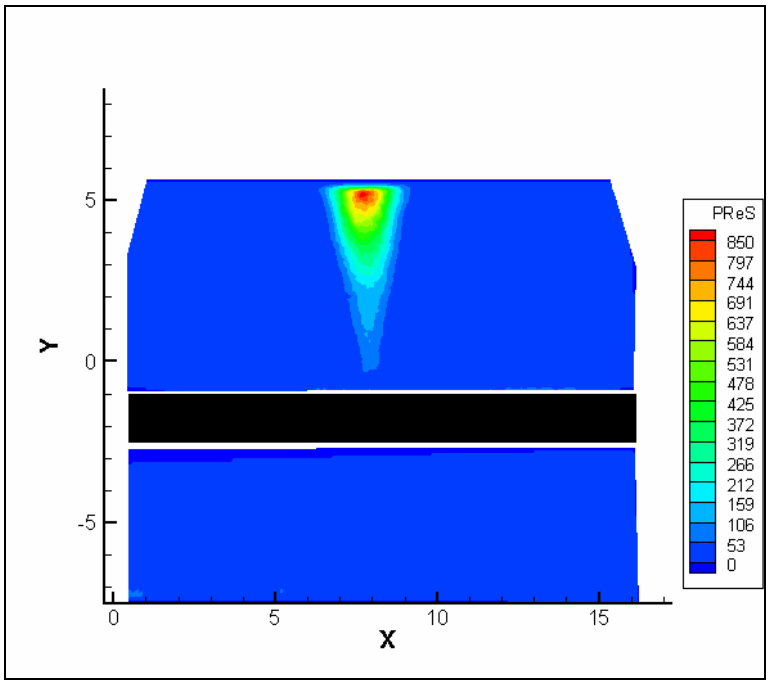

FIGURE C.2.5. Principal Reynolds stress (PReS) field for the 800 µm round orifice jet. Pulse separation was 200 µs. PReS units are dyn/cm^2. PRes magnitudes are color coded according to the legend.

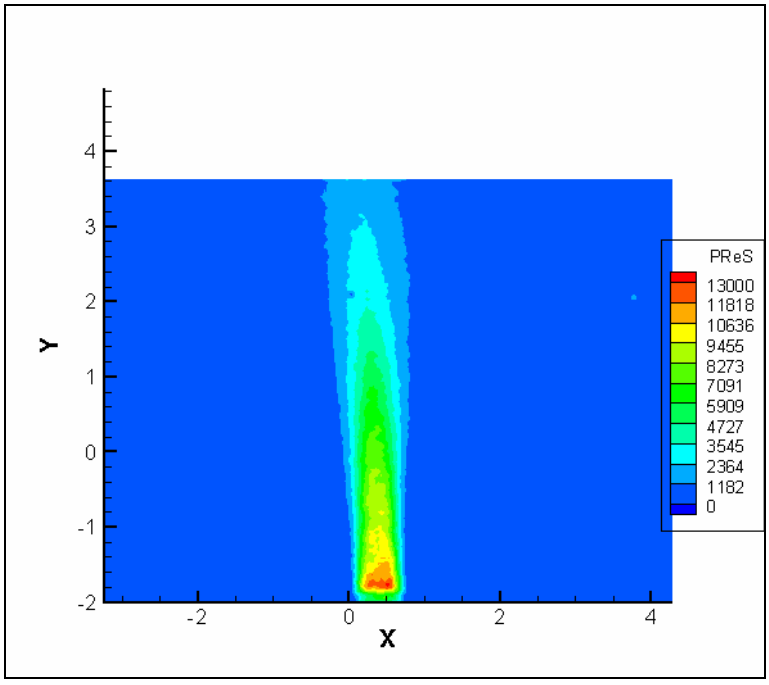

FIGURE C.2.6. Principal Reynolds stress (PReS) field for the 800 µm round orifice jet. Pulse separation was 5 µs. PReS units are dyn/cm^2. PRes magnitudes are color coded according to the legend.

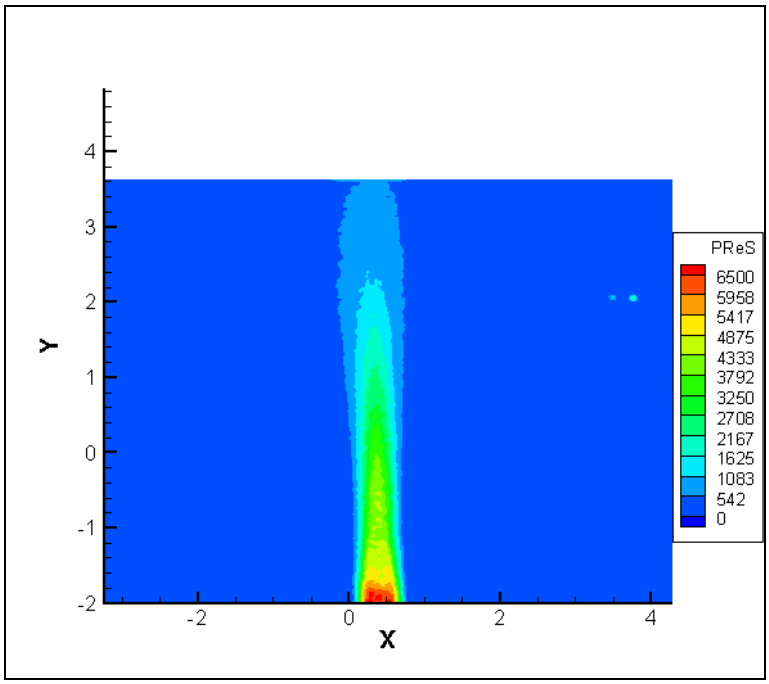

FIGURE C.2.7. Principal Reynolds stress (PReS) field for the 800 µm round orifice jet (1500 RPM). Pulse separation was 5 µs. PReS units are dyn/cm^2. PRes magnitudes are color coded according to the legend.

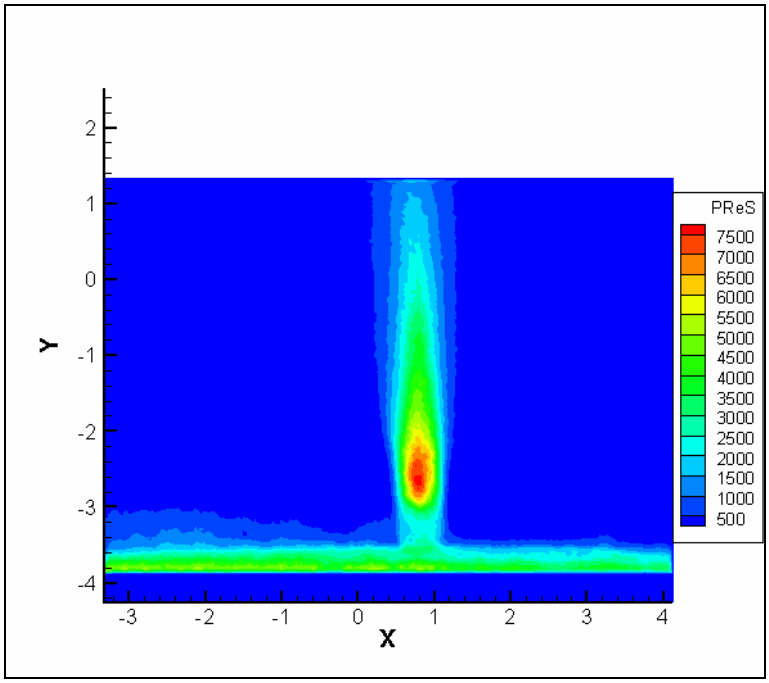

FIGURE C.2.8. Principal Reynolds stress (PReS) field for the 800 µm round orifice jet. Pulse separation was 10 µs. PReS units are dyn/cm^2. PRes magnitudes are color coded according to the legend.

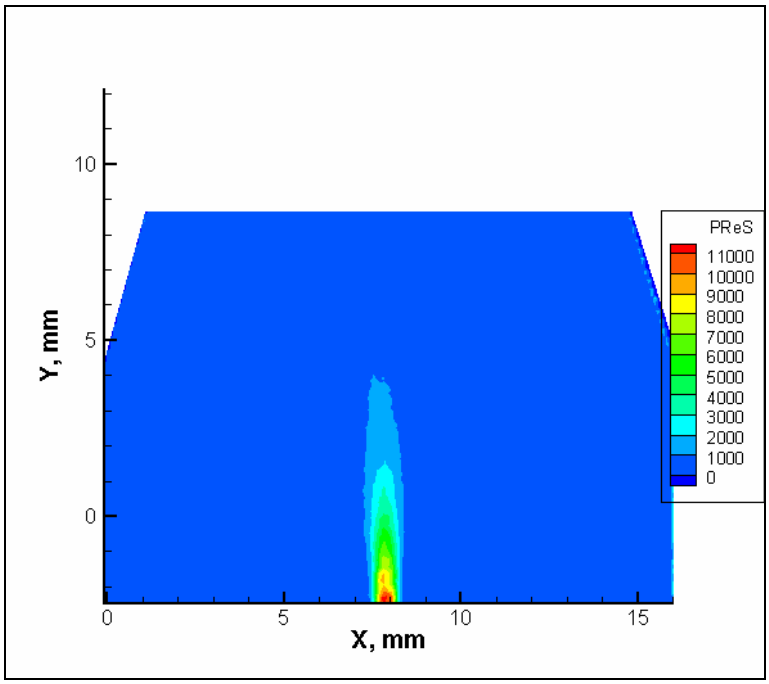

FIGURE C.2.9. Principal Reynolds stress (PReS) field for the 800 µm round orifice jet. Pulse separation was 8 µs. PReS units are dyn/cm^2. PRes magnitudes are color coded according to the legend.

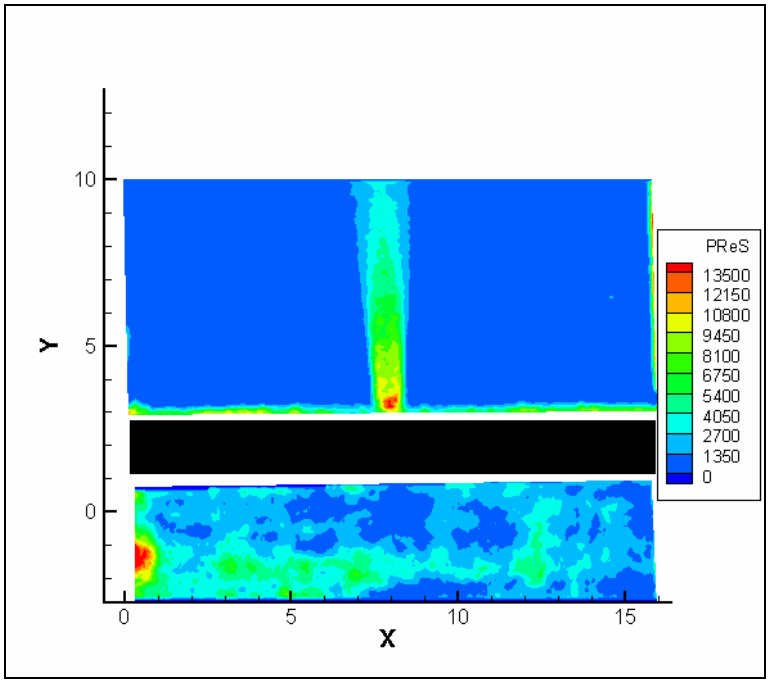

FIGURE C.2.10. Principal Reynolds stress (PReS) field for the 1200 µm round orifice jet. Pulse separation was 10 µs. PReS units are dyn/cm^2. PRes magnitudes are color coded according to the legend.

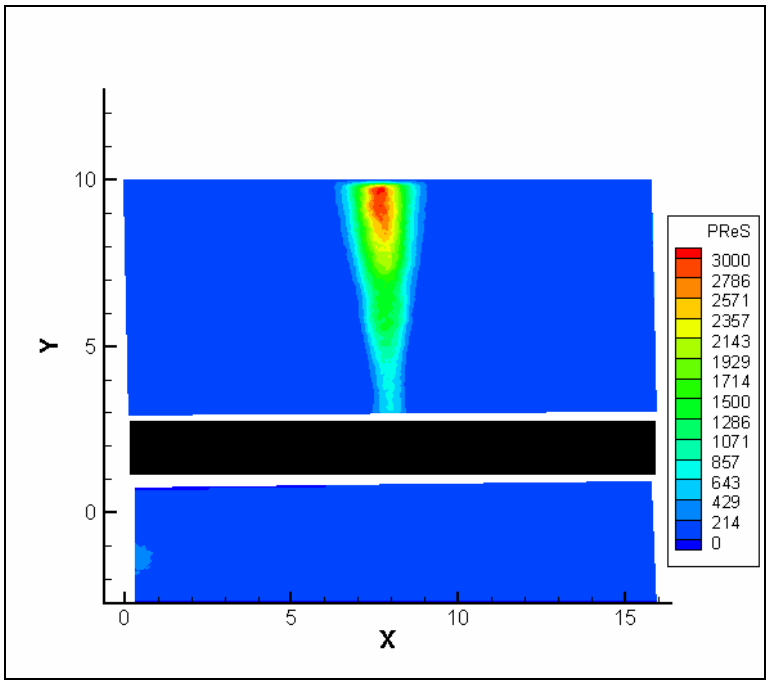

FIGURE C.2.11. Principal Reynolds stress (PReS) field for the 1200 µm round orifice jet. Pulse separation was 75 µs. PReS units are dyn/cm^2. PRes magnitudes are color coded according to the legend.

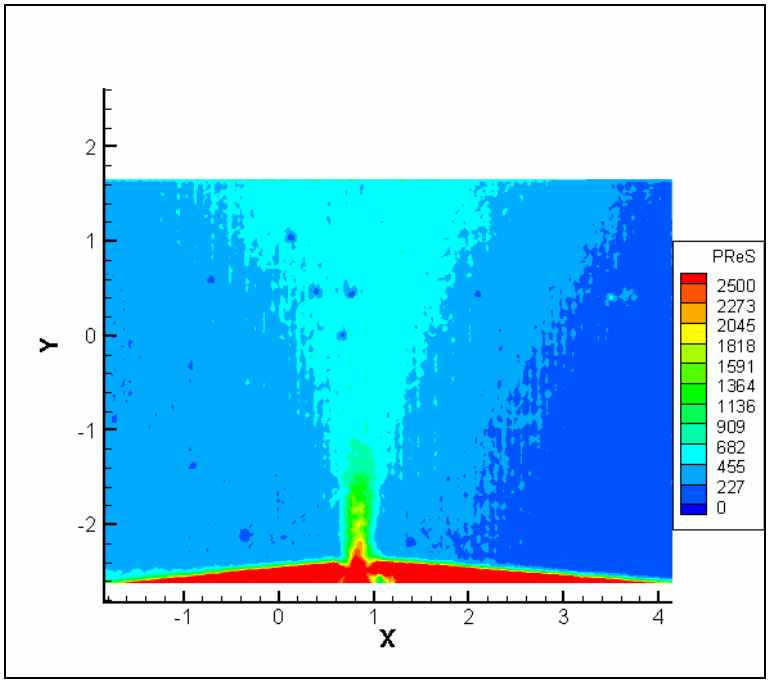

FIGURE C.2.12. Principal Reynolds stress (PReS) field for the 200 µm slit orifice jet. Pulse separation was 5 µs. PReS units are dyn/cm^2. PRes magnitudes are color coded according to the legend.

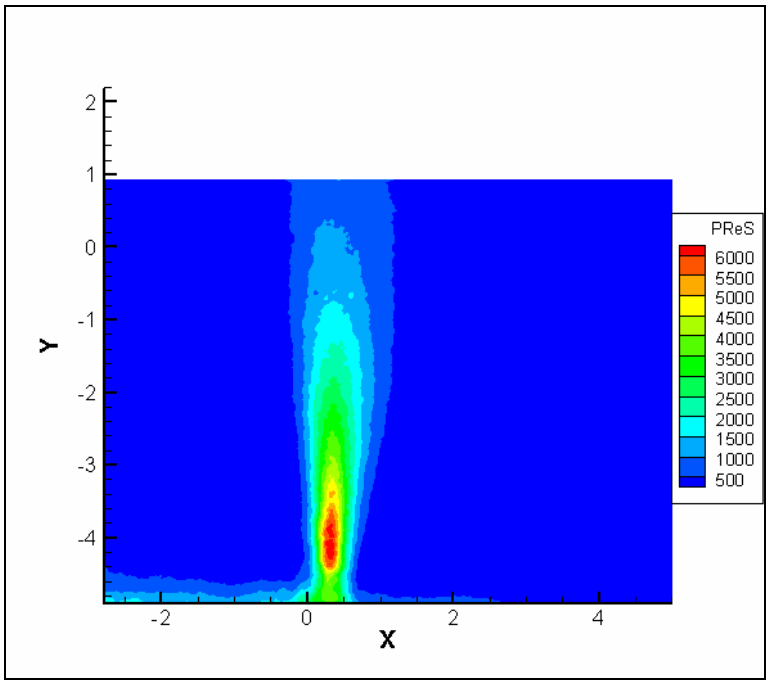

FIGURE C.2.13. Principal Reynolds stress (PReS) field for the Channel 8 jet. Pulse separation was 10 μs. PReS units are dyn/cm^2. PRes magnitudes are color coded according to the legend.

BIBLIOGRAPHY

1. Guyton AC, Hall JE. Textbook of Medical Physiology. Tenth ed. Philadelphia, PA: W.B. Saunders Company; 2000.

2. Yoganathan AP, He Z, Jones SC. Fluid Mechanics of Heart Valves. Annu Rev Biomed Eng. 2004;6:331-62.

3. AHA. Heart Disease and Stroke Statistics; 2004.

4. DeWall RA, Qasim N, Carr L. Evolution of mechanical heart valves. Ann Thorac Surg. 2000 May;69(5):1612-21.

5. Hufnagel CA, Gillespie JF, Conrad PW, Mercier C, Evangelist FA. Cardiac valve replacement-its current status. Med Ann Dist Columbia. 1966 Sep;35(9):457-62.

6. Grunkemeier GL, Li HH, Naftel DC, Starr A, Rahimtoola SH. Long-term performance of heart valve prostheses. Curr Probl Cardiol. 2000 Feb;25(2):73-154.

7. Anderson JM. Interactions of Blood with Artificial Surfaces. In: Butchart EGB, Endre, editor. Thrombosis, Embolism and Bleeding. United Kingdom: ICR Publishers; 1992. p. 160-71.

8. Butchart EG. Thrombogenicity, Thrombosis and Embolism. In: Butchart EGB, Endre, editor. Thrombosis, Embolism and Bleeding. United Kingdom: ICR Publishers; 1992. p. 172-205.

9. Yoganathan AP, Chaux A, Gray RJ, Woo YR, DeRobertis M, Williams FP, et al. Bileaflet, tilting disc and porcine aortic valve substitutes: in vitro hydrodynamic characteristics. J Am Coll Cardiol. 1984 Feb;3(2 Pt 1):313-20.

10. Yoganathan AP, Travis BR. Fluid Dynamics of Prosthetic Valves. In: Otto CM, editor. The Practice of Clinical Echocardiography. 2 ed; 2000.

11. Yoganathan AP, Wick TM, Reul H. Influence of Flow Characteristics of Prosthetic Valves on Thrombus Formation. In: Butchart EG, Bodnar E, editors. Thrombosis, Embolism and Bleeding. United Kingdom: ICR Publishers; 1992. p. 123-48.

12. Walker PGY, A.P. In vitro pulsatile flow hemodynamics of five mechanical aortic heart valve prostheses. Eur J Cardio-thorac Surg. 1992;6(suppl. 1):S113-S23.

13. Ellis JTT, B.R.; Yoganathan, A.P. An in vitro study of the hinge and near-field forward flow dynamics of the St. Jude Medical Regent bileaflet mechanical heart valve. Ann Biomed Eng. 2000;28(5):524-32.

14. Liu JSL, P.C.; Chu, S.H. Turbulence Characteristics Downstream of Bileaflet Aortic Valve Prostheses. Transactions of the ASME 2000;122:118-24.

15. Ellis JT, Healy TM, Fontaine AA, Saxena R, Yoganathan AP. Velocity measurements and flow patterns within the hinge region of a Medtronic Parallel bileaflet mechanical valve with clear housing. J Heart Valve Dis. 1996 Nov;5(6):591-9.

16. Steegers A, Paul R, Reul H, Rau G. Leakage flow at mechanical heart valve prostheses: improved washout or increased blood damage? J Heart Valve Dis. 1999 May;8(3):312-23.

17. Travis BR, Leo HL, Shah PA, Frakes DH, Yoganathan AP. An analysis of turbulent shear stresses in leakage flow through a bileaflet mechanical prostheses. J Biomech Eng. 2002 Apr;124(2):155-65.

18. Cape EG, Yoganathan AP, Levine RA. A new theoretical model for noninvasive quantification of mitral regurgitation. J BIOMECH. 1990;23(1):27-33.

19. Cape EG, Skoufis EG, Weyman AE, Yoganathan AP, Levine RA. A new method for noninvasive quantification of valvular regurgitation based on conservation of momentum. In vitro validation. Circulation. 1989 Jun;79(6):1343-53.

20. Rodriguez R. 1989.

21. Cape EG, Nanda NC, Yoganathan AP. Quantification of regurgitant flow through bileaflet heart valve prostheses: theoretical and in vitro studies. Ultrasound Med Biol. 1993;19(6):461-8.

22. Travis BR, Christensen TD, Smerup M, Olsen MS, Hasenkam JM, Nygaard H. In-vivo turbulent stresses of bileaflet prosthesis leakage jets. J Heart Valve Dis. 2005 Sep;14(5):644-56.

23. Gross JM, Shu MC, Dai FF, Ellis J, Yoganathan AP. A microstructural flow analysis within a bileaflet mechanical heart valve hinge. J Heart Valve Dis. 1996 Nov;5(6):581-90.

24. Leo HL, He Z, Ellis JT, Yoganathan AP. Microflow fields in the hinge region of the CarboMedics bileaflet mechanical heart valve design. J Thorac Cardiovasc Surg. 2002 Sep;124(3):561-74.

25. Leo HL. Investigation of flow fields through trileaflet polymeric and bileaflet mechanical heart valves. Atlanta: Georgia Institute of Technology; 2005.

26. Simon HA, Leo HL, Carberry J, Yoganathan AP. Comparison of the hinge flow fields of two bileaflet mechanical heart valves under aortic and mitral conditions. Ann Biomed Eng. 2004 Dec;32(12):1607-17.

27. Saxena R, Lemmon J, Ellis J, Yoganathan A. An in vitro assessment by means of laser Doppler velocimetry of the medtronic advantage bileaflet mechanical heart valve hinge flow. J Thorac Cardiovasc Surg. 2003 Jul;126(1):90-8.

28. Healy TM, Ellis JT, Fontaine AA, Jarrett CA, Yoganathan AP. An automated method for analysis and visualization of laser Doppler velocimetry data. Ann Biomed Eng. 1997 Mar-Apr;25(2):335-43.

29. Wang J, Yao H, Lim CJ, Zhao Y, Yeo TJ, Hwang NH. Computational fluid dynamics study of a protruded-hinge bileaflet mechanical heart valve. J Heart Valve Dis. 2001 Mar;10(2):254-62; discussion 63.

30. Kini V, Bachmann C, Fontaine A, Deutsch S, Tarbell JM. Integrating particle image velocimetry and laser Doppler velocimetry measurements of the regurgitant flow field past mechanical heart valves. Artif Organs. 2001 Feb;25(2):136-45.

31. Subramanian A, Mu H, Kadambi JR, Wernet MP, Brendzel AM, Harasaki H. Particle image velocimetry investigation of intravalvular flow fields of a bileaflet mechanical heart valve in a pulsatile flow. J Heart Valve Dis. 2000 Sep;9(5):721-31.

32. Hoffman M, Monroe DM, 3rd. A cell-based model of hemostasis. Thromb Haemost. 2001 Jun;85(6):958-65.

33. Cadena DL. 1994.

34. Chow TW, Hellums JD, Moake JL, Kroll MH. Shear stress-induced von Willebrand factor binding to platelet glycoprotein Ib initiates calcium influx associated with aggregation. Blood. 1992 Jul 1;80(1):113-20.

35. Ruggeri ZM. Mechanisms of shear-induced platelet adhesion and aggregation. Thromb Haemost. 1993 Jul 1;70(1):119-23.

36. Englund GD, Bodnar RJ, Li Z, Ruggeri ZM, Du X. Regulation of von Willebrand factor binding to the platelet glycoprotein Ib-IX by a membrane skeleton-dependent inside-out signal. J Biol Chem. 2001 May 18;276(20):16952-9.

37. Shankaran H, Alexandridis P, Neelamegham S. Aspects of hydrodynamic shear regulating shear-induced platelet activation and self-association of von Willebrand factor in suspension. Blood. 2003 Apr 1;101(7):2637-45.

38. Mazzucato M, Pradella P, Cozzi MR, De Marco L, Ruggeri ZM. Sequential cytoplasmic calcium signals in a 2-stage platelet activation process induced by the glycoprotein Ibalpha mechanoreceptor. Blood. 2002 Oct 15;100(8):2793-800.

39. Ruggeri ZM. Mechanisms initiating platelet thrombus formation. Thromb Haemost. 1997 Jul;78(1):611-6.

40. Goto S, Ikeda Y, Saldivar E, Ruggeri ZM. Distinct mechanisms of platelet aggregation as a consequence of different shearing flow conditions. J Clin Invest. 1998 Jan 15;101(2):479-86.

41. Ikeda Y, Handa M, Kawano K, Kamata T, Murata M, Araki Y, et al. The role of von Willebrand factor and fibrinogen in platelet aggregation under varying shear stress. J Clin Invest. 1991 Apr;87(4):1234-40.

42. Savage B, Saldivar E, Ruggeri ZM. Initiation of platelet adhesion by arrest onto fibrinogen or translocation on von Willebrand factor. Cell. 1996 Jan 26;84(2):289-97.

43. Matsui H, Sugimoto M, Mizuno T, Tsuji S, Miyata S, Matsuda M, et al. Distinct and concerted functions of von Willebrand factor and fibrinogen in mural thrombus growth under high shear flow. Blood. 2002 Nov 15;100(10):3604-10.

44. Joist JH, Bauman JE, Sutera SP. Platelet adhesion and aggregation in pulsatile shear flow: effects of red blood cells. Thromb Res. 1998 Dec 15;92(6 Suppl 2):S47-52.

45. O'Brien JR. Shear-induced platelet aggregation. Lancet. 1990 Mar 24;335(8691):711-3.

46. Nesbitt WS, Giuliano S, Kulkarni S, Dopheide SM, Harper IS, Jackson SP. Intercellular calcium communication regulates platelet aggregation and thrombus growth. J Cell Biol. 2003 Mar 31;160(7):1151-61.

47. Schoephoerster RT, Oynes F, Nunez G, Kapadvanjwala M, Dewanjee MK. Effects of local geometry and fluid dynamics on regional platelet deposition on artificial surfaces. Arterioscler Thromb. 1993 Dec;13(12):1806-13.

48. Lamson TC, Rosenberg G, Geselowitz DB, Deutsch S, Stinebring DR, Frangos JA, et al. Relative blood damage in the three phases of a prosthetic heart valve flow cycle. Asaio J. 1993 Jul-Sep;39(3):M626-33.

49. Travis BR, Marzec UM, Leo HL, Momin T, Sanders C, Hanson SR, et al. Bileaflet aortic valve prosthesis pivot geometry influences platelet secretion and anionic phospholipid exposure. Ann Biomed Eng. 2001 Aug;29(8):657-64.

50. Bluestein D, Yin W, Affeld K, Jesty J. Flow-induced platelet activation in mechanical heart valves. J Heart Valve Dis. 2004 May;13(3):501-8.

51. Maugeri N, Santarelli MT, Lazzari MA. Circulating platelet/polymorphonuclear leukocyte mixed-cell aggregates in patients with mechanical heart valve replacement. Am J Hematol. 2000 Oct;65(2):93-8.

52. Francis JL. Platelet dysfunction detected at high shear in patients with heart valve disease. Platelets. 2000 May;11(3):133-6.

53. Chang BC, Lim SH, Kim DK, Seo JY, Cho SY, Shim WH, et al. Long-term results with St. Jude Medical and CarboMedics prosthetic heart valves. J Heart Valve Dis. 2001 Mar;10(2):185-94; discussion95.

54. Sparrow E, Lin S, Lundgren T. Flow Development In The Hydrodynamic Entrance Region Of Tubes And Ducts. Phys Fluids. 1964;7(3):338-47.

55. Bounameaux H, de Moerloose P, Perrier A, Reber G. Plasma measurement of D-dimer as diagnostic aid in suspected venous thromboembolism: an overview. Thromb Haemost. 1994 Jan;71(1):1-6.

56. Dong JF, Berndt MC, Schade A, McIntire LV, Andrews RK, Lopez JA. Ristocetin-dependent, but not botrocetin-dependent, binding of von Willebrand factor to the platelet glycoprotein Ib-IX-V complex correlates with shear-dependent interactions. Blood. 2001 Jan 1;97(1):162-8.

57. Alevriadou BR, Moake JL, Turner NA, Ruggeri ZM, Folie BJ, Phillips MD, et al. Real-time analysis of shear-dependent thrombus formation and its blockade by inhibitors of von Willebrand factor binding to platelets. Blood. 1993 Mar 1;81(5):1263-76.

58. Zhang JN, Bergeron AL, Yu Q, Sun C, McBride L, Bray PF, et al. Duration of exposure to high fluid shear stress is critical in shear-induced platelet activation-aggregation. Thromb Haemost. 2003 Oct;90(4):672-8.

59. Goel MS, Diamond SL. Adhesion of normal erythrocytes at depressed venous shear rates to activated neutrophils, activated platelets, and fibrin polymerized from plasma. Blood. 2002 Nov 15;100(10):3797-803.

60. Balasubramanian V, Vele O, Nemerson Y. Local shear conditions and platelet aggregates regulate the incorporation and activity of circulating tissue factor in ex-vivo thrombi. Thromb Haemost. 2002 Nov;88(5):822-6.

61. Patel D, Vaananen H, Jirouskova M, Hoffmann T, Bodian C, Coller BS. Dynamics of GPIIb/IIIa-mediated platelet-platelet interactions in platelet adhesion/thrombus formation on collagen in vitro as revealed by videomicroscopy. Blood. 2003 Feb 1;101(3):929-36.

62. Travis BR, Marzec UM, Ellis JT, Davoodi P, Momin T, Hanson SR, et al. The sensitivity of indicators of thrombosis initiation to a bileaflet prosthesis leakage stimulus. J Heart Valve Dis. 2001 Mar;10(2):228-38.

63. Zhang JN, Bergeron AL, Yu Q, Sun C, McIntire LV, Lopez JA, et al. Platelet aggregation and activation under complex patterns of shear stress. Thromb Haemost. 2002 Nov;88(5):817-21.

64. O'Brien JR, Salmon GP. An independent haemostatic mechanism: shear induced platelet aggregation. Adv Exp Med Biol. 1990;281:287-96.

65. Pope SB. Turbulent Flows. Cambridge, United Kingdom: University Press; 2000.

66. Chhabra S, Shipman TN, Prasad AK. The entrainment behavior of a turbulent axisymmetric jet in a viscous host fluid. Experiments in Fluids. 2005 Jan;38(1):70-9.

67. Zhang JN, Wood J, Bergeron AL, McBride L, Ball C, Yu Q, et al. Effects of low temperature on shear-induced platelet aggregation and activation. J Trauma. 2004 Aug;57(2):216-23.

68. Wolberg AS, Meng ZH, Monroe DM, 3rd, Hoffman M. A systematic evaluation of the effect of temperature on coagulation enzyme activity and platelet function. J Trauma. 2004 Jun;56(6):1221-8.